Technische Universität München
Fakultät für Chemie

"*In situ* structural studies of the ciliary pore"

Hugo Guus van den Hoek

Vollständiger Abdruck der von der Fakultät für Chemie der Technischen Universität München zur Erlangung des akademischen Grades eines Doktors der Naturwissenschaften genehmigten Dissertation.

Vorsitzender:	Prof. Dr. Bernd Reif
Prüfer der Dissertation:	1. Hon.-Prof. Dr. Wolfgang Baumeister
	2. Prof. Dr. Michael Sattler

Die Dissertation wurde am 14.12.2021 bei der Technischen Universität München eingereicht und durch die Fakultät für Chemie am 30.03.2022 angenommen

To my parents, Jos and Annelies,
my sister, Hilde,
and my grandfather, Laurens, who roped me into this whole science thing.

Summary (EN)

The cilium (sometimes called *eukaryotic flagellum*) is a complex organelle protruding from the surface of eukaryotic cells. It is an ancient organelle, most likely present in the last eukaryotic common ancestor, and is therefore pervasive amongst eukaryotes. It has many important roles in eukaryotic biology, such as sensing, signaling, motility/fluid flow, reproduction, and development. Cilia are therefore found all across the body: in the airpipe (trachea), inside the brain, in kidneys, in bones, in sperm and oviducts… it's hard to find a cell that does *not* have a cilium at some point during its life cycle. Since cilia are so widespread and fulfill so many important roles, their dysfunction leads to a plethora of syndromic diseases named *ciliopathies*.

To understand more about how cilia function, one needs to consider the region where they're anchored to the cell: the ciliary base. The cilium is a non-membranous organelle, i.e., it maintains a distinct molecular composition without having a membranous barrier between it and the rest of the cell. At the base of the cilium lies the transition zone, which acts as this selective barrier without the need for a membrane. How this barrier's molecular machinery constitutes the cilium's distinct composition, with around a thousand distinct ciliary proteins, and how it regulates transport into- and out of the cilium through transport processes like *intraflagellar transport* (IFT), has been subject to study for decades now. Yet, no comprehensive structural studies have been performed on the *native* (unaltered, natural state) ciliary base and transition zone. Unfortunately, this region has been a blind spot for high-resolution structural studies for a long time. However, recent breakthroughs in cryo-electron tomography (cryo-ET) have opened doors which now allow this region to be examined in great detail.

In this thesis, I'll show the results of two studies that utilize these recent advancements in cryo-ET with focused ion beam milling of vitrified frozen cells, targeting the ciliary base. We present the first native structure of the ciliary base in algae and in mammalian cells. We used two model systems: *Chlamydomonas reinhardtii*, a biflagellate green alga which is a model organism for both ciliary- and broader eukaryotic cell biology, and multiciliated mouse tracheal epithelial cells (MTECs), which provide a step up towards therapeutic research on cilia by providing a mammalian cellular context.

We found that in *Chlamydomonas*, IFT pre-assembles in the periciliary cytoplasm prior to ciliary entry through the transition zone. We found that the train-like assemblies they form, pre-assemble in a specific sequential order. Using limited data, we moreover obtained a comprehensive *in-situ* map of the entire native-state transition zone, in which we mapped back structural averages of each component. We also found a novel structure there, decorating microtubule doublets (MTDs) at the site where the flagella can sever off the cell body, which we named the MTD Sleeve. We moreover combined our method with a technique in fluorescence light microscopy called ultrastructure expansion microscopy, which further complemented and deepened our insights.

We then applied the same methodology to the ciliary base in MTECs, from which we got a wealth of data, which we're still analyzing. I'll show the most current advancements on this project, which include structural averages of microtubule-associated structures specific to the transition zone, as well as a distinct ring at the apical end of the basal body.

Understanding the molecular machinery that underpins ciliary function will pave the way to future therapeutic options. We believe this work makes great strides towards fully understanding this enigmatic and important region of the cell.

Zusammenfassung (DE)

Das Cilium (manchmal auch als eukaryotisches Flagellum bezeichnet) ist ein komplexes Organell, das aus der Oberfläche von eukaryotischen Zellen herausragt. Es handelt sich um eine uralte Organelle, die wahrscheinlich schon beim letzten gemeinsamen Vorfahren der Eukaryoten vorhanden war und daher in allen Eukaryoten vorkommt. Es spielt in der Biologie der Eukaryoten viele wichtige Rollen, z.B. bei der Wahrnehmung, der Signalgebung, der Motilität/Flüssigkeitsströmung, der Fortpflanzung und der Entwicklung. Zilien sind daher überall im Körper zu finden: in der Luftröhre (Trachea), im Gehirn, in den Nieren, in den Knochen, in Spermien und Eileitern... es ist schwer, eine Zelle zu finden, die nicht irgendwann in ihrem Lebenszyklus ein Zilium hat. Da Zilien so weit verbreitet sind und so viele wichtige Aufgaben erfüllen, führt ihre Fehlfunktion zu einer Fülle von syndromalen Krankheiten, die als Ziliopathien bezeichnet werden.

Um mehr über die Funktionsweise der Zilien zu erfahren, muss man die Region betrachten, in der sie in der Zelle verankert sind: die Zilienbasis. Das Zilium ist eine nicht-membranöse Organelle, d.h. es behält eine bestimmte molekulare Zusammensetzung bei, ohne dass eine Barriere in Form einer Membran zwischen ihm und dem Rest der Zelle besteht. An der Basis des Ziliums liegt die Übergangszone, die als diese selektive Barriere fungiert, ohne dass eine Membran erforderlich ist. Wie die molekulare Maschinerie dieser Barriere die besondere Zusammensetzung des Ziliums mit etwa tausend verschiedenen ziliaren Proteinen ausmacht und wie sie den Transport in das und aus dem Zilium durch Transportprozesse wie den intraflagellaren Transport (IFT) reguliert, ist seit Jahrzehnten Gegenstand von Studien. Bisher wurden jedoch keine umfassenden strukturellen Studien an der nativen (unveränderten, natürlichen) ziliaren Basis und Übergangszone durchgeführt. Leider war diese Region lange Zeit ein blinder Fleck für hochauflösende Strukturstudien. Jüngste Durchbrüche in der Kryo-Elektronentomographie (Kryo-ET) haben jedoch Türen geöffnet, die es nun ermöglichen, diese Region sehr detailliert zu untersuchen.

In dieser Arbeit werde ich die Ergebnisse von zwei Studien vorstellen, die diese jüngsten Fortschritte in der Kryo-ET mit fokussiertem Ionenstrahlfräsen von vitrifizierten, gefrorenen Zellen nutzen und dabei die Ziliarbasis ins Visier nehmen. Wir präsentieren die native Struktur der Ziliarbasis in Algen und in Säugetierzellen. Dafür haben wir zwei Modellsysteme verwendet: *Chlamydomonas reinhardtii*, eine biflagellate Grünalge, die ein Modellorganismus sowohl für die Zilien- als auch für die breitere eukaryotische Zellbiologie ist, und multiziliierte tracheale Epithelzellen der Maus (MTECs), die einen Schritt weiter in Richtung therapeutischer Forschung an Zilien gehen, indem sie einen zellulären Kontext für Säugetiere bieten.

Wir fanden heraus, dass sich die IFT in Chlamydomonas im periziliären Zytoplasma vor dem Eintritt der Zilien in die Übergangszone zusammensetzt. Wir fanden heraus, dass sich die von ihnen gebildeten zugähnlichen Assemblierungen in einer bestimmten Reihenfolge vormontieren. Unter Verwendung begrenzter Daten haben wir außerdem eine umfassende in-situ-Karte der gesamten nativen Übergangszone erstellt, in der wir die strukturellen Durchschnittswerte jeder Komponente zurückverfolgen konnten. Wir fanden dort auch eine neuartige Struktur, die Mikrotubuli-Doubletten (MTDs) an der Stelle schmückt, an der sich die Geißeln vom Zellkörper abtrennen können, und die wir MTD-Hülse nannten. Darüber hinaus kombinierten wir unsere Methode mit einer Technik der Fluoreszenzlichtmikroskopie, der Ultrastruktur-expansionsmikroskopie, die unsere Erkenntnisse weiter ergänzte und vertiefte.

Anschließend haben wir dieselbe Methode auf die Ziliarbasis in MTECs angewandt, wodurch wir eine Fülle von Daten erhalten haben, die wir noch immer auswerten. Ich werde hier die aktuellsten Fortschritte in diesem Projekt präsentieren. Dazu gehören strukturelle Durchschnittswerte von Mikrotubuli assoziierten Strukturen, die spezifisch für die Übergangszone sind, sowie ein deutlicher Ring am apikalen Ende des Basalkörpers.

Das Verständnis der molekularen Maschinerie, die der ziliaren Funktion zugrunde liegt, wird den Weg für zukünftige therapeutische Optionen ebnen. Wir glauben, dass diese Arbeit einen großen Beitrag zum vollständigen Verständnis dieser rätselhaften und wichtigen Region der Zelle leistet.

List of publications

(1) **In situ architecture of the ciliary base reveals the stepwise assembly of IFT trains**

Hugo van den Hoek, Nikolai Klena, Mareike A. Jordan, Gonzalo Alvarez Viar, Miroslava Schaffer, Philipp S. Erdmann, William Wan, Jürgen M. Plitzko, Wolfgang Baumeister, Gaia Pigino, Virginie Hamel, Paul Guichard, Benjamin D. Engel

BioRxiv pre-print; under revision at Science Journal (per 2021-10-25)
Volume p. 2021.10.17.464685 October 17th 2021

Available from: https://www.biorxiv.org/content/10.1101/2021.10.17.464685v1

(2) **Architecture of the centriole cartwheel-containing region revealed by cryo-electron tomography**

Nikolai Klena, Maeva Le Guennec, Anne-Marie Tassin, **Hugo van den Hoek**, Philipp S. Erdmann, Miroslava Schaffer, Stefan Geimer, Gabriel Aeschlimann, Lubomir Kovacik, Yashar Sadian, Kenneth N. Goldie, Henning Stahlberg, Benjamin D. Engel, Virginie Hamel, Paul Guichard

EMBO Journal, volume 39(22):e106246 November 16th 2020

(3) **A helical inner scaffold provides a structural basis for centriole cohesion**

Maeva Le Guennec, Nikolai Klena, Davide Gambarotto, Marine H. Laporte, Anne-Marie Tassin, **Hugo van den Hoek**, Philipp S. Erdmann, Miroslava Schaffer, Lubomir Kovacik, Susanne Borgers, Kenneth N. Goldie, Henning Stahlberg, Michel Bornens, Juliette Azimzadeh, Benjamin D. Engel, Virginie Hamel, Paul Guichard

Science Advances, volume 6(7):eaaz4137 February 14th 2020

Table of contents

Sections marked with an asterisk (*) have not been performed by the author of this thesis

1 Introduction to cryo-electron tomography

1.1 Preface

Ever since prehistoric times, humanity has wondered about the nature of the world surrounding it, and its place therein. We've come a long way since the days of naturalistic deities and superstitions, developing proper methodologies leading to the scientific method, to try and understand the workings of the natural world. Modern microbiology started in the 17th century as part of the Enlightenment, with the advent of the humble glass lens, which for the first time allowed inquisitive naturalists to investigate vastly different scales than just the one that is observed with the naked eye. We could now not only look further upwards, with telescopes, but also further inwards, with microscopes.

Figure 1.1. Antonie van Leeuwenhoek (1632-1723).
Dubbed "grandfather of microbiology".

It was in 1675 that organisms smaller than the eye could see were observed for the very first time. This is when Dutch businessman and self-taught proto-scientist Antonie van Leeuwenhoek (Figure 1.1) first described tiny creatures, *dierkens*, swimming around in a drop of water (4). He observed these *dierkens*, later translated to English as *animalcules*, through a self-made microscope, which was not the first: that credit goes to the lens makers Hans and Zacharias Janssen, a Dutch father and son, who in the 1590s developed the first compound microscope with a whopping 9*x* magnification factor. Van Leeuwenhoek however further improved on this using a different design; simple yet powerful (Figure 1.3). its magnification factor of 275*x* was an order of magnitude greater than that of similar instruments made by his contemporaries in the 1670s, which could only go up to ~30*x*. This allowed him to be the very first to describe these *animalcules*, and his findings utterly shook the world. It was hard to believe that there was an entire world, hidden in front of our eyes, full of fantastical creatures. After the cries of disbelief and accusations of blasphemy, the real questions started to rise. Why did God create these creatures? What is their purpose in this world? How many of these *animalcules* are there around us? What effect could they have on bigger organisms?

Figure 1.2. Van Leeuwenhoek's comparison of *Giardia duodenalis* to a woodlouse.
Giardia duodenalis (left), first described in fecal matter by Van Leeuwenhoek, but here observed using SEM, and the common striped woodlouse (right), as seen by eye.

Van Leeuwenhoek ended up being a highly prolific scientist, trying to address these questions and thereby adding many more observations with his microscopes. He wrote most of it up in hundreds of letters to the *Royal Society of London,* all the way up until his death in 1723. He was the first to describe protists and bacteria, but also parts of larger organisms, such as spermatozoa and muscle fiber striations. He even went as far as to describe organisms in his own runny stool, which he described as looking like *pissebedden*, or woodlice. Looking back, this was the first documented case (at least

recognized as such) of giardiasis, caused by the unicellular gut parasite *Giardia duodenalis*, which due to its cilia looking like little legs indeed bears a faint resemblance to a woodlouse (Figure 1.2).

Van Leeuwenhoek, now dubbed "the grandfather of microbiology", was a brilliant mind who lived at the right time. He not only created the technology necessary to allow his observations to be made; he also possessed the intellect and intuition to place his observations in context, and *understand* what he was looking at. He knew which questions were most relevant to ask, and in the process of answering those, he stumbled upon a slew of other questions: the science of microbiology was born.

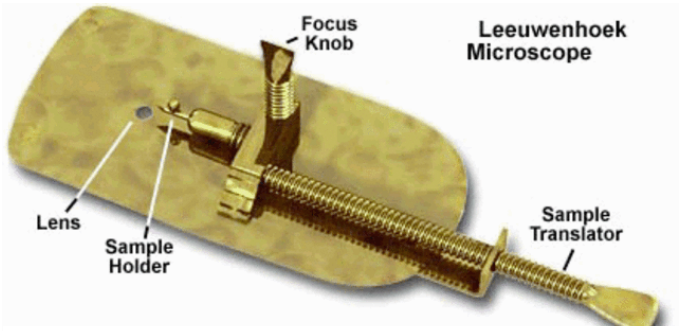

Figure 1.3. Van Leeuwenhoek's microscope.
This is a simple microscope, relying on just a single lens and a sample holder. The ~10 cm sized apparatus would be held close to the eye by hand.

However, as important as Van Leeuwenhoek's enlightened mindset was, what really lay central to the story was his invention: the light microscope. It took another ~250 years to perfect the technique of light microscopy, and over time, many improvements were made. However, by the 1930s, Ernst Ruska and Max Knoll in Berlin were pioneering an advanced microscopic technique that would bring about yet another revolution in biology: electron microscopy. The sheer resolving power of this technique is what allowed for much deeper understanding of biology, down to the molecular scale, which eventually made this thesis possible.

1.2 Basic principles of cryo-transmission electron microscopy (cryo-TEM)

1.2.1 Microscopic methods and their resolution limits

As just described, in order to ask and answer the proper questions in cellular and structural biology, it is critical one observes the right model system at the right scale. In structural biology, which is central to this thesis, many microscopic techniques are available (Figure 1.4), each with their strengths and weaknesses.

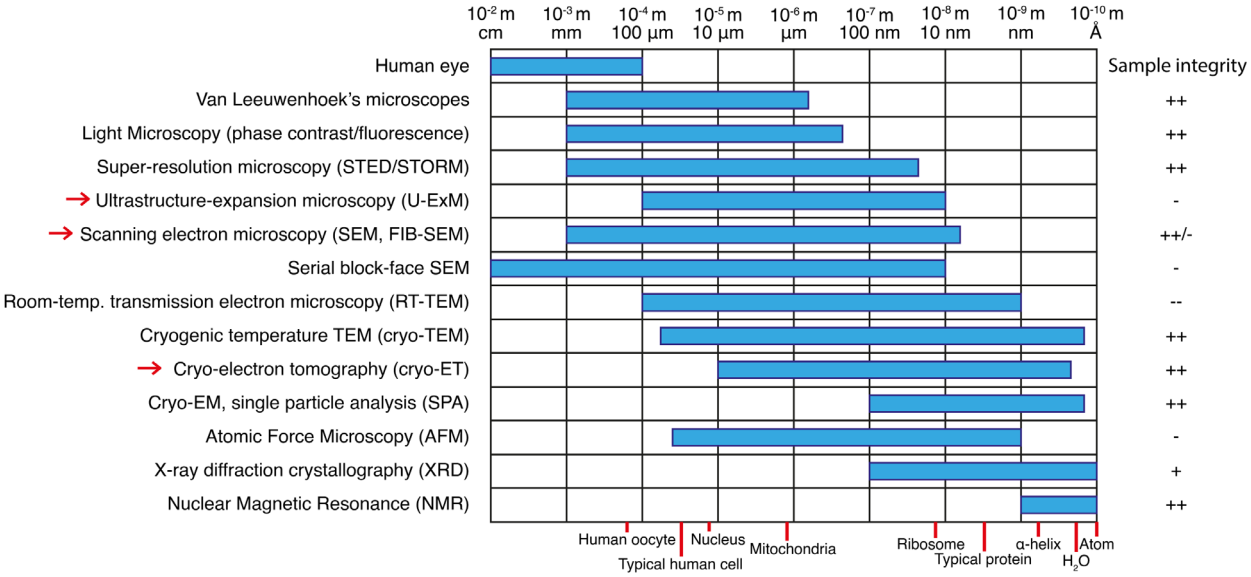

Figure 1.4. Resolution ranges of microscopic techniques often used in structural biology
The approximate resolution range for each technique is noted with a blue bar; red arrows indicate techniques used in this study. Sample integrity (how far from the natural state of the sample) is approximated ranging from -- (heavily altered) to ++ (near-native). Sizes of typical biological examples are noted below with a red marker. Scale is logarithmic.

However, maximum resolution is not the only important factor in choosing a method in structural biology. Resolution range (cellular context) and sample integrity (how closely the sample resembles the natural state, and therefore provides correct information on its biology) are just as important. The choice of method also depends heavily on which type of question you're trying to answer; for example, do you want to know something about a specific residue in a specific molecule, do you want to know the 3D structure of a protein, or are you looking at molecular machinery in a bigger cellular context? And do you care about the approximation of the native state of a system (cryo-methods), or do you just want to see cellular ultrastructure (RT-TEM on chemically fixed samples and related methods)?

Since we wanted to look at the (near-)native eukaryotic ciliary base within a larger cellular context, we opted to use mainly cryo-electron tomography (cryo-ET); however, scanning electron microscopy (SEM, in Focused Ion Beam-Scanning Electron Microscope (FIB-SEM) context) and Ultrastructure-Expansion Microscopy (U-ExM) are also used to complement this technique.

1.2.2 How the properties of electrons allow for higher resolution imaging

Electrons bear a striking resemblance to photons of light; they possess a particle-wave duality, and therefore are subject to many of the same principles as light inside a microscope. Before moving to the case of electron microscopy, let's first discuss the case of photons; their wave-like properties lead to the phenomena of diffraction, chromatic and spherical aberration, and astigmatism. Diffraction in particular poses a hard limit of what resolution one can achieve with conventional light microscopy. This diffraction limit is described by the Abbe diffraction limit formula (Equation 1):

$$d = \frac{\lambda}{2n \sin\alpha} = \frac{\lambda}{2NA}$$

Equation 1. The Abbe diffraction limit.

In which d = the minimum resolvable distance between two imaged objects, λ = the wavelength of the radiation used, n = the refractive index of the medium travelled through, and α = the half-angle of the incident radiation (how strongly the beam converges from the objective lens to the sample itself). The term "$n \sin \alpha$" is also known as the numerical aperture, or NA.

The Abbe diffraction limit leads to an inherent "blur" of any particular point source. This blur is in the form of an Airy pattern (Figure 1.5), a series of concentric rings of signal (amounting to ~16% of total intensity) around the main signal peak around the center point (amounting to ~84% of total intensity). The first zero of this function is found at ~1.22λ/NA. Now, when two point sources overlap only slightly in their central airy disc density, they can still be resolved. However, when the overlap becomes greater, at some point the added signal from the two convolves into a single peak (Figure 1.5, left and middle). The cut-off between these two situations is most often determined by the Rayleigh criterion, which is taken as half the radius (1.22λ) between center peak and first Airy disc zero (Equation 2, also Figure 1.5, right). This criterion is however chosen somewhat arbitrarily, and different cut-off values such as the Sparrow-, Abbe- and FWHM-limits will sometimes be used instead (0.47, 0.50 and 0.51 λ/NA, respectively)(5).

$$d = \frac{0.61\lambda}{NA}$$

Equation 2. The Rayleigh criterion.

In which θ = the angle in radians of the first airy zero projected away from the imaged point source, λ = the wavelength of the radiation used, and d = the width of the aperture in meters.

Looking at Equation 2, one could imagine further increasing the resolution of light microscopy by using much smaller wavelengths, such as X-rays, but that poses big challenges, since X-rays are almost impossible to properly focus: no practical X-ray lens has been developed. Moreover, X-rays cause severe radiation damage to the imaged sample. A strong beam of X-rays can however temporarily be diffracted in a protein crystal, and its scattered rays can be reconstructed through Fourier transformations into a 3D electron density model, which can have a theoretical resolution down to ~1.0 Å. This is X-ray protein crystallography, which has been the gold standard in atomic-resolution structural biology for many decades now. However, this is changing thanks to the so-called "resolution revolution" in cryo-EM (see Section 1.2.4.6).

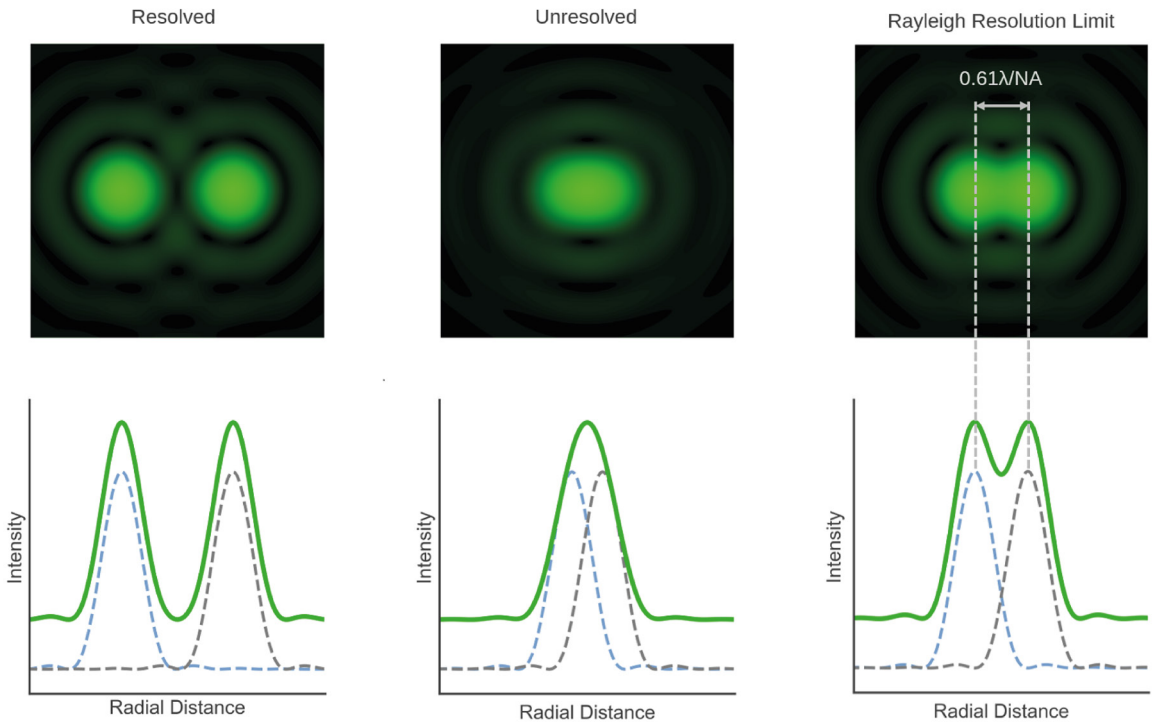

Figure 1.5. Airy discs of two overlapping point sources and the Rayleigh criterion.

Two point sources can be resolved when their peaks barely overlap (left), but not be resolved when their added signal amounts to a single peak (middle). A commonly used criterion for the cut-off between the two situations is the Rayleigh criterion (right), which is 0.61λ / NA (with NA = n sin α). Adapted from (5).

Just like photons, electrons possess a particle-wave duality. The wavelength of electrons, however, is much smaller than that of light. The behavior of electrons in a microscope can be described by a set of equations, which tie into the previous formulas (Equation 1, Equation 2), but are better at describing the wave-like behavior of electrons (or any particle, for that matter). First of all, let's consider De Broglie's equation (Equation 3), which lets us calculate the wavelength of any particle that has momentum p, meaning mass m and velocity v:

$$\lambda = \frac{h}{p} = \frac{h}{mv}$$

Equation 3. De Broglie's equation.

De Broglie's equation states that a wavelength λ can be found for any particle with momentum, by dividing Planck's constant h by the particle's momentum p, which is mass m times velocity v.

De Broglie's equation (Equation 3) allows us to consider the case of electrons accelerated through a potential difference inside the electron microscope, but first we have to take this acceleration into account (Equation 4):

$$eV = \frac{1}{2} m_0 v^2 = m_0 v$$

Equation 4. Kinetic energy of an electron undergoing acceleration.

In the case of the accelerated electron, momentum *p* can be substituted by kinetic energy *eV*, which is dependent on the rest mass of the electron m_0 times velocity *v* squared.

So, *p* in Equation 3 is substituted with Equation 4, and thus Equation 3 becomes:

$$\lambda = \frac{h}{\sqrt{2 m_0 eV}}$$

Equation 5. Wavelength of an electron undergoing acceleration.

In the case of the accelerated electron, the De Broglie wavelength is described as a function of Planck's constant *h*, electron rest mass m_0, and kinetic energy *eV*.

Equation 5 shows us that the wavelength is inversely proportional to electron acceleration. Thus, the higher the potential difference, the shorter the wavelength. However, in reality, electrons inside an electron microscope are accelerated so fast, that they take on relativistic speeds, and thus we have to account for relativistic effects. We therefore have to factor in a Lorentz factor (Equation 6):

$$\gamma = \frac{1}{\sqrt{1 - \frac{c^2}{v^2}}}$$

Equation 6. The Lorentz factor.

When considering relativistic effects, the Lorentz factor γ has to be added to an existing equation. It is dependent on the speed of light in a vacuum *c* and velocity *v*.

When substituting the Lorentz factor from Equation 6 into Equation 5 by taking $p = m_0 v$ and adding the Lorentz factor, making $p = m\gamma v$ and therefore $eV = m_0 \gamma v = m_0 \gamma v^2/2$ (from Equation 4), after some rewriting we finally get the equation that calculates the electron's wavelength at relativistic speeds (Equation 7):

$$\lambda = \frac{h}{\sqrt{2 m_0 eV \left(1 + \frac{eV}{2 m_0 c^2}\right)}}$$

Equation 7. The wavelength of electrons, taking relativistic effects into account.

When considering relativistic effects, the Lorentz factor γ has to be added to an existing equation. This can be done with Equation 4 and Equation 5, which after rewriting becomes this equation, in which factors *h* (Planck's constant), m_0 (electron rest mass), and *c* (speed of light in a vacuum) are all constants, and therefore wavelength λ is inversely proportional only to the acceleration potential *eV*.

Equation 7 allows us to calculate the wavelength of electrons accelerated in an electron microscope. In the case of the Titan Krios, the acceleration voltage *eV* amounts to ~300 kV. Plugging in the numbers gives us a corresponding electron wavelength of 1.97 picometers (6).

So, whereas photons in the visible light spectrum have a wavelength ranging from ~380 to ~720 nm, which limits them to a maximum resolution of only ~200 nm, electrons have a wavelength on the order of single picometers, so about five orders of magnitude (10^5 times) smaller. Electrons therefore possess a much greater potential for high-resolution imaging than photons, at least in theory.

In reality however, we're dealing with a non-perfect system, which introduces optical errors, mainly spherical aberration (different focal positions dependent on the distance away from the optical axis within a lens), chromatic aberration (due to the non-exact monochromaticity, or energy spread, of electrons from the electron gun), astigmatism (different focal lengths in X versus Y direction, leading to a slightly "elliptical" beam), and coma (uneven magnifications across the field of view due to misalignment of the rotation center, especially off-axis). These optical errors can to a large extent be corrected for by proper alignment of the beam throughout the microscope column. Some errors can also partially be corrected for after data acquisition.

Apart from these aberrations, other practical factors limit the resolution of electron microscopes, including radiation damage to the biological sample, signal-to-noise ratio, vibrational stability, local charging effects, and more. Therefore, in practice, the resolution of electron microscopy is ~10^3 higher than that of diffraction-limited light microscopy (LM), and ~10^2 times higher than that of non-diffraction limited LM methods (STED, STORM, PALM, etc.), which is lacking two orders of magnitude from what would be expected from wavelength limitations alone. Still, ~10^3-10^2-fold better resolution than cutting-edge light microscopy means that an entire world between hundreds of nanometers (the size of organelles) down to atomic structures in the range of single Ångströms is now made visible, and that is more than enough to address almost any structural biology question (see Figure 1.4).

1.2.3 Electron scattering modes and contrast formation

1.2.3.1 Elastic versus inelastic scattering

Electrons can scatter in a couple of different ways. Roughly speaking, there are two types of scattering (see Figure 1.6): *elastic scattering*, in which a nucleus in the sample/medium electrostatically bends the electron towards a new path, but barely takes away any of its energy, and *inelastic scattering*, which means an electron gives away a great deal of its energy by bumping into the medium it is passing through. When an electron is *elastically* scattered, it can carry information about the medium that scattered it, and due to its small energy spread (compared to unscattered or other elastically scattered electrons), it can be properly magnified by the lenses and thus used for imaging of samples in transmission electron microscopy (TEM). However, when it is *inelastically* scattered, it excites electrons in the medium to a higher orbital around their parent nucleus, and so it loses considerable energy. A variable but often significant amount of energy is lost compared to other electrons' energies, which alters the scattered electron's propensity to be bent by the lenses (see Section 1.2.4.1). This gives the electrons a randomized focal length and makes it impossible to use them for imaging in TEM. Moreover, upon inelastic scattering, the electrons in the medium emit X-rays (or other photons) as they decay back to their ground state. This is also why an electron microscope is lined with lead: to prevent these X-rays from leaking out and harming the user.

1.2.3.2 TEM, SEM, STEM and more

While only small-angle, elastically scattered electrons are useful for TEM, other EM techniques cleverly make use of the other modes of electron scattering (Figure 1.6).

For instance, elastically scattered electrons (Figure 1.6, left) can be bent strongly around nuclei, up to a full 180 degrees. These *backscattered* electrons can be observed in a technique called Scanning Electron Microscopy (SEM), which we use in the FIB-SEM microscope (see Section 1.3.7). This technique uses its electron beam to scan the surface of the sample in a rasterized manner, and measure the amount of elastically backscattered signal at each spot (hence "scanning"). This forms an image that can reveal a great deal about the surface of the sample, creating beautiful images of microscopic objects. Secondary electrons and even positive ions (knocked loose by inelastic scattering events) can also be used for SEM.

STEM, or Scanning Transmission Electron Microscopy, is related to SEM: it raster-scans (both elastically and inelastically) scattered electrons' signal at high angles away from the optical axis, but only after the electrons have passed through the sample ("transmission").

Other, more exotic techniques can also be utilized to get to know more about the sample. The photons emitted after inelastic scattering events can be observed coming out of the sample; usually these are X-rays, but they can even be photons in the visible range. The useful thing about these photons, is that they're emitted on a spectrum, which can tell you what elements are present in the sample the electron beam is hitting. This type of chemical analysis is called Electron Microprobe Analysis (EMA).

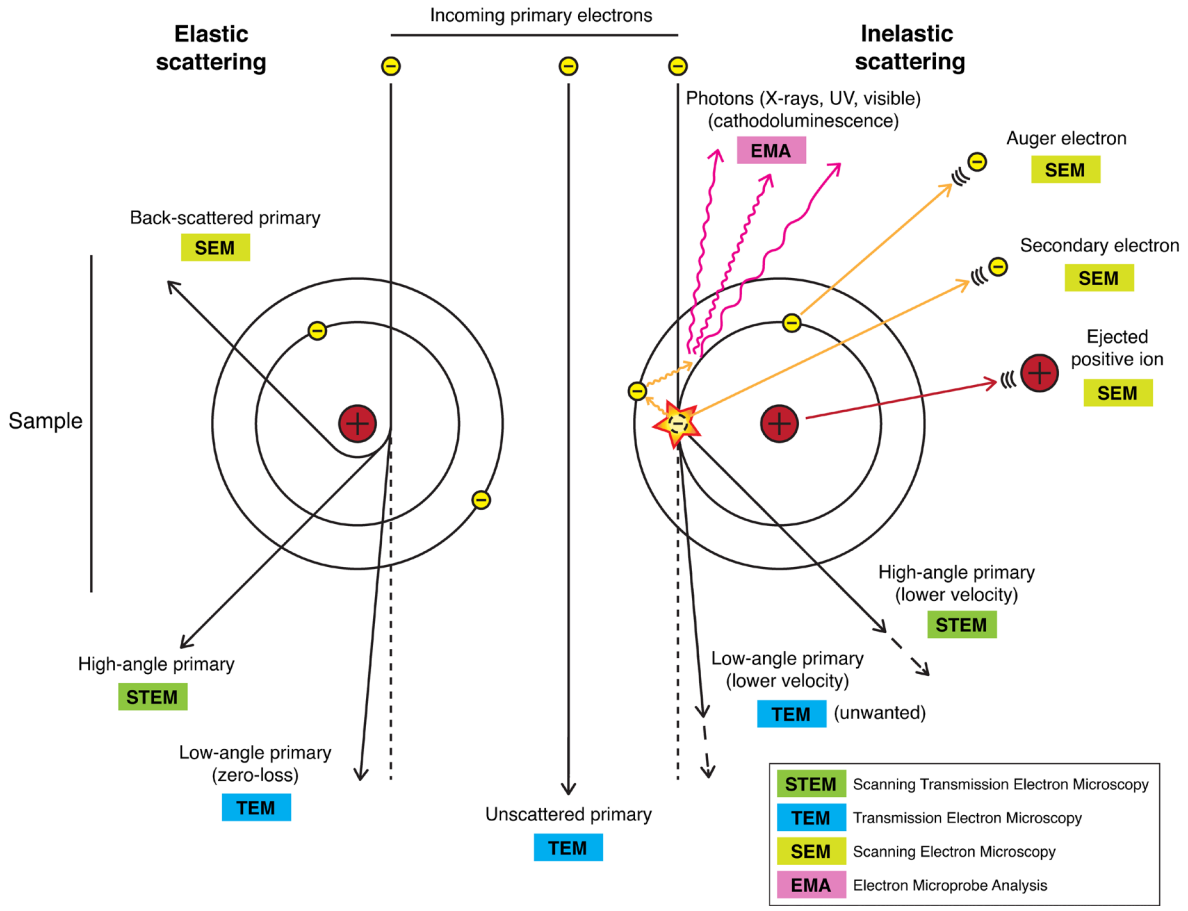

Figure 1.6. Elastic vs. inelastic electron scattering.

Common modes of electron-sample interactions in the case of elastic (left) versus inelastic (right) scattering, and the different techniques that can utilize these interactions for sample analysis.

1.2.3.3 Amplitude contrast vs. phase contrast

Image contrast in electron microscopy is constituted by two distinct components: amplitude contrast and phase contrast. *Amplitude contrast* is formed when amplitude of the electrons' waveform changes between regions. This makes most sense if one considers the electron as a particle: regions that are opaque to electrons block them, meaning comparatively fewer electrons make it to the detector. The missing electrons are usually ones that got strongly scattered and therefore got captured by the objective aperture or energy filter. This strong scattering is usually due to differences in atomic number and therefore scattering propensity within the sample. This is especially useful in material science, where one is not hindered by dose limitations as much as in native biological TEM. Moreover, and more importantly, the low atomic number of biomolecules (containing a lot of H, C, N, O, and smaller amounts of S, P) and the small contrast compared to the surrounding aqueous environment makes amplitude contrast only a small contributor to overall contrast. One way around this problem is to stain the biological sample with heavy metals to increase scattering, and therefore create more amplitude contrast.

The majority of native contrast in biological samples is instead formed by *phase contrast*. Phase contrast is formed when electrons are elastically scattered inside the sample, and end up with slightly delayed phases, leading to an interference pattern further down the column. This makes most sense if one considers the electron as a wave. Scattering centers within the biological object elastically scatter electrons at varying degrees, depending on distance to one another, leading to a convoluted scattered wave pattern. Phase contrast can be induced by slight under-focus ("defocus"); this is called *defocus imaging*, which is widely used in cryo-EM and cryo-ET. However, this leads to effects on the so-called contrast transfer function (CTF, see below), which makes higher frequencies, and therefore high-resolution information, less available.

1.2.3.4 Contrast transfer function (CTF)

In every microscope, electrons interfere constructively and destructively, no matter if an object is being imaged or not. These interferences lead to certain frequencies being boosted, and others being down-weighted, or even zero. There exists a function that describes how different frequencies are transferred to the detector (Equation 8):

$$CTF(k, \Delta z) = -2 \sin\left[\pi \left(-\Delta z \lambda k^2 + \frac{C_s \lambda^3 k^4}{2}\right)\right]$$

Equation 8. The contrast transfer function (CTF).

The contrast transfer function (CTF) is present in every microscope, and is dependent on spatial frequency k and defocus Δz, as well as microscope-specific spherical aberration C_s and the electron's wavelength λ, which is approximated to be 1.97 picometer at 300 kV using Equation 7. The latter two remain constant in cryo-TEM, while the former two can be manipulated by using different defoci.

This function (Equation 8) is dependent on spatial frequency, defocus, spherical aberration and acceleration potential, and is a complicated sinusoid, which has periodic peaks and zeros. Keeping spherical aberration (dependent on the microscope itself) and acceleration potential (300 kV in this study) the same, we find that tuning defocus changes the CTF, and therefore the spatial frequencies it boosts/suppresses. On top of this equation, there is an envelope function that tapers the amplitude of the CTF near higher frequencies. Together, the CTF and its envelope function determine which frequencies can be detected.

An example of the effect of the CTF on the abundance of certain frequencies can be seen below in Figure 1.7. At low or near-zero defocus (blue and black curves, respectively), the sinusoid wave alters slowly and periodically from negative contrast to positive contrast contribution (Y-axis), when plotting against spatial frequency (X-axis). Meanwhile, higher defocus values (red curve) make the CTF contributions flip much more rapidly; moreover, the envelope function tapers off its signal near higher frequencies, while the low-defocus CTF curves taper off much more slowly. Low-defocus imaging is therefore able to transfer higher frequencies more readily than high-defocus imaging. Conversely, higher defocus leads to a much better sampling of low-resolution frequency space (left end of the plot).

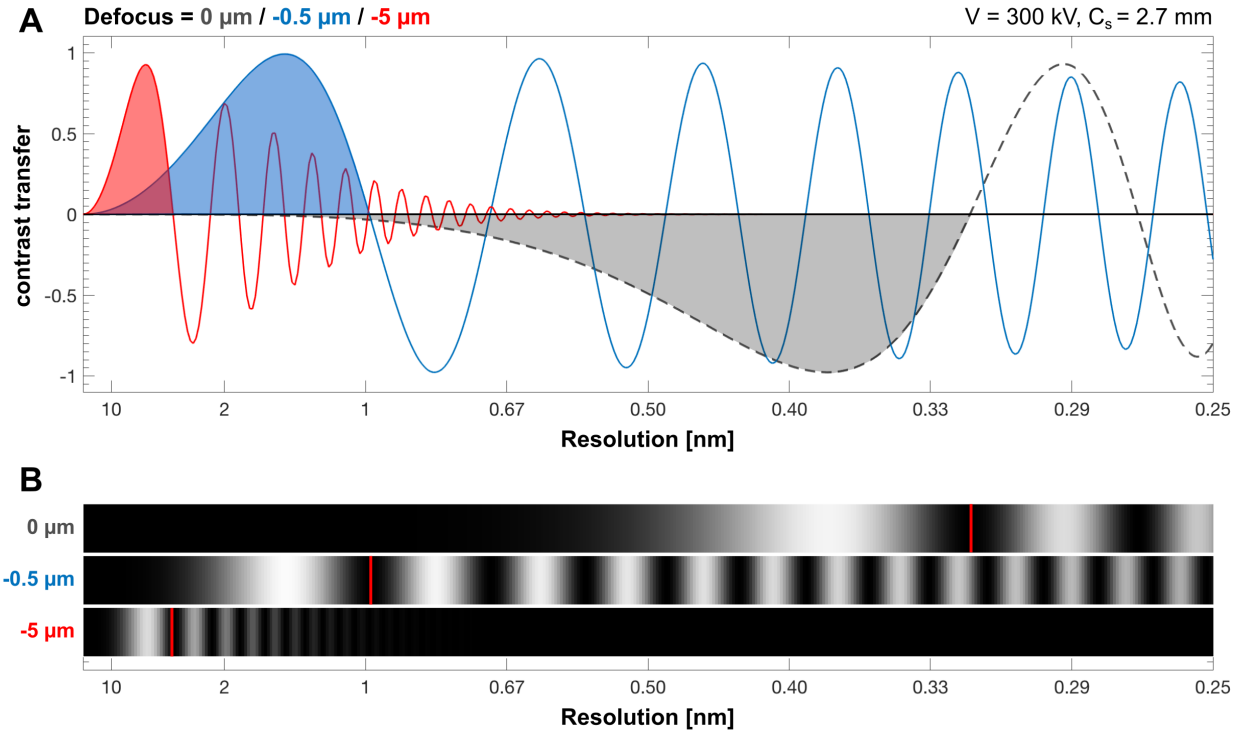

Figure 1.7. Example contrast transfer function (CTF) at different defocus values.

(A) Three CTFs plotted as function of spatial frequency; black: zero defocus; blue: low defocus (-0.5 µm); red: high defocus (-5.0 µm). The sinusoid CTF (Equation 8) alters periodically from negative contrast to positive contrast contribution. Low defocus imaging (black & blue curves) conveys more high-resolution information (right end of graph) due to diminished tapering of amplitude by the envelope function, but also leads to lower sampling of low-resolution information (left end of graph), while the inverse is true for high defocus imaging (red curve); **(B)** graphical representation of (A), using absolute values only; black = no information transfer and white = full information transfer; first-order peak indicated by a red line. From (7).

The effect of the CTF is unavoidable, but can in a large part be corrected for (see Section 1.4.1) by normalizing the curve, trying to approximate a constant, positive contribution to contrast. This is done by down-weighting highly transferred frequencies, while boosting frequencies that contribute less, and inverting the negative contributions to become positive ones. However, the frequencies at which the CTF crosses zero will remain unsampled. In order to diminish the effect of gaps caused by zeros at certain resolutions, it is wise to obtain data at a range of different defoci. Another way to manipulate the CTF is by using a so-called phase plate, in particular the Volta Phase Plate (VPP)(see Section 1.2.4.4).

1.2.4 The transmission electron microscope (TEM)

Let's now take a look at the fundamental components of a modern transmission electron microscope (TEM). TEM is performed by accelerating a beam of electrons to near-relativistic speeds through an evacuated column, through electromagnetic lenses and apertures (Figure 1.9), through a sample, and then through more electromagnetic lenses and apertures to achieve the proper magnification factor. Finally, the electrons arrive at a detector for imaging. Let's now consider the workings of the particular model used in this thesis: the TFS Titan Krios, starting from the top of the column and working our way down towards the detector.

1.2.4.1 Electron source: the electron gun

Electrons start at the electron source at the top of the column, called the electron gun. Since the electron beam has to be manipulated in many ways during its descent through the column and small differences in energy multiply, it's paramount that the electrons have a small energy spread with strong spatial and temporal coherence, which means: moving straight and parallel to one another, and having the same acceleration energy and thus optical properties, respectively. The newest versions of electron microscopes have a Field Emission Gun (FEG)(Figure 1.8, right), which has a very thinly crafted tungsten tip ("Müller type"), which besides the accelerating anode utilizes an extra "pulling" anode to create a strong electric field (hence "Field Emission"). With the help of quantum tunneling even at room temperature ("cold" FEG), this liberates high-energy electrons in a bright, spatially and temporally coherent beam, with only a very small energy spread. Formerly, thermionic emission guns were used, in the form of a bent tungsten filament or a LaB_6 crystal, heated with electric current to liberate the electrons more readily (Figure 1.8, left and middle). However, since the (cold-)FEG is far superior to these designs, it is preferred in high-resolution applications.

After leaving the gun and being initially accelerated by the two gun anodes, the electrons then enter the acceleration stack (NB: not shown in Figure 1.9). This is a stack of metal plate anodes with a hole in the middle, between which a voltage is applied. Usually, the gun is held at -300 kV compared to ground, while ten accelerator plates are kept 30 kV apart, so stepping up from -300, to -270, …, to 0 kV, in order to create a very homogeneous and parallel electric field, and thus a parallel beam of accelerated electrons coming out the bottom end. The high voltage between these plates requires a good vacuum as to not attract pollutants that might form a short-circuit between them. Therefore, the plates are well-isolated from each other.

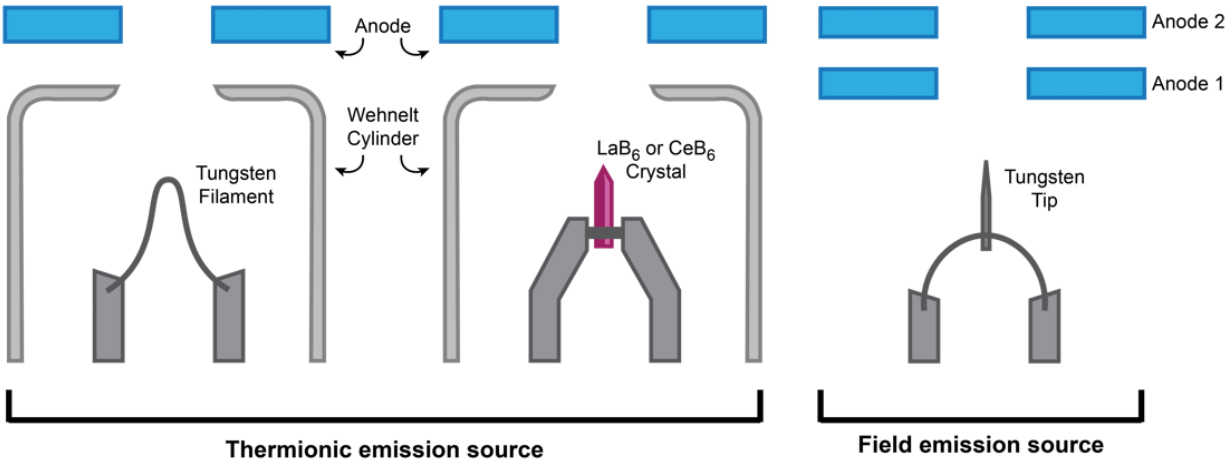

Figure 1.8. Types of electron sources.
Thermionic emitters (left, middle) and a modern-day Field Emission Gun (FEG)(right). Image from (8).

1.2.4.2 The illumination system

After the electrons are accelerated, a series of electromagnetic lenses, apertures and stigmators shape the beam in order to get the desired well-defined illumination area at the height of the sample (Figure 1.9, top half of column) and proper magnification of the imaged object (Figure 1.9, bottom half of column). There are three main sets of lenses in most TEMs including the Titan Krios: the condenser lens system that creates a perfectly parallel and correctly-sized beam before the sample, the objective lens system around the sample, and the projection lens system that performs the real magnification of the imaged object, before the beam exits the lens system through the energy filter and proceeds to the detector. All electron beam-manipulating elements, which means not only lenses, but also stigmators and deflectors, are very precisely tuned electro-magnets.

The components of a lens system

Each lens set is composed of two deflectors, the lens(es), aperture(s), and a stigmator. The deflectors, also called pivot points, are electromagnets with a field perpendicular to the beam path, which can nudge the beam around. They take any possibly off-axis and/or tilted beam that approaches the lens, and bend it so that the beam moves to the middle of the optical axis (first deflector), and then bend it again so that the beam ends up pointed exactly straight down along the optical axis (second deflector). This is important, because the lenses greatly magnify any existing error of the beam that enters them. Apart from slight misalignments over time, this also corrects for possible misalignment during assembly of the physical parts inside the microscope, and therefore decreases the otherwise extremely tight tolerances at which they have to be installed.

The beam then reaches the actual lens, the body of which is also called a pole piece, which is a tightly wound and finely tuned electromagnet, with a field pointing exactly along the optical axis. It consists of thousands of copper wire turns, which are of a very specific diameter, as to not cause any localized differences in current strength, and therefore magnetic field. The copper windings are encased in a metallic sheath, which stabilizes the coil turns and also helps to guide the magnetic field that is produced by the magnets. The magnetic lenses work by slowing electrons down, a bit like how a glass lens works by slowing down photons inside it (Figure 1.10); this bends their waveform around and makes the beam converge. The slowing down of electrons is caused by the Lorentz force giving the electrons a push in the direction perpendicular to the magnetic field lines and the optical axis, which means the electrons start moving in a spiral about the optical axis. This spiraling motion gives the electrons a longer path length, which is what influences their emergent waveform and causes the beam to converge, and thereby magnify the illuminated object. After passing through the lens, the spiraling path of the electrons reconverges with the optical axis. A side effect of the lensing process is that since the electrons travel in a spiral, the magnified image rotates strongly. This rotation can be set to a specific value by choosing currents in all the lenses carefully (this is usually pre-set by the manufacturer).

In tandem with the lenses, there is usually a stigmator, which corrects for astigmatism (uneven focus lengths in X versus Y dimensions) by applying some extra magnetic field strength where needed, caused by any remaining imperfections in the lenses. Every lens system also has at least one aperture, which is a metal disc with a hole in the middle. The aperture catches any strongly scattered electrons that strayed away from the beam and might cause random noise at the detector if not retained in the column.

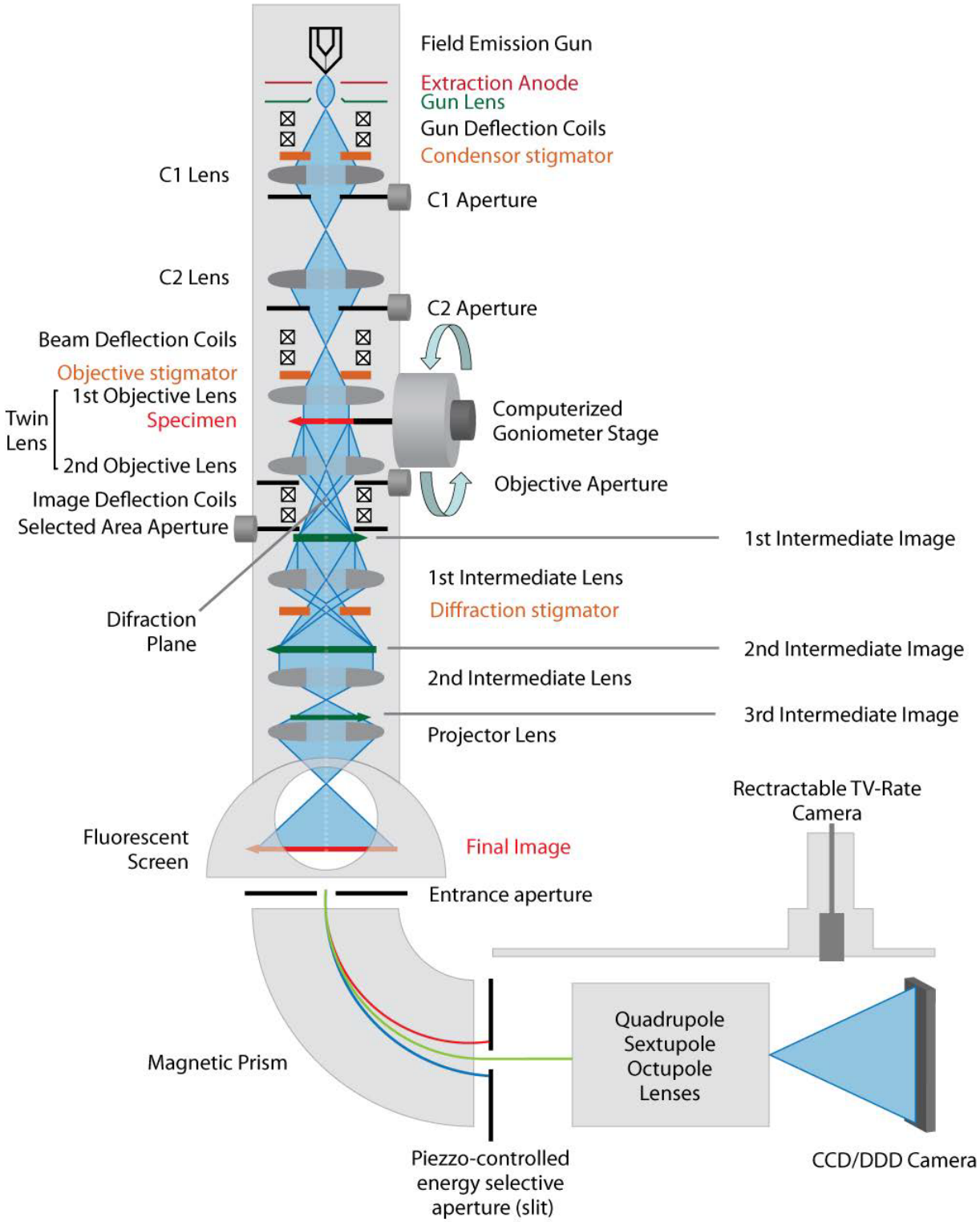

Figure 1.9. Overview of a modern cryo-electron microscope's column.
Schematic view inside a cryo-TEM column. The electron beam's path is marked in blue. Image from (9).

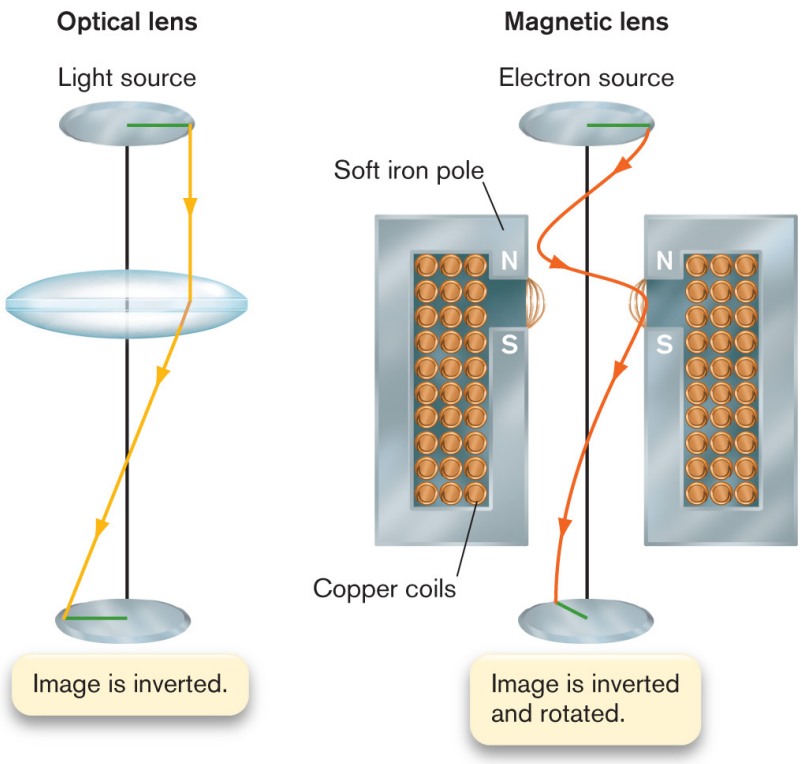

Figure 1.10. How a magnetic lens works, compared to an optical lens.
An optical lens (left) works by bending the waveform of photons, caused by the higher refractive index of glass, slowing down the light passing through it. This, combined with the shape of the lens, causes the beam to converge. The emerging convergent waveform causes an inversion of the image after the focal point. A magnetic lens (right) works slightly differently: it applies a Lorentz force to the passing electrons, causing them to spin around the optical axis. The longer path of the electron's waveform makes the electrons slow down with respect to the optical axis, which is what gives the electromagnetic lens its "higher refractive index" for electrons. The spiral path not only inverts the beam/image through a focal point, but also rotates it. Image from (10).

The condenser lens system

The first lens set, the condenser lens system (Figure 1.9, from "gun deflector coils" to "C2 aperture"), prepares the beam that comes from the accelerator stack under the gun, before it enters the sample. After moving through the deflectors and a stigmator, the beam reaches the two condenser lenses: C1 and C2 (each with their own). These work together to obtain the correct beam spot size and intensity to properly illuminate the sample object. In the case of the Titan Krios, a third lens (C3) works with the FEG (not shown in Figure 1.9) to achieve an even better parallel illumination.

The objective lens system

The second lens set, the objective lens system (Figure 1.9, from "beam deflector coils" to "objective aperture"), is situated around the sample position. The beam deflectors shift the beam from side to side, and can thereby illuminate several areas of the sample consecutively, and also correct for offset caused by non-eucentric rotation of the sample. After the deflectors, the beam passes through the objective stigmator and then through two objective lenses, situated directly above- and below the sample stage. These lenses help shift the focus of the beam to the correct height (also taking non-eucentricity into account). The image deflectors, part of the projector lens system, bring the beam back to the optical axis before magnification.

The projector lens system

The third major lens set, the projector lens system (Figure 1.9, from “image deflection coils” to “final image”), is what performs the actual magnification of the imaged object. The lens system, besides deflectors, stigmator and apertures, contains three lenses, called intermediate lens 1 and 2 (I1 and I2), and finally the projector lens. These lenses work together at specific sets of current strengths, to together form a coherent image at the final image plane. The projector lens is always on, and forms the final image. At low magnifications (“LM” imaging mode), the projector lens by itself has a strong enough magnification to create the desired magnification. But at intermediate- and high magnifications (“M” and “SA” imaging modes), the I1 and I2 lenses are activated to create a compound magnification of up to more than a million times the actual size of the imaged object, which is what makes the electron microscope so capable. The combination of current strengths of the intermediate- and projector lenses is often chosen such that the rotations of the image due to the properties of electromagnetic lenses (Figure 1.10, also described above) adds up to about zero.

1.2.4.3 Sample stage

The sampled object, often in the form of material deposited or frozen onto an EM grid (a very thin metal wafer with a sample support such as carbon coated on it), is loaded onto the sample stage. The sample stage in the cryo-TEM is a metal arm, which is in thermal contact with liquid nitrogen that is piped through channels inside the stage arm. The arm is part of a goniometer; it grips the EM grid and rotates it precisely inside the sample chamber, along the axis of the arm. During cryo-electron tomography (cryo-ET)(see Section 1.3), imaging is performed at periodic tilt intervals while rotating the sample.

The arm, carrying the sample grid, rotates around its longitudinal axis. When the object of interest is lying exactly in the extension of this longitudinal rotational axis, this means that any rotation about the axis will not result in any movement of the sample out-of-plane while rotating the arm. This is called “eucentricity”. The sample stage works together with the objective lens system to establish eucentricity, even if the sample is not exactly within the arm’s rotational axis. This is accomplished by varying the beam’s shift and focus height (also see Section 1.2.4.2, “The objective lens system”).

1.2.4.4 Volta phase plate (VPP)

After passing through the sample, the electron beam passes through the objective aperture, which catches any stray electrons with an unwanted energy due to strong scattering. Instead of the objective aperture, however, one could also install a Volta phase plate (VPP) in this position. A VPP is a very thin film of carbon, which is place exactly in the back focal plane of the electron beam (in the crossover point at the height of the objective aperture). This thin carbon film shifts the phase of the electrons in the beam by ~1/2 π. This changes the properties of the image at the final image plane, such that low-resolution information is boosted, greatly enhancing contrast in- or near-focus. The VPP therefore removes the need for defocus imaging, and therefore tapered high-resolution information and requirement for cumbersome CTF correction (see Section 1.2.3.4).

The VPP has been shown to work for subtomogram averaging in cryo-ET (11,12), but results for this are on par with not using the phase plate. Not only is the VPP unnecessary for high resolution averaging, but there are scattering losses (~16%), the VPP has to be set up in an extremely precise and time-consuming manner, and the ~1/2 π phase shift is often not reproducible due to imperfections or contamination on the VPP carbon film. Therefore, using the VPP is currently not recommended in the general user case (13). It was therefore not used in this thesis; we used conventional defocus imaging and CTF correction. Note, however, that emerging advancements with a laser phase plate may bring phase plate methodology back into cryo-EM and cryo-ET workflows.

1.2.4.5 Energy filter

Beyond the final image plane, modern TEMs often contain a so-called energy filter. Energy filters come in two types: post-column and in-column (also called “omega-filters” due to their shape that resembles the letter Ω). They work roughly the same way; they are an electromagnetic prism that bends the beam sideways, thereby separating it into a spectrum of electron energies, just like an optical prism would separate different wavelengths of light (14). By applying an aperture-like slit, one can select for a specific range of electron energies. This is done to select for only the desired, elastically scattered electrons (see Section 1.2.3). These have an energy that is nearly exactly equal to the acceleration potential of unscattered electrons, with a spread of less than ~20 eV, i.e., ~300.000 eV ± 10 eV. This portion of the electron energy spectrum is therefore called the “zero-loss peak”. Remaining undesired inelastically scattered electrons (see Section 1.2.3) that would otherwise make it to the detector, usually fall relatively far outside that margin, and are thus filtered away at the slit.

1.2.4.6 Electron detectors

Finally, at the very end of the column, comes the detector. The electrons emanating from the energy filter are first led through a series of electromagnets, which re-extract the electrons from the energy filter’s slit into a 2D plane, to form the final image at the detector. Electron detector technology is far from trivial. In fact, the advent of the direct electron detector (DED) enabled a huge improvement in image quality that was the major driving force behind the recent “resolution revolution”. This is due to several advantages DEDs have over other detectors, but to understand those, let’s first look at other electron detector technologies.

Fluorescent screens and TV output

Fluorescent screens are a low-tech solution to visualizing an electron beam. They work by the process of cathodoluminescence; this is the same principle as used in older TV screens (cathode ray tubes). It consists of a plate coated with a “phosphor”, usually zinc sulfide (ZnS), which upon excitation by incoming electrons emits photons in the visible spectrum. This process is based on inelastic scattering interactions, and is also depicted in Figure 1.6. Instead of the flat-lying fluorescent screen, one can also directly guide the beam onto a TV recording screen (also based on cathodoluminescence), which can then transduce the signal to a monitor near the user, so the user doesn’t have to directly observe the fluorescent screen itself inside the column.

Photographic film

Historically, EM data collection was based on photography using electron-sensitive film. Although this might feel archaic in the age of advanced digitalized detectors, film still has some major strengths. The interaction space of incident electrons with film's tiny grains is very localized, and can therefore produce very high-resolution images compared to methods using scintillators (see below). Film is usually digitized after development, for digital data processing. The size of digitized film images can be very large, owing to film's dense resolving power.

There are of course some major disadvantages in using film. First of all, it's very slow. The film has to be stowed, taken out of the vacuum chamber, developed, and then digitized. This disallows direct feedback into the imaging conditions in case something isn't perfectly set up. Additionally, the film usually isn't perfectly stable under vacuum and trace amounts of water vapor or other volatile substances can evaporate from the film; this can compromise the vacuum.

CCD cameras

With the advent of the digital age, electron microscopy was also digitized. This gave a big advantage over traditional photographic film, as direct digitization and thus direct feedback on imaging settings could now be implemented, often automated within EM software.

Charged Coupled Device (CCD) cameras were implemented for digital imaging in EM. These detectors consist of pixels that are silicon-based photodiodes, which take in photons, and through the photoelectric effect release electrons, which in turn are stored in the pixels until the chip is read out, resulting in a digital signal. However, to create the photons that are detected by the sensor, the electrons must first be amplified in a microchannel plate (MCP), and then converted to light in a scintillator. A scintillator releases photons upon activation by incident electrons.

This process converts electrons to photons, and then converts those photons back to electrons, which sounds redundant, and indeed brings a much lower readout speed and, more importantly, a lower signal transfer efficiency. This signal transfer efficiency is a part of the "detector quantum efficiency" (DQE)(Figure 1.11), which is an overarching measure of the ratio of useful detected electrons to incident electrons, and in the ideal case would be 1.0. DQE is highly dependent on detector efficiency, and a high DQE means that less electron dose is needed to image the sample, and therefore less radiation damage occurs for the same amount of signal. Moreover, electrons can take stochastic paths through the scintillator (sometimes even sideways or back up through the detector, portrayed in Figure 1.12), exciting neighboring pixels and leading to false signal, moreover randomizing the amount of signal per incident electron. This further decreases DQE, while introducing noise. Unfortunately, CCDs provide a lower readout speed and DQE than newer options involving direct electron detectors (see below; see Figure 1.11), but CCDs were for a long time the only available digital detector option.

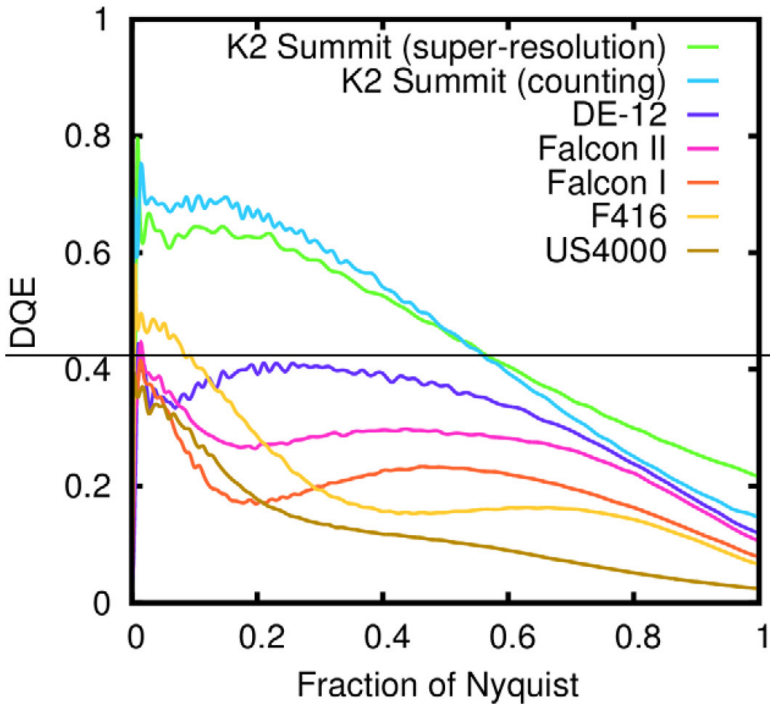

Figure 1.11. Detector quantum efficiency (DQE) of several detector types.

This graph shows DQE of several frequently used electron detectors, all at 200 kV, as a function of the Nyquist limit. DEDs (K2, DE-12, Falcon) outperform scintillator-based detectors (F416, US4000). Image from (15).

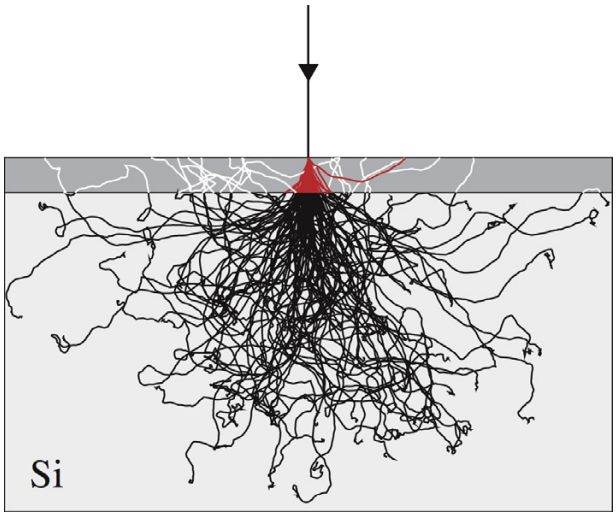

Figure 1.12. Simulated paths an electron can take in a detector surface.

Monte Carlo simulation of electron paths, showing how electrons worsen the point spread function by taking random paths through the detector surface, sometimes creating secondary signal (light gray traces in the upper layer), far away from the primary scattering event (red traces). Back-thinning to 35 µm thickness (dark gray top layer) decreases the number of these false signals. Image from (16).

Direct Electron Detectors (DED)

A somewhat recent and revolutionary new detector technology is the direct electron detector (DED). It is based on complementary metal-oxide-semiconductor (CMOS) technology; this allows for single incident electrons to directly be detected in a very thin detector. This does away with the intermediate steps required to obtain a signal on a CCD, including electron amplifying waveguides (in the form of microchannel plates (MCP)), scintillator, and fiber-optic coupling layer between scintillator and CCD sensor.

In a DED, electrons hit only a small amount of very localized pixels, from which the initial interaction location can be triangulated. There are no MCP or scintillator to randomize signal strength per electron, or introduce noise due to sideways scattering events inside the scintillator, which would broaden a detection event's point spread function. Moreover, modern detectors are "back-thinned", which means that once electrons are detected, they escape the detector, limiting the amount of secondary (back)scattering events drastically. This greatly increases DQE (16).

Modern DEDs not only allow for a much more localized signal, but also a very high framerate, often in the order of hundreds of frames per second. This opens up the possibility of using the detector in "counting mode": by sampling more often over time, the possible overlap between separate detection events is greatly reduced, so every electron detection event can now be counted separately. Instead of some stochastic amount of signal, every electron now accounts for exactly 1 unit of signal. Moreover, the high framerate allows tilt images to be fractionized into frames, which can then be aligned and added to recover the full tilt image, thereby correcting for beam-induced motion of the sample (see Section 1.4.1).

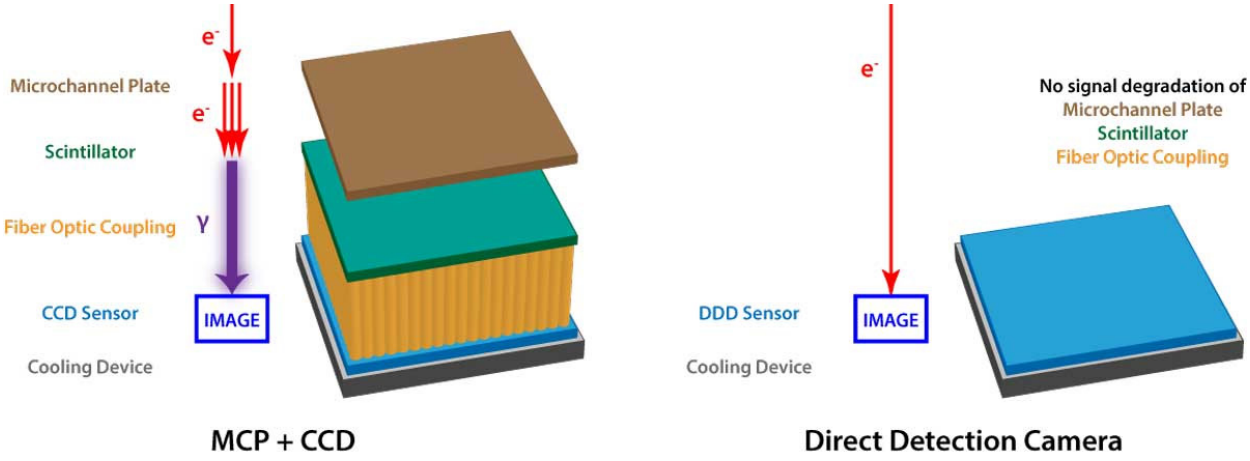

Figure 1.13. CCD detector (left) and the direct electron detector (DED, right).
A CCD detector (left) has several intermediate steps between incident electron arrival and digitization on the chip, and moreover have a thick support underneath. These factors lead to a low DQE and backscattering noise (see Figure 1.12). A back-thinned DED (right, thinning not visible as it is underneath the chip) doesn't have these issues and allows for a much higher DQE and framerate. Image from (17).

1.3 Cryo-electron tomography (cryo-ET)

1.3.1 Basic principles of cryo-ET

Cryo-electron tomography (cryo-ET), sometimes called electron cryotomography, is a powerful technique in structural biology that utilizes cryo-TEM to study biological samples in their native state. The sample is vitreously frozen and tilted around one or more axes in order to obtain a series of 2D projection images from different viewing angles, which can then be "back-projected" to form a 3D image of the sample (Figure 1.14). This 3D image is called a "tomogram", which contains a 3D representation of the native density of biomolecules in the sample.

As opposed to other cryo-TEM techniques such as single particle analysis (SPA) or electron crystallography, cryo-ET works with cells preserved in a near-native state. This means that after vitreous freezing, the cells are suspended in a state of suspended animation, a sort of "snapshot" in which all the dynamic processes inside the cell are paused.

The power of this technique lies mainly in the ability to not only get high-resolution information of biomolecules, but more importantly, to put this information into cellular context. Cryo-ET bridges a gap between atomic structures and whole organelles (Figure 1.4), a scale containing a wealth of information. One can fit atomic models of known proteins into their structural densities *in situ*, but also look at larger-scale dynamic processes coordinated by many different proteins and other biomolecules inside the native cellular environment. Cryo-ET can therefore take mechanistic details from structures obtained by methods such as cryo-EM SPA, X-ray-/electron crystallography, and NMR, and couple them to how molecular machinery works in concert within the cell. In other words, how molecules lead to life.

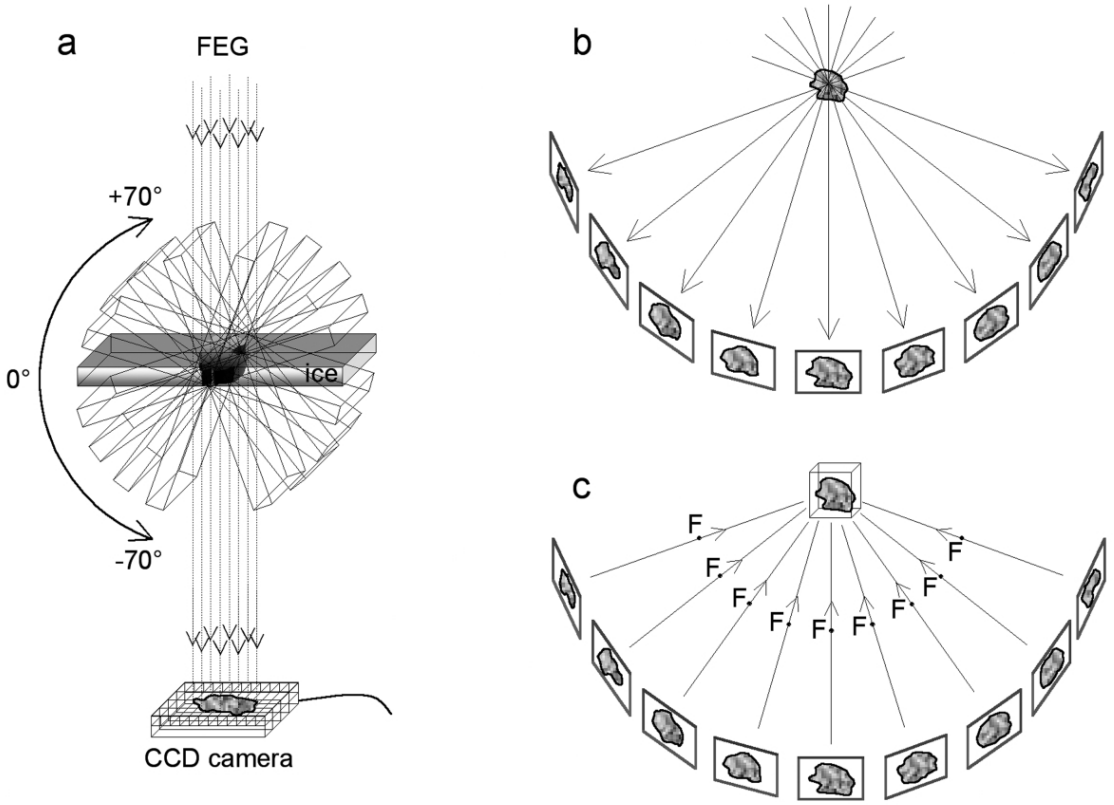

Figure 1.14. The principle of tomography: weighted back-projection of a tilt series.

(a) The sample is tilted and imaged many times to obtain a tilt series; **(b)** representation of the tilt series with respect to the original object; **(c)** weighted back-projection; each tilt is assigned a weight F and is back-projected to obtain a reconstructed volume, also called a tomogram. Image from (18).

1.3.2 Advantages of cryogenic temperatures

One of the major advantages of cryo-ET as opposed to conventional room-temperature TEM (RT-TEM), is that biological samples are kept in their native, aqueous state. In conventional EM methods, samples have to be chemically fixated, stained, dehydrated, and resin-embedded. This is done to improve contrast, as well as make the samples stable in the high vacuum needed inside the TEM; however, this drastically alters the sample away from its native state.

Cryo-ET shifts the paradigm by maintaining the sample at cryogenically temperatures. Not only can native electron density of proteins and other biomolecules (containing elements like H, C, N, O, P, S) without external staining be used to obtain near-atomic resolution structures of these molecules, but the sample is also stable inside the high vacuum of the microscope, as the vapor pressure of water at cryogenic temperatures is almost negligible.

Another advantage of the cryogenic temperature range is that radiation damage to the sample, caused by incident electrons, is reduced. The energy these inelastically scattered electrons dump into the sample leads to radiolysis, i.e., energetic breaking of molecular bonds, which releases free radicals. These would otherwise diffuse through the object and damage many molecules within it, but instead are fixed in place due to the extremely reduced thermal motion and diffusion coefficient. Dose limitation is still a key limiting factor in the imaging of cryo-ET samples, but the cryogenic temperatures make it at least feasible. Cryo-ET is limited to ~100-120 $e^{-}Å^{-2}$ in practice (19), but this limit varies depending on the type of material absorbing the dose. At higher accumulated dose, pockets of radiolysis-liberated hydrogen gas start accumulating (bubbling). However, when it comes to obtaining atomic resolution structures, radiation damage becomes a factor already at ~20-30 $e^{-}Å^{-2}$ (20), and minimizing the effects of electron dose is therefore necessary.

1.3.3 EM grids

Samples in cryo-TEM are often deposited on grids (see Figure 1.15): very thin metal sheets ~3 mm in diameter, usually made of copper or gold with square holes in a grid-like pattern, coated thinly with carbon for sample support. The grid can also be made of other materials such as molybdenum, or have other supports such as silicon oxide or graphene. If needed, these can be varied to minimize problems due to differential thermal expansion coefficients, which can make the support and coating shrink in different amounts, leading to warping of the support coating. The carbon coat usually has holes in it, which drain away buffer while leaving cells supported; the size and shape of these holes can be varied depending on the sample type.

Before freezing cells, the grid's hydrophobic carbon layer has to be made hydrophilic in order to let the cell suspension adhere to it. This is done in a plasma glow discharger, which applies an electromagnetic field to rarefied air to create a plasma. This plasma attacks the carbon coat, and adds hydrophilic functional groups to the carbon's surface. This makes the grid hydrophilic enough for sample application.

1.3.4 Vitrification

Before cells can be imaged using cryo-TEM, they have to be frozen onto the grid, making sure to freeze so rapidly that the ice is in an amorphous, or vitreous, state. Vitreous ice is a metastable, glass-like transition state of ice, which doesn't occur naturally. It only forms below -137 °C and can only occur if the water is cooled down extremely rapidly, so that the ice crystals have no time to form. This is required for both sample integrity and imaging: ice crystals not only expand and disturb the native conditions in cells and puncture membranes; they also strongly diffract the electron beam, hindering observation of the sample. Moreover, most dynamic biological processes are frozen in time, as thermal Brownian motion and diffusion are all but completely stopped at these temperatures.

There are two main methods that are used in cryo-ET to vitrify biological samples: plunge freezing and high-pressure freezing (HPF). HPF applies a high pressure to the sample while cooling down rapidly. This prevents ice crystals from forming, as they need room to expand. Therefore, HPF allows for a much smaller temperature gap (~44 K as opposed to ~92 K in plunge freezing) to cross from supercooled water to vitreous ice. This method requires a specialized HPF machine and has issues with reproducibility; the resulting ice can be of differing quality. It is most often used for tissue and small multicellular organisms, as it can handle samples that are ~100-300 µm thick. In contrast, plunge-freezing can only vitrify ~5-10 µm-thick samples, which limits that technique to moderately sized individual cells.

High-pressure freezing (HPF) is unfortunately still mostly incompatible with FIB milling used for cryo-ET, since the so-called lift-out procedure needed to extract thin slices from high-pressure frozen samples is still being optimized. This will be shortly discussed at the end of Section 1.3.7.

Plunge freezing

The most frequently used method for vitrification is “plunge freezing” (Figure 1.15). The grid is mounted with a fine tweezer onto a robotic or manual plunger arm. Roughly 4 µL of cell suspension (usually in the order of 100-1000 cells per µL) is applied to the grid, after which excess buffer is wicked away for a set amount of time by a filter paper. Instead of cells, a purified protein solution can be used instead, as is standardly performed for single particle analysis (SPA) cryo-EM. After this blotting process, the grid is then rapidly plunged into a cup of liquid ethane or ethane-propane mixture, kept at liquid nitrogen temperature. Unlike liquid nitrogen, the liquid ethane does not boil, even as a room-temperature object is introduced to it. This means there is no Leidenfrost effect, the insulating phenomenon caused by gas expansion due to boiling of liquid when a comparatively hot object is introduced to it. Therefore, liquid ethane closely sticks to the surface of the sample and grid, allowing for good thermal conductivity between the ethane and grid. This causes the extremely rapid drop in temperature needed to ensure vitrification of the sample. The negative effect of temperature sinks on this process limits vitrification to very small objects, in the range of single cells (~5-10 µm). Cryoprotectants such as glycerol can be added to cells shortly before plunging to improve vitrification quality; in fact, cells provide their own “cryoprotectant” due to strong molecular crowding in the cytosol. However, adding additional cryoprotectant can cause osmotic stress to the cells, straying further away from native cellular conditions, which is supposed to be one of the major strengths of cryo-ET.

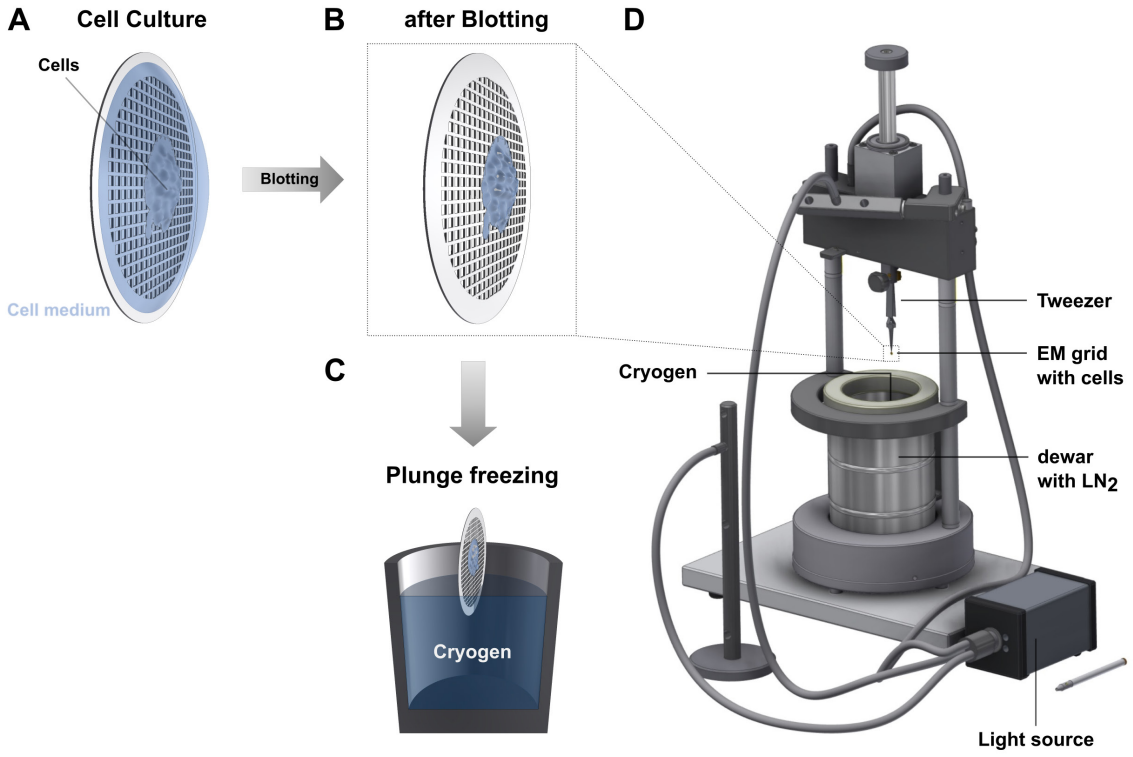

Figure 1.15. A typical (manual) plunge freezing setup.
This setup plunge-freezes cells in liquid ethane, making plunge-freezing reproducibly successful. A suspended tweezer clamps an EM grid (D), cell suspension is applied (A), then the excess buffer is wicked away using a filter paper, leaving the cells behind on the grid’s support (B), and finally, the grid is plunge frozen in liquid ethane kept at liquid nitrogen temperatures (C). Image from Tim Laugks (with permission).

1.3.5 The missing wedge

Cryo-ET produces 3D information by imaging a biological sample from many different angles. Taking a series of 2D projection images in this manner is called a tilt series (see Section 1.3.6). In the ideal case, one would view the sample in from every possible angle and sample the object in all of 3D space. However, due to the nature of the sample, which is deposited on a thin metal grid, looking at the sample from within the plane of the grid is impossible. The grid itself would come into view; moreover, the ice thickness of the sample increases dramatically at high tilt angles, whereas 300-kV cryo-TEM can only yield usable images through about 200-300 nm of ice. Therefore, in practice, one can rotate the sample up to ~60-70° in any given direction away from the zero-tilt plane. This will lead to a missing piece of information, which assumes a specific shape in Fourier space (Figure 1.16). Although taking tilt series on multiple tilt axes has been tried, tilt series are generally acquired around just one rotation axis. In this case, the missing information in Fourier space is shaped like a wedge and is therefore called the “missing wedge” (Figure 1.16). In the case of multiple tilt axes, this missing wedge can take the shape of a pyramid (2 axes) or a cone (multiple axes). Some information will always be missing, and due to dose limitations involved with imaging along multiple axes as well as issues with tilt series alignment, a single tilt-axis is almost always preferred.

The problem of the missing wedge is an inherent limitation of cryo-ET using flat EM grids. Luckily, advances have recently been made by using deep learning algorithms (21) to try and fill up missing information in Fourier space, i.e., predict where certain densities should be using machine learning, even if they’re otherwise absent due to the missing wedge. Although this brand-new method brings some considerations with it and has yet to stand the test of time, it has already proved to be a powerful tool in applications like visual inspection of tomograms, especially in rotations far away from the zero-tilt imaging plane.

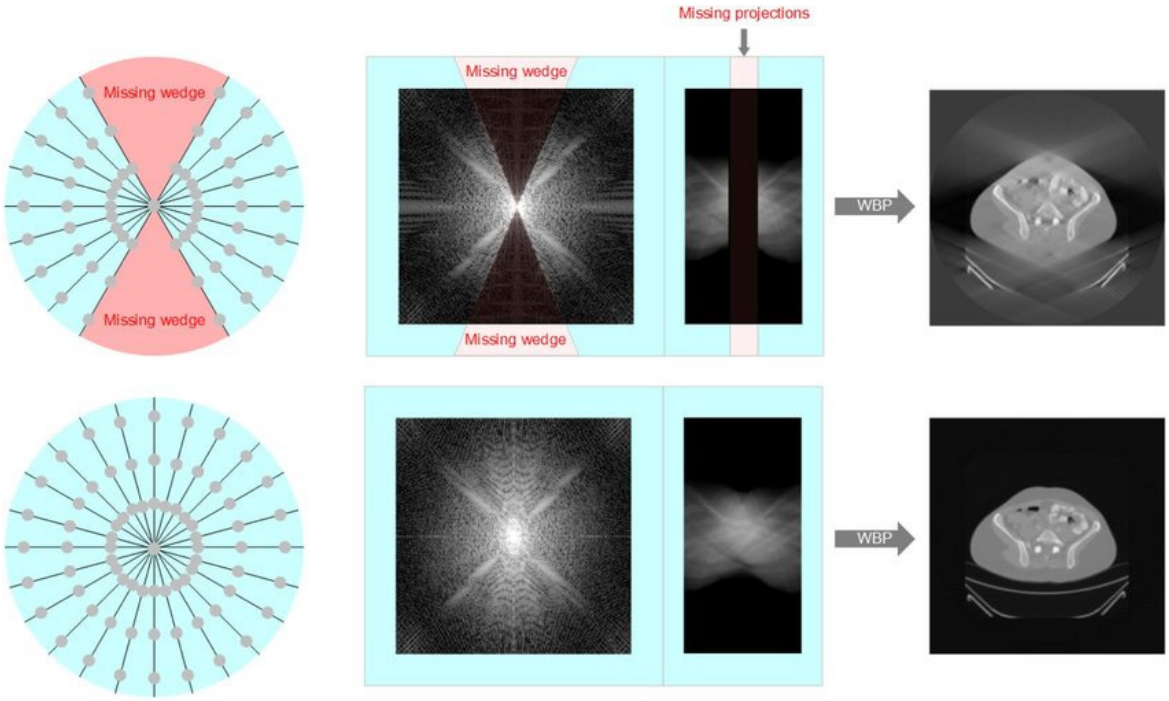

Figure 1.16. The effects of the missing wedge.

Tomography of a flat sample is limited in its higher tilt range (top left) compared to the ideal case (bottom left). This leads to a wedge-shaped piece of missing information in Fourier space (middle, top). This missing information causes image artefacts in real space in the resulting tomogram (right). Image from (22).

1.3.6 Tilt schemes for cryo-ET

There are several strategies to obtain a tilt series, called tilt schemes (Figure 1.17). Tilt schemes try to find an optimized balance between several factors: sample ice thickness, dose accumulation, sampling of information space, and acquisition time. It is key to maximize information sampling at near-zero tilt angles, as the path travelled by the electrons through the ice is thinnest at those angles, and the signal-to-noise ratio is therefore maximized, while accumulated dose is lowest. Simple tilt schemes like the unidirectional tilt scheme (Figure 1.17, left) provide fast acquisition speed, as the goniometer has to step the same number of degrees in the same direction between every tilt image. A bidirectional tilt scheme (Figure 1.17, middle) provides a balance of acquisition speed and information/accumulated dose at near-zero tilts, by introducing a break between the two halves of the scheme. This tilt scheme was most often used in tomography until the advent of the dose-symmetric tilt scheme (23). This tilt scheme heavily focuses on optimization of near-zero tilt information, while extending acquisition time to accommodate more stage movements and drift settling. Acquisition time for the dose-symmetric tilt scheme is the longest of these three schemes, since the goniometer has to jump back and forth between tilts on both sides of the zero tilt. It takes time to rotate, settle, recalibrate and focus every time the goniometer rotates, especially from end to end. Nevertheless, data quality is optimized, and therefore this scheme is nowadays often used in high-precision cryo-ET.

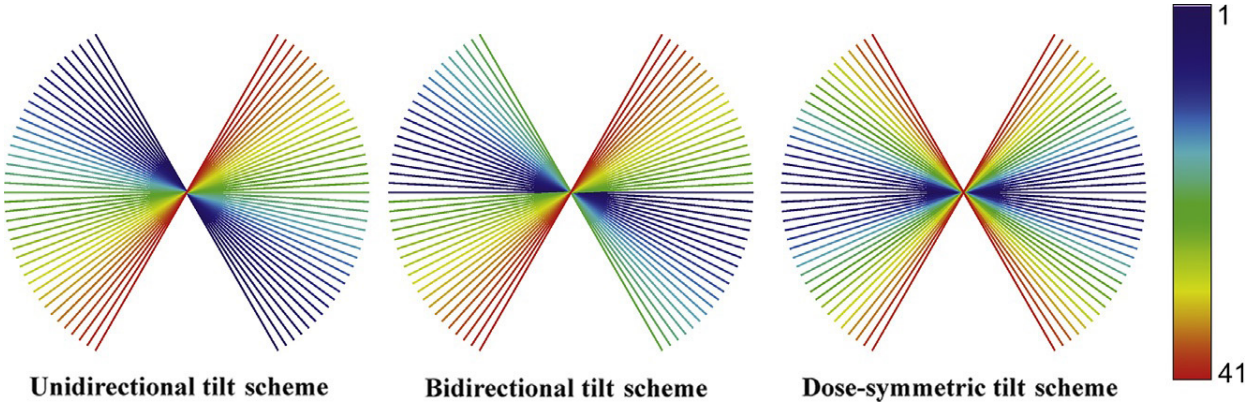

Figure 1.17. Three tilt schemes that are often used for cryo-ET.

Accumulated total dose per tilt is indicated by color; blue indicates low accumulated dose, red indicates high accumulated dose. Low dose accumulation near the zero-tilt is preferable, due to the optimal minimum ice thickness and therefore best signal-to-noise ratio at that rotation angle. The unidirectional tilt scheme (left) is simplest and fastest, but provides little low-dose information at near-zero tilts. The bidirectional scheme (middle) provides a balance of acquisition speed and low-dose information at near-zero tilts. The dose-symmetric tilt scheme (right) is most complicated, as the goniometer has to jump back and forth, which is especially time-consuming near higher tilts. This scheme is presently most often used, owing to its resolution-optimizing dose regime. Image from (24).

1.3.7 Focused ion beam milling of vitrified samples (FIB-SEM)

Sample thickness: a major limitation of cryo-ET

300-kV cryo-ET can be performed on samples with a maximum ice thickness of ~200-300 nm, ideally less. Beyond this range, the exponential increase of inelastic electron scattering events becomes so dominant that few electrons are left as usable signal at the detector. Moreover, more electron dose is needed to obtain enough signal, which leads to more radiation damage. Especially high-resolution information is lost quickly with increasing ice thickness.

Formerly, this limited cryo-ET to small bacteria and regions located at the periphery of eukaryotic cells. Structures such as filopodia and cilia have been studied extensively this way. Unfortunately, this of course leaves the majority of the cell's interior inaccessible.

A way around the problem of ice thickness is to serially section thin sheets of cell using a cryo-microtome, a technique called cryo-electron microscopy of vitreous sections (CEMOVIS) (25,26). This, however, introduces strong cutting and compression artefacts, which distorts the ultrastructure of the biological sample. The thermal and electrical contact with the supporting grid are also very low, which leads to problems during imaging.

The advent focused ion beam milling at cryogenic temperatures (cryo-FIB)

Luckily, material science had a high-precision non-mechanical technique at its disposal: focused ion beam (FIB) milling. The implementation of this technique in the cryo-ET workflow was pioneered in 2006 (27) and further improved for implementation on vitrified whole cells (28,29). This has led to a range of cutting-edge biological studies (30–33), and continues to do so, including the work presented in this thesis (1–3)(Section 4-6). The combination of native-state cellular interior imaging with high-resolution structural averaging has proven to be a powerful tool in structural biology (34).

FIB milling is performed inside a dual-beam scanning electron microscope (SEM, combined as FIB-SEM). The FIB-SEM instrument (Figure 1.18) has a raster-scanning electron beam coming from the top and another raster-scanning focused beam of gallium ions coming from the side. The sample grid is clipped into a holder, and loaded onto a cryo-stage, which is in thermal contact with gas cooled to liquid nitrogen temperatures (~ -170-180 °C). This keeps the sample vitrified while being processed.

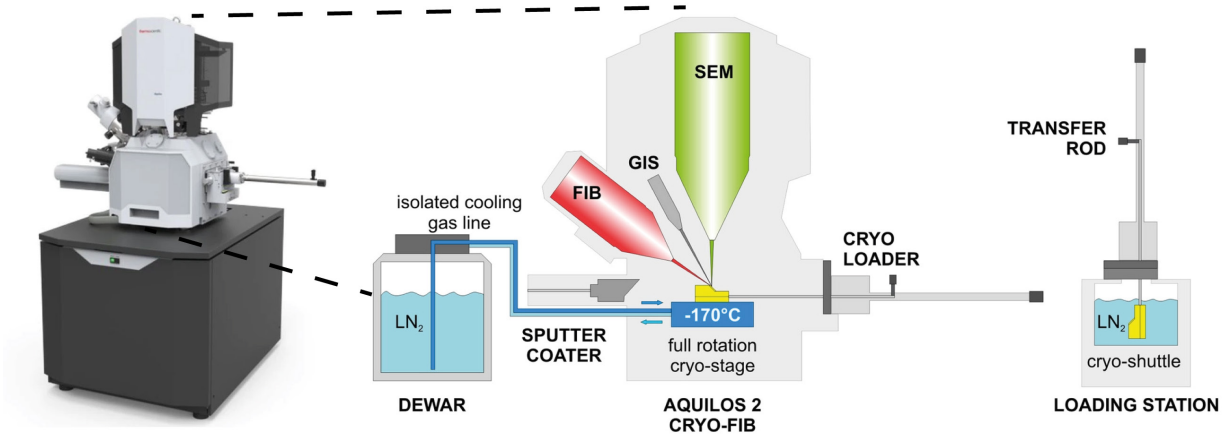

Figure 1.18. The dual-beam focused ion beam scanning electron microscope (FIB-SEM).
A modern TFS Aquilos 2 cryo-FIB-SEM instrument (left) and a schematic representation of its principle components (middle and right, adapted from (35)).

The FIB milling process

The sample to be milled can be any biological vitreously frozen material such as a cell, isolated protein solution, nanocrystal solution, mat of prokaryotic cells, etcetera. The ablation by the FIB also cuts away a trench, which leaves space for the TEM to rotate the sample to high tilt angles without material on the sides coming into view (Figure 1.19).

Before the FIB is activated, a thin layer of protectant such as organic platinum is applied by the gas injection system (GIS) to the surface of the sample, in order to reduce erosion damage from stray gallium ions. A thin conductive coat of sputtered platinum metal can also be applied, to reduce charging effects due to charge building up in the sample during imaging.

The gallium ion beam is able to ablate material from the sample without devitrifying it. However, the beam current must be low in order to keep the ion beam highly focused, minimizing collateral damage or devitrification in sections that need to be preserved (further aided by the GIS-deposited organometallic layer).

In order to balance the total time the FIB milling process takes, the milling is performed in several steps, with decreasing beam currents. During the first “rough milling” step, the bulk of the cell including some surrounding grid support is ablated using high beam currents (~0.5-1 nA). Additionally, parallel side trenches can be cut into the grid support, to relieve thermal contraction stresses due to plunge freezing, and thereby stabilizing the milling target (36). When the remaining slab of sample material is ~1.5-2 µm thick, the beam current is decreased to start the “fine milling” step. With lower and lower beam currents and increasing precision, a thin slab of ~500 nm thickness is produced. Finally, this slab is polished with a 30-50 pA beam until it’s less than 200 nm in thickness, ideally between 70 and 150 nm, yielding the final thin slab of sample. This slab is often called a “lamella”, a “window into the cell”(37). After polishing, the sample should not be left in the vacuum chamber for too long, to limit redeposition of material onto the lamella.

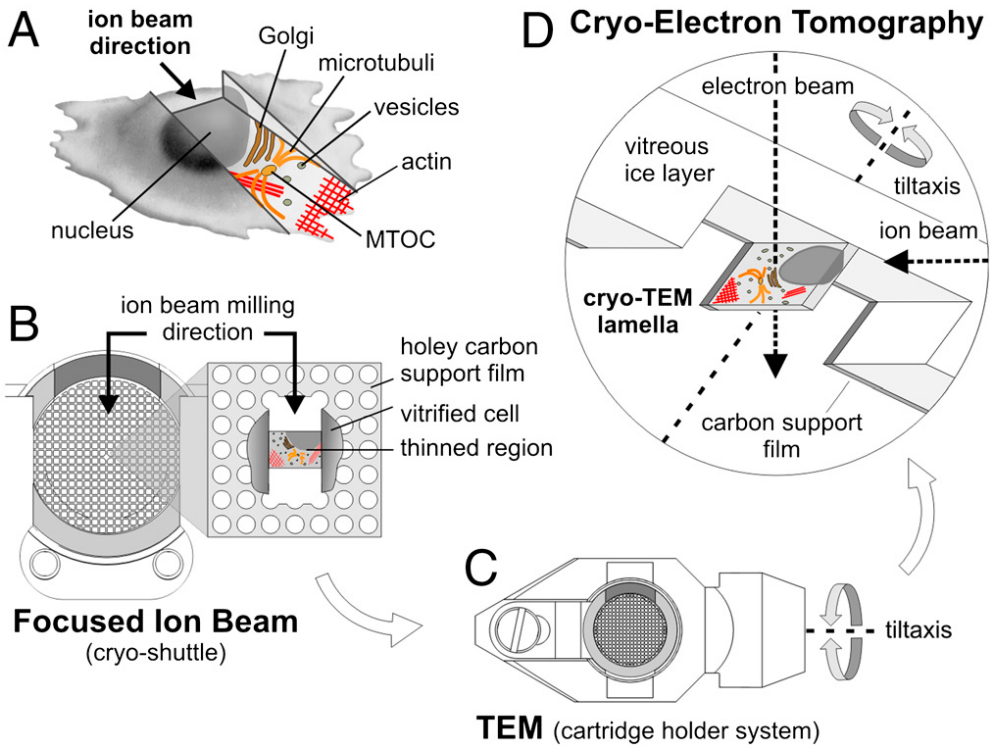

Figure 1.19. Cryo-TEM following FIB-SEM sample preparation.

After preparation of a lamella inside the FIB-SEM (A-B), lamella now has the right thickness and geometry to be imaged in the cryo-TEM (C-D). Figure from (38).

Improving targeting in FIB milling: correlative light electron microscopy (CLEM)

One limitation of the FIB milling technique is targeting of small, low-copy-number targets inside a cell, or targets that are found in only a small subpopulation of cells within a given cell culture. Although milling of easily discernable surface features, or brute force random milling can work (such as in the case of this thesis' MTEC and *Chlamydomonas* projects, respectively), it can be helpful to apply a more targeted approach. One of these approaches has made rapid advancements recently: correlative light electron microscopy. In this technique, target proteins of interest are expressed with a fluorescent protein such as GFP or mCherry, and the cell culture is vitrified by regular plunge freezing or high-pressure freezing (see next section). The grid is then transferred to a cryo-light microscope, which images the cells of interest and can excite the fluorophores inside. This gives an overview of the grid, highlighting the cells expressing the proteins of interest, and even their subcellular localization.

The 3D localization map of targets of interest obtained by CLEM can then be transposed onto the FIB's ion beam view, using fluorescent fiducial markers that are also visible in the FIB. This is then used to target FIB milling of cells belonging to a subpopulation, and/or of a structure that's hard to target inside each cell. Lamellas can also be checked for fluorescent signal after FIB milling, or even after data acquisition in cryo-TEM.

Frontiers of FIB milling: automated milling, lift-out and in-FIB CLEM

Cryo-FIB methodology in cryo-ET is still rapidly undergoing development, and there are promising frontiers to push. Recently, automated milling has been implemented for reproducible and high-throughput production of lamellae. Automated FIB milling uses image recognition to home in on the exact target, resulting in a "point and click" method, which makes FIB much more user-friendly and less time consuming. It can also run overnight with a larger nitrogen dewar to keep the stage cold for extended operation.

Another method that has shown great promise, but is unfortunately still not standard due to its cumbersome and hard to reproduce protocol, is "lift-out". Lift-out is a procedure that follows after high-pressure freezing (HPF), in which a small section of tissue, or small multiciliated organisms such as *C. elegans*, fly embryos or tardigrades can be vitreously frozen in an HPF machine (39). During this process, the sample becomes embedded in a rather large block of vitreous ice. Lift-out extracts a thin slab of material from the HPF ice, using the FIB's ion beam to cut and a micromanipulator to lift. The slab of material is then placed onto a specially designed EM grid, after which a thin lamella is milled from it. This concept has been proven to work (35), but unfortunately, the process is still laborious and takes many hours to complete, with varying results. As promising as it is, this technique still needs further development to enhance reproducibility, throughput and user-friendliness.

Finally, a novel CLEM setup is being developed, which images grids inside the FIB-SEM's vacuum chamber. This eliminates grid handling steps between FIB-SEM and the cryo-light microscope by fusing these two instruments into one. This could enable real-time correlative milling, in which the fluorescent signal of the protein/target of interest is monitored between or even during FIB milling steps, allowing for much more direct feedback to the user, and therefore hopefully higher success in using CLEM.

1.4 Computational data analysis following cryo-ET

The workflow in cryo-ET data analysis can be divided into roughly three categories: pre-processing, main analysis, and post-processing. This suggests linearity of the cryo-ET pipeline; however, most methods here are used iteratively, in different combinations with one another, at different points in the workflow. I'll briefly discuss some of the most used methods.

1.4.1 Pre-processing and tomogram reconstruction

Before starting the bulk of the cryo-ET data analysis, a number of pre-processing steps can be performed to ensure high tomogram quality.

Motion correction

With the advent of the direct electron detector (DED), very high detector framerates are now possible. This allows the total exposure of a single tilt (~1-1.5 s) to be divided over several frames: usually 10-15 separate exposures of ~0.1 s each. These frames can then be aligned using software, in our case Motioncor2 (40), and added back together to obtain the full tilt image. The division into individual frames helps to correct for beam-induced motion, leading to sharper tilt images.

Exposure dose filtering

While acquiring a tomogram, the sample will cumulatively acquire more and more electron dose with each tilt. This leads to radiation damage, especially during the later stages of the tilt scheme. This means that the early tilts, with low accumulated dose, contain useful high-resolution information; However, later tilts, with high accumulated dose, do not. Any high-resolution information they contain will be affected by radiation damage, and it is therefore wise to low-pass-filter later tilts, as to not introduce high-frequency noise. We used exposure dose filtering in STOPGAP (41), which applies a down-weighting factor on higher-resolution information, proportional to accumulated dose of each tilt.

Tilt alignment

The most crucial step in tomogram reconstruction is the alignment of the individual tilt images that are fed into it, using software such as IMOD (42) or Dynamo (43). Several methods have been developed to align tilts.

One method uses strongly contrasting fiducial markers; colloidal gold beads of a specific size are most frequently used, usually 10 or 15 nm in size. These markers are added to the sample before plunge freezing; ideally, they're evenly dispersed around the sample. With enough fiducial beads in view, these can be used as fiducials for aligning the tilt images. This method is precise and leads to high-quality alignments. One downside to this method is that the object of interest needs to be accessible to the fiducial beads; with *in situ* tomography using FIB-milling, this is often not the case.

Another method, which is less precise than fiducial alignment, but works for most types of samples, is called "patch tracking". This is an approach in which software (such as IMOD (42)) divides tilt images into smaller patches, and tries to guess the alignment of the tilts by comparing patches between tilts. The major advantage of this method is that any type of tilt series can be used; accessibility of the imaged object is not limited by accessibility of fiducial beads. This method is therefore most often used in cellular cryo-FIB/cryo-ET.

Tomogram reconstruction algorithms

Three common tomogram reconstruction methods are weighted back-projection (WBP), algebraic reconstruction techniques (ART) and simultaneous iterative reconstruction techniques (SIRT). The latter two are iterative algorithms, which back-project, and then re-project the back-projected tomogram to find the difference between the tomogram and its tilts, thereby iteratively converging to a 3D reconstruction. Weighted back-projection is simple back-projection, in which higher-resolution information is given a greater weight than low-resolution information.

CTF estimation and correction

The contrast transfer function (Section 1.2.3.4) results in the differential transfer of information at different frequencies. One way to correct for this, is to apply 2D-CTF correction. One can apply 2D-CTF correction on individual tilts that are fed into tomogram reconstruction. One example of how this is done is shown in Figure 1.20. The CTF is first estimated from the Fourier spectrum of the tilt. If properly done, CTF estimation should result in a model of Thon rings that aligns well with the Thon rings observed (Figure 1.20, left). With this model as input, negative contrast (Figure 1.20, A/middle) can then be flipped in a process called “phase flipping”, leading to a power spectrum with only positive values (Figure 1.20, B/right). These values can then be further boosted to normalize to a signal strength of 1.0 across nearly all frequencies, except at frequencies where the CTF approaches zero: this signal cannot be retrieved. Instead, image acquisition should be done over a range of different defoci, to change the CTF up and fill the gaps where it approaches zero.

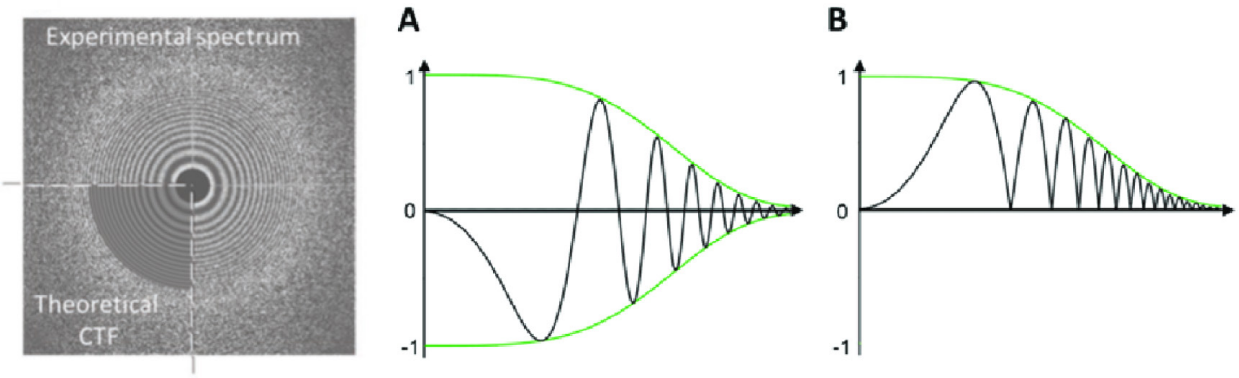

Figure 1.20. 2D CTF correction.

An example of 2D-CTF correction. (A-B) are plots of the radially averaged CTF such as seen on the left. The CTF is first estimated (left), and once a good match is found with the CTF of the real tilt, phases of the Thon rings (A) are flipped to obtain a power spectrum with just positive contrast contributions (B). Adapted from (44).

3D-CTF correction

CTF estimation can be improved compared to the 2D case mentioned above, by using software such as NovaCTF (45). The 2D case fails to take into account the thickness of the sample; it only estimates the average CTF of the entire tilt. However, using a 3D iterative approach, the CTF can be estimated locally, so across a gradient of defoci in a 3D tilted slab (a lamella, usually). This leads to an improved CTF model, which can then be used to reconstruct CTF-corrected volumes.

Deep learning improvement of volumes: denoising and missing wedge compensation

Advances in deep learning methods have recently provided multiple tools to improve the quality of tomograms. A deep learning algorithm can be trained on tomograms containing noise, by correlating tilt images to each other, or even frames within tilts. It can then find the difference between these frames or tilts, which is most often noise. It can then correct for this noise, resulting in a denoised tomogram (46). An example of software using this method is CryoCARE (47). Not only can deep learning algorithms detect and correct for noise; another new method named IsoNet now also applies these algorithms to the missing wedge, to try and fill in missing wedge information (21).

1.4.2 Main data analysis

Once a tilt series has successfully been reconstructed into a tomogram, data analysis can start. Since a tomogram is a snapshot of every process in the cell happening simultaneously, every tomogram contains a wealth of information, which can be used in different ways, in multiple projects. Data analysis in cryo-ET relies on a diverse toolbox; which tools are applied depends on the project, and they're often tailor-made.

One of the main ways to investigate proteins *in situ* is to obtain a particle average. Before alignment and averaging, the protein of interest must first be picked from tomograms with reliable accuracy.

Manual picking

A straight-forward method to pick particles is to simply pick them by hand. Many tomogram visualization software packages can be used for this, such as IMOD (42), Dynamo (43) or Chimera (48). However, as simple as it is, there are a few drawbacks to this method. The target particle should be easily recognized by eye, which can be problematic for featureless or small proteins, and human error can lead to bias. Moreover, this method usually doesn't give any initial orientational information. Finally, manual picking is also just a very time-consuming and laborious process; it's unsuitable for large datasets.

Template matching

Particles can instead be picked by a computer, by using computational matching of a template. As this template is searched in the tomogram, every voxel is taken as a center point, around which the template is rotated in every direction. The best scoring positions and angles are noted, and after applying a threshold of the cross-correlation score (CC), one should ideally be left with instances of the template-matched structure.

One big problem with the template matching approach is that even noise can lead to a representation of the template. This is called model bias, and can be avoided by not using a template at all, but picking particles within the dataset for an initial *de novo* average, which can then be used for further template matching. Template matching is an iterative process; better templates lead to better matches, which lead to an even further improved template. Unfortunately, this process is very resource-heavy, as it requires the template volume to be matched at many angles for every voxel in the 3D volume.

Deep learning methods

A newly developed alternative to template matching is to apply deep learning algorithms. Neural networks (often CNNs) are trained by feeding them “ground truth”: known particle positions of real particles in example training tomograms. The algorithm then tries to guess what it should be looking for, and will output the positions of any other similar particles that it found in new test tomograms. This has been shown to improve accuracy, while also providing improved computational speed (49).

Fourier shell correlation (FSC)

During subtomogram averaging, the resolution of the obtained average should improve with better alignment. To keep track of the resolution at which useful information turns into high-frequency noise, one needs to do Fourier shell correlation (FSC). For a given subtomogram average, the subtomograms that went into it can be divided into independent groups, of which averages are then produced. FSC correlates two or more of these partial averages, and plots the degree of correlation per frequency. In 3D Fourier space, this takes the form of a shell around the zero-frequency center point; hence the name “Fourier shell correlation”.

The frequency at which the individual partial averages stop matching is empirically set. The “gold standard” of the FSC cutoff is a correlation of 0.143 between independent half-sets; the frequency at which this correlation is reached is defined as the resolution of the resulting average (which should then be filtered to that resolution).

3D analysis of cellular volumes

Tomograms can also be used to obtain useful 3D information about cell structure and biophysical processes in the cell. Membranes can be segmented (volume filled, in 3D) and used to demarcate certain subvolumes of the cell, such as organelles. Subtomogram averages can be mapped back into the tomographic volume from which they came. Using this type of information, all kinds of calculations can be performed, such as counting the number of protein complexes in a given volume, giving an estimate of the concentration of said protein complexes (50,51). Distributions of proteins in different states (as a result of classification, for example) can be plotted in 3D, yielding useful information about spatial regulation of cellular processes (32). Membrane curvature can also be examined (52). There are many methods, often tailor-made, depending on the type of application.

1.4.3 Post-processing

Sharpening

After a subtomogram average is obtained, one can use sharpening methods to further boost the resolution of the average. This can be done using one of several approaches, including deep learning and Bayesian statistics, incorporated in software packages such as M (53) and emClarity (54).

Tilt refinement

A newer, more advanced method of tilt alignment performs iterative refinement of tilts. First, a rough alignment is made using another method, such as patch tracking. From this rough alignment, an initial tomogram is reconstructed. Tilt refinement software such as WARP (55) can then estimate deformations in tilt images, and correct accordingly.

Native fiducial markers

In the near future, this should enable tilt alignment using particles of a large common molecular complex (such as ribosomes). Using existing alignment methods such as patch tracking, an initial tomogram is reconstructed. In this volume, fiducial particles are then picked, for instance by using template matching (see Section 1.4.2), and aligned. Projections of the resulting aligned particles can then be retraced to each individual tilt image, and its position there used to function as a local fiducial marker. These fiducial markers can then be used to obtain a new, improved alignment of tilt images, which results in a higher-quality tomogram.

2 Introduction to ciliary biology

Cilia (also called eukaryotic flagella, not to be confused with bacterial flagella) are evolutionarily-conserved organelles. They are ancient; the cilium was most likely present in the last eukaryotic common ancestor (LECA), and is therefore present across many eukaryotes today. Cilia extend from the cell surface (Figure 2.1) and carry out a wide variety of important functions. These functions include including cell motility (sperm, unicellular organisms), fluid flow generation (multiciliated epithelia such as in ependyma, trachea, oviducts), sensing (kidneys, photoreceptors, inner ear), signaling (Wnt, Hedgehog, etc.), and related development (56,57).

At the cilium's base, the transition zone (also known as the ciliary pore) forms a gateway that connects the cilium with the rest of the cell. This region of the cilium is extremely important for ciliary homeostasis, but it is severely understudied, mostly due to the lack of biochemical methods needed to isolate it in an intact state. However, thanks to recent advances in the field of cryo-electron tomography (cryo-ET), it has become feasible to study this region in great detail within the native cellular environment (34). In this thesis, we used cryo-ET on two different model systems, *Chlamydomonas reinhardtii* and murine tracheal epithelial cells (MTECs), to address several open questions concerning the ciliary pore.

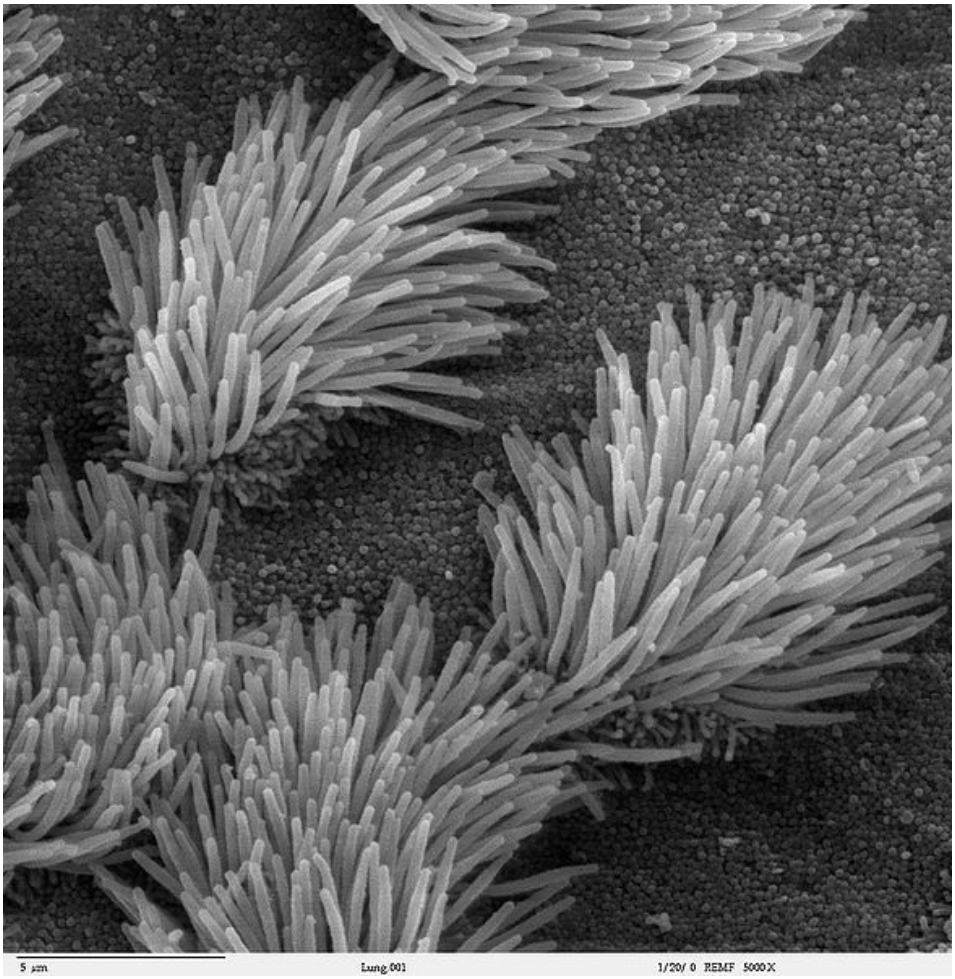

Figure 2.1. SEM image of lung epithelium, showing multiciliated cells.
Image credit: Charles Daghlian

2.1 Ciliopathies: ciliary function and their involvement in disease

Because cilia perform many important roles, defects in cilia structure and function are linked not only to cancer and obesity, but also to pleiotropic human diseases, together called “ciliopathies” (58). Since cilia are so widespread throughout the body, but moreover important during embryonal development, ciliopathies tend to be broad developmental syndromes, with a variety of overlapping pathological phenotypes (Figure 2.2).

Confirmed ciliopathies include Nephronophthisis (NPHP), Meckel-Gruber syndrome (MKS), primary ciliary dyskinesia (PCD, a.k.a. Kartagener syndrome), retinitis pigmentosa (RP), Joubert syndrome (JBTS), Senior-Løken syndrome (SLS), Bardet-Biedl syndrome (BBS), Jeune asphyxiating thoracic dystrophy (JATD), orofaciodigital syndrome (OFD), autosomal dominant/recessive polycystic kidney disease (AD/AR-PKD), von Hippel-Lindau disease, oculomotor apraxia (OMA), Leber’s congenital amaurosis (LCA), Alström syndrome (ALMS), McKusick-Kaufman syndrome (MKKS), Usher syndrome, Sensenbrenner syndrome, Marden-Walker syndrome (MWS), Ellis van Creveld syndrome (EvC)(59–61). Many other syndromes are likely candidates for ciliopathies as well, such as hydrolethalus syndrome (HYLS).

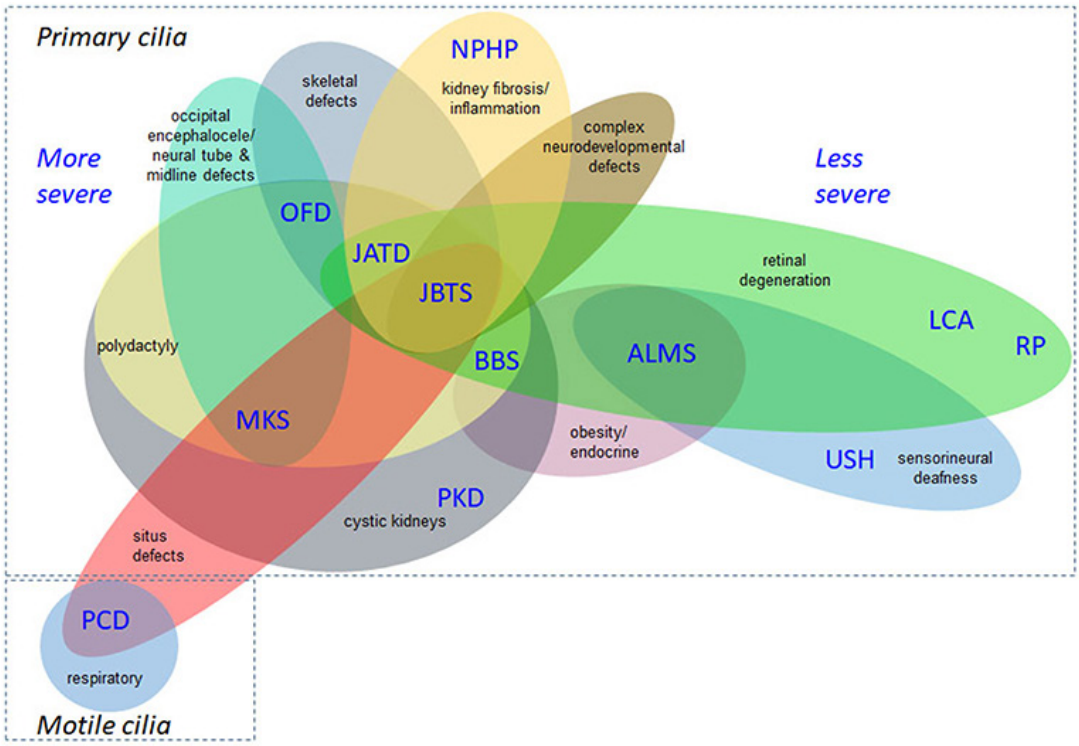

Figure 2.2. Some common ciliopathies and their associated disease phenotypes.

Common ciliopathies (blue) and their disease phenotypes (black), which often overlap between syndromes. PCD: primary ciliary dyskinesia; MKS: Meckel-Gruber syndrome; OFD: orofaciodigital syndrome; JATD: Jeune asphyxiating thoracic dystrophy; JBTS: Joubert syndrome; PKD: polycystic kidney disease; NPHP: nephronophthisis; BBS: Bardet-Biedl syndrome; ALMS: Alström syndrome; USH: Usher syndrome, LCA: Leber’s congenital amaurosis; RP: retinitis pigmentosa. List is not exhaustive. Severity of each syndrome approximated; ranging from more severe (left) to less severe (right). Image from (61).

Cilia can be separated into roughly two categories: motile and non-motile. Most ciliopathies listed above and in Figure 2.2 and Figure 2.3 involve the function of the so-called “primary cilium”, which is present on most cells in the human body as a single, non-motile “cellular antenna”. The signaling function and widespread presence of the primary cilium make it responsible for most of the broad, developmental effects of ciliopathies.

Conversely, motile cilia are found only in specific tissues, and are involved in fewer ciliopathies, with only two listed in Figure 2.2. However, this list of ciliopathies is not exhaustive: motile cilia defects can cause other disease phenotypes, such as for example infertility, both in male (sperm tail defects) and female (oviduct epithelial defects).

Some of the major ciliopathies involve proteins that are part of the ciliary transport machinery, while others are part of a region at the ciliary base called the transition zone (TZ). The TZ gates entry and exit of both membrane-bound and soluble ciliary proteins (62–64), which are imported via the ciliary transport machinery. Defects in either system lead to altered cilium composition, leading to ciliopathies like Jeune- and Joubert syndromes (JATD, JBTS), Nephronophthisis (NPHP) and Meckel-Gruber syndrome (MKS)(65,66). This will be further discussed in Sections 2.2.5 and 2.3.

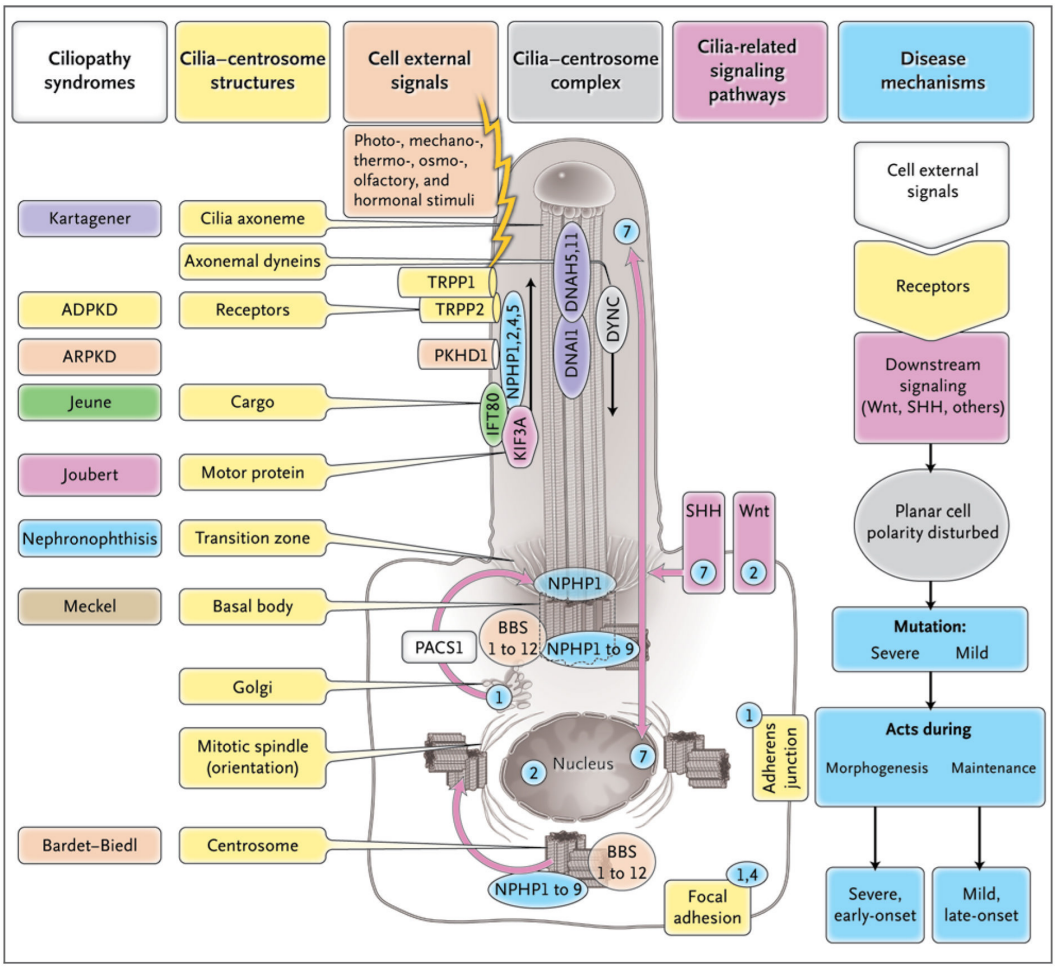

Figure 2.3. Overview of some common ciliopathies, listing ciliary components linked to their pathology.

This overview links some of the common ciliopathies (left column) to components of the cilium (second to left, yellow), and shows how the effects of mutations in these components constitute the disease phenotype of ciliopathies (right). Image from (59).

2.2 Basic architecture of the eukaryotic cilium

The cilium's ultrastructure (Figure 2.4) consists of a cytoskeletal core called an "axoneme", generally composed of nine microtubule doublets (MTDs), which extend from the microtubule triplets (MTTs) of a modified, anchored centriole (also known as basal body) at the ciliary base. The axoneme is ensheathed in a ciliary membrane. Both the ciliary lumen and the ciliary membrane have a molecular composition which is distinct from the rest of the cell.

All cilia are non-membrane enclosed organelles. This means they have a seemingly open connection to the cytosol. However, this is far from the truth: the contents of the cilium and the transport into- and out of the cilium is tightly regulated by a strong barrier. The barrier is located at the ciliary base; specifically, in the so-called "transition zone" (TZ), at the very start of the ciliary sheath, which forms the transition between cell body and ciliary lumen. The two sides of this transition zone have a distinct composition, not only in soluble contents in the ciliary lumen versus cytosol, but also in membrane composition. This will be further discussed in Section 2.2.5.

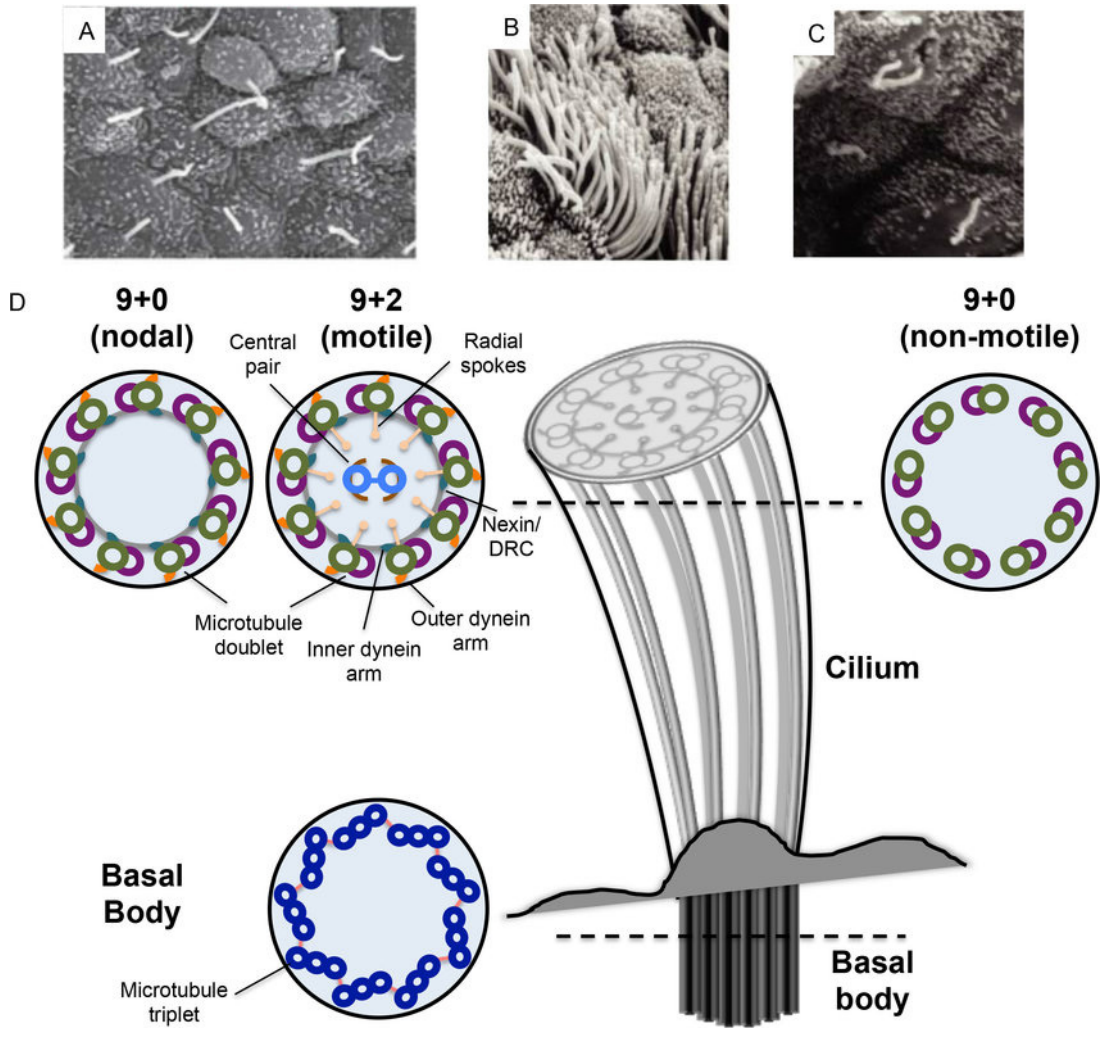

Figure 2.4. Schematic overview of ciliary structure in different types of cilia.

Figure from (67). **(A)** Scanning electron micrograph of nodal cilia on the mouse embryonal node (image originally from S. Nonaka); **(B)** motile cilia are often found in arrays of hundreds of cilia, here in a scanning electron micrograph of mammalian multiciliated tracheal epithelial cells (image from (60)); **(C)** primary cilia, have many sensing/signaling functions, and come as a single copy per cell; in this case on kidney tubule epithelium (scanning electron micrograph from (60)); **(D)** schematic representation of axonemal cross-sections in different types of cilia, both motile (left) and non-motile (right).

2.2.1 Cytoskeletal scaffolding of the cilium: the microtubule doublet (MTD)

The microtubule doublet (MTD) forms the main scaffolding unit onto which the majority of ciliary components are built. It is composed of a fully cylindrical A-tubule, with 13 protofilaments made up of individual tubulin dimers. Onto the side of this cylinder, the B-tubule is formed; this microtubule is an incomplete cylinder made up of 10 protofilaments, with protofilament 1 and 10 attaching to the outside walls of the A-tubule. In a similar fashion, a third C-tubule can attach to the B-tubule, which is the case in microtubule triplets (MTTs) found in the centriole/basal body. The MTD's protofilaments assemble such that neighboring tubulin dimers form a pseudo-helical shape (Figure 2.5). This pseudo-helix is interrupted, in a so-called "open washer" conformation; its seam runs between protofilaments A9 and A10.

Aside from motility-related molecular machinery (see Section 2.2.2), MTDs can incorporate many different proteins in their structure. These proteins are together called microtubule-associated proteins (MAPs), of which a substantial portion bind on the inner luminal surface of the microtubules. These are called microtubule inner proteins (MIPs), of which many cryo-EM structures are known and mapped in the MTD (Figure 2.6)(68). Together with post-translational modifications to tubulin, many of these proteins stabilize the otherwise dynamically reshaped microtubules in the axoneme and are even theorized to deform the tubulin lattice and put inherent mechanical stress on the MTDs, influencing the cilium's physical properties such as waveform of the ciliary beat (69). They could also function as a length ruler, to determine the intervals at which certain ciliary components should bind to the MTD.

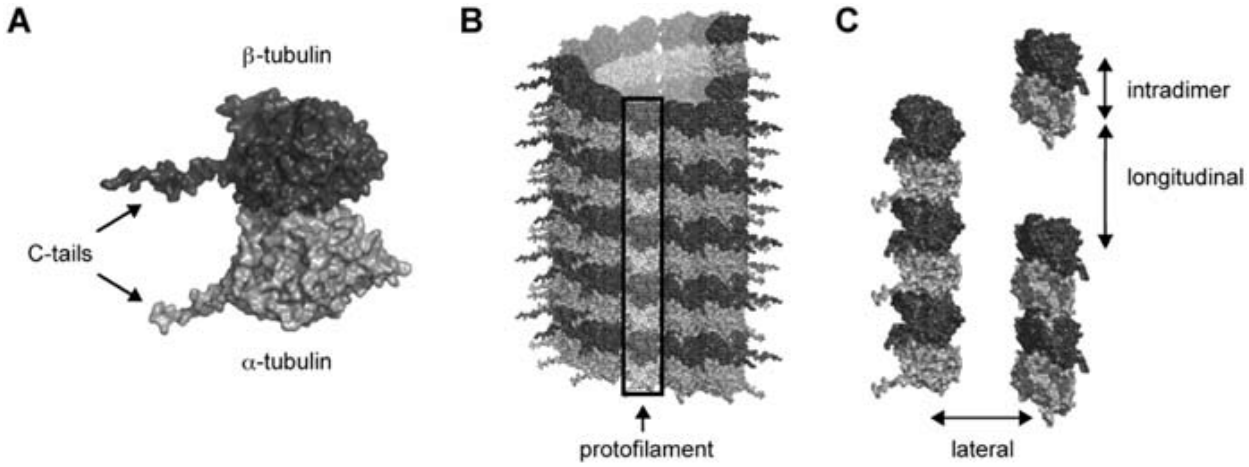

Figure 2.5. The tubulin lattice in microtubules.

Tubulin dimers (A) self-assemble end-to-end into protofilaments (C). 13 protofilaments then in turn self-assemble into a regular microtubule, which has a typical pseudo-helical ~1.5-start "open washer" conformation (B). This means that every spiral of dimers disconnects at a seam, in this case on the right side of the MT shown in (B); the overhang of 1.5 tubulin dimers can be seen (top right). Image from (70).

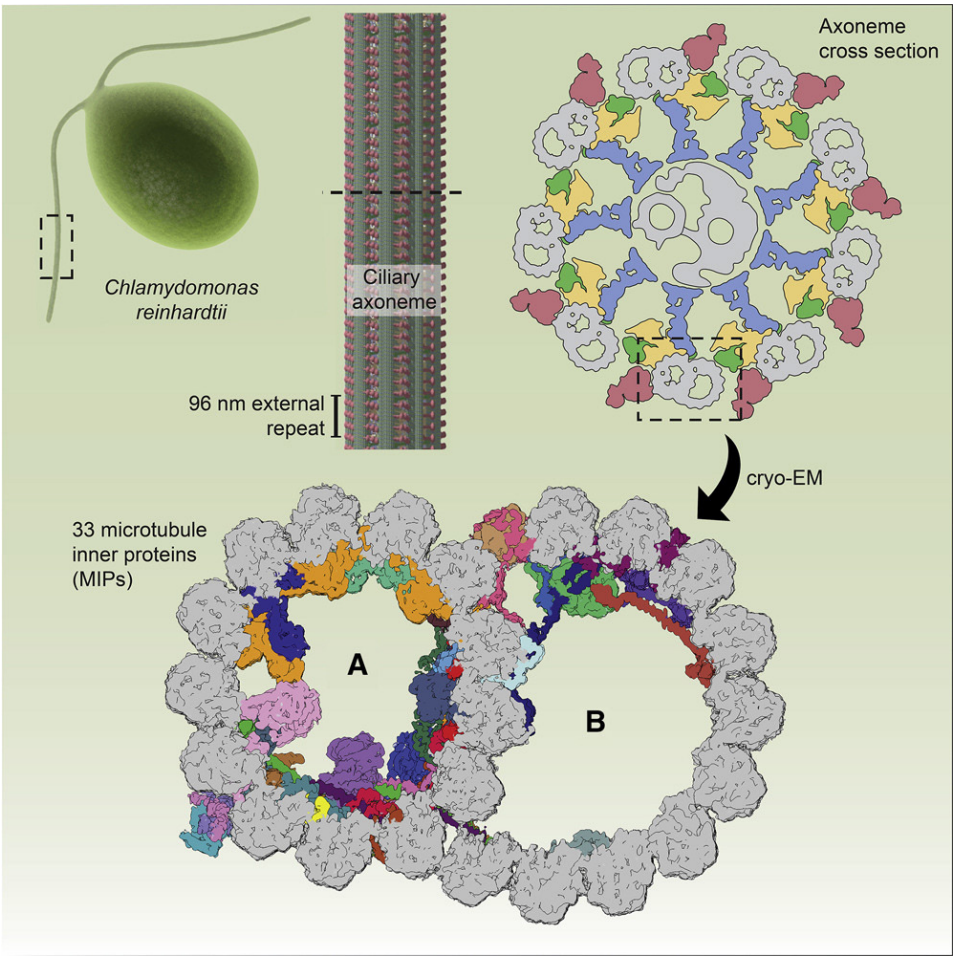

Figure 2.6. Overview of MIPs found in the ciliary axoneme in *Chlamydomonas*

Cryo-EM structure of the decorated axonemal MTD of motile *Chlamydomonas* flagella. Tubulin dimers in gray, microtubule inner proteins (MIPs) in various colors. Figure from (68).

2.2.2 Structure and function of motile cilia

Cilia can roughly be divided into two classes: motile and non-motile (Figure 2.4). The primary function of motile cilia is to provide cell motility or fluid flow, such as across an epithelial surface. The primary function of non-motile cilia is often sensing-/signaling-related, such as in photoreceptors or olfactory cells. However, functions aren't exclusive and often overlap; for instance, some motile cilia are known to also be involved in sensing/signaling. Non-motile cilia are widespread throughout the mammalian body, but motile cilia are only found in a small subset of tissue types, mainly epithelia.

Motile cilia in mammals (except for sperm cells) are often found in arrays on the surface of epithelia as part of "multiciliated cells" (MCCs), cells with hundreds of cilia on their apical (outward facing) side. Here, the cilia beat in coordinated wave-like motion to provide fluid flow. This is crucial for proper circulation of cerebrospinal fluid in the brain, clearing of debris from the lungs and airways, and transport of oocytes through the oviduct.

The structure of motile cilia most often consists of a "9+2" arrangement (Figure 2.4, Figure 2.6, Figure 2.7), in which nine microtubule doublets form the bulk of the axoneme, and a pair of singlet microtubules reside in its core. These singlets and their associated ciliary structures help to coordinate ciliary motion in order to constitute the required complex ciliary waveforms.

An exception to this rule is the case of embryonal nodal cilia, which appear early in embryonal development and constitute consistent left-right asymmetry patterning of internal organs (71,72). These motile cilia lack the coordinating double singlet core ("9+0" arrangement), and therefore only beat in an uncoordinated, simple circular pattern.

Motile cilia are quite literally filled with molecular machinery that constitutes their complex motility. The majority of this machinery is tasked with either motility, or regulation thereof. Dynein motor proteins provide the motile power; in particular, a subset of fixed dynein motors known as "axonemal dyneins", which are anchored to the MTDs.

Axonemal dyneins are divided into two groups, connected to an inner dynein arm (IDA) and outer dynein arm (ODA) (Figure 2.7). They work by pulling on the neighboring MTD, which makes the MTDs slide past each other. This motion is then repeated in the next neighboring MTDs, and the motion goes around all nine MTDs, until the axonemal dyneins of the original MTD are ready for the next power stroke. This cyclic sliding motion is tightly coordinated by the central pair (CP) of singlet microtubules, through the radial spokes (RS), as well as by the nexin-dynein regulatory complex (N-DRC)(73) which interconnects the MTDs. Specific MTDs contain elements that break the 9-fold symmetry, thereby introducing a more complex and coordinated waveform, which can even be tuned. Many ciliated organisms, including *Chlamydomonas,* can switch between different waveforms when triggered by certain stimuli. *Chlamydomonas* switches between its regular asymmetric waveform, a two-part power-stroke/return-stroke whip-like motion comparable to the breast stroke in swimming which propels the cell forward, and the symmetric, corkscrew-like waveform, which propels the cell in the reverse direction, as a protection mechanism from stimuli such as high light stress (Figure 2.8).

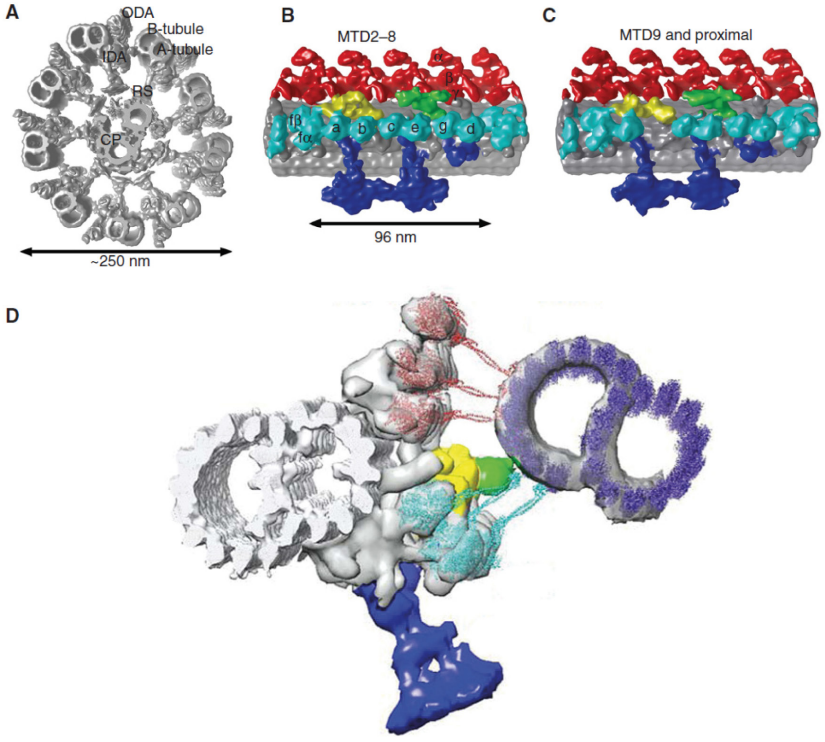

Figure 2.7. Cryo-ET structures of axonemal components found in motile cilia.

Adapted from (74). **(A)** General internal structure of motile cilia, as determined by several cryo-ET studies (75); inner dynein arms (IDA), outer dynein arms (ODA), radial spokes (RS) and central pair (CP) are indicated; **(B-C)** 3D cryo-ET structure of the 96-nm repeating unit along the motile cilium's MTDs (76,77); **(D)** distal-to-proximal view of the motility-providing machinery between two MTDs, with atomic models of axonemal dyneins fitted into the ODA and IDA densities. Red: ODA; cyan: IDA; green: Nexin-dynein regulatory complex (N-DRC); yellow: intermediate/light chain; dark blue: radial spokes; purple: tubulin.

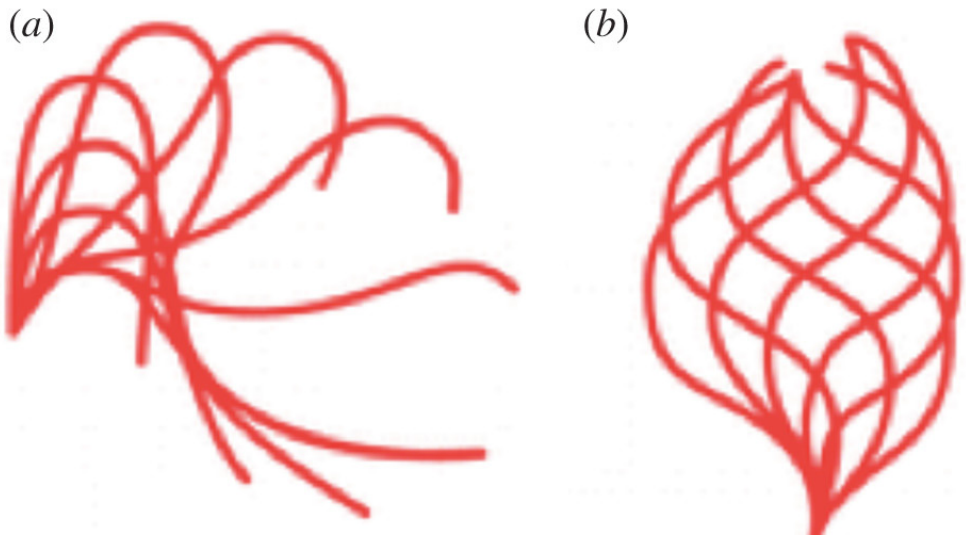

Figure 2.8. The two flagellar waveform modes in *Chlamydomonas*.

The two modes of propulsion used by *Chlamydomonas*. **(A)** the principal asymmetric "breaststroke" waveform, used to propel the cell under normal circumstances; **(B)** the secondary symmetric "reversing corkscrew" waveform, used to evade stressors such as high light. Image from (78).

2.2.3 Structure and function of non-motile cilia/primary cilia

Whereas most motile cilia are found only in certain tissues, most animal cells contain a single non-motile "primary cilium", which is often a cellular sensing/signaling "antenna". Primary cilia are based on the same cytoskeletal core as motile cilia, but lack the intricate machinery required for motility. The axonemal architecture of the primary cilium therefore only consists of the microtubule doublets and ciliary membrane (Figure 2.4D). However, most of the machinery that is required for a proper cilium is present in primary cilia as well.

The majority of ciliopathies can be traced to dysfunction of the primary cilium (Figure 2.2). However, the mutations that lead to this dysfunction are not limited to primary cilia. Many disease-linked mutations are mutations in general ciliary machinery, specifically at the ciliary base, with ciliopathies such as Bardet-Biedl syndrome, Meckel-Gruber syndrome and nephronophthisis (Figure 2.3). This also affects motile cilia, however the extent to which motile cilia contribute to disease phenotypes is generally small. Abnormalities in cilia motility can be used as a marker of ciliopathies, though.

Structural studies of the primary cilium have proved to be very challenging, because of the low copy number (one) per cell. Biochemical isolation of primary cilia is difficult as well, especially when trying to maintain near-native conditions. Fortunately, this hasn't stopped recent pioneering work on the structure of the primary cilium (79), which uses the "cryo peel-off" method, in which a substrate to which primary cilia attach can be used to physically rip off the cilia from a monolayer of cells. Combined with conventional resin-embedded EM, it was shown that intraflagellar transport (IFT) is abundant in primary cilia (Figure 2.9K-L), which is to be expected, as it is crucial for primary ciliary function and therefore correlates with ciliopathies such as Jeune (JATD) and Joubert (JBTS) syndromes. Moreover, they found that microtubule doublets do not continue all the way to the tip of the primary cilium; instead, many doublets end in the middle of the primary cilium, after which mostly singlet A-tubules continue to the tip (Figure 2.9B-I).

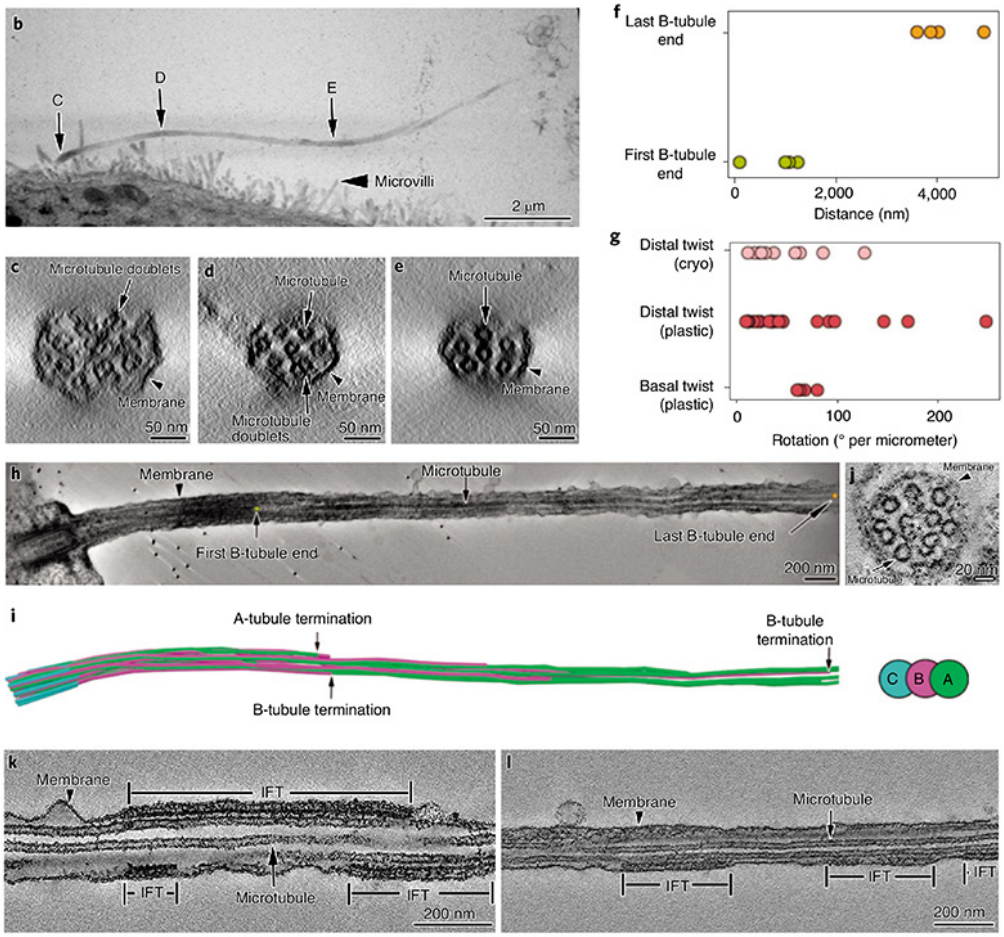

Figure 2.9. Resin-embedded EM of the primary cilium on mammalian MDCK-II cells.

Resin-embedded micrographs of thin sections showing the primary cilium on MDCK-II cells. **(B-I)** The full "9+0" MTD architecture associated with primary cilia ends prematurely along the length of the axoneme, as shown in cross-sections in (C-E) and segmentation in (I), leaving only A-tubules to reach the tip. (L-K) IFT is abundant in these primary cilia. Figure adapted from (79).

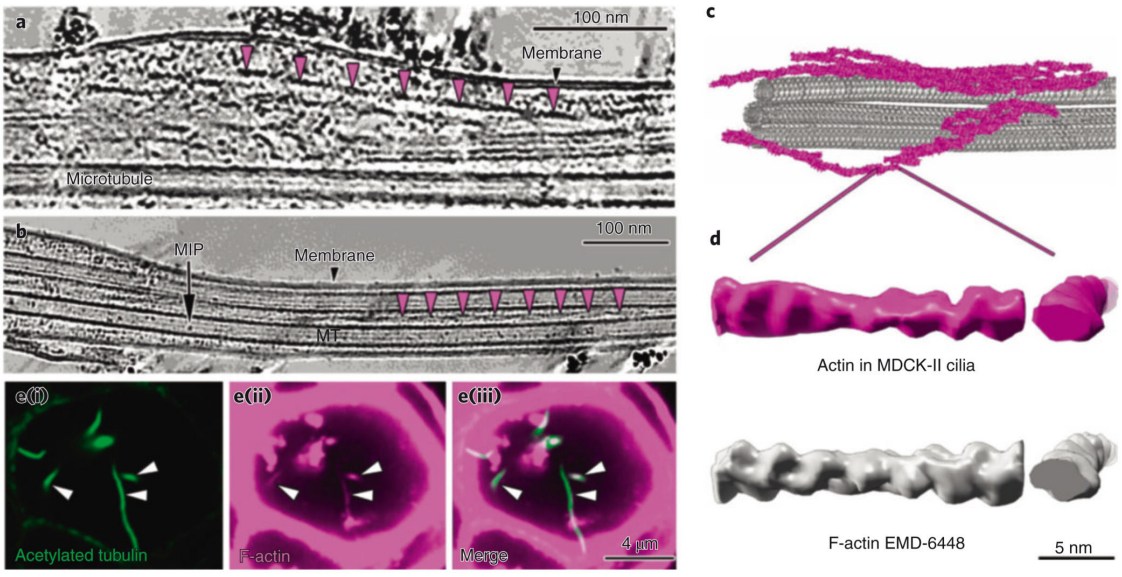

Figure 2.10. Actin can be found in primary cilia on mammalian MDCK-II cells.

Cryo-ET of the primary cilium shows actin filaments (A-D, pink), confirmed with FM (E). Figure from (79).

2.2.4 The basal body

At the very base of the ciliary superstructure lies the basal body (BB). This is a modified centriole, anchored to the periciliary membrane by transitional fibers (TFs), sheet-like fibrous structures sometimes called “distal appendages” (DAPs) or “Alar sheets”. The BB can be further anchored to the internal superstructure of the cell through rootlets, which are flexible spring-like structures, providing additional mechanical robustness. Without rootlets, mechanical stress can break off cilia from the cell body.

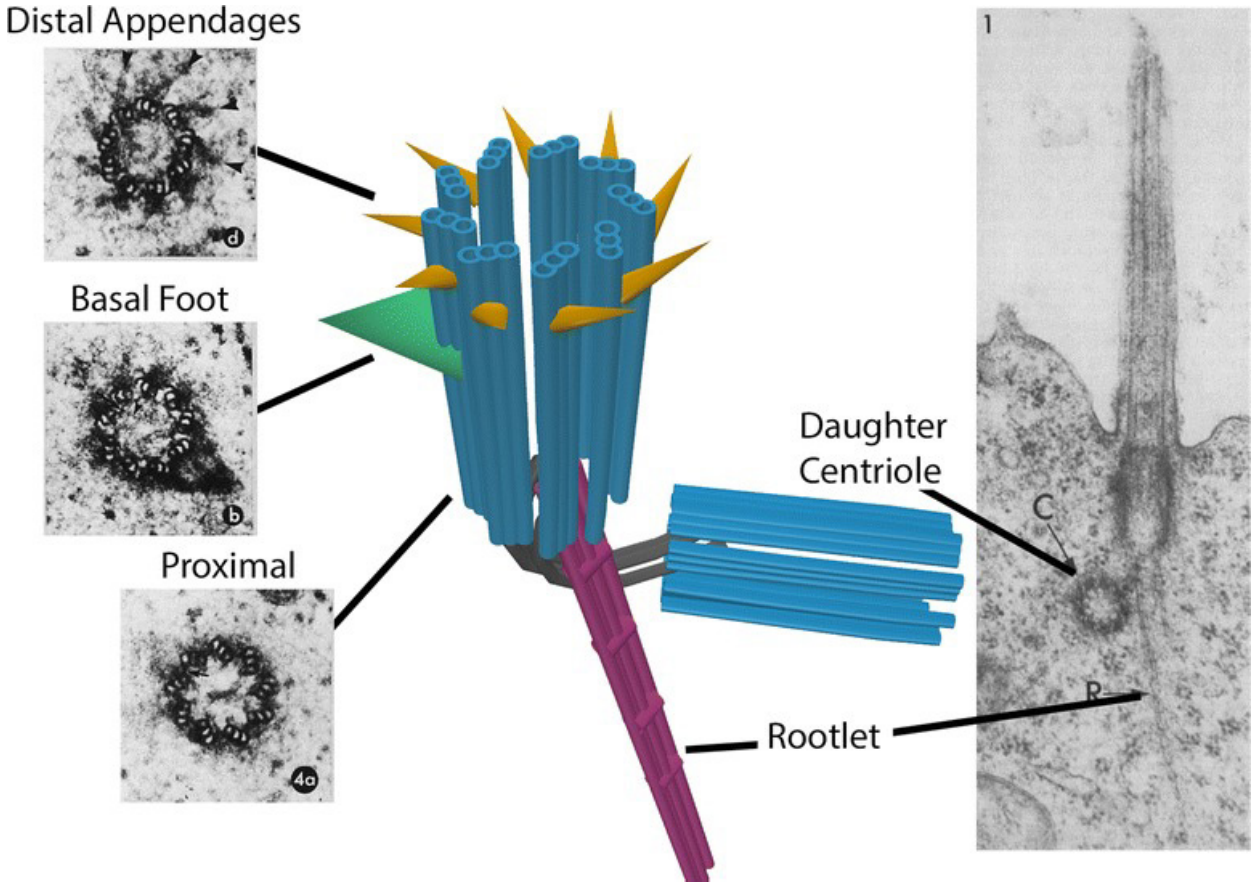

Figure 2.11. Schematic structure of the basal body.

Figure from (80). Schematic overview showing common features of basal bodies. Left: electron micrographs of resin-embedded thin sections of basal bodies in cross-section (originally in (81)). Middle: 3D model of the basal body complex, showing the basal body’s MTTs (dark blue), distal appendages/transitional fibers (yellow), basal foot (green), rootlet (purple), daughter centriole (light blue), and the connecting fibers to the daughter centriole (gray). Right: electron micrograph of plastic-embedded thin section of basal bodies at the root of a renal primary cilium, in longitudinal cross-section (originally in (82)).

Basal bodies are found in many different shapes and sizes, depending on cilium type and organism (83), and can take on different parallel roles, depending on the cell cycle. Just before mitotic entry, when the primary flagellum is resorbed, the basal body turns itself into a mitotic hub, called the microtubule organization center (MTOC). The MTOC is a phase-separated condensate which, through local tubulin enrichment and presence of gamma-TuRC complexes as MT nucleation sites, nucleates and grows microtubules required to pull on chromosomes during mitosis. This ties into the involvement of cilia and centrosomes in cancer; supernumerary centriole production is a marker of advanced tumorigenesis (84), likely due to aberrations in mitosis.

Basal body production

Conventional centrosome/basal body duplication (Figure 2.11) is tightly controlled and starts during late-G1/early-S-phase. During this phase, the mother-daughter pair of centrosomes each template the growth of a procentriole (precursor to a mature centriole). This duplication happens on the side of the centriole barrel, through binding of PLK-4 and PLK-1 to the existing centriole's outer wall, which templates the growth of the cartwheel. The cartwheel in itself is an important centriole-templating structure at the proximal end of the centriole. Its core is composed of SAS-6, which can spontaneously self-assemble into 9-folded symmetrical structures (85), thereby likely imposing the classic 9-fold symmetry on the basal body and cilium before recruiting tubulin to form microtubule triplets (86). Before mitosis, each procentriole matures into a new daughter centriole, and the two mother-daughter pairs split from each other, in order to end up at the opposing sides of the dividing cell during mitosis, where they form the microtubule organizing center (MTOC), which splits the chromosome pairs.

Another way of forming new basal bodies takes place in multiciliated cells (MCCs) during ciliogenesis. Basal bodies there are formed on many basal body-producing hubs made of protein condensates, called deuterosomes (87). These allow for hundreds of basal bodies to be produced simultaneously, instead of templating to the sides of existing centrioles, which only doubles the number of centrioles every cycle and therefore would need many cycles to produce the hundreds of basal bodies needed for multiciliated cells. However, deuterosomes are dispensable for normal ciliogenesis in MCCs (88), which makes them accessory structures that perhaps only aid the speed of basal body production.

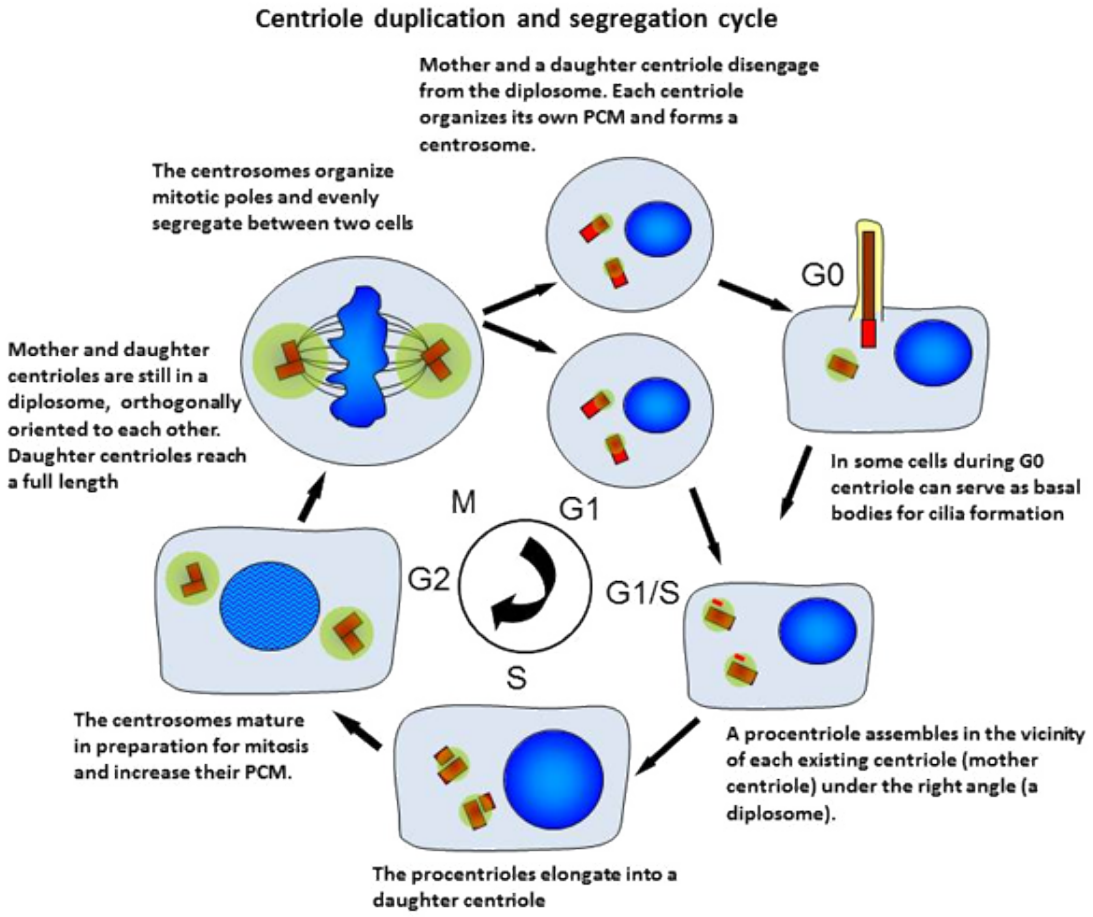

Figure 2.12. The conventional centriole/basal body duplication cycle.
Centriole duplication involves templating onto existing centrioles. Image credit: J. Loncarek (89).

2.2.5 Gatekeeper of the ciliary pore: the transition zone

All cilia are non-membrane enclosed organelles. This means they have a seemingly open connection to the cytosol. However, this is far from the truth: the contents of the cilium and the transport into- and out of the cilium is tightly regulated by a strong barrier. The barrier is located at the ciliary base; specifically, in the so-called “transition zone” (TZ), the very start of the ciliary sheath, which forms the transition between cell body and ciliary lumen. The two sides of this transition zone have a distinct composition, not only in soluble contents in the ciliary lumen versus cytosol, but also in membrane composition.

The importance of this barrier is clear, as many ciliopathies (Figure 2.3, Figure 2.13) arise from mutational defects in proteins residing in this region (Figure 2.14) which lead to altered ciliary composition. The transition zone contains many structural components (Figure 2.12) that together are theorized to form this barrier: Y-links, transitional fibers, and the membrane-embedded ciliary necklace and ciliary bracelet. In *Chlamydomonas* there exists an additional structure, centrally located in the TZ: the nine-pointed stellate assembly, composed of contractile fibers which contain centrin (Figure 2.12D, left middle panel). This contractile assembly is theorized to help pinch off the flagella upon excision (severing/shedding).

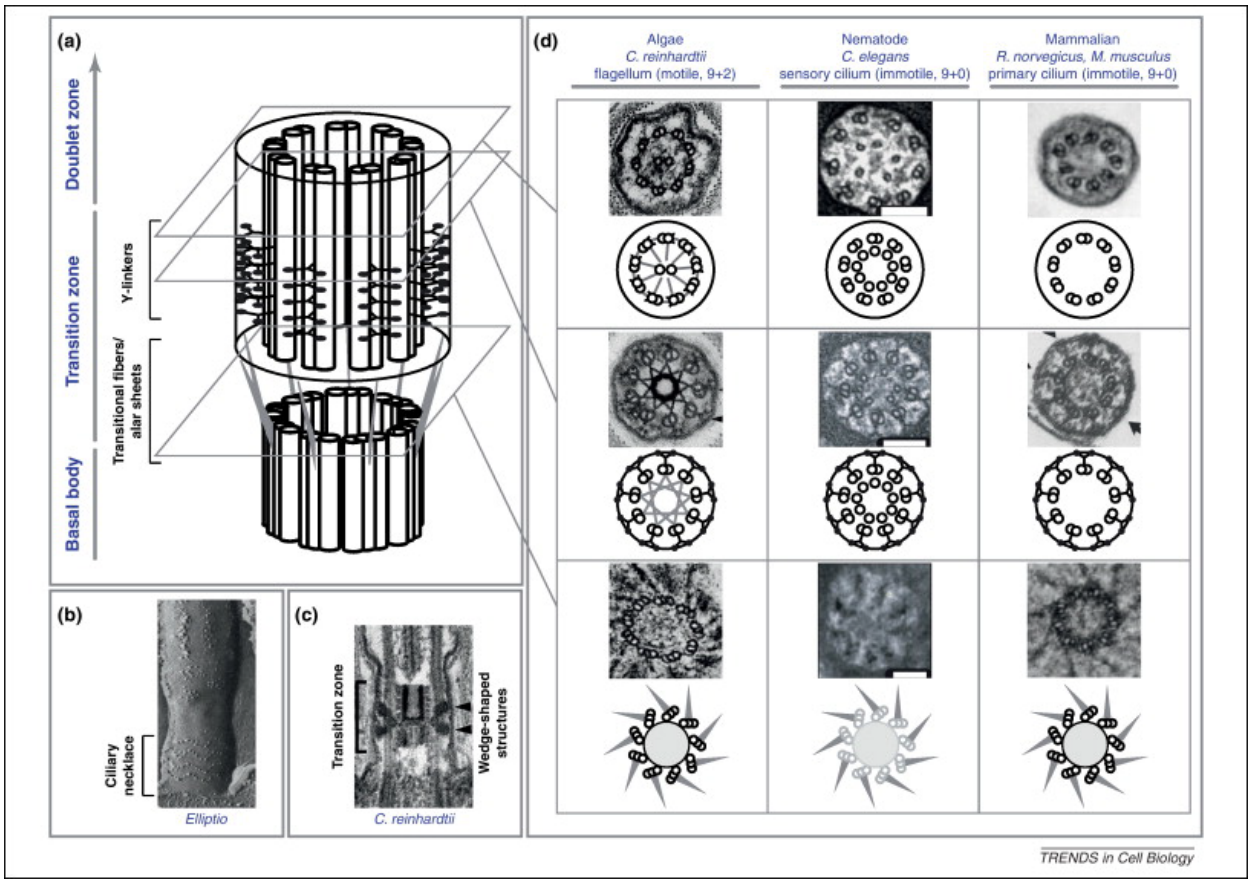

Figure 2.13. Electron micrographs showing structural elements of the transition zone.

(A) The ciliary transition zone, general overview; (B) the outside membrane of the TZ shows protruding densities, named the “ciliary necklace”; (C) longitudinal cross-section of a *Chlamydomonas* transition zone; (D) Three cross-sectional slices through each part of the transition zone, in *C. reinhardtii* (left), *C. elegans* (middle) and mammals (*R. norvegicus/M. musculus*). Top: proximal axoneme; middle: mid-TZ, showing Y-links and in the case of *Chlamydomonas,* the nine-pointed stellate assembly; bottom: transition fibres anchoring the basal body to the periciliary membrane. Figure from (90).

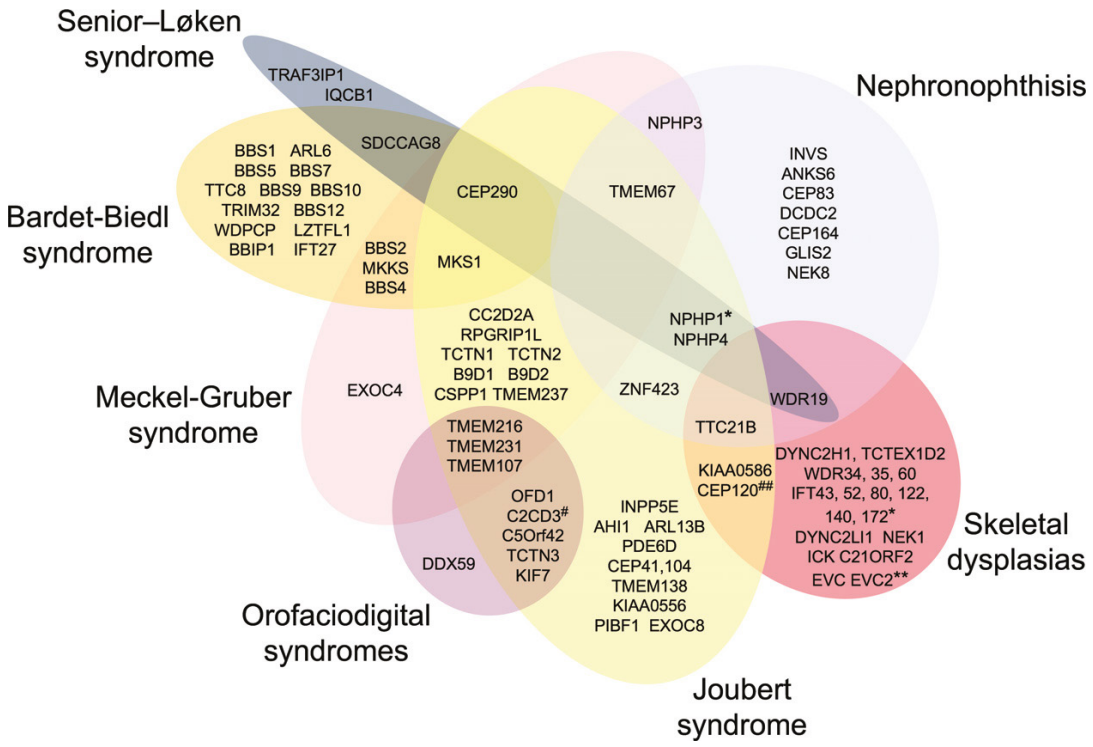

Figure 2.14. Transition zone proteins are involved in many common ciliopathies.

Venn diagram showing many known transition zone proteins and their involvement in each ciliopathy.

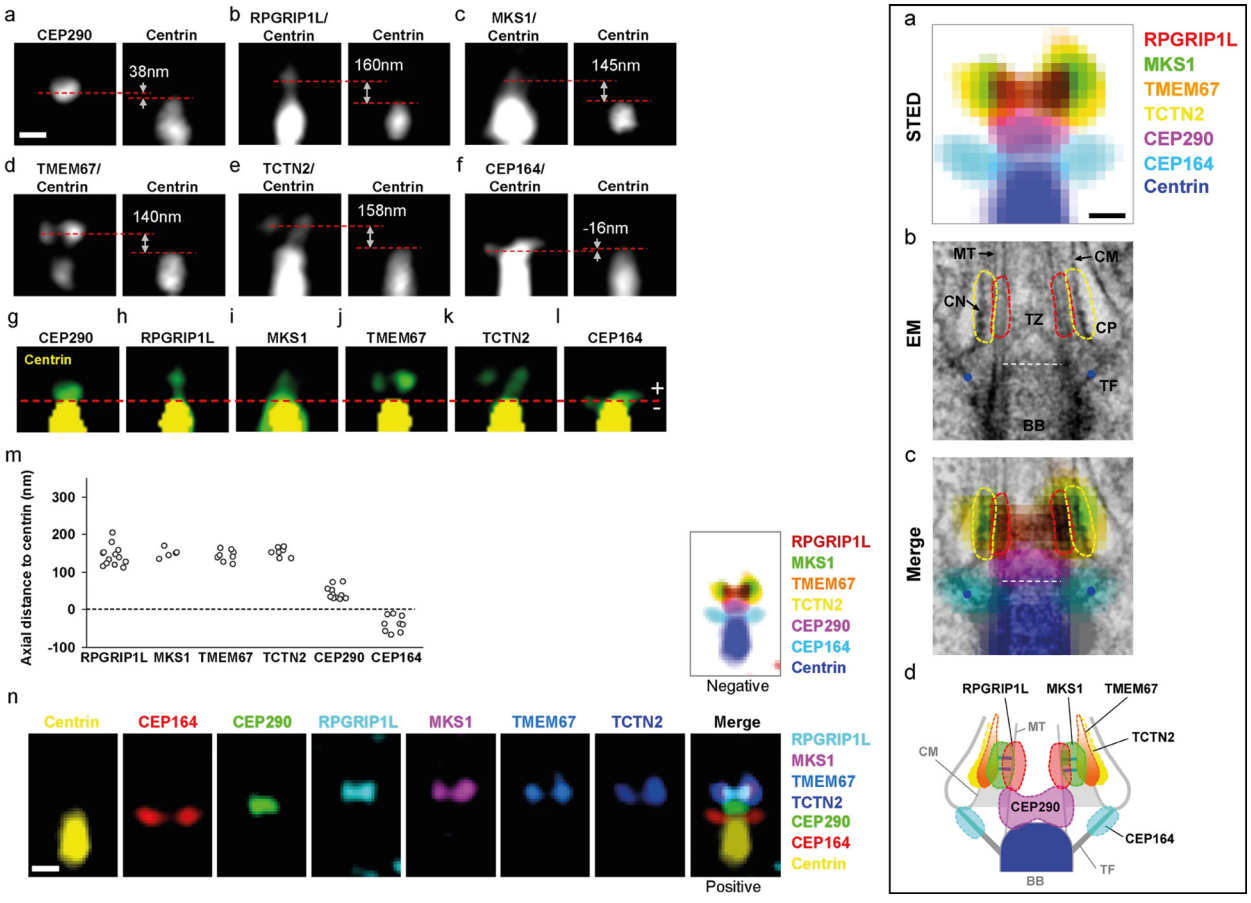

Figure 2.15. TZ proteins mapped back using STORM/PALM.

Localization map showing the exact localization of some of the principal TZ components, obtained using super-resolution microscopy. Inset: enlarged, overlaid with electron micrographs. Adapted from (91).

Y-links

First and foremost, there's the Y-link (Figure 2.12D, middle panels). This structure is named after its shape, and it connects the MTDs to the periciliary membrane. The membrane-bound ends of the Y-links protrude to the extracellular space, to form the ciliary necklace (Figure 2.16, red arrow), a structure that together with the ciliary bracelet (Figure 2.16, blue arrow) is theorized to lie central to the membrane-embedded diffusion barrier. It contains crucial TZ proteins such as CEP290, NPHP1, NPHP4, MKS1 and RPGRIP1L, all deeply involved in multiple ciliopathies (central portion of Figure 2.13). Other than the rough structure obtained using conventional RT-TEM (Figure 2.12), not much is known about the Y-link's structure. An interaction map is proposed (92), showing that most of the important TZ proteins are central to the Y-link, especially its connection to the MTD.

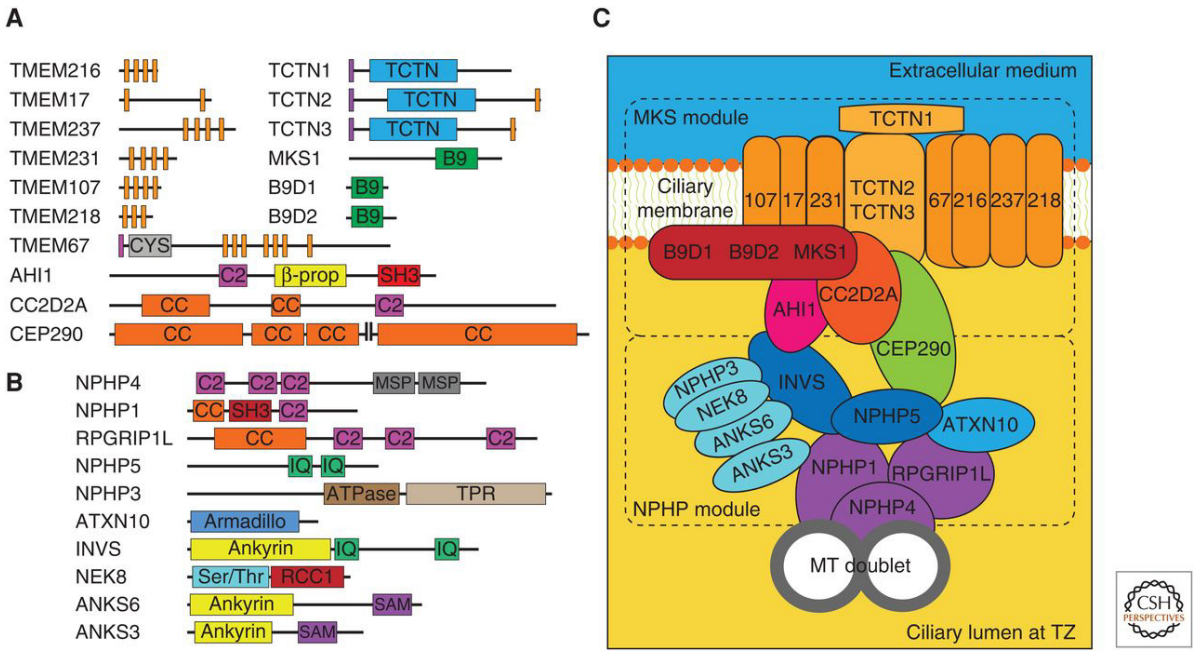

Figure 2.16. Proposed interactome of Y-link proteins

NPHP1-4 and RPGRIP1L form the MTD attachment (purple) while other components such as CEP290 and MKS1 form the arms of the Y-links. TCTN proteins form the transmembrane portion, and are most likely part of the ciliary necklace (Figure 2.16). Figure and proposed interactome from (92).

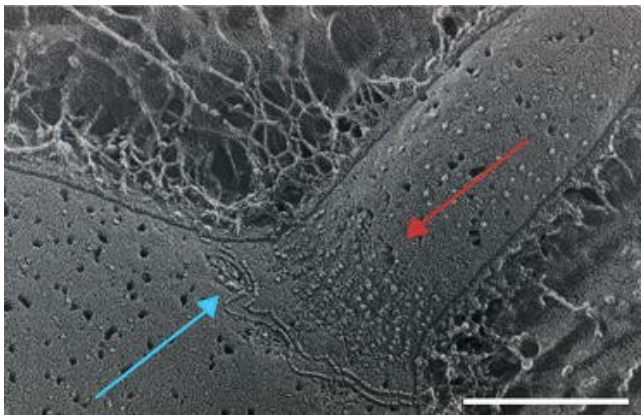

Figure 2.17. Quick-freeze/deep-etch (QFDE) micrograph of the ciliary base in *Chlamydomonas* show two distinct structures in the periciliary membrane.

This micrograph shows two structures embedded inside the transition zone membrane at the ciliary base in *Chlamydomonas reinhardtii*: the ciliary necklace (red arrow) and the ciliary bracelet (blue arrow). These are theorized to be part of the membrane diffusion barrier. Scalebar: 200 nm; image from (93).

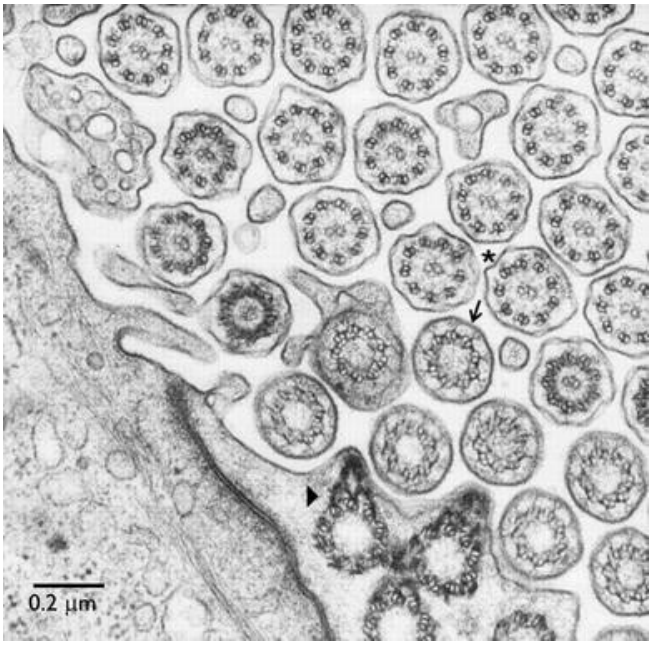

Figure 2.18. Y-links in mouse oviduct multiciliated epithelial cells.
Black arrow indicates Y-links in the TZ. Image from (94), originally from Dirksen and Satir (unpublished).

The Y-links are located in the region of the TZ characterized by a heavily staining double-wedge structure in *Chlamydomonas* (Figure 2.12C), which connects the stellate plate (central to the stellate assembly) to the membrane. In this region, cytosolic proteins larger than ~30 kDa are blocked from entering the cilium, while smaller molecules are allowed to enter through diffusion. This seems to be a size-dependent process, as multiple GFPs linked together (27 kDa each) can still pass through this barrier, whereas lighter polysaccharides with a larger diameter are not. It's not entirely clear how this barrier exactly works, but it's clear that the Y-links are involved, as mutation of its components lead to a leaky barrier, and therefore ciliopathies. The molecular and mechanistic similarities between the nuclear pore and the ciliary pore suggest that Y-links might be a platform for some of the intrinsically disordered proteins found in the TZ, which together form a gel-like meshwork, just like in the nuclear pore.

Nucleoporins?!

One more clue as to what constitutes the transition zone barrier for soluble components comes from an exciting but puzzling finding: nucleoporin proteins, normally found in the nuclear pore, sometimes localize to the ciliary TZ, as was found serendipitously using fluorescently tagged nucleoporins (NUPs)(63). As mentioned above, the nuclear pore bears a striking resemblance to the ciliary TZ: it's a meshwork of intrinsically unstructured proteins, containing many FG-repeats, which are anchored onto more structured parts. The whole forms a size-exclusion barrier, blocking larger macromolecules from entering. Unless they are carried actively through this barrier, that is: there exists a RanGTP/GDP gradient across both the nuclear pore and the ciliary pore, and importin-β2, which transports cargoes across this barrier, is also present in both cases. However, the localization of specifically nucleoporins near the ciliary TZ is a heavily contested conclusion, since these proteins have not been endogenously expressed, and this finding might therefore not be physiological. Moreover, the signal for each NUP is smeared out and seems to localize more towards the area around the basal body, not directly inside the TZ (Figure 2.17). This area is known to contain a lot of intrinsically disordered proteins (95–97), and possible capture of NUPs in this area might be nonspecific.

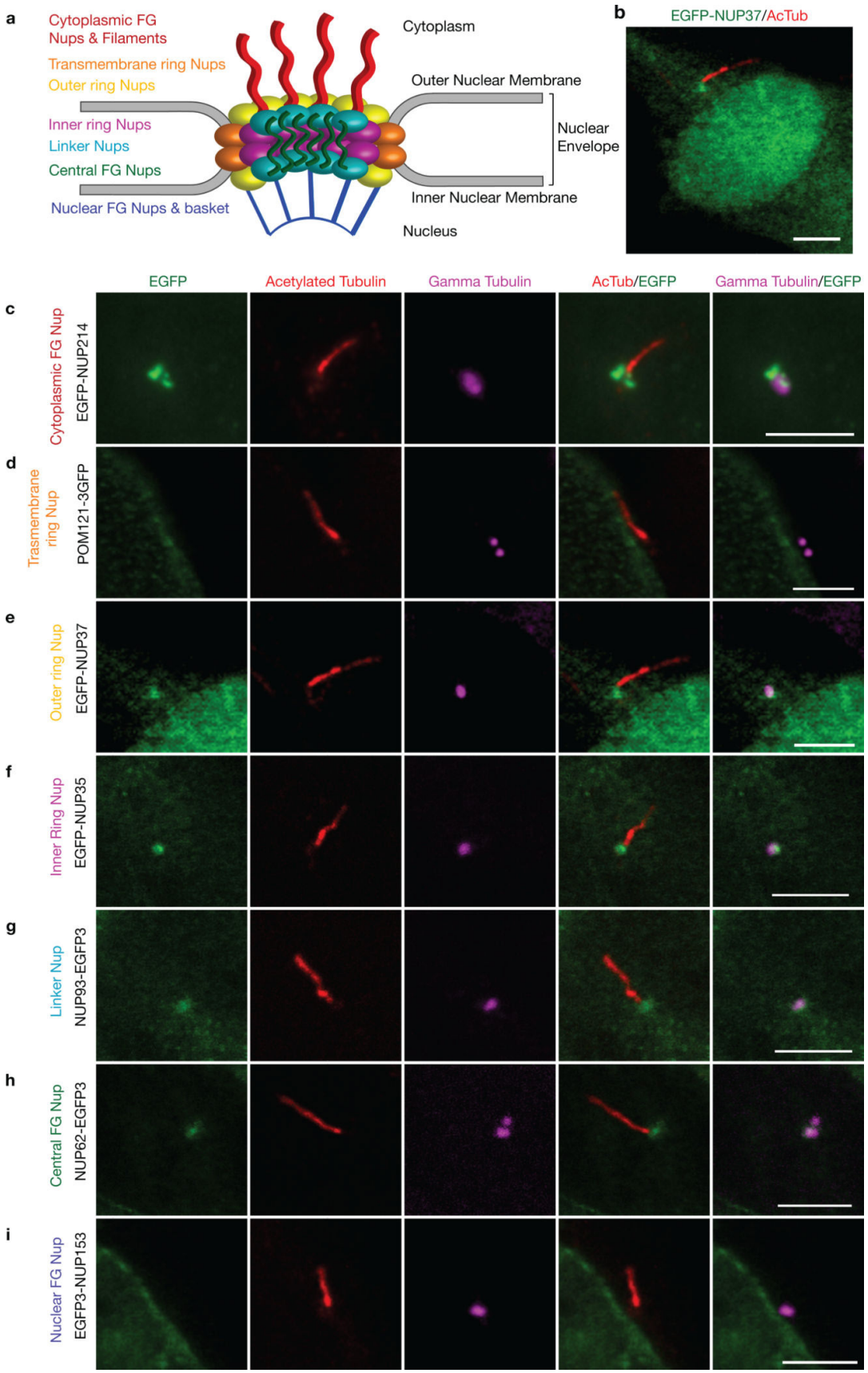

Figure 2.19. Fluorescently tagged nucleoporin proteins (NUPs) can localize to the TZ.
NUPs can sometimes be found in the ciliary TZ, although this finding is contested. Acetylated tubulin (red) is a ciliary marker; NUPs are color coded. Figure from (63).

Transitional fibers

Transitional fibers (TFs), also known as distal appendages (DAPs) or Alar sheets, are large trapezoidal wing-like sheets, radiating upwards and outwards from the apical end of basal bodies, anchoring them to the periciliary membrane (Figure 2.12D, bottom; Figure 2.14, right; Figure 2.18). Similar to the Y-link containing part of the transition zone, the transitional fibers provide structural support, and regulate ciliary entry. The TFs contain five core proteins, which are indispensable for ciliogenesis: CEP83/CCDC41, CEP89/CCDC123/CEP123, CEP164, SCLT1 and FBF1 (92). Other important but in principle dispensable proteins are Chibby1/CBY1, OFD1, C2CD3, ODF2. Some interaction with IFT proteins is hypothesized. It is not clear if- and how the TFs exactly influence IFT; it's likely that IFT is merely present in the matrix between the distal appendages, not interacting much with the TFs.

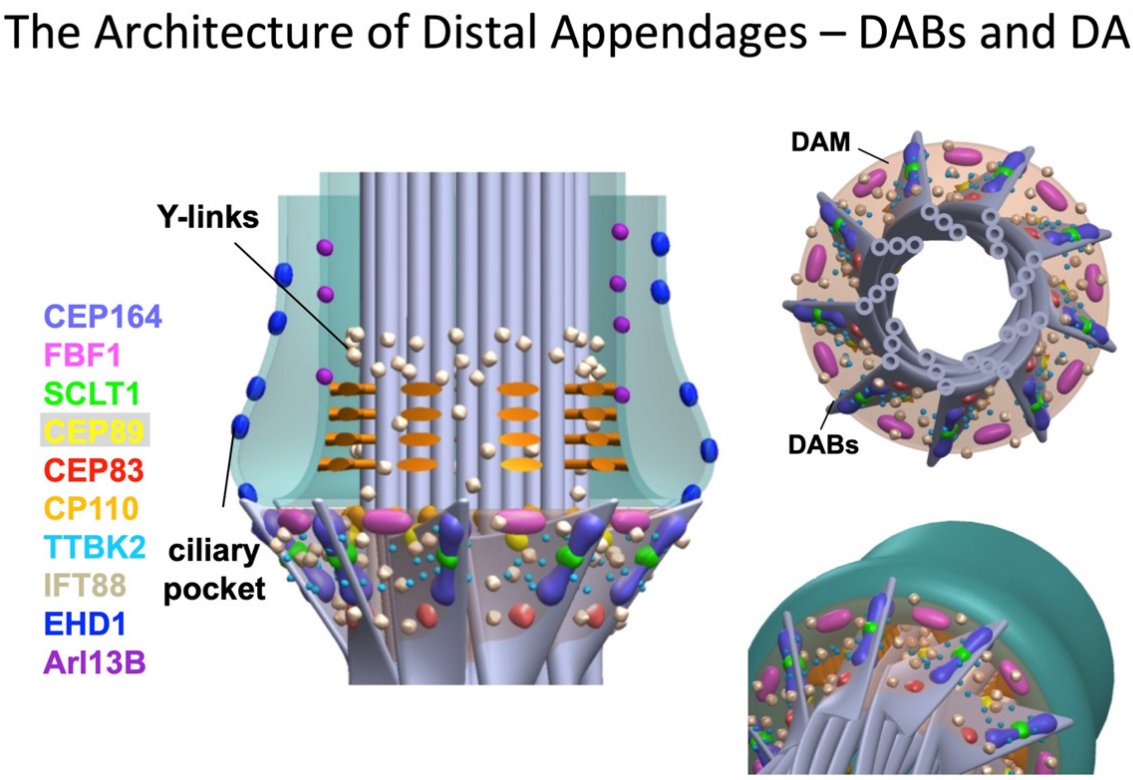

Figure 2.20. Localization map of distal appendage/TF proteins, found using dSTORM.
CEP164, FBF1, SCLT1, CEP89 and CEP83 are TF components indispensable for this basal body anchoring structure. Also shown are markers of different parts of this zone: CP110 (orange, distal end of centriole), TTBK2 (light blue, ciliogenesis-promoting kinase associated with CEP164), IFT88 (gold, intraflagellar transport), EHD1 (dark blue, periciliary membrane component) and Arl13B (purple, ciliary membrane component). Adapted from (91).

2.3 Ciliary transport processes and homeostasis

Hundreds of proteins are found to specifically localize to the cilium. When protein composition is altered, this leads to ciliopathies (Section 2.1). Yet, there is no clear consensus on how exactly ciliary proteins find their way to the cilium, which signal sends a protein there. The cilium might be a non-membranous organelle, but no protein larger than 30 kDa can freely diffuse into the cilium, due to the diffusion barrier inside the transition zone (see Section 2.2.5). Any ciliary component therefore has to be actively transported into the cilium, either by association with IFT and the BBSome, or with importin-β2. Let's look at these ciliary transport processes and how they manage to build, maintain and, when needed, deconstruct the cilium.

2.3.1 Intraflagellar transport

Intraflagellar transport (IFT) is a process of active transport into the cilium, which is performed by IFT proteins. These proteins form large, multi-megadalton transport protein complexes, which in turn assemble into larger filaments called "IFT trains", which run along the microtubule doublets at the core of the cilium, driven by the ubiquitous microtubule-binding motor proteins kinesin and dynein, found in most eukaryotic cells. Heterotrimeric kinesin-2 drives "anterograde" IFT along the MTD's B-tubule towards the tip of the cilium, where the IFT complex is disassembled and remodeled, after which cytoplasmic dynein-1b (also known as "IFT dynein") takes over and shuttles the complex back to the cell body along the MTD's A-tubule, known as "retrograde" IFT (98).

IFT is crucial to ciliogenesis, ciliary maintenance and signaling. Dysfunctional IFT is linked to disease phenotypes falling under the majority of ciliopathies. Specific IFT mutations have been shown to lead to ciliopathies such as Bardet-Biedl syndrome, Sensenbrenner syndrome, Jeune syndrome and Joubert syndrome.

IFT proteins, as well as proteins in the related BBSome, evolved from coatomer proteins, as they share a common ancestor with COPI, COPII and Clathrin (99). Some IFT components still associate with membranes, and carry membrane-embedded cargoes and cargo adapters.

IFT structure

Unfortunately, IFT proteins are hard to biochemically isolate in sufficient quantities. Moreover, IFT proteins contain many complex hydrophobic protein-protein interfaces, and therefore become highly unstable or insoluble when not in complex with other IFT proteins. This has made crystallization efforts nearly impossible, although crystal structures are now known for several (partial) IFT proteins/domains.

The partial structures of IFT proteins, combined with yeast two-hybrid binding assays and functional studies on IFT components, have led to an interaction map (Figure 2.19)(100). IFT proteins form a few distinct complexes: IFT-A, IFT-B1 and IFT-B2 (the latter two are often taken together and referred to as "IFT-B"). Both complexes, IFT-A and IFT-B consist of "core" and "peripheral" sub-complexes. IFT proteins can differ between species, but the general makeup of these complexes is often maintained.

IFT-B1 is considered to be the "IFT-B core" and is composed of 10 different proteins: IFT22, -25, -27, -46, -52, -56, -70, -74, -81 and -88, which together form a salt-stable subcomplex. Proteins in this complex are known to bind cytosol-soluble ciliary cargoes such as tubulin, BBSome components, outer dynein arms (ODAs) and inner dynein arms (IDAs).

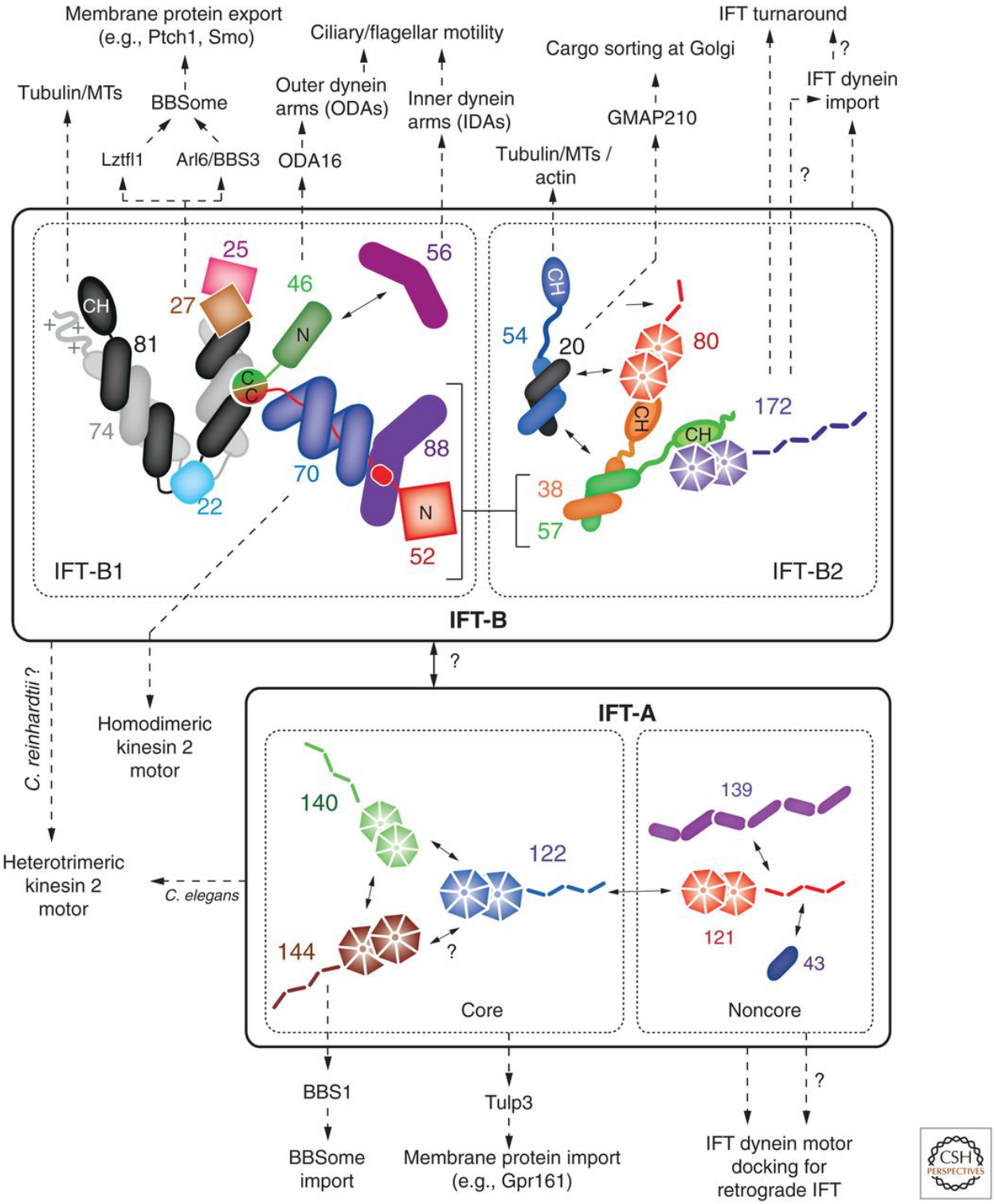

Figure 2.21. The interaction map of IFT proteins.

IFT is composed of two major complexes, IFT-A and IFT-B, which are each divided into “core” (IFT-A core, IFT-B1) and “noncore”/”peripheral” (IFT-A noncore, IFT-B2) subcomplexes. This interaction map is the result of many binding assays and functional studies (100). Known interactions of IFT components with ciliary cargoes are indicated. Figure from (100).

IFT-B2 is considered to be “peripheral IFT-B”, and is composed of 6 proteins: IFT20, -38, -54, -57, -80 and -172. These are involved in binding cytosolic components such as tubulin, actin, dynein-1b (“IFT dynein”), and also have roles in cargo transport from the Golgi to the cilium, and IFT turnaround at the tip of the cilium.

IFT-A is divided into three “core” proteins, IFT-122, -140 and -144, and three “noncore” proteins, IFT43, -121 and -139. These provide transport of cargo adapters such as Tulp3 and the BBSome, which help transporting many membrane-associated ciliary cargoes, including important receptors for signaling.

Although crystallization efforts of IFT complexes proved too difficult, the cryo-ET IFT structure of the full IFT complex of *in situ* anterograde IFT trains in *Chlamydomonas* is now available (101)(Figure 2.20). This landmark paper found that different IFT components form three characteristic densities, each with their own periodicity. Knockdowns of principal IFT components were used to determine which subcomplex belongs to which density (Figure 2.20): IFT-A near the membrane (yellow), IFT-B near the MTD (green) and dynein-1b bound in an inactivated “cross-legged” conformation on the side of IFT-B (blue and gray).

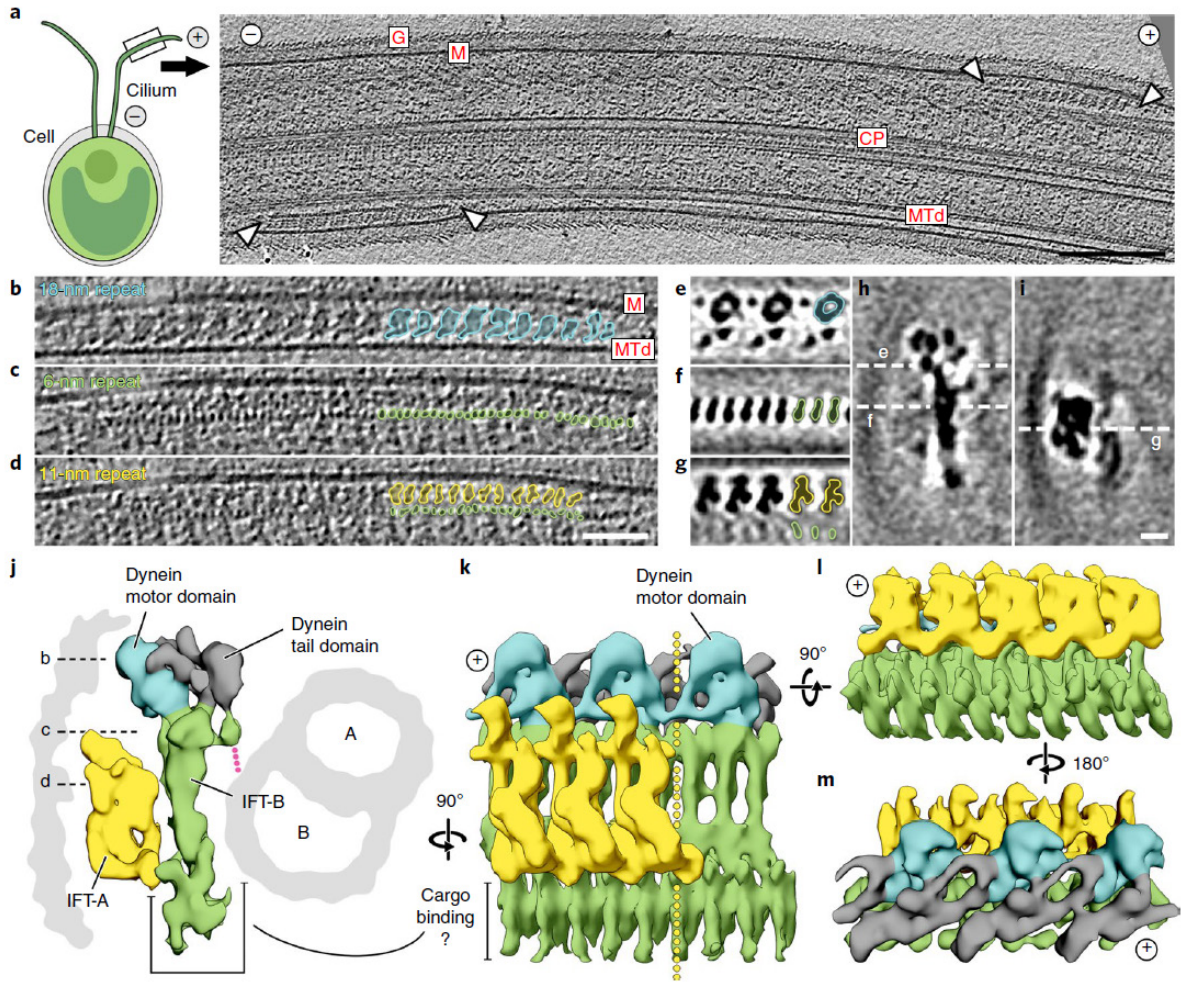

Figure 2.22. The cryo-ET structure of *in situ* mature IFT in the *Chlamydomonas* cilium.
Tomograms of the *Chlamydomonas* cilium (A) show repeating densities found to be IFT, between MTDs and the ciliary membrane, divided into three principal components with differing periodicities (B-D). The subtomogram averages of these components (E-G) show their large, intricate repeating structures. Knockdowns of principle IFT components identified these densities as IFT-A (yellow), IFT-B (green) and dynein-1b (motor domains in blue, tail domains in gray), which is in a “cross-legged” inactivated conformation in this anterograde kinesin-driven IFT train (J-M). “+” = distal end (towards ciliary tip), “-“ = proximal end (towards cell body). Figure from (101).

Models of IFT train behavior and cargo loading

A dynamic pool of IFT components is known to reside at the ciliary base, as was shown using FRAP experiments (102). The turnover rate of these components differs: for example, kinesin-2 has a very quick turnover rate, recovering fluorescence in only ~4 seconds in the basal pool of IFT proteins. Meanwhile, IFT-B turns over in ~6 seconds, while IFT-A components such as IFT43 take the longest, recovering fluorescent signal in ~9 seconds.

IFT trains are known to start their journey to the ciliary tip about once per second, which means that (assuming they run on each doublet equally often) every MTD has a train running on it every nine seconds (103,104). This corresponds with the FRAP experiments mentioned above, with every component being able to be incorporated into trains during those nine seconds. How exactly this assembly process happens, is one of the main subjects of this thesis (Section 5).

At least in the case of *Chlamydomonas,* the behavior of IFT trains entering the cilium is still debated. What's known is that it's a stochastic process, with "avalanche-like" behavior (105). This means that IFT proteins find their way to trains at the ciliary base, and accumulate there, until a certain threshold is reached and the entire built-up pool of IFT is injected in one go (like an avalanche). This threshold seems to be stochastic; no matter the state of the cilium, trains always depart from the base once per second.

Several models exist that try to explain the behavior of IFT trains in *Chlamydomonas*: the "differential cargo loading model", the "time-of-flight model", and the "balance-point model" (Figure 2.21). The time-of-flight model assumes that the time IFT particles take travelling inside the cilium is a length sensor. However, this is not what was observed: slowing down IFT trains using dynein mutants did not affect ciliary length, and even increased IFT train entry (106).

The differential cargo loading model poses that IFT trains are always the same length, but with different amounts of cargo bound to them, depending on required transport of ciliary components (102). This would imply that train length is not affected in steady-state versus growing cilia, only cargo loading is.

The balance-point model poses that the length of the existing cilium controls IFT train assembly itself, with shorter cilia needing more buildup, and longer ones needing less, to reach ideal ciliary length (103). In this model, since train departure frequency is unaffected, trains could instead be longer or shorter, depending on the transport requirements of ciliary components. This could imply that IFT abundance in the cell is regulated depending on transport requirements, which has not been found to be the case. Alternatively, IFT abundance could be kept constant, while only using a portion of this IFT pool for train assembly, leading to different train lengths.

Instead of regulating IFT abundance, it is however possible to instead use kinesin-2 availability at the ciliary base as a limiting factor for IFT entry: IFT abundance remains stable, but IFT activity is tuned by kinesin-2 availability (107,108). Although kinesin-2 is a crucial part of anterograde trains, it is not found to move back to the cell body with retrograde trains. Instead, it has been found to diffuse freely inside the axonemal lumen. This diffusion happens along the ciliary axis, which limits the diffusion to only one dimension, making it quite fast. When the kinesin then reaches the base of the cilium, it can be re-incorporated into IFT trains. The shorter a cilium is, the more concentrated and readily available the pool of kinesin-2 becomes, and the longer trains could be. This would imply that kinesin-2 diffusion rate back to the cell body is the ruler which determines ciliary length; hence it's called "diffusion as a ruler" model.

However, the "diffusion ruler" model requires a closed loop of IFT turnover in order to determine ciliary length, and FRAP experiments have shown that fresh kinesin-2 can be added by the cell to the basal pool, making it a (semi-)open system (102). Thus, the mechanisms that regulate entry of IFT trains and ciliary length remain unresolved.

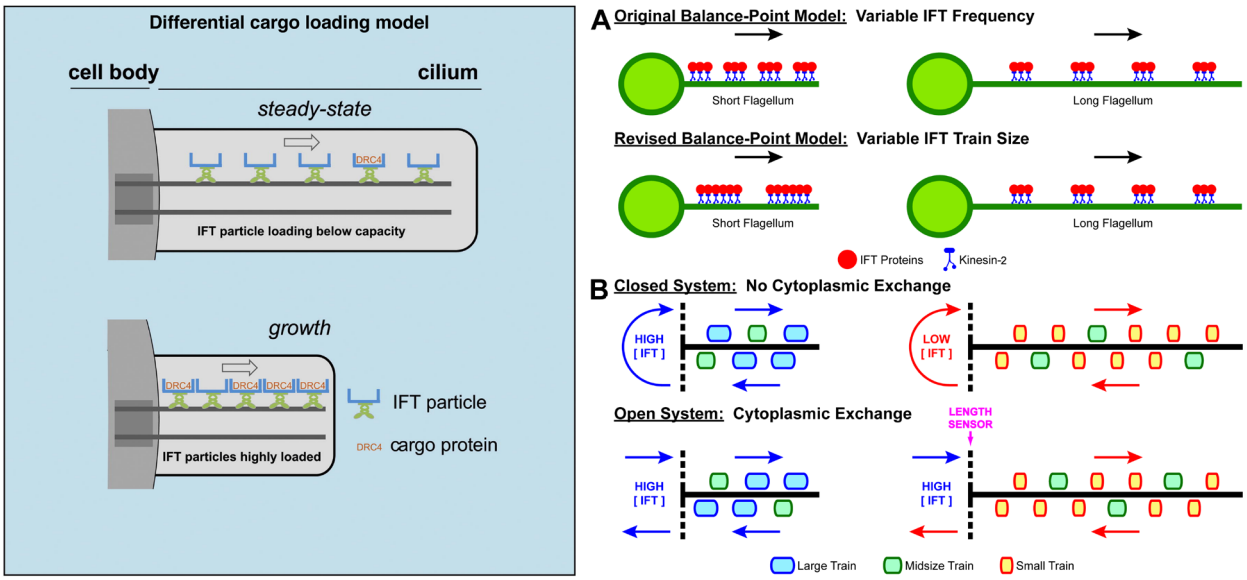

Figure 2.23. IFT train regulation models.

The differential cargo loading model (left) assumes stable train length, but differing amounts of cargo loading depending on ciliary growth requirements. The balance-point model (right, A) assumes differing train length depending on ciliary growth requirements, and full cargo loading. Adapted figures from (102) (left) and (103) (right).

Other remaining questions regarding IFT

Now that the principal IFT complexes have been identified, it's becoming possible to search for other densities known to bind to IFT, such as kinesin-2 and cargoes. However, unfortunately, the location of individual IFT proteins within this structure is still unknown, as the resolution of the existing average is too low to discern which density belongs to which subcomplex protein. For that to happen, a much higher-resolution structure must first become available. Efforts are currently being made by several labs, to reconstitute IFT trains *in vitro* for cryo-EM single particle analysis.

Since no higher-resolution structures are available, cargo loading still remains a bit of a mystery. It is for instance not clear if the current IFT structure (Figure 2.20) contains any cargo densities. To get more detailed information on which cargo binds where under which conditions, their exact binding interfaces must first be found. Getting more information on cargo loading could help verify which IFT train loading models are at play (see above).

It further remains unclear how exactly IFT components are delivered to the ciliary base. It's suggested that vesicular transport from the Golgi plays a large role in bringing in IFT components, but since IFT components are soluble in the cytosol, it's unclear to which extent vesicular transport plays a role, and should further be examined *in situ*.

Another open question is the structure of retrograde trains. Hints of retrograde trains were found in (101), however they seemed very loosely defined, lacking structural details and contrast.

The BBSome has also not yet been identified *in situ*, so its mode of ciliary entry and association with IFT trains remains to be addressed.

2.3.2 Other modes of ciliary transport

BBSome

IFT (Section 2.3.1) is the main mode of ciliary import, but not the only one. The BBSome is another important factor in ciliary import, also associated with IFT. The BBSome is a large, octameric protein complex, also sharing a common ancestor with coatomer proteins, like IFT. Its atomic structure has been resolved by several labs (109–111). The BBSome recruits ciliary cargoes, and is theorized to bind to IFT trains sub-stoichiometrically to deliver those cargoes. It is dispensable for ciliogenesis in itself, but it does lead to Bardet-Biedl syndrome (BBS) if dysfunctional. It can therefore be considered another peripheral, but independent, large cargo adapter for IFT trains.

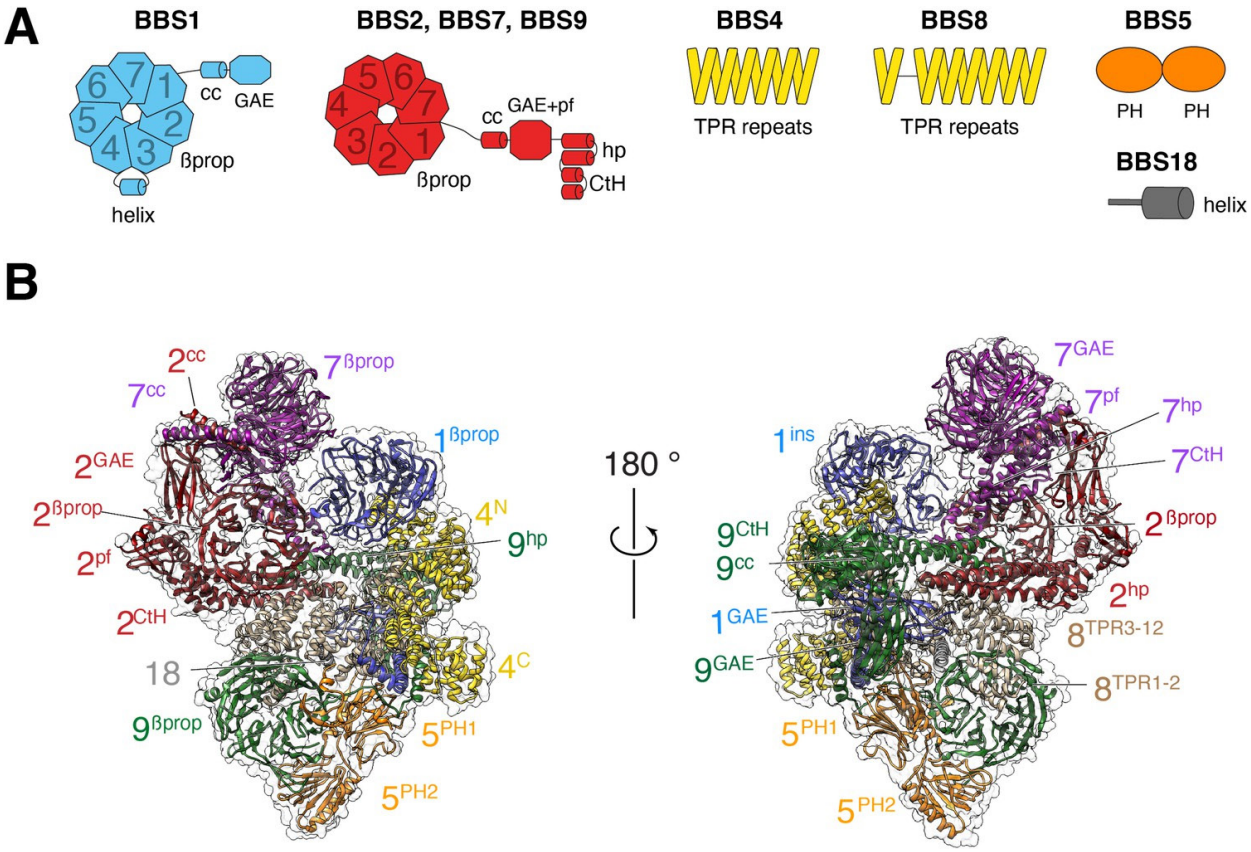

Figure 2.24. Structure of the BBSome.

The BBSome is an octameric protein complex which acts as a ciliary cargo adaptor for IFT, responsible for shutting of many ciliary cargoes across the TZ. From (112).

RanGTP/GDP gradient and importin-β2

Another, IFT-independent mechanism to shuttle cargo proteins across the TZ's diffusion barrier exists at the ciliary base. This is the RanGTP/GDP gradient coupled with presence of importin-β2: in the cilium, there is an abundance of RanGTP, which can be bound and hydrolysed by importin-β2 (113). This process is known to happen at the nuclear pore, using RanGTP found in the nucleus. There, importin-β2 binds RanGTP, exits the nucleus, hydrolyses RanGTP in the cytosol, whereupon it gets activated, ready to accept a binding partner. Once bound, importin-β2 then shuttles its binding partner back through the nuclear pore, into the nucleus, likely through many weak interactions with intrinsically disordered nucleoporin proteins that are found there. This is theorized to also happen at the ciliary base, with similarly intrinsically disordered proteins of different species.

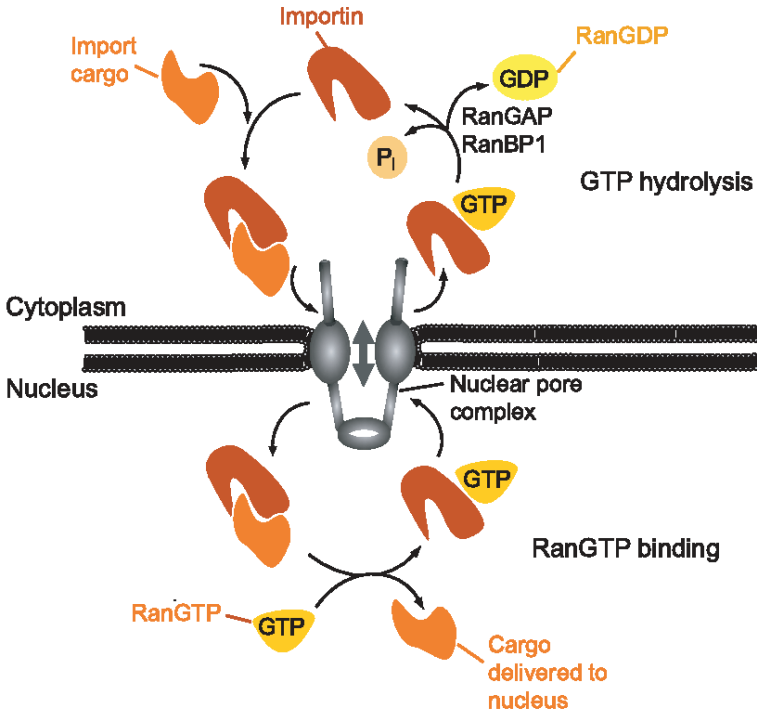

Figure 2.25. The nucleus' RanGTP/GDP gradient and importin-β2, also present in cilia.
This process transports binding partners of importin through hydrolysis of RanGTP into RanGDP. RanGTP is loaded onto importin in the nucleus, then the complex exits through the nuclear pore. RanGTP is hydrolysed in the cytoplasm, upon which importin is activated. It then binds its cargo, and shuttles back through the nuclear pore to deliver this cargo. The same is theorized to happen at the ciliary base, with the cilium being the RanGTP-enriched zone, instead of the nucleus. Adapted from (114).

2.3.3 Building the cilium: ciliogenesis

Ciliogenesis, or the construction of cilia, happens in a few stages (Figure 2.24)(115). First, basal bodies are produced in the cytosol, either by templating off an existing centriole (in the case of one or a few cilia), or by forming on deuterosomes (cytoplasmic basal body forming hubs, in the case of multiciliated cells) (see Section 2.2.4). These gather basal body components, and when they're complete, they start recruiting transitional fibers. These fibers dock to a so-called ciliary vesicle (CV), after which the transition zone starts building up; IFT seems to be required for this process. After the transition zone is completed, the cilium starts to elongate through regular import of ciliary components via IFT. The newly formed cilium-basal body complex then docks its ciliary vesicle to the plasma membrane, where the cilium is further extended until it reaches full length.

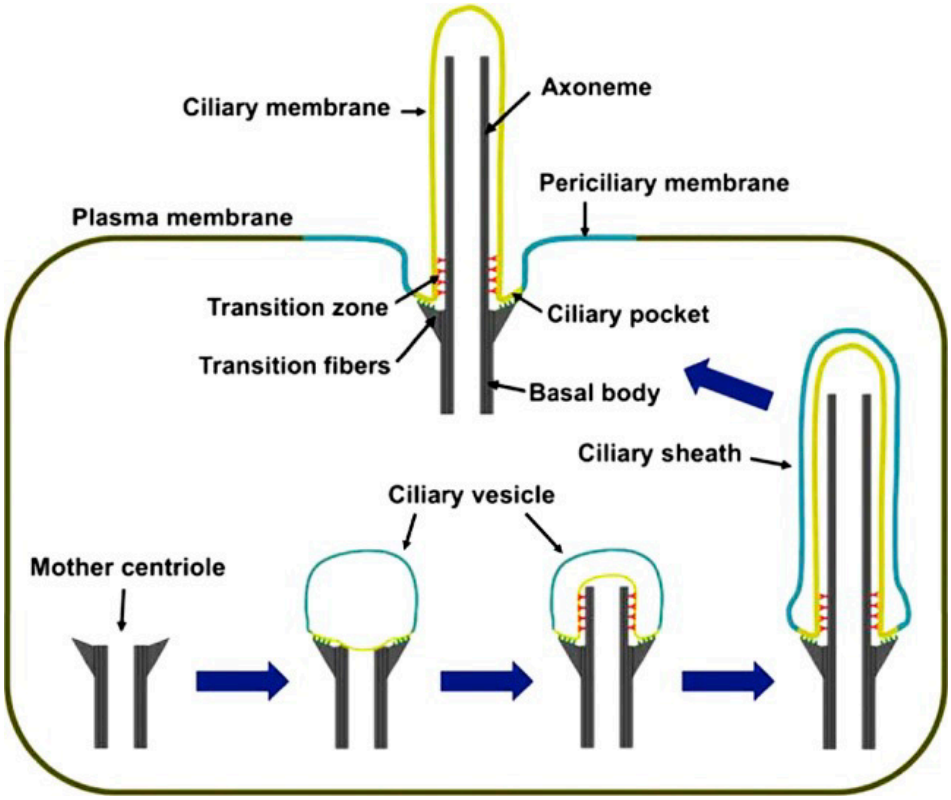

Figure 2.26. Stages of ciliogenesis.

Ciliogenesis starts with the production of a basal body, indicated here as "mother centriole". This centriole recruits a ciliary vesicle using its transitional fibres, after which a transition zone starts building up (indicated by orange Y-links). Once the TZ and a small part of the cilium are complete, the ciliary vesicle then fuses with the plasma membrane, exposing the cilium and allowing it to grow to full length. Image from (115).

2.3.4 Removing the cilium: flagellar autotomy or resorption

The cilium is often able to be shed or resorbed by cells, if needed. In the case of primary cilia, the cilium is resorbed by the cell. This happens before mitotic entry, since the basal bodies are needed to form the MTOC during mitosis (see Section 2.2.4)(116).

In *Chlamydomonas*, there exists a different way to remove the cilium, often as a response to stress, such as pH shock(117). *Chlamydomonas* can contract its transition zone, due to the release of Ca^{2+} ions towards the basal apparatus. Here, centrin binds the calcium ions and strongly contracts the entire basal apparatus, especially the (centrin-containing) stellate assembly (Figure 2.25)(118,119).

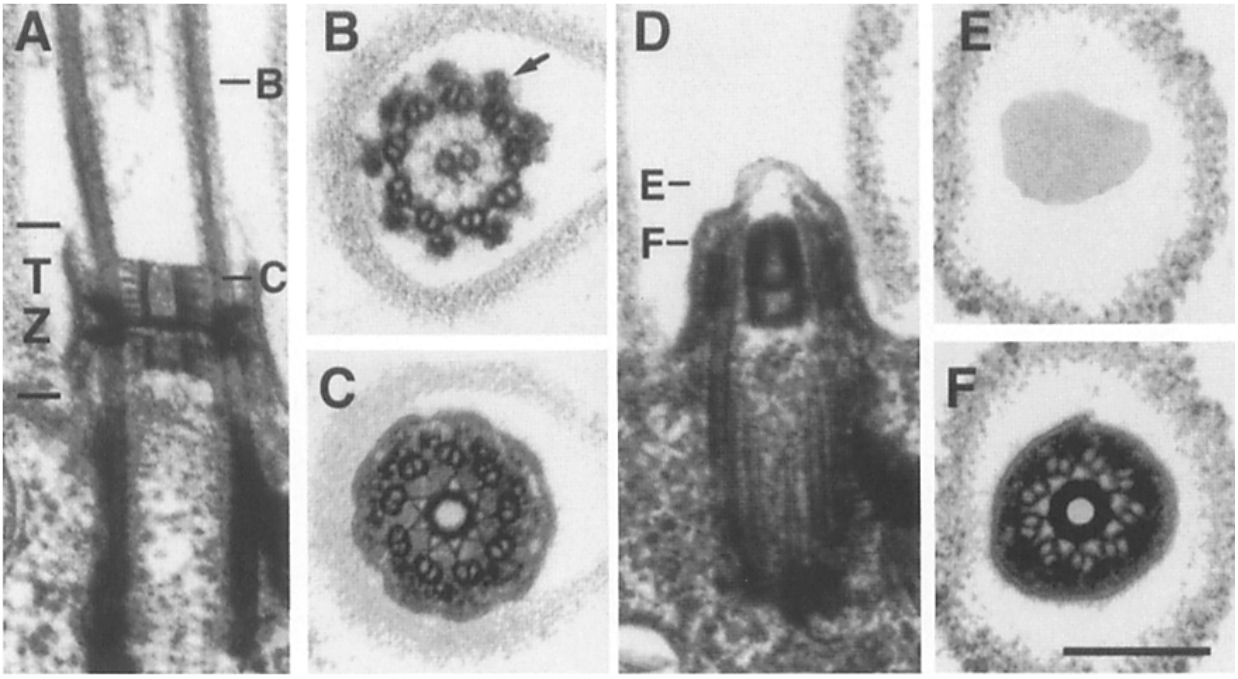

Figure 2.27. Flagellar excision in *Chlamydomonas*.

Thin sections of the *Chlamydomonas* TZ, before (A-C) and after (D-F) flagellar autotomy. As seen in (A) and (D), the axoneme severs cleanly at the distal end of the transition zone, leaving the TZ behind. During this process, the stellate strongly contracts and pulls the remaining MTD ends inwards (C, F). From (118).

The axoneme severing process was proposed to be mediated by Katanin (120), a hexameric, hexagonally shaped microtubule-severing protein. However, Katanin could not be found in the TZ, and thus the exact method of severing the otherwise very sturdy MTDs remains unclear.

3 Overview and scope of this thesis

3.1 General overview

Cilia are ancient and versatile organelles that extend from the surface of eukaryotic cells. At the cilium's base, the transition zone (also known as the ciliary pore) forms a gateway that connects the cilium with the rest of the cell. This region of the cilium is extremely important for ciliary homeostasis, but it is severely understudied, mostly due to the lack of biochemical methods needed to isolate it in an intact state. However, thanks to recent advances in the field of cryo-electron tomography (cryo-ET), it has become feasible to study this region in great detail within the native cellular environment (34). In this thesis, we used cryo-ET on two different model systems to address several open questions concerning the ciliary pore.

3.2 Scope of chapter 1: the ciliary pore in *Chlamydomonas reinhardtii*

In this chapter, the first of this thesis' two major studies will be discussed: the ciliary base in *Chlamydomonas reinhardtii.* This green alga is a model organism for the study of eukaryotic cilia, since its molecular composition and general architecture of its cilia are very similar to those found in other eukaryotes, including humans. Moreover, owing to its clear contrast in cryo-ET we chose to use this organism to study the basic principles of the ciliary transition zone. A major hurdle was the difficulty of targeting the low copy number of *Chlamydomonas* flagella (two per cell) before the advent of more advanced Correlated Light Electron Microscopy (CLEM) methods. Over the course of 5 years, a mere twenty tomograms would be collected. Nevertheless, this fortunately proved to be enough for a comprehensive study, which focused on two main aspects: first, the first native *in situ* structure of the ciliary transition zone, and second, the assembly of intraflagellar transport complexes into so-called "IFT trains". The contents of this chapter are currently under revision at *Science*; a preprint is available (1).

3.3 Scope of chapter 2: the ciliary pore in multiciliated Murine Tracheal Epithelial Cells

In this chapter, the second of this thesis' two major studies will be discussed: the ciliary base in a multiciliated system, specifically Murine Tracheal Epithelial Cells (MTECs). In contrast to *Chlamydomonas reinhardtii*, MTECs are more challenging to culture; however, the implications for mammalian ciliary research are much greater, as this system is a direct representation of the mammalian cilium in its native state. In addition, the abundant cilia are much easier to target by FIB milling, and the high copy number of cilia in each lamella/tomogram make this system a superb specimen for cryo-ET. This study focuses on multiple aspects: the first native *in situ* structure of the ciliary transition zone in mammalian cells, with multiple structural averages (MTD structures, centriolar structures) mapped back into the cell volumes. The contents of this chapter have not yet been published, but will soon be combined with fluorescence microscopy localization data and submitted for peer-review.

3.4 Scope of chapter 3: observational differences between cryo-ET and classical EM

This chapter came to life as a result of not being able to equate our observations in cryo-ET with what we expected to see based on available literature on ciliary structure using classical EM methods. Certain structures that are highly visible using classical EM methods proved to be nearly invisible using native contrast cryo-ET, and vice versa. Here, we attempt to explain the differences in observations between different methods, and try to marry the different observations by taking into account both the strengths and blind spots of each technique.

4 Materials and methods

4.1 Materials

4.1.1 Chemicals and consumables

Material/additive	Manufacturer	Cat. no.
ALI filter supports (collagen-coated PTFE, 12 mm ø) 12x	Corning	3493
ALI filter supports (collagen-coated PTFE, 24 mm ø) 6x	Corning	3491
Antibiotic/-mycotic mix (AB/AM) 100x	ThermoFisher Gibco	15240062
Apo-transferrin	Sigma	T1147
Bovine Pituitary Extract (BPE)	Merck	02-104
Bovine Serum Albumin (BSA)	Sigma	A-2153
Cell culture flasks T25 (with rebreathing caps)		
Cholera Toxin (CT)	Sigma	C8052
Collagenase-IV		
DNAseI (from bovine pancreas)	Sigma	DN25
Dulbecco's Modified Eagle Medium/Nutrient Mixture F-12, buffered with HEPES (DMEM:F12)	ThermoFisher Gibco	11330032
EDTA		
Epidermal Growth Factor (EGF)	BD Biosciences	354001
Ethanol (EtOH)		
Falcon tubes 15 mL		
Falcon tubes 50 mL		
Fetal Bovine Serum (FBS)	ThermoFisher Gibco	10082139
Gold fiducial markers		
Hank's Balanced Salt Solution (HBSS)	ThermoFisher Gibco	14025092
Hydrochloric acid (HCl) 1M	Merck	109057
Insulin	Sigma	I6634
L-Glutamine 200 mM	ThermoFisher Gibco	25030149
NuSerum	BD Biosciences	355100
Phosphate Buffered Saline (PBS)		
Primaria plates		
Pronase E from *S. Griseus*	Sigma	P6911
Retinoic Acid (RA)	Sigma	R-2625
ROCK inhibitor (121)		
Sodium Bicarbonate ($NaHCO_3$) 7.5%	ThermoFisher Gibco	25080094
Sterilization filters 0.22 µm pore size (for syringes)		
Trypsin		

4.1.2 Buffers and stock solutions

Deionized water (diH_2O) was produced by a Milli-Q Plus Ultrapure Water Purifier.

All buffers were prepared under sterile conditions in a laminated flow cabinet.

DMEM:F12 AB/AM

500 mL DMEM:F12
5 mL AB/AM 100x mix

Pronase E, 1.5 mg/mL solution

20 mL DMEM:F12 AB/AM
30 mg Pronase E

Bovine Serum Albumin, 100 mg/mL stock

1.00 g BSA (lyophilized)
Filled up to 10 mL with HBSS

Epidermal Growth Factor, 25 µg/mL stock

3.96 mL HBSS
100 µg EGF
40 µL BSA (100 mg/mL)

Cholera Toxin, 100 µg/mL stock

9.9 mL HBSS
100 µL BSA (100 mg/mL)
1.00 mg CT

Transferrin, 5 mg/mL stock

19.7 mL HBSS
100 mg apo-transferrin
200 µl BSA (100 mg/mL)

Insulin, 2 mg/mL stock

25 mL 4 mM HCl (100 µL 1 M HCl + 24.9 mL diH_2O)
50 mg insulin

Bovine Pituitary Extract, 35 mg/mL stock

3.75 mL diH_2O

150 mg lyophilized BPE

Pellet precipitated with 2 spins for 20' at 13,000 x *g* at 4 °C (tossed)
Supernatant filter-sterilized through 1.2, 0.8, 0.45, 0.22 µm filters (used)

Retinoic Acid, stock A, 1.5 mg/mL (100*k*x)

Stock prepared in darkroom with red light

33.3 mL 95% ethanol
50 mg RA

Retinoic Acid, stock B, 1.5 µg/mL (100x)

Stock prepared in darkroom with red light

49.45 mL HBSS
50 µL RA stock A
500 µL BSA (100 mg/mL)

DNAse, 0.5 mg/mL solution

Prepared fresh each time

10 mL DMEM:F12 AB/AM
100 mg BSA
5.0 mg DNaseI

Trypsin solution

Prepared fresh each time

10 mL trypsin-EDTA (1.25% & 1 mM) 5x

4.1.3 Cell culture media

All cell culture media prepared under sterile conditions in a laminated flow cabinet.

TAP medium

Tris-acetate-phosphate buffer
(Chlamydomonas-optimized)
Formulation described in (122)

MTEC basic medium (BM)

500 mL DMEM:F12
3.75 mL L-glutamine 200 mM
2 mL $NaHCO_3$ 7.5%
5 mL AB/AM 100x

MTEC complete (CM-RA)

91.0 mL DMEM:F12
500 µL Insulin 2 mg/mL stock
100 µL Transferrin 5 mg/mL stock
100 µL EGF 25 µg/mL stock
100 µL CT 100 µg/mL stock
5.0 mL FBS
750 µL L-Glutamine 200 mM
400 µL $NaHCO_3$ 7.5%
1.00 mL AB/AM 100x
All contents were mixed and 0.22-µm filter-sterilized via 50 mL syringe

MTEC complete (CM+RA)

Prepared fresh each time

19.7 mL CM-RA
100 µL pre-filter-sterilized BPE
200 µL RA stock B 100x
4 µL ROCK inhibitor (only until day 4)

MTEC NuSerum medium (Nu+RA)

Prepared fresh each time

19.4 mL BM
400 µL NuSerum (final 2% v/v)
200 µL RA stock B 100X

MTEC serum free medium (SF-RA)

98.6 mL BM
250 µL insulin 2 mg/mL stock
100 µL transferrin 5 mg/mL stock
20 µL EGF 25 µg/mL stock
25 µL CT 100 µg/mL stock
mL BSA 100 mg/mL stock

MTEC serum free medium (SF+RA)

Prepared fresh each time

19.7 mL SF-RA
100 µL pre-filter-sterilized BPE
200 µL RA stock B 100x

4.2 Sample preparation

4.2.1 Sample preparation (*C. reinhardtii*) *

** This section was performed by Dr. P. S. Erdmann and Dr. M. Schaffer.*

Cell culture

C. reinhardtii cells were obtained from the Chlamydomonas Resource Center (University of Minnesota, Minneapolis, MN USA). For *in situ* cryo-ET, we used strain CC-3994 (*mat3-4* mt+) (123). This strain has smaller cells, which is beneficial for vitrification during plunge freezing and also increases the chances of hitting a ciliary transition zone region by non-targeted FIB milling. For cryo-ET of basal bodies following ciliary abscission, we used strain CC-4533 (*cw15* mt-; Jonikas CMJ030) (124). This strain lacks a cell wall and thus easily ruptures during blotting onto EM grids, enabling cryo-ET of basal bodies in thin ice without FIB milling. For U-ExM, we used *C. reinhardtii* strains expressing IFT46-YFP (125), KAP-GFP (CC-5408) (126,127), and D1bLIC-GFP (CC-4488) (128). For all experiments, cells were grown in Tris–acetate–phosphate (TAP) medium, with constant light (approx. 90 µmol photons m^{-2} s^{-1}), bubbling through normal atmosphere, at room temperature.

Cell vitrification and cryo-FIB milling

Both vitrification and FIB milling protocols were performed as described in (29,3). Using a Vitrobot Mark 4 (FEI Thermo Fisher), 4 µL of ~1,000 cells per µL of cell culture (mid-log phase) was blotted onto holey carbon-coated 200-mesh EM grids (Quantifoil Micro Tools) and plunge-frozen into a liquid ethane/propane mixture. CC-3994 and CC-4533 cells were blotted onto R2/1 and R3.5/1 grids, respectively. Cryo-FIB sample preparation was performed using either a Quanta or Scios dual-beam FIB/SEM instrument (FEI, Thermo Fisher Scientific). Mounted in an Autogrid support, the grids were first coated with an organometallic platinum layer using a gas injection system. Subsequently, the cells were milled with a gallium ion beam to produce ~70- to 200-nm-thick lamellas, exposing the cellular interior.

4.2.2 Sample preparation (MTECs)

Air-to-Liquid-Interface (ALI) cell culture

MTEC cells were obtained from primary culture of tracheal epithelial cells from wild-type CD-1 or transgenic GFP-centrin2 mice (University of Minnesota, Minneapolis, MN USA)(129). After CO_2 asphyxiation, ~10 mice (per ALI culture) were dissected; trachea were isolated, cut open lengthwise, and stored in a petri dish with ice-cold PBS solution. After two washes with ~10 mL of ice-cold PBS and removal of extraneous tissue, trachea were then incubated with 20 mL of 1.5 mg/mL Pronase E solution (in DMEM:F12 AB/AM), and incubated undisturbed for 18h (overnight) at 4 °C, to dissociate epithelial and basal cells from the tracheal husks. After incubation, the flasks were gently inverted 2-5 times in order to further dissociate the epithelial and basal cells. 2.0 mL of FBS was then added to a final concentration of 10%, quenching enzymatic activity. The trachea/cell suspension was then vigorously inverted 12 times, for full dissociation of the cells. The trachea were removed using a Pasteur pipet, washed twice with two more rounds of 5 mL of fresh Ham's F-12/Pen-Strep medium with 10% FBS, and inverted vigorously for 12 times each time. After removing the now empty tracheal husks, the three cell suspensions were pooled together and centrifuged at 600 x *g* at 4 °C for 10 min. Cells were resuspended in 1.0 mL DNAse, and incubated on ice for 5 min. After spinning down at 300 x *g* for 10 min at 4 °C in a microcentrifuge, pellets were resuspended in 20 mL of 10% FBS in DMEM:F12 AB/AM, and incubated for 4h at 37 °C, 5% CO_2 in a 10 cm ø Primaria plate, to which fibroblasts would adhere, while leaving epithelial and basal cells in suspension. After this step, the cell suspension in the Primaria plate was gently swirled to detach non-adhered cells, and carefully transferred into two 15 mL Falcon tubes. The cells were spun down at 400 x *g* at room temperature for 10 min, then resuspended in ~6 mL CM+RA. Corning Transwell Air-to-Liquid-Interface (ALI) culturing filter supports with collagen coating were shortly washed with CM+RA, after which 1 mL of cell suspension (in CM+RA) was added to each 6-well filter support insert (or 250 µL to each 24-well insert) to seed the primary culture. To the bottom well, below each filter support, 1.5 mL of CM+RA medium was added (0.5 mL in case of 24-well plates).

The cells on filter supports were incubated undisturbed at 37 °C, 5% CO_2 for 5-6 days. Every second day, the CM+RA medium was refreshed, taking care not to disturb the cells on the filter supports. ROCK inhibitor (121) was added to all CM+RA until day 4 of culture, after which it was left out. At day 5-6, confluency and compacting/columnar appearance of the newly formed cell layer was checked using a light microscope. If the cell layer had sufficiently developed, the switch to ALI culture was made by removing the medium in the filter support to create the air-to-liquid interface, and the medium in the bottom well was changed to 1.0 mL of either Nu+RA or SF+RA. The medium in the bottom well was then replaced every second day, and the air interface of the cell layer carefully rinsed with ~1.5 mL of PBS every time to get rid of mucus and contaminants. Ranging from day 7 to day 30 of ALI culture, filters were prepared for enzymatic dissociation by rinsing each well twice with BM. Trypsin solution (1.25%) was then added (0.5 mL to bottom well, 0.25 mL to filter support) and enzymatic dissociation was performed overnight (18 h) at 37 °C, 5% CO_2. To quench the reaction, 0.25 mL of FBS was added to the pooled trypsinized cell suspensions, resulting in 1.00 mL of cell suspension. Cells were counted using a hemacytometer, while simultaneously checking for active ciliary beating, then spun down at 600 x*g* for 10 min at room temperature. The cell pellet was resuspended in BM with 10% FBS, in a volume that corresponded to the desired cell concentration for blotting onto EM grids, ranging from 125 to 500 cells per µL.

Cell vitrification, transport, and cryo-FIB milling

Both vitrification and FIB milling protocols were performed as described in (29). Using a Leica EM Grid Plunger (Leica Microsystems), 4 µL of ~125-500 cells per µL of cell culture was mixed with 1 µL of 10- or 15-nm gold fiducial beads suspended in BSA solution, then blotted onto carbon-coated 200-mesh copper EM grids (Quantifoil Micro Tools). Blotting was performed at 95% humidity and 30 °C only from the back of the grid; a tiny drop of cell medium was applied to the back of the grid for better contact of liquid to filter paper, and therefore more reproducible wicking of the medium. The grids were plunge-frozen into liquid ethane.

The grids were then stored in sealed plastic containers under liquid nitrogen, and air-shipped to the home lab in a liquid nitrogen-based dry shipping container. Upon arrival, grids were mounted in an Autogrid support, for further cryo-ET processing. Cryo-FIB sample preparation was performed using either a Scios or Aquilos dual-beam FIB/SEM instrument (FEI, Thermo Fisher Scientific). The grids were first coated with an organometallic platinum layer using a gas injection system. Subsequently, after milling stress relief trenches to improve FIB milling stability (36), the cells were milled with a gallium ion beam to produce ~70- to 200-nm-thick lamellas, exposing the cellular interior.

4.3 Data acquisition

4.3.1 Cryo-electron tomography (*C. reinhardtii*) *

** This section was performed by Dr. P. S. Erdmann and Dr. M. Schaffer.*

EM grids with FIB-thinned cells were transferred to a 300-kV Titan Krios microscope (FEI, Thermo Fisher Scientific), equipped with a post-column energy filter (Gatan) and a K2 Summit direct detector camera (Gatan). Using SerialEM software (130), tilt-series were acquired from −60° to +60°, with 2° increments (bidirectional, separated at −0° or −20°). A subset was collected using a dose-symmetrical tilt scheme (23). Images were recorded in movie mode at 12 frames per second, with an object pixel size of 3.42 Å (magnification of 42,000x) and a defocus of −4 to −6 µm. The total accumulated dose for the tilt-series was kept below ~100 $e^-/Å^2$. Each tomogram was acquired from a separate cell and therefore can be considered a biological replicate. Several different cell cultures and >10 imaging sessions were used to produce the dataset of 19 tomograms.

4.3.2 Cryo-electron tomography (MTECs)

EM grids with FIB-thinned cells were transferred to a 300-kV Titan Krios microscope (FEI, Thermo Fisher Scientific), equipped with a post-column energy filter (Gatan) and a K2 Summit direct detector camera (Gatan). Using SerialEM software (130), tilt-series were acquired from −60° to +60°, with 2° increments using a dose-symmetrical tilt scheme (23). Images were recorded in movie mode at 12 frames per second, with an object pixel size of 3.52 Å (magnification of ~42,000x) and a defocus of −4 to −6 µm. The total accumulated dose for the tilt-series was kept below ~100 $e^-/Å^2$. Each tomogram was acquired from a separate cell and therefore can be considered a biological replicate. Several different cell cultures and 7 imaging sessions were used to produce the dataset of 72 tomograms.

4.4 Image reconstruction and processing

Tomogram reconstruction

Prior to reconstruction, frames from the K2 detector were drift-corrected with MotionCor2 software (40) using 3 × 3 patches, after which tilt-series stacks were assembled. The defocus of each tilt was estimated using Gctf (131) (*C. reinhardtii* dataset) or CTFFIND4 (132) (MTEC dataset), and after low-pass filtering each tilt proportionate to accumulated dose ("dose filtering"), CTF-correction was applied using the CTFphaseflip tool in IMOD software (42). Using IMOD, the tilt-series were aligned with patch tracking and reconstructed with weighted back-projection and a Lanczos 2 lobes antialiasing filter to generate tomographic volumes. We applied quality control criteria including tilt-series alignment scores and the power spectra of individual tilts to omit poor tilts from tomograms. Contrast enhancement for display purposes, and distance measurements in the *Chlamydomonas* dataset, was achieved using the tom_deconv deconvolution filter (https://github.com/dtegunov/tom_deconv) (55). A selection of MTEC tomograms was further processed using the CryoCARE package, which utilizes machine learning algorithms to suppress noise and enhance contrast for visualization purposes (47). The resulting selection of tomograms was further processed with IsoNet (21), a deep learning software package that predicts and fills in missing wedge information, further aiding visualization (used in Section 6).

4.5 Computational analysis

Particle picking and subtomogram averaging

In both projects, particles for subtomogram averages (IFT-A, IFT-B, dynein-1b, stellate fibers, Y-links, MTD sleeve, MTEC MTD class averages 1-3, and the ACR) were manually picked along the train or MTD in a consistent distal-to-proximal (*C. reinhardtii*) or proximal-to-distal (MTEC) fashion, in deconvolution-filtered bin4 tomograms (13.68 Å pixel size for *C. reinhardtii*, 14.08 Å pixel size for MTECs) using IMOD's 3dmod viewer (42). Subtomogram alignment and averaging was performed using STOPGAP (*C. reinhardtii*: v0.3.1, MTECs: v0.7.1)(41). STOPGAP is a subtomogram averaging package that uses real-space refinement to iteratively align and average subtomograms. Initial positions for each type of particle were twice oversampled (compared to their roughly measured repeat lengths) and extracted along an interpolated line running through the filament's corresponding particle positions in the CTF-corrected, dose-filtered tomograms. By aligning these initial subvolumes to their own average, generated using randomized rotations along the filament's longitudinal axis, bias-free de novo averages were obtained after particle positions and rotations converged. These averages were low-pass filtered to 40 Å and iteratively realigned using several cylindrical masks, tolerances and Euler angle sampling cones. Using the "place object" tool in UCSF Chimera software (49, 50), we visually inspected the relative orientations of particles at different cross correlation (CC) thresholds. We cleaned each average by omitting particles with aberrant orientations (and therefore low CC score) by setting a global CC score cutoff (Table 1). These low-scoring particles, as well as overlapping redundant particles (from oversampling), were discarded using functions in the STOPGAP toolbox (41). The final round of alignment and averaging was performed with bin2 dose-filtered, CTF-corrected subvolumes (pixel size: 6.84 Å for *C. reinhardtii*, 7.04 Å for MTECs), using a wide cylindrical alignment mask, a very tight cylindrical cross correlation mask (XYZ translational sampling space), and a narrow Euler angle sampling cone. The resolution of the final averages (Table 1) was estimated using body-shaped mask-corrected Fourier shell correlation (133) after splitting each set of particles into two half-sets (even and odd particle numbers) during the last alignment step (*C. reinhardtii*). The MTEC averages were split into half-

sets comprised of odd and even particle numbers from the very beginning of alignments, and MTD averages were later reassigned to classes comprised of individual filaments ("object half-sets"), strengthening the independence of each half-set, thereby aiding FSC estimation.

Particle type	Number of particles	Box size (px bin2)	Resolution @ FSC 0.500 (Å)	Resolution @ FSC 0.143 (Å)	CC score cutoff (cleaning step)	
IFT-A	571	128	36.2	27.3	0.200	
IFT-B	1361	128	28.6	24.4	0.100	
Dynein-1b	146	128	38.2	29.9	0.350	
MTD Sleeve	110	192	42.9	34.7	0.350	
Stellate	206	256	34.6	28.2	0.140	CC score final round of class.
ACR	617	128	39.1	35.4	0.100	
MTD class 1 (TZ only)	7437	128	32.3	22.8	0.050	0.370 ± 0.137
MTD class 2 (BB/Prx.Ax)	9627	128	32.7	22.9	0.050	0.297 ± 0.121
MTD class 3 (Intermed.)	7242	128	33.1	23.2	0.050	0.293 ± 0.126

Table 1. Parameters of the subtomogram averages.

For each density map averaged in this study, this table lists the number of particles in the average, the subvolume box size, the resolution determined at FSC=0.5 and FSC=0.143 thresholds (Figure 5.2, Figure 5.6), CC score cutoff used to clean particle sets (based on visual inspection) and CC scores of the final round of classification for each of the three MTD classes from the MTEC dataset.

Classification of particle averages (MTECs)

After obtaining an initial subtomogram average of the MTDs, particles were randomly divided into 7 classes, and aligned in STOPGAP using the ali_multiref function for several iterations, until classes remained relatively stable. After inspection of the resulting averages and their localization pattern across the MTDs, and finding several redundant classes, it was decided to decrease the number of classes to 5, and finally to 3. After more rounds of iterative alignment, using different cylindrical and later body-shaped masks, the three classes were each further refined, yielding the resulting averages in Figure 6.2, Figure 6.3 and Figure 6.4.

Length measurements of transition zone components

Measurements of transition zone components (Figure 5.1B, Table 2) were performed using IMOD's 3dmod viewer tool (42). Using the "slicer" function, we aligned each bin4 deconvolution-filtered tomogram, so that the length of each desired structure would be exactly in the viewing plane. Using 3dmod's measuring tool, the length in pixels was noted and multiplied with pixel size (bin4: 1.368 nm for *C. reinhardtii*, 1.408 nm for MTECs) to obtain the final set of measurements. Per cilium, each of the nine MTT/MTD/TZ assemblies was measured separately. Structures were only measured if both ends were clearly visible and contained within the lamella. The number of repeats for each component was determined by dividing their extent along the transition zones (Figure 5.1B, Figure 5.4) by their measured repeat length (Figure 5.3).

Assignment of IFT-A and IFT-dynein proximity with respect to IFT-B (*C. reinhardtii*)

After careful revision of the manually picked densities of IFT-A, IFT-B and IFT-dynein, we used UCSF Chimera's "place object" function to manually assign identities to each IFT-B subunit. We compared the original IFT-B, IFT-A, and IFT-dynein positions relative to each other, noting for each IFT-B subunit if it was associated with IFT-A (~one IFT-A per two IFT-B subunits) and/or IFT-dynein (one per three IFT-B subunits). Additionally, we noted if the manually picked positions were included into the final average; poorly identified/resolved IFT trains were discarded. IFT train location with respect to transition zone components was measured using IMOD's 3dmod "slicer" tool. We aligned each bin4 deconvolution-filtered tomogram, so that the first part of the IFT train would be in plane with one of four easily recognizable TZ structures (top and bottom of the stellate fiber, stellate plate, and the MTD-MTT transition point). The distance between the cross-secting plane of the transition zone component and the first IFT-B subunit of each train was noted, and multiplied by pixel size (1.368 nm @ bin4) to obtain the final relative position of each IFT train to each TZ component. This distance in nm could additionally be converted into number of IFT-B repeats, using the average repeat length we observed (6.1 nm). The attachment point of IFT-B to the MTDs was estimated by eye, by taking 20 nm (roughly the length of a fully extended kinesin complex) as cutoff while also looking at the IFT trains' angle with respect to the MTDs to judge where it bends away too strongly to be considered MTD-bound.

Combination of averages

Individual averages (Figure 5.6, Figure 5.7) were fused to form a composite map of the complete assembling IFT train structure (Figure 5.5D, Figure 5.8A) using the UCSF Chimera "fit in map" tool. We used the full IFT-B average, which contained blurred densities of IFT-A and dynein-1b, as a framework upon which to fit segmented maps of the IFT-B, IFT-A and dynein-1b subcomplexes. We cross-checked the fit by also using the blurred densities of IFT-B in the full averages of IFT-A and dynein-1b to confirm that the parts were properly positioned with respect to each other.

A similar approach was applied to assemble a composite map of the transition zone (Figure 5.1C-E). Particle averages of the Y-links and stellate were fit together onto an MTD backbone (part of the stellate average) using the UCSF Chimera "fit in map" tool. Segmented single subunits of the Y-links, stellate, and MTD sleeve were then fit into the composite model and copied both longitudinally and helically, applying shifts and rotations (tom_rotate and tom_shift functions) using the Matlab-based TOM Toolbox (134). The number of repeats for each component was determined by measuring their repeat length (Figure 5.3) and extent along the transition zones (Figure 5.1B, Figure 5.4).

Tomogram visualization

Slices through tomographic volumes were generated using the IMOD 3dmod viewer (42). Using the UCSF Chimera (48) "Place Object" plugin, 3D surface models of IFT and TZ structures were mapped back into the tomograms at the refined positions determined by subtomogram averaging (Figure 5.5A-C). These models were then exported to ChimeraX software (135) for display. Subtomogram averages of individual complexes were also displayed in ChimeraX.

4.6 Ultrastructure Expansion Microscopy (U-ExM) *

** This section was performed by Dr. Nikolai Klena, centriole lab, UNIGE.*

Ultrastructure expansion microscopy (U-ExM) of *C. reinhardtii*

After growing the IFT46-YFP, KAP-GFP, and D1bLIC-GFP strains in TAP medium for three days, cells were sedimented on 12 mm coverslips coated with Poly-D-Lysine for 5 minutes. Following sedimentation, the U-ExM protocol was followed as previously described in (136). Briefly, the 12 mm coverslips containing unfixed *C. reinhardtii* cells were incubated in a solution containing acrylamide and formaldehyde in PBS for 5 hours at 37°C. TEMED (2.5 µL) and APS (2.5 µL) were added to monomer solution and vortexed before adding to the coverslips. The gelation proceeded for 5 min on ice, followed by 1 hour of incubation at 37°C. Samples embedded in the gel were then added to denaturation buffer (200mM SDS, 200mM NaCl, 50mM Tris-base) for 1.75 hours at 95°C. Denatured samples were then exposed to the first round of expansion overnight. The following day, gels were stained for 3 hours with anti-tubulin antibodies AA344 (β-tubulin, 1:400, scFv-S11B) and AA345 (α-tubulin, 1:400, scFv-F2C) (137), in combination with either anti-GFP (1:200, Torrey Pines Biolabs, TP401) or anti-PolyE (1:500, AdipoGen, AG-25B-0030). After 30 min of washing in PBS with 0.1% Tween-20 (PBST), gels were incubated for 3 hours with a secondary antibody solution containing goat anti-rabbit Alexa Fluor 488 IgG (1:400, Thermo Fisher Scientific, A11008) and goat anti-mouse Alexa Fluor 568 IgG H +L (1:400, Thermo Fisher Scientific, A11004). All immunolabeling steps were carried out at 37°C with gentle shaking. Following secondary antibody incubation, gels were washed for 30 min in PBST, and expanded overnight in ddH_2O. The final expansion factor varied from 4.2x to 4.6x, determined by using a caliper to measure the dimensions of the expanded gel.

Fluorescence microscopy

Imaging was performed using either an inverted Leica TCS SP8 confocal microscope or a Leica Thunder DMi8 widefield microscope. Confocal Z-stacks were acquired with a 63x 1.4 numerical aperture oil objective (using Lightning dual-color deconvolution), a step size of 0.12 nm, and a pixel size of 35 nm. Widefield Z-stacks were acquired with a 63x 1.4 numerical aperture oil objective (using the Thunder Small Volume Computational Clearing mode), a step size of 0.14 nm, and a pixel size of 100 nm.

Fluorescence microscopy data analysis

Image analysis and maximal intensity projections were performed using Fiji software (138). PolyE coverage (Figure 5.11) was measured by generating maximal projections of side-view basal bodies and measuring the full width-half maximum of the PolyE signal compared to the tubulin signal. For semi-automated IFT tracing, we used the Fiji Simple Neurite Tracer (SNT) plugin (139) with default settings and the “A* search” algorithm. Z-stacks of equivalent orientation and dimensions for IFT46, KAP, and D1bLIC were cropped to equal dimensions and individually opened in the SNT plugin. Using Z-stacks with obvious train-like structures, strongly stained points along the train were selected in 3D. The semi-automated software traced the complete train, and faithful tracing was validated by eye. The tracing profiles of each train were superimposed onto one image (Figure 5.12). To convert train lengths from pixels to nanometers, we calculated local expansion factors using the basal body attached to each train as an internal ruler (basal body proximal end = 225 nm), as previously measured by *in situ* cryo-ET (3). Train lengths were then plotted and statistically analyzed using Graphpad Prism 8.

5 Chapter 1: the ciliary pore in *Chlamydomonas reinhardtii*

This section is published as a pre-print on BioRXiv. Adapted from the latest version (23-11-2021).

5.1 Abstract of this chapter

The ciliary base is home to the ciliary transition zone (TZ), a structure that is crucial to the assembly and maintenance of the cilium, as well as many important cellular functions such as motility, sensing, and signaling. The TZ forms a selective diffusion barrier between the cell and the cilium, in both the cytosol and membrane. The TZ regulates the entry of intraflagellar transport (IFT) trains: assemblies of multi-megadalton transport protein complexes, which selectively bind and carry cargo proteins that require entry into the cilium.

The native architecture of the transition zone and the ciliary base in general, has remained unresolved. The advent of major advances in cryo-ET have now made it possible to have a closer look at this enigmatic region. In this study, we used cryo-ET to describe the molecular landscape of the ciliary base and the native structure of the TZ that resides therein. Structural averaging performed on tomograms of this region shows how the nine-pointed “stellate apparatus” is in fact a helical assembly that connects the nine microtubule doublets (MTDs), how MTD-membrane tethering structures called “Y-links” attach to the MTDs, but are hard to visualize near the periciliary membrane/ciliary necklace, and how a newly discovered density sits prominently at the Site Of Flagellar Autotomy (SOFA), even though its exact molecular composition and function remain elusive. Finally, all these components are put back together to form a reconstructed model of the entire TZ and how each component relates to one another.

Moreover, we identified anterograde IFT trains in a state of assembly, which we found happens in a hierarchical manner. On every MTD, a string of IFT-B complexes assembles, which then recruits IFT-A and dynein-1b complexes in a sequential manner, completing the bulk of IFT trains from front-to-back (from cilium-to-cytoplasm). Structural averaging of the different IFT complexes resulted in an average of the anterograde IFT train, which closely matched the known structure of mature *in cilio* anterograde IFT, except for one peculiar density on the microtubule-associating side of the IFT train, the function of which remains elusive and should be subject to further study. The direct visualization cryo-ET provides was coupled with a complementary technique called ultrastructure expansion microscopy (U-ExM) in order to validate and further add to the story. With this technique, we not only could confirm the order of assembly found with cryo-ET (dynein-1b forms shorter subfilaments than IFT-B), but also add the anterograde IFT motor protein kinesin-2 to the picture: immunostained Kinesin Associated Protein (KAP, part of the heterotrimeric kinesin-2 complex) localized to IFT trains as very short subfilaments, closest to the TZ compared to other IFT components. Therefore, we concluded that it is added as one of the last IFT components. Immunostained KAP also located to the inner lumen of the axoneme, which is a novel observation, but adds to previous observations that KAP freely diffuses back to the cell body, instead of being transported by retrograde IFT. This hints towards the so-called “balance-point-model”, in which retrograde diffusion of kinesin is a rate-limiting step for IFT transport activity and ciliary growth/maintenance.

5.2 In situ structure of the native ciliary transition zone

Native structure of the *Chlamydomonas* transition zone

As described in Sections 4.2.1 and 4.3.1, vitrified *Chlamydomonas* cells were thinned with a focused ion beam (29) then imaged by cryo-ET, yielding 19 tomograms of the ciliary base inside the native cellular environment. Focusing on the TZ, we observed several different structures attached to the MTDs (Figure 5.1A-B), which we resolved in molecular detail by subtomogram averaging (Figure 5.1C-H, Figure 5.2). The proximal ~180 nm of the TZ is occupied by peripheral Y-links (Figure 5.1, turqoise) and luminal stellate fibers (Figure 5.1, purple), which resemble a 9-pointed star in cross-section (140). Our structure reveals that the stellates form a helical cylinder with a 6-start helix and a pitch of 49.2 nm (Figure 5.1E, H, Figure 5.3). Interestingly, this matches the pitch of the inner scaffold, a 3-start helical cylinder in the lumen of the centriole (3). The nine points of the stellate star bind MTDs at protofilament A3, with a longitudinal periodicity of ~8.1 nm along each MTD, which matches the 8.2 nm length of one tubulin dimer (Figure 5.1F, Figure 5.3). TZ stellates have been observed in certain algae and early-evolving land plants, and have a contractile function that is believed to trigger ciliary abscission (118).

Y-links are present in many species. They connect MTDs to the ciliary membrane and contain NPHP- and MKS-family proteins that are proposed to gate transport into and out of the cilium (65,66). Our structure reveals a broad density attaching the Y-links to the MTD, spanning protofilaments A9-10 and B1-4, with a longitudinal repeat of ~8.3 nm (Figure 5.1F, Figure 5.3). However, the outer densities of the Y-links that connect to the ciliary membrane were not resolved, likely due to flexibility of these filamentous structures. Interestingly, we observed that the Y-links extend along the MTDs proximal of the region where the ciliary membrane aligns with the axoneme (Figure 5.1A). Thus, connection to the membrane is not a prerequisite for MTD Y-link decoration, suggesting that the Y-links may have more functions in addition to membrane-axoneme tethering.

Immediately distal to the stellates and Y-links, we found a distinct helical density completely decorating the MTDs (Figure 5.1, dark blue), which to our knowledge has not been described before. This helical “sleeve” spans 76 ±6 nm along the MTDs, with a periodicity of ~16.4 nm (Figure 5.1G, Figure 5.3). To gain hints into the function of this structure, we also analyzed tomograms of basal bodies isolated immediately following ciliary shedding (Figure 5.4B). The *in situ* position of the MTD sleeve overlaps with the ciliary cleavage site observed in isolated basal bodies, also known as the site of flagellar autotomy (SOFA)(141) (Figure 5.1B). Consistent with this finding, the MTD sleeve was absent from the distal ends of these basal bodies. The sleeve was also not observed on the proximal ends of isolated cilia (142). We therefore hypothesize that this structure might help regulate axoneme severing and is lost during the process. Since the sleeve density covers every MTD protofilament, it should sterically hinder the attachment of molecular motors, and thus, may also play a role in regulating IFT entry or exit.

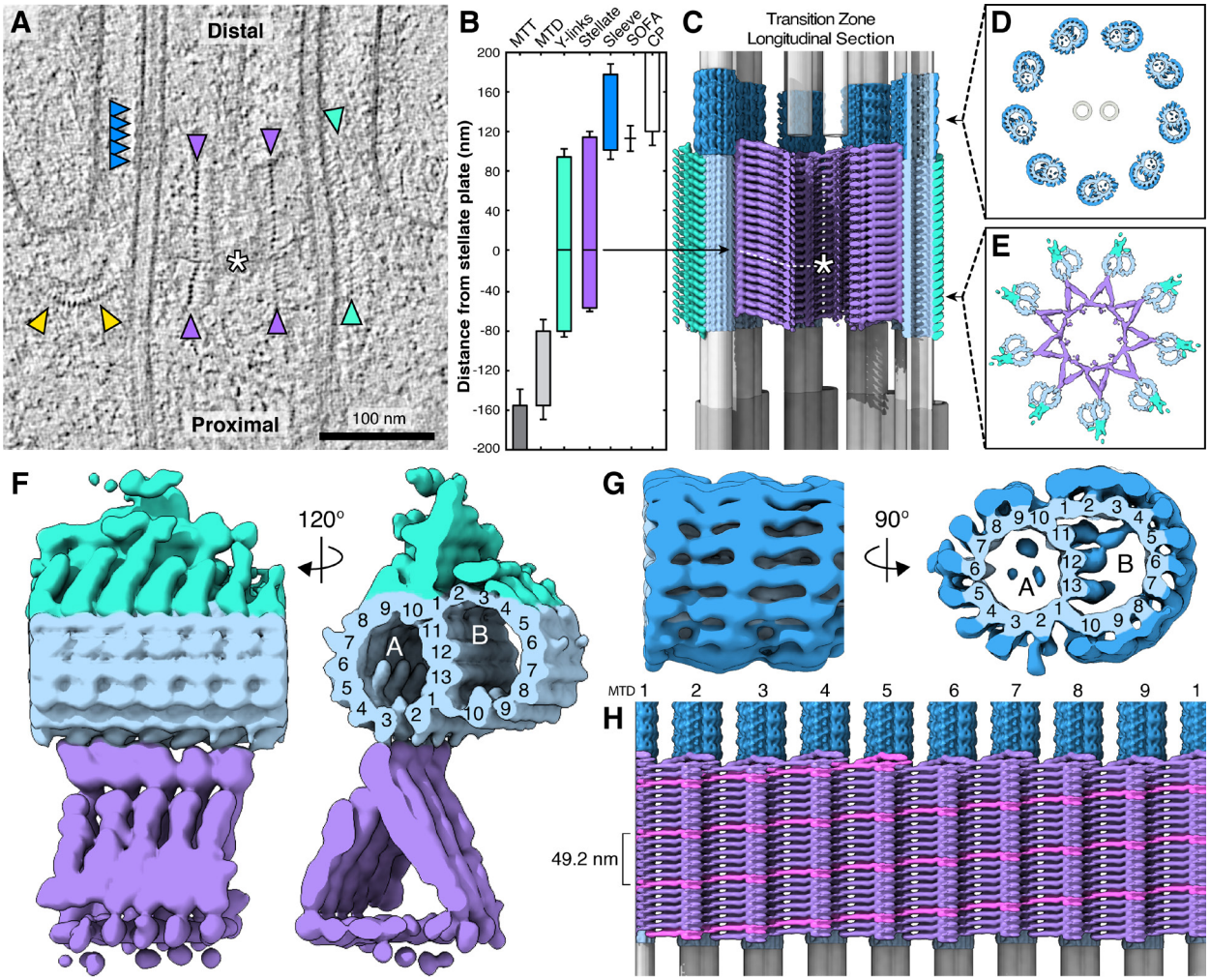

Figure 5.1. Cryo-ET structure of the ciliary transition zone inside *Chlamydomonas* cells.

(A) 2D slice through a cryo-electron tomogram, showing a TZ in longitudinal cross-section. Purple: stellate fibers, turquoise: Y-links, dark blue: MTD helical sleeve, white asterisk: stellate plate, yellow: IFT (see Figure 5.5). Scale bar: 100 nm. **(B-G)** Composite model of the TZ, combining averages of the stellate (purple), Y-links (turquoise), MTD sleeve (dark blue), and associated MTD (light blue), with schematic renderings of MTTs (dark gray), MTDs (light gray), and the central pair (CP, white). **(B)** Position along the TZ occupied by different structures. Distances are measured relative to the stellate plate ("0 nm" origin point marked with arrow). SOFA: "site of flagellar autotomy", where the cilium is cleaved (see Figure 5.4). Error bars: standard deviation. **(C)** Longitudinal section view of the complete composite model, assembled according to the measured lengths and positions of each component, with 21 Y-link repeats, 21 stellate repeats (7 proximal of the plate, 14 distal), and 5 MTD sleeve repeats. The model shows straight MTTs and MTDs, but as seen in panel A and quantified in (3), the centriole is actually a slightly convex barrel. **(D-E)** Cross-section views through the indicated regions of the composite model, showing **(D)** MTDs encased in the helical sleeve, with the CP in the middle, and **(E)** the nine-pointed stellate cylinder attached to MTDs decorated with Y-links. (**F-G)** Side and cross-section views a single MTD attached to **(F)** stellate fibers and Y-links, and **(G)** the helical sleeve. Protofilaments of the A- and B- microtubules are numbered. **(H)** Unrolled composite model, viewed from the center of the TZ, looking outward toward the inner wall of the stellate cylinder. One continuous helical density of the stellate's six-start stellate helix is marked in pink (pitch: 49.2 nm). MTDs are numbered.

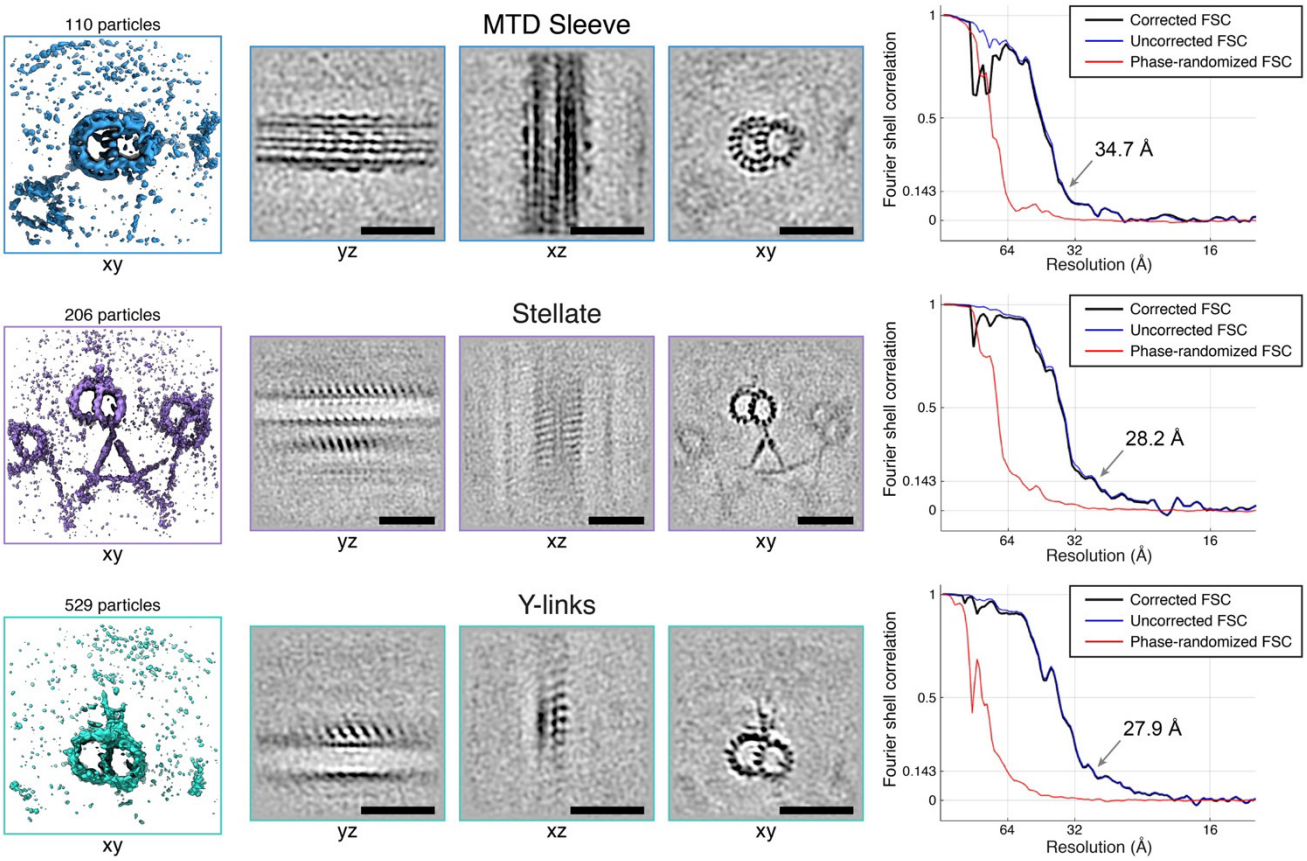

Figure 5.2. Individual subtomogram averages focused on different TZ structures.

Subtomogram averages focused on individual components of the transition zone: the MTD helical sleeve (top row), stellate (middle row), and Y-links (bottom row). These averages were fused to generate the TZ model shown in Figure 5.1. Left panels: 3D isosurface views, with the number of subvolumes (particles) in each average indicated. Central panels: 2D grayscale slices through the averages from three orientations (scale bars: 50 nm). Right panels: Fourier shell correlation curves showing the determined resolution of each average.

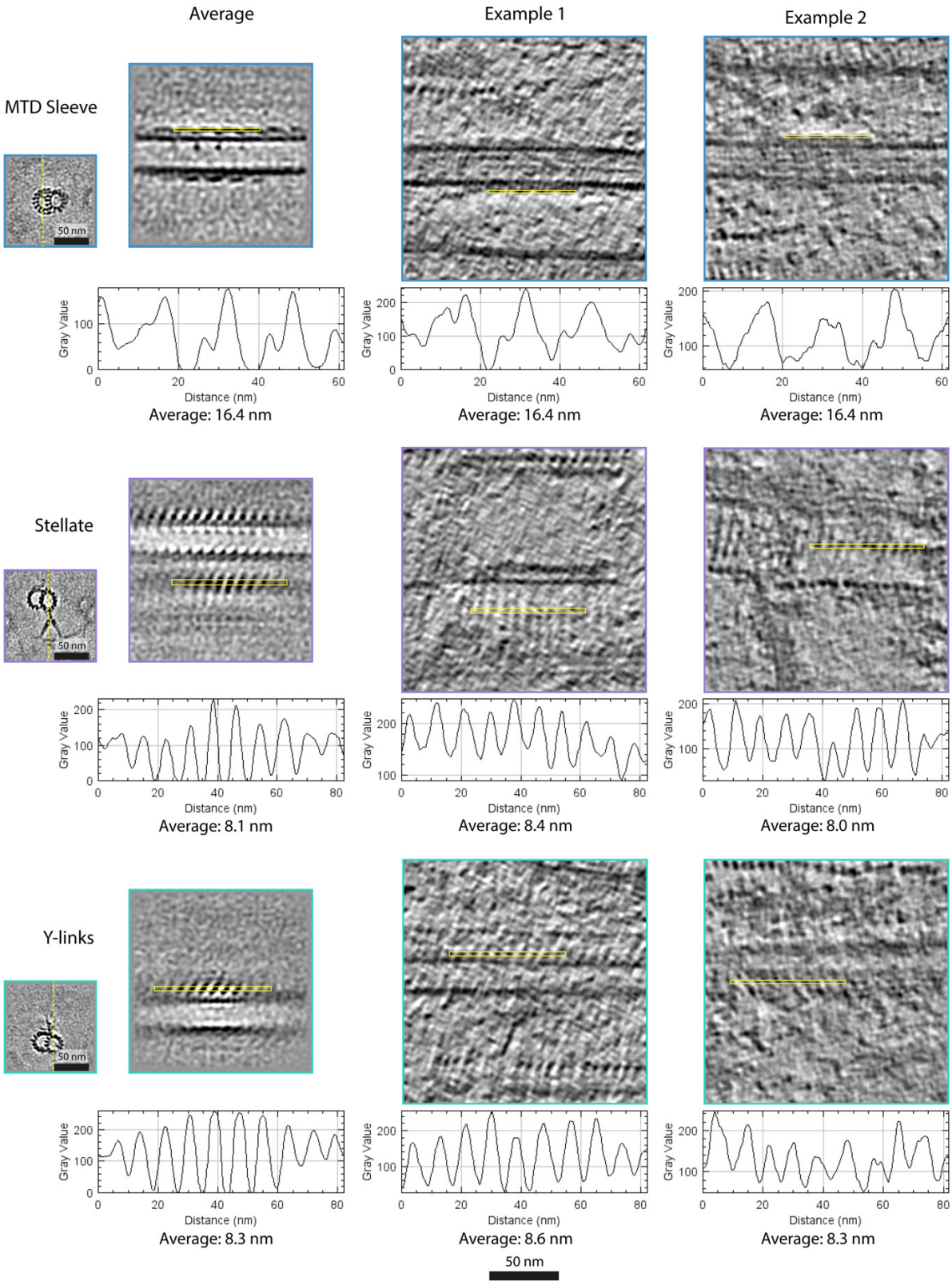

Figure 5.3. Periodicity of each TZ structure measured from grayscale 2D slices.

For each structure, subtomogram averages are shown on the left, and two examples of raw tomograms are shown on the right. The orientations of the longitudinal slices are indicated with dashed yellow lines in the cross-section views on the far left. Line scans along the yellow boxes in the longitudinal views were generated with FIJI software (138). Corresponding intensity plots are shown below each longitudinal slice, along with the average periodicity measured from each plot.

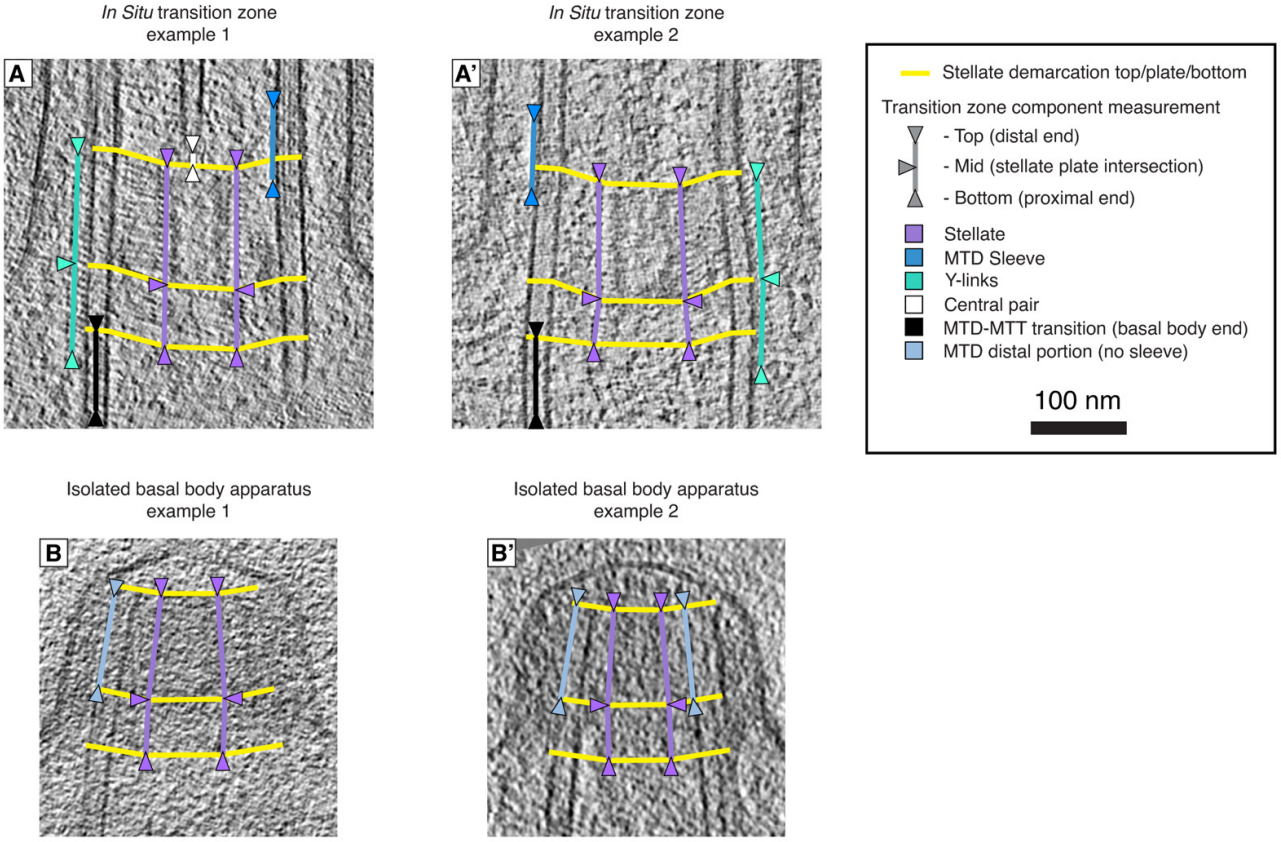

Figure 5.4. Methodology for manually measuring each TZ component.

In cells **(A, A')** and in basal bodies isolated immediately after ciliary abscission **(B, B')**. The position and extent of each structure was measured relative to one or more clear demarcations of the stellate apparatus: the proximal end, the central plate, and the distal end. In the isolated basal bodies, note how MTDs lack the helical sleeve decoration and terminate immediately at the distal end of the stellate. Measurement of the cleaved MTD ends (labeled "MTD distal portion") was used to position the site of flagellar autotomy (SOFA, Figure 5.1B). The overlap of the SOFA with the in-situ position of the MTD helical sleeve, as well as the absence of the sleeve from basal bodies after ciliary abscission, suggests that the sleeve structure may be involved in MTD severing.

Measurement	Proximal end (nm)	Distal end (nm)	Length (nm)	Repeats (rounded)
Zero - Central Pair	0.00	121.58 ± 13.79	-	-
MTD Sleeve (via Stell. D.)	85.79 ± 6.32	161.74 ± 9.16	75.95 ± 6.62	5
Zero - SOFA	0.00	112.78 ± 14.15	-	-
Zero - Stellate Distal	0.00	113.88 ± 6.32	113.88 ± 6.32	14
Stellate Proximal - Zero	-54.15 ± 3.50	0.00	54.15 ± 3.50	7
Zero - Y-Links Distal	0.00	95.32 ± 8.63	95.32 ± 8.63	11
Y-Links Proximal - Zero	-82.35 ± 6.56	0.00	82.35 ± 6.56	10
MTD/MTT Trans. - Zero	-155.78 ± 15.06	0.00	-	-

Table 2. Measurements of TZ components in C. reinhardtii.

For each transition zone component measured as shown in Figure 5.4 and displayed in Figure 5.2B, this table lists the lengths, repeat numbers, and the location of the proximal- and distal ends of each component along the TZ. The stellate/transitional plate is defined as "Zero".

5.3 Anterograde IFT trains assemble in the cytoplasm prior to ciliary entry

It has been known for decades that a pool of IFT proteins is localized near the base of the cilium (143,144), but the structural organization of this basal pool has remained a mystery. In our tomograms, we observed filamentous strings of particles with one end attached to the TZ and the other end splayed into the cytosol (Figure 5.5A). These strings appeared to consist of three layers, each with a different shape and periodicity (Figure 5.5B-C). Iterative 3D alignment of particles picked along each layer yielded subtomogram averages that we combined to produce a composite molecular structure of the strings (Figure 5.5D, Figure 5.6). Comparison to a previously published cryo-ET structure of mature anterograde IFT trains within the cilium (101) confirmed that the cytosolic strings are indeed IFT trains. Our structure of cytosolic trains was similar to the anterograde train structure, enabling us to assign densities to IFT-B complexes, IFT-A complexes, and dynein-1b motors, which have longitudinal periodicities of ~6 nm, ~11 nm, and ~18 nm, respectively (Figure 5.7). As was shown for anterograde IFT, we observed that dynein-1b is loaded onto cytosolic IFT trains as a cargo in an autoinhibited state (101,145). We therefore conclude that much of the IFT pool at the ciliary base consists of TZ-tethered anterograde IFT trains that are undergoing assembly prior to entry into the cilium. We did not notice obvious retrograde trains at the ciliary base, implying that they rapidly disassemble, perhaps even before exiting the TZ.

We observed two notable differences between assembling and mature IFT trains. First, assembling trains are flexible and display regions of high curvature (Figure 5.5A-C, Figure 5.7), whereas trains in the cilium have an extended straight conformation (Figure 5.7), which is likely maintained by interactions with cargos and the ciliary membrane. Second, assembling IFT-B has a prominent extra density on the side opposite IFT-A (Figure 5.5D, Figure 5.8; red asterisks), close to IFT-B's proposed kinesin-2 binding site (101). In regions where IFT trains are bound to the TZ, this extra density is positioned immediately adjacent to the MTD. The density is not part of the MTD structure itself, since it is also present on IFT-B in the sections of trains that dangle into the cytosol (Figure 5.8E). One possibility is that this density acts a molecular brake that prevents entry of IFT trains into the cilium until they are fully assembled and loaded with cargo. However, in a few cases, we also observed the density on trains along the axoneme just distal of the TZ (Figure 5.8D). Understanding the interactions and function of the extra IFT-B density will require a high-resolution IFT structure that reveals the position of each IFT protein within the train.

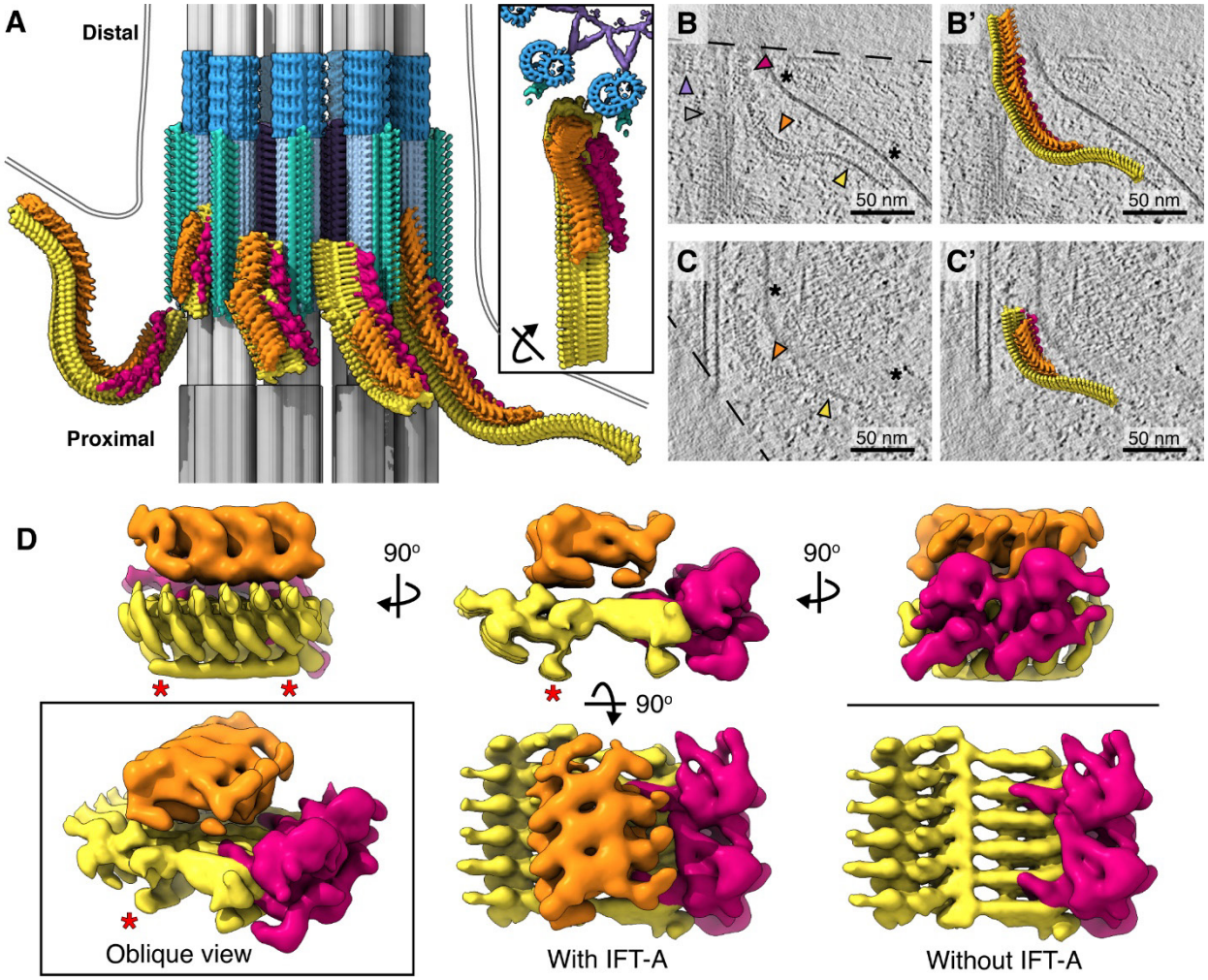

Figure 5.5. Cryo-ET structures of assembling IFT trains attached to the transition zone.

(A) Composite structures of assembling IFT trains (yellow: IFT-B; orange: IFT-A; red: dynein-1b) engaging the ciliary TZ (colored as in Figure 5.1). A schematic membrane has been added (gray double lines). Subtomogram averages have been mapped back into their positions inside a representative tomogram. **Inset:** rotated top view of rightmost IFT train from the main panel. **(B-C)** 2D slices through tomograms, showing assembling IFT trains, and **(B'-C')** overlaid 3D train structures, with their front ends attached to the TZ. In panel B, note the double AAA+ ATPase rings of the dynein-1b motors. Arrowhead colors correspond to panel A, and additional white arrowheads indicate the membrane. Scale bar: 50 nm. **(D)** Different views on the cytosolic IFT train composite subtomogram average. Colored as in panel A. Red asterisks indicate the extra IFT-B density, which was not observed on mature trains inside cilia (see Figure 5.8).

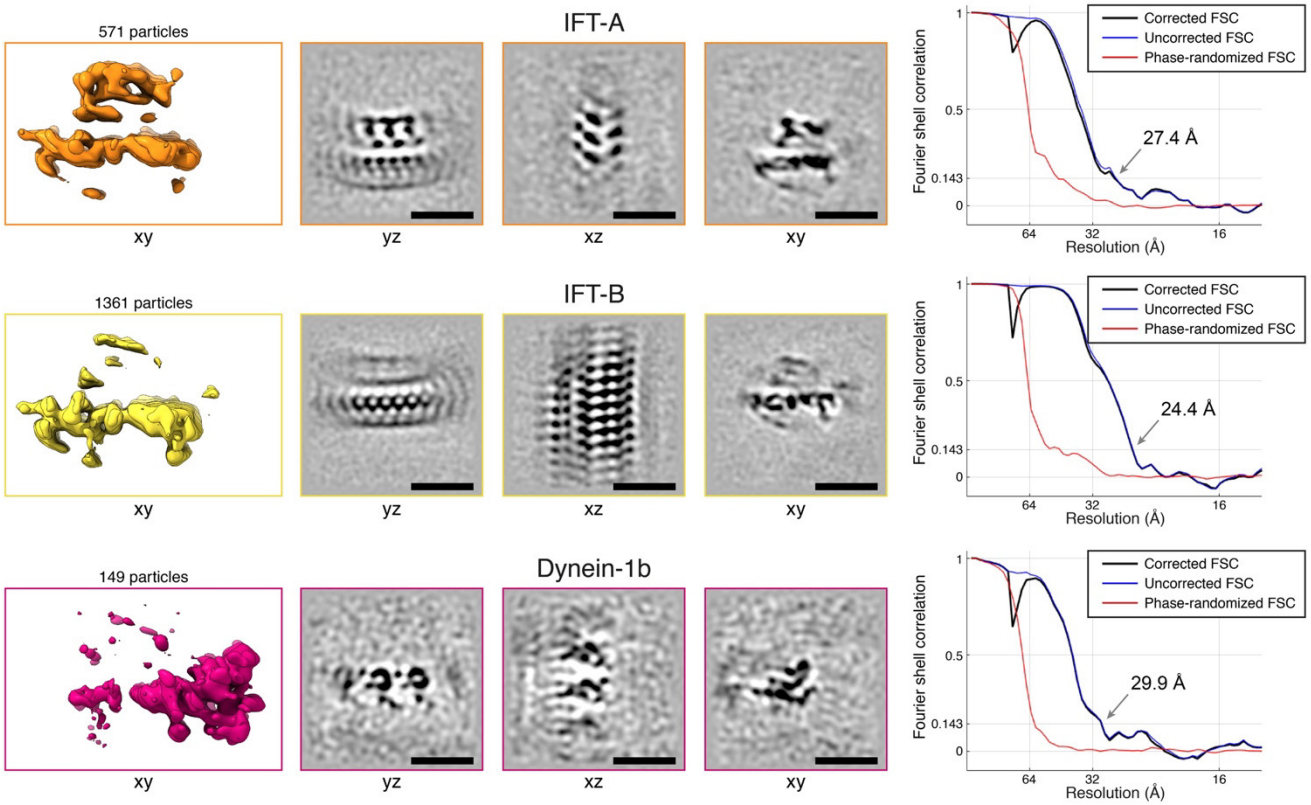

Figure 5.6. Individual subtomogram averages focused on different IFT train structures.

Subtomogram averages focused on individual components of the IFT train: IFT-A (top row), IFT-B (middle row), and dynein-1b (bottom row). These averages were fused to generate the IFT model shown in Figure 5.5. Left panels: 3D isosurface views, with the number of subvolumes (particles) in each average indicated. Central panels: 2D grayscale slices through the averages from three orientations (scale bars: 30 nm). Right panels: Fourier shell correlation curves showing the determined resolution of each average.

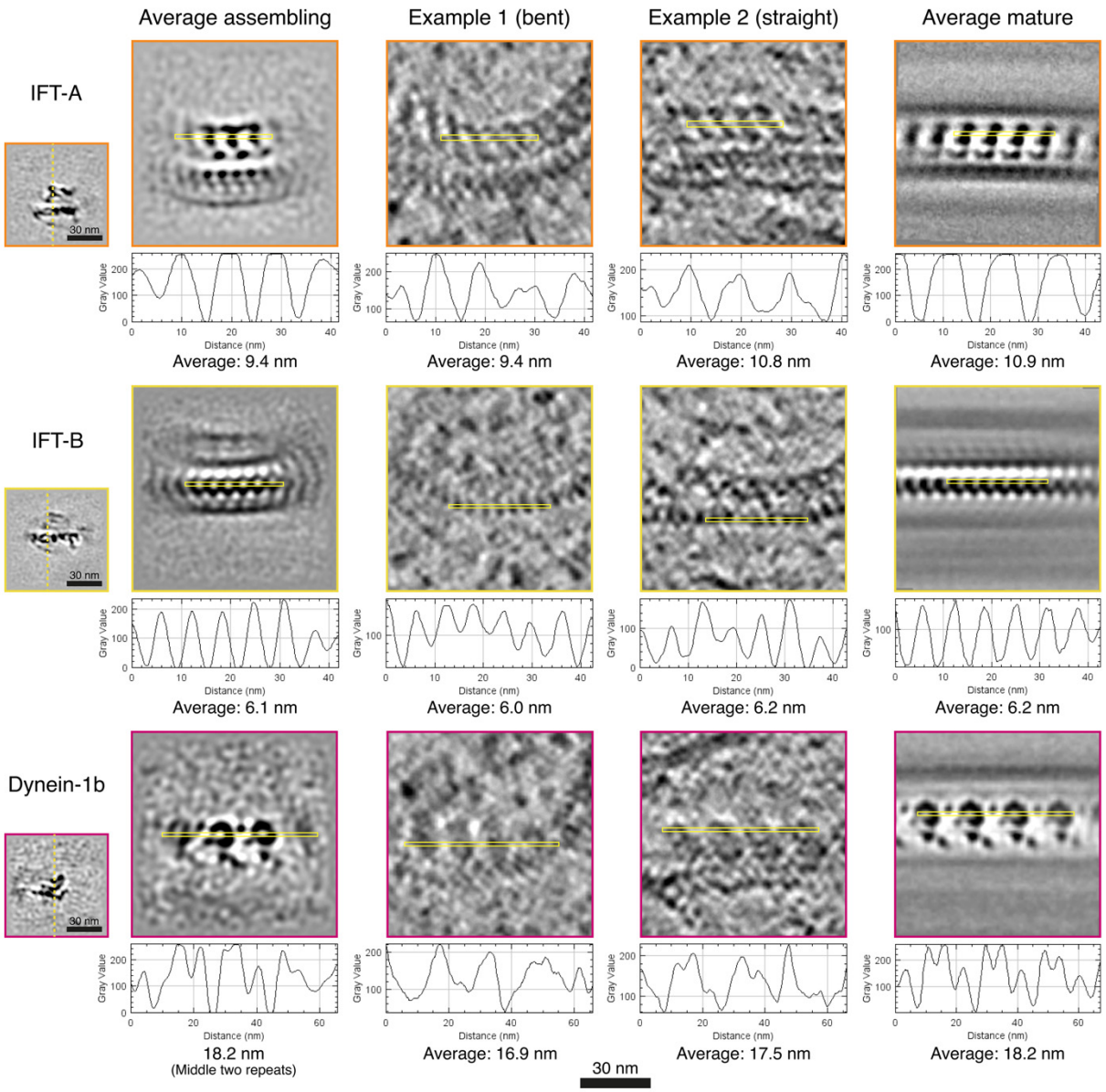

Figure 5.7. Periodicity of each IFT structure measured from grayscale 2D slices.

For each structure, subtomogram averages of assembling trains are shown on the left, two examples of assembling trains from raw tomograms are shown in the middle, and subtomogram averages of mature trains (101) are shown on the right. The orientations of the longitudinal slices are indicated with dashed yellow lines in the cross-section views on the far left. Line scans along the yellow boxes in the longitudinal views were generated with FIJI software (138). Corresponding intensity plots are shown below each longitudinal slice, along with the average periodicity measured from each plot. Due to the flexibility and curvature of assembling trains in the cytoplasm, the IFT-A repeat is ~11 nm at its interface with IFT-B but only ~9.5 nm on the side that will face the membrane in mature trains after ciliary entry (see "average assembling" on left). In contrast, IFT-A in the cilium has an extended straight conformation with ~11-nm periodicity on both sides (see "average mature" on right). This difference between assembling and mature trains demonstrates the flexibility of IFT-A.

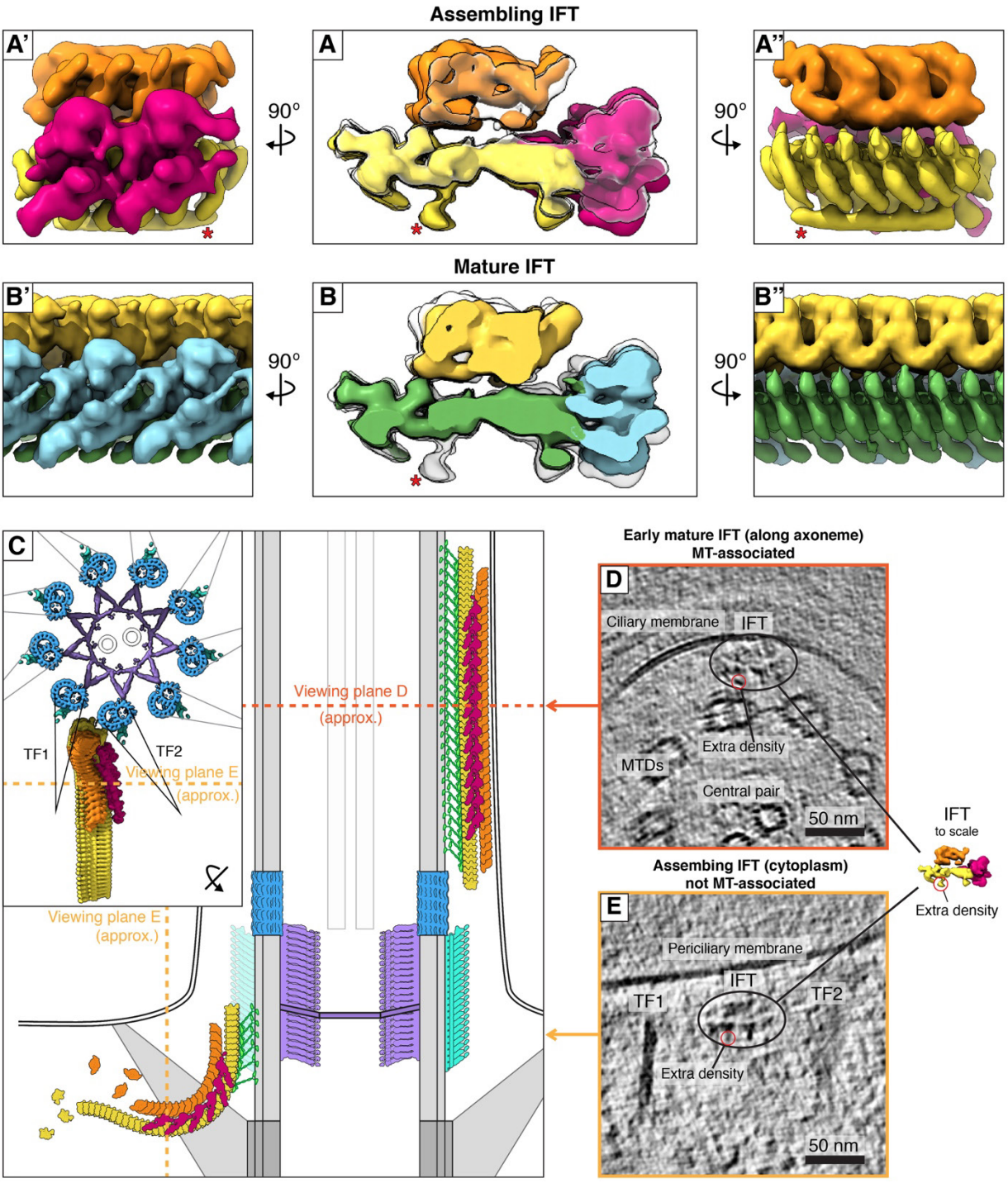

Figure 5.8. The extra IFT-B density on assembling trains.

(A) 3D isosurface overlay between the subtomogram averages of the assembling IFT train at the ciliary base (colored as in Figure 5.5) and the mature IFT train inside the cilium (from (101), white silhouette). Side views of the assembling train structure (without overlay) are shown in **A'** and **A''**. The extra IFT-B density observed on assembling trains is indicated with a red asterisk. **(B)** 3D isosurface overlay between the structure of the mature IFT train (colored as in (101,146)) and the assembling IFT train (white silhouette). Side views of the mature train structure (without overlay) are shown in **B'** and **B''**. **(C-E)** The IFT-B extra density is clearly observed in 2D slices through raw tomograms (approximate viewing planes are diagrammed in **C**). **(D)** The extra density seen on a train that has just entered the cilium. Here, the extra density is positioned close to an unknown structure emanating from the MTD. **(E)** The extra density seen on a cytosolic assembling train passing between two transitional fibers (TF1 and TF2).

5.4 IFT trains assemble front-to-back in a stepwise fashion

In situ cryo-ET combines native molecular structures with precise cellular localization, enabling us to plot the spatial relationship between assembling IFT trains and the TZ (Figure 5.9A-B). Although many IFT trains in our dataset were not completely contained within the thin FIB-milled cellular sections, 40 trains were largely intact and could be analyzed. The front segments of IFT trains attach to MTDs (but never to the MTTs of the centriole) and then continue in the distal direction along these microtubule tracks, while the back regions curve away from the TZ into the cytosol. The front ends of IFT trains were frequently observed at the Y-links, but only very rarely further distal at the MTD sleeve (Figure 5.9A-B). By mapping the IFT-B, IFT-A, and dynein-1b structures along the IFT trains (as shown in Figure 5.5A), we visualized the sequential order of train assembly. Anterograde trains always contain IFT-B, which forms a backbone scaffold upon which other components are attached. Thus, we plotted the train assembly state relative to each IFT-B subunit. While we observed variability between individual trains (Figure 5.9A), the cumulative plot shows a clear distribution of IFT train components (Figure 5.9B). The front parts of the trains are more complete, whereas the back segments are in a less assembled state, with IFT-B extending the furthest, followed by IFT-A and then dynein-1b. No gaps were observed in the regions occupied by IFT-A and dynein-1b, suggesting these components linearly oligomerize upon the IFT-B scaffold. These results support a front-to-back mode of assembly, where IFT-B forms a backbone onto which IFT-A and then dynein-1b are sequentially added.

Next, we compared the assembling cytosolic trains to mature anterograde trains within the cilium (Figure 5.9C-D). Mature trains exhibited a continuum of lengths from 223 to 558 nm, comprising 36 to 90 IFT-B subunits with an average of 62 ±16 IFT-B. In comparison, the longest assembling train we observed contained 88 IFT-B subunits, and the average length was 44 ±17 IFT-B. Therefore, we conclude that just one IFT train is assembled at a time per MTD. Cytosolic and ciliary IFT trains have similarly incomplete front ends, whereas the incomplete segment at the back of cytosolic trains is longer, as these regions are still undergoing assembly (Figure 5.9D). Perhaps as IFT trains enter the cilium, part of the incompletely assembled back end is left behind at the TZ to nucleate the front of the next train. As assembly of IFT-A and dynein-1b proceeds front-to-back, the front end of the new train would remain incomplete, as we see in mature anterograde trains in the cilium (Figure 5.9C).

A side note on IFT-A assembly: we have occasionally observed what appear to be pre-assemblies of IFT-A on the periciliary membrane, adjacent to the assembling ends of some IFT trains. One pre-assembly was even found without an accompanying train nearby. This could perhaps explain the longer dwell time of IFT-A around the basal body compared to that of IFT-B components, as observed by FRAP (102). The IFT-A could linger longer, perhaps recruiting cargoes, before joining an assembling IFT train and showing up in our analysis.

A final remark on the mode of IFT component recruitment to the ends of IFT trains: similarly to the rest of the basal body (95), we think that the whole peri-ciliary region may be a liquid-liquid or gel-like phase-separated condensate. It is devoid of large macromolecules such as ribosomes or proteasomes - a key indicator that this area is different from regular cytosol. We believe this phase separation can, via higher affinity for IFT proteins and -cargoes and therefore their retention in this zone, facilitate a “diffusion and capture” model such as proposed in (147), without the explicit need for active directed transport from the Golgi to the ciliary base (this active transport is however not excluded as a secondary mode of IFT component import). Moreover, we believe the combination of the diffusion-and-capture model with the flexibility of the back ends of IFT trains that can dangle around in order to recruit new IFT components inside this IFT-enriched pool makes for an elegantly localized IFT assembly system.

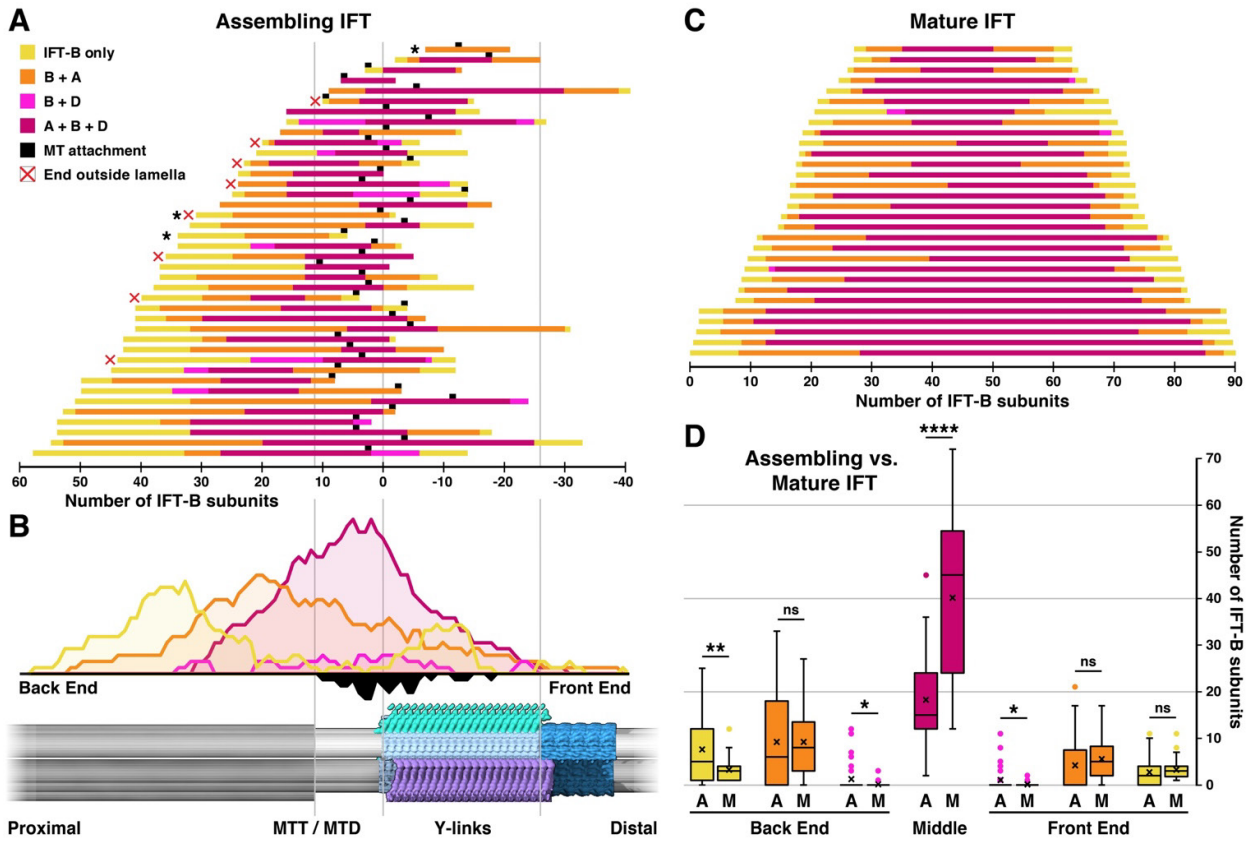

Figure 5.9. IFT trains undergo stepwise assembly from front to back.

(A-B) Assembly states of IFT trains relative to structures of the TZ (shown at the bottom of panel B). Distances are measured in number of IFT-B subunits relative to the onset of the Y-links (defined as the "0 IFT-B" origin point). **(A)** Position and train assembly state, measured for each IFT-B subunit of each assembling IFT train. Assembly states (color code in legend) were determined based on occupancy of IFT-A and/or dynein-1b on the IFT-B backbone. Black squares indicate train attachment points, i.e., the most proximal IFT-B subunit that is close enough to the MTD (<20 nm) to be considered bound to the microtubule. The three trains marked with black asterisks lack a "middle" (no dynein is bound), and thus a "back end" could not be distinguished from a "front end", so they were omitted from analysis in panel D. Of the 70 trains in our dataset, 30 had front ends cropped by the FIB milling, and therefore were not quantified, as their starting point relative to the TZ could not be determined. Eight more trains had cropped back ends (indicated with red "x"), but were included in the analysis. **(B)** Cumulative plot of all assembling IFT trains in panel A, with positions in relation to the TZ (shown at bottom). Colored curves above the line show the summed abundance of each IFT assembly state. The black curve below the line shows the distribution of MTD attachment points, summed from the black squares in panel A. **(C)** Distribution of IFT train lengths and completeness of assembly (colored as in panel A) for mature anterograde trains found in the cilium (*14*). **(D)** Comparison of the abundance of assembly states at the front and back ends of assembling ("A") vs. mature ("M") trains (i.e., trains in panel A vs. trains in panel C). Box: median and 25%–75% percentiles; X: mean; whiskers: 1.5× interquartile range; points: outliers. Statistical significance assessed by unpaired t-test (****, $P < 0.0001$; **, $P = 0.002$; *, $P = 0.03$; ns, not significant, $P > 0.05$). Because the backs of some assembling trains in this analysis were clipped by the FIB milling ("x" in panel A), the IFT-B only region of assembling trains should be slightly more pronounced than the quantification shown here.

5.5 Kinesin is loaded onto IFT trains close to the transition zone

The kinesin-2 anterograde IFT motor is difficult to identify by cryo-ET due to its relatively small size and flexible structure. Therefore, we turned to U-ExM super-resolution microscopy to examine the occupancy of kinesin-2 on assembling trains. We imaged three strains containing fluorescently-tagged IFT proteins: a kinesin-2 component (KAP-GFP), a dynein-1b component (d1bLIC-GFP), and an IFT-B component (IFT46-YFP). All three strains revealed train-like filamentous strings at the ciliary base, with their distal ends in close proximity to the TZ (marked by its lack of polyglutamylated tubulin, Figure 5.11) and their proximal ends curving into the cytoplasm (Figure 5.10A-E). Using semi-automated tracing, we plotted the 3D trajectories of each IFT string relative to the TZ (Figure 5.10F-G). IFT46 traces were longer than d1bLIC traces, consistent with our cryo-ET observations. KAP traces were the shortest and were localized close to the TZ. Thus, our combined cryo-ET and U-ExM measurements support a consensus model of IFT train assembly: IFT-B first forms the backbone, which scaffolds the sequential attachment of IFT-A, dynein-1b, and finally, kinesin-2 close to the TZ (Figure 5.10H).

U-ExM revealed an apparent 9-fold occupancy of IFT around the TZ (Figure 5.10D-E), consistent with recent observations in *Tetrahymena* (148). Given that each of these 9 signals corresponds to a single assembling IFT train (Figure 5.9), and that trains enter the cilium with a frequency of ~1 train/sec (103,104), we predict that trains should linger at the ciliary base for an average of 9 seconds during assembly. Consistent with this hypothesis, FRAP analysis of the *Chlamydomonas* basal pool showed that several GFP-tagged IFT proteins require ~9 seconds to recover peak fluorescence (102). Regardless, ciliary entry of IFT trains appears to be stochastic rather than sequential, with an avalanche-like relationship between lag time and train size (105).

The big question remains: what regulates entry of IFT into the cilium? In other words, what prevents the front end of the train from entering the cilium as assembly proceeds toward the incomplete back of the train? Maybe the extra IFT-B density we observed acts as a molecular brake, or perhaps IFT entry is dictated by kinesin-2 loading at the TZ. Interestingly, we observed a strong KAP-GFP signal inside the axoneme but excluded from the TZ and centriole (Figure 5.12). One possible explanation could be that kinesin-2 strongly binds central pair microtubules, as an antibody raised against a *Drosophila* kinesin motor domain was shown to decorate central pairs isolated from *Chlamydomonas* (149). However, this is hard to envision because this pair of microtubules is almost completely ensheathed in central apparatus proteins (150). Alternatively, the KAP-GFP localization may suggest that kinesin-2 diffuses back to the ciliary base through the axoneme lumen. The diffusion of KAP-GFP from the ciliary tip has been well documented in Chlamydomonas (103,108,127). In addition, high-speed super-resolution fluorescence microscopy showed that KIF17, the mammalian homolog of kinesin-2, diffuses within the axoneme lumen of primary cilia (151). It has been proposed that diffusive return of kinesin-2 from the ciliary tip could serve as a “ruler” that regulates the entry of new IFT trains (107,108). However, FRAP experiments indicate that the cilium is an open system for kinesin-2; new trains bind fresh kinesin from the cytosol in addition to recycled kinesin from the cilium (102).

Regardless, it is clear from our study that kinesin-2 loading is limited to the front regions of assembling trains (Figure 5.10). A simple explanation could be that assembly factors required to load kinesin-2 onto trains are localized to the TZ. However, the architecture of the TZ itself may also play a role. Perhaps the stellates block proximal diffusion of kinesin-2, redirecting it from the axoneme lumen to load onto the front ends of assembling IFT trains (Figure 5.10H). Indeed, IFT-bound kinesin-2 likely mediates train attachment to MTDs at the TZ (Figure 5.9A-B, black). When sufficient kinesin-2 is bound to the front of the train, these motors may begin to drag the train in the distal direction through the dense matrix surrounding the Y-links that form the cilium's diffusion barrier. As the train moves forward, additional kinesin-2 would be able to bind further back along the train as these parts enter the TZ. Eventually enough kinesin-2 would be bound along the train to propel it past the TZ structures and onward to start its anterograde journey through the cilium.

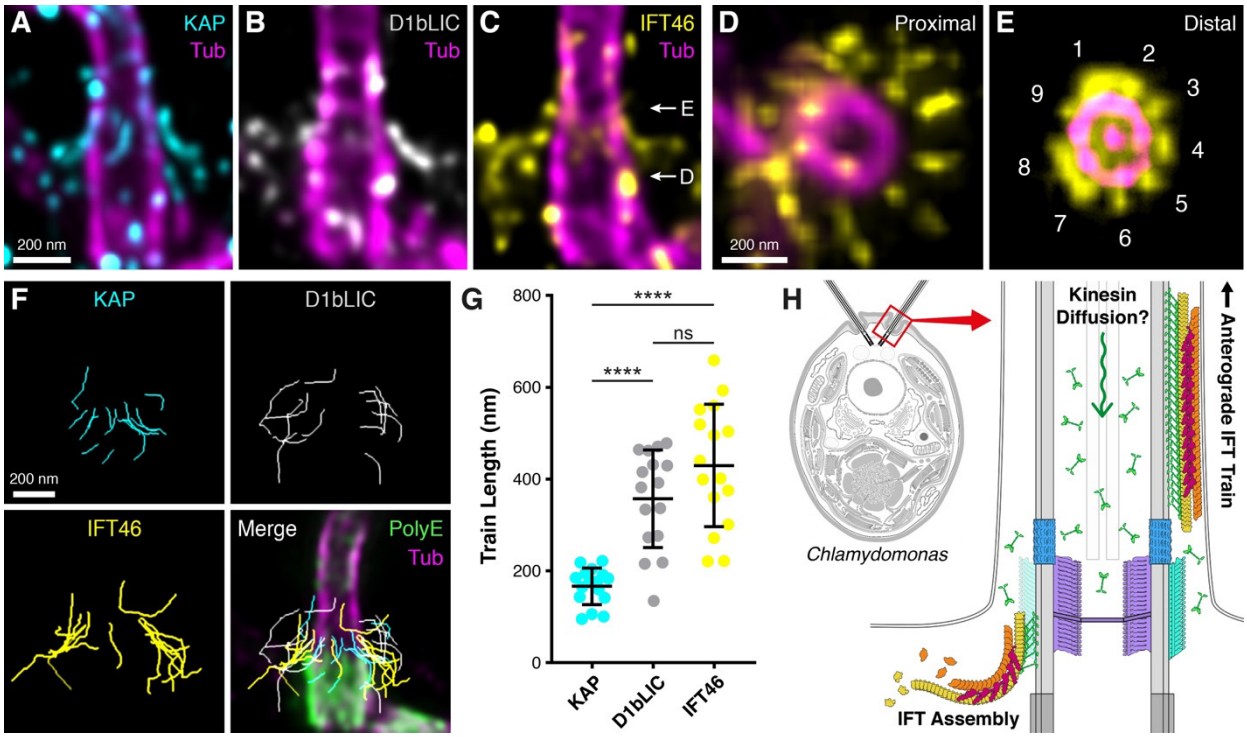

Figure 5.10. Assembly of anterograde IFT trains examined by U-ExM.

(A-C) Longitudinal views of assembling IFT trains at the ciliary base, visualized by antibody staining and U-ExM. **(A)** KAP-GFP (cyan). **(B)** D1bLIC-GFP (gray). **(C)** IFT46-YFP (yellow). Tubulin staining is magenta. White arrows indicate the approximate region of top view z-projections presented in panels D and E. **(D, E)** Top view z-projections displaying 9-fold occupancy of IFT trains at the proximal TZ (D) and more distal TZ (E), confirmed by the presence of the central pair. **(F)** 3D traces of individual IFT trains stained for KAP, D1bLIC, and IFT46. Bottom right panel, all traces merged and overlaid on single ciliary base stained for polyglutamylated tubulin (PolyE, green) and tubulin (magenta). The gap in PolyE staining marks the TZ (see Figure 5.11). **(G)** Measured lengths of 3D traces. N= 16 trains per stain, from 2 independent experiments. Statistical significance assessed by unpaired t-test (****, $P < 0.0001$; ns, not significant, $P > 0.05$). **(H)** Consensus model of IFT train assembly from cryo-ET and U-ExM measurements. New IFT-B subunits are added to the back of the train, forming a scaffold that is sequentially loaded with IFT-A, dynein-1b, and finally, kinesin-2 close to the TZ. U-ExM of KAP-GFP indicates that kinesin-2 may diffuse from the ciliary tip to base through the axoneme lumen (Figure 5.12). Scale bars: 200 nm.

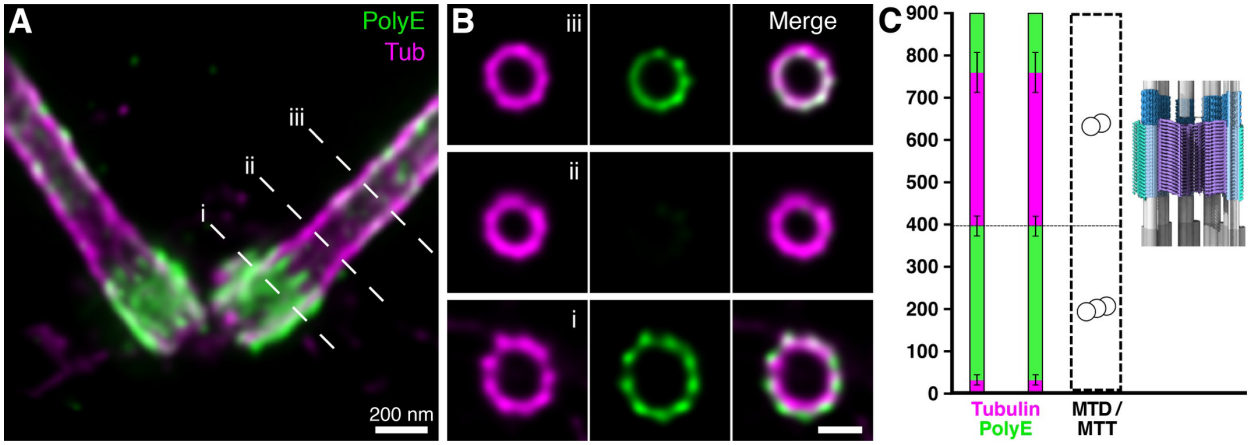

Figure 5.11. U-ExM shows a gap in PolyE staining at the TZ.

(A-C) Tubulin staining is magenta, and PolyE staining is green. **(A)** Longitudinal overview and **(B)** corresponding cross-section views through the centriole (i), TZ (ii), and ciliary axoneme (iii). Signal for PolyE terminates at the distal end of the basal body, approximatively at the position of the MTT to MTD transition, leaving the TZ devoid of PolyE. PolyE signal reappears on the axoneme, distal of the TZ region. **(C)** Quantification of the PolyE signal from the proximal end of the centriole (0 nm on the Y-axis) through the TZ and the proximal ciliary axoneme. The cryo-ET model of the TZ is displayed to scale. Error bars show standard deviation. N= 30 centrioles and axonemes from 3 independent experiments. All scale bars: 200 nm.

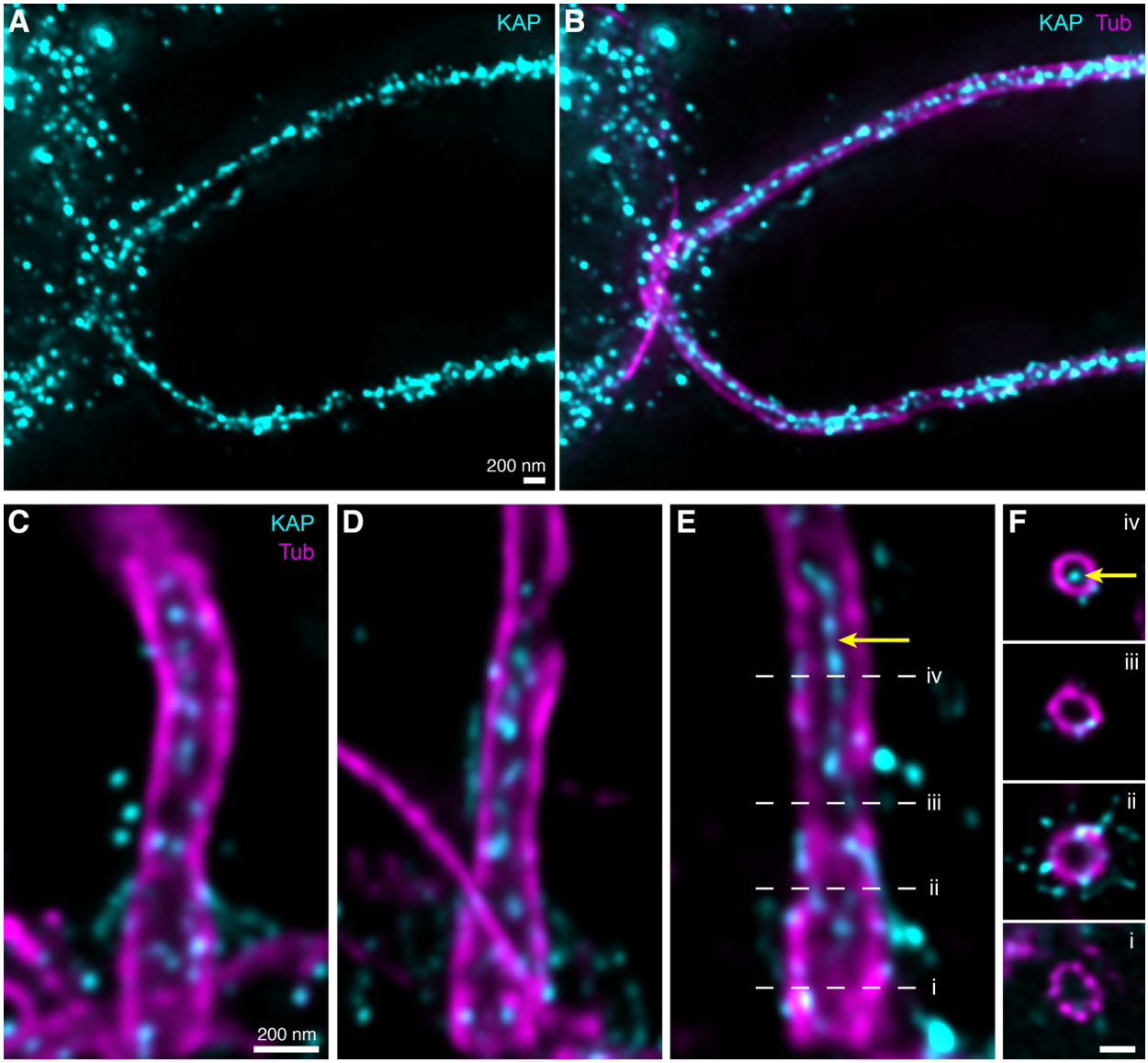

Figure 5.12. U-ExM reveals abundant KAP signal in the axoneme lumen, which is excluded from the TZ and centriole.

Tubulin staining is magenta, and KAP-GFP staining is cyan. **(A-B)** Overview images of cilia extending from a *Chlamydomonas* cell. Panel A shows only the KAP-GFP signal, and panel B is a merge with tubulin. **(C-E)** Longitudinal views and **(F)** corresponding cross-section views through the centriole (i), proximal TZ (ii), distal TZ (iii), and ciliary axoneme (iv). The strong KAP-GFP signal in the axoneme lumen (yellow arrowhead) is excluded from the TZ and centriole. Presumably, the luminal KAP-GFP protein cannot diffuse past the stellate plate (Figure 5.10H). All scale bars: 200 nm.

6 Chapter 2: the ciliary pore in multiciliated cells (MTECs)

6.1 Abstract of this chapter

After investigating the ciliary base in *Chlamydomonas*, we wanted to extend our findings to a mammalian context. Therefore, we decided to look at the ciliary base in multiciliated cells, and our model of choice became Murine (Mouse) Tracheal Epithelial Cells (MTECs). Despite the similarity of the *Chlamydomonas* basal apparatus to that of mammals, the MTECs should more closely resemble the situation in human cilia, and therefore carry more direct medical relevance. However, this is not the only advantage of switching to MTECs: whereas *Chlamydomonas* has only two cilia/basal bodies per cell, MTECs have hundreds. This greatly enhanced FIB targeting, FIB milling success and the copy number of structures in each lamella and tomogram.

The culturing of MTECs is more challenging than culturing *Chlamydomonas*, since an air-to-liquid-interface (ALI) mammalian cell culture has to be performed using basal tracheal cells as seeds. This is quite complicated, but highly worth the effort, considering the amount of data that we obtained from it. With help of the lab of Prof. Tim Stearns (during my visit to Stanford University), we managed to freeze enough EM grids to collect a dataset of 72 tomograms from 4 different cell cultures, predominantly from three GFP-Centrin2 cultures and one WT cell culture.

The computational analysis for this project is still under way, but there are a number of observations we can already make. We currently have bin2 structures of multiple stretches of microtubule doublets (MTDs), spanning from the basal body/centriole to the axoneme. Classification of the MTDs led to three major classes of particles, which we could map back along the TZ. These classes show a distinct localization pattern. We also have a bin2 structure of an interesting ring-shaped structure at the distal (apical) end of the centriole, which has been observed using classical EM and is named the Apical Ring (152). From here on, I will refer to it as the Apical Centriolar Ring (ACR).

Two structures stood out in our high-resolution MTD-centered class average from the central transition zone: an helix composed of microtubule inner proteins (MIPs) and inter-MTD connectors. The MIP helix shows a very distinct interrupted helical confirmation (“open washer” conformation), which indicates tubulin association, and shows a striking similarity to a previously described inner helix in sperm tails, named TAILS (153). During the course of this project, some of these structures were described in low resolution by the lab of Prof. David Agard (154), using isolated and demembranated bovine trachea basal bodies/axonemes (not *in situ*). Therefore, our structures are no longer entirely novel. However, we are expanding much more on this work, aiming to present a high-resolution map of the entire basal body – transition zone – axoneme region within native cells, akin to that of the *Chlamydomonas* project.

One thing that stood out in MTECs compared to *Chlamydomonas* was the extremely low apparent abundance of IFT trains. Whereas *Chlamydomonas* has IFT train preassemblies dangling from almost every MTD (such as shown in Figure 5.5A), MTECs did not show any considerable IFT preassemblies. The only instance of short IFT trains observed by eye was near an immature basal body, which was attached to a vesicle, in the process of docking to the plasma membrane. We hypothesize that motile cilia in multiciliated cells are rather static structures, which require little maintenance by IFT. The ATP that provides the energy for motility is a small enough molecule to be able to freely diffuse through the ciliary pore (64), without the involvement of IFT. However, the lack of IFT doesn’t fully explain how motile cilia can perform signaling functions (155), a process for which IFT is usually important.

6.2 *In situ* structure of microtubule doublets in the native MTECs TZ

Example tomograms of the ciliary TZ in MTECs (Figure 6.1A, D) reveal the typical appearance of the transition zone in this system. Looking at the general architecture, from proximal to distal, starting from the basal body, MTDs converge into an hourglass-shaped constriction, after which they diverge again to connect to the proximal part of the axoneme. Around the hourglass-shaped constriction, MTDs contain a very strong repeating inner density, which appears to be helical (Figure 6.1B-C). Connecting fibers between neighboring MTDs could sometimes be observed, but Y-links are hard to discern (Figure 6.1E).

First, I manually picked each TZ-associated MTD in each tomogram methodically and directionally from the distal end of the basal body to the proximal portion of the axoneme past the TZ, including ~500 nm of the proximal axoneme as well where possible. Next, I input all of these particles into STOPGAP to generate a *de novo* initial average of the MTD across the whole region. For this average, directionality was preserved by randomizing the phi angle about the rotational axis of the filament, and subsequent particle alignment and averaging was done by sampling a cone-shaped space around this filament axis. This quickly converged to a rough average of the MTD. This rough average was then subjected to classification; after trying 8, 5 and 3 classes, three major distinct classes emerged (judged by shape, as seen in Figure 6.2, Figure 6.3 and Figure 6.4, and relative positioning inside the TZ, see Figure 6.5). Class 1 (Figure 6.2) is an MTD with strong densities inside and between MTDs which corresponded to the MTDs' inner helix (Figure 6.1B-C) and inter-MTD connectors (Figure 6.1E). Class 2 (Figure 6.3) is a smooth, "bare" MTD with a microtubule inner protein (MIP) at protofilament A9, and also containing bits of the basal body's C-tubule density. And finally, class 3 (Figure 6.4), a class that appeared to be a mix of the former two, but would not really separate into either of these classes.

Plotting back the particle positions (after cleaning out poorly scoring and overlapping particles due to initial oversampling) in example tomograms (Figure 6.5) shows a distinct distribution of each particle class. The MTD with strong TZ-associated densities localized to the middle of the constriction in the TZ, as was expected. The bare MTD appeared at- and just distal of the basal body, as well as further out towards the axoneme. The last "mixed" class localized to the boundaries between the two other classes, at the edges of the TZ constriction, but was also found sporadically within the main zones of the other two.

Class average 1: pronounced inner-MTD helix and inter-MTD connectors

Focusing on the first and most interesting main class, we can see a couple of pronounced features (Figure 6.2): an inner-MTD helix and inter-MTD connectors. Pink arrows in Figure 6.2 indicate the inner MTD helix. We resolved how it's composed of individual densities matching the pattern of tubulin repeats. We therefore think that each subunit density is associated with a tubulin dimer in the MT wall. The helical pattern of this structure is interrupted at each turn; this matches the "open washer" pseudo-helical conformation of tubulin dimers in the MT tubular lattice.

Purple arrows in Figure 6.2 indicate inter-MTD connectors, which weren't inside the alignment mask, but were well resolved after alignment/classification. The molecular identity of this connector is as of yet unknown. It spans from protofilaments 6-8 of one MTD's A-tubule to protofilaments 7 and 8 of the adjacent MTD's B-tubule (see Figure 6.2D). Its shape and MT attachment points resemble that of the A-C linker, which connects adjacent MTTs in the basal body of many organisms, including *Chlamydomonas* and *Paramecium tetraurelia* (2). We don't know yet if the inter-MTD linker could be composed of the same proteins as this inter-MTT linker, since we know the molecular composition of neither.

We assume the MIP helix (Figure 6.2, pink arrows) is identical or at least similar to two previously reported structures. The first is an inner-MTD helix in bovine tracheal epithelial cells (BTECs), reported by Prof. Agard's lab (154). This paper reports several low-resolution averages of MTD structures found along the basal body-to-axoneme transition, of which two closely resemble class 1 and 2 in our study (Figure 6.6). Side-by-side comparisons (Figure 6.6A-B) and overlays of the structures (Figure 6.6E) show that the inner helix overlaps well with ours. The "seam" in the A-tubule (the interruption of the helix in the MT-associated "open washer" conformation) runs at the same position in both structures (Figure 6.6, marked with a red "+" throughout). However, with high-resolution structures from a native-state tracheal TZ, we think we can improve substantially on this work, as it's already clear from the grayscale averages (Figure 6.6A-B) that our densities at this early stage of data analysis are already more defined and higher resolution than theirs. For example, our structure resolves the individual subunits of the MIP helix. The inter-MTD linkers (Figure 6.2 and Figure 6.6, purple arrows) are also found in both averages. The density and shape of this linker are however considerably more pronounced in our average (Figure 6.6A-B, E, purple arrows).

The inner helix also matches the so-called Tail Axoneme Intra-Luminal Spiral (TAILS), which has been described before by the Höög lab in sperm tails (153). Unfortunately, the authors haven't released the corresponding density maps, but examining projection images of their averages side by side with ours shows their similarity (Figure 6.6G-I). Again, the shape of the inner helix closely matches and has a seam at the same position at protofilament A9 (Figure 6.6G, I). We note that our structure appears to be much better resolved, as the TAILS inner helix does not show individual subunits. This average does not show any inter-MTD connectors; we think this is a TZ-related structure, and TAILS inner helical densities in sperm were found near their tail ends, not in the transition zone.

The functions of the MIP helix and inter-MTD connectors remain uncharacterized. As long as their molecular identities are unknown, mutation studies and U-ExM localization won't be available, and therefore claims about their function are limited to structural observations. However, as the authors of (153) propose, the MIP helix could possibly function as an internal MTD scaffold, imparting rigidity and stability to the microtubular lattice in crucial high-stress regions, of which the ciliary base in motile cilia is obviously one. We agree that this is the most plausible hypothesis, which should be further tested.

The function of the inter-MTD connectors is less clear. Apart from the likely conclusion that they are important for constricting this part of the TZ, the functional relevance of this constriction itself remains unknown. We propose that this constriction could provide structural to this region by holding neighboring MTDs together. It could perhaps also aid flagellar waveform initiation/propagation. A role in processes such as TZ barrier formation or selectivity of cross-TZ transport of ciliary components could also be possible, as it could be an attachment point for other proteins that perform these functions, much like the Y-links that have structural functions, but also contain traffic-regulating protein modules such as the NPHP- and MKS-protein families.

On the topic of Y-links, the class 1 average also shows a faint density at the location of the Y-links (Figure 6.2A&C, solid orange arrows), located at the outer junction point between the A- and B-tubules, like in *Chlamydomonas* (1). Unfortunately, this density appears delocalized and smeared out, so it is not visible in the isosurface representation, at least not at the chosen threshold; we did however mark its position (Figure 6.2D&G, light orange arrows). Looking at raw tomograms doesn't show much of a density at this location at all (Figure 6.1E), unlike the Y-links in *Chlamydomonas* (Figure 5.1A-C & E-F, Figure 5.2, Figure 5.3). Aside from class 1, the Y-links can barely be seen in MTD class 3 (Figure 6.4A), but even less pronounced.

Y-links have been observed in mouse epithelial cells using classical EM methods, such as in oviduct epithelia (Figure 2.18). Unfortunately, the Y-links show a much higher contrast in classical EM compared to cryo-ET, a phenomenon which we have observed more often (see Section 0). For now, the Y-links in MTECs remain elusive, although efforts are being made to try elucidate their structure.

Class average 2: smooth microtubule wall and a MIP

In the second main class average, the "bare" MTD (Figure 6.3), not much stands out apart from the normal tubulin repeat, except for a Microtubular Inner Protein (MIP), which can be seen on the inner surface near protofilament 9 and 10 in the A-tubule (see cross-section in Figure 6.3E). A faint signal for the C-tubule (indicated with gray arrows) is also seen in this class average, which is due to bits of the distal basal body that were incorporated into this average.

This structure seems to closely match that of one of the averages from BTECs (154), namely their average of the distal basal body (Figure 6.6C-D,F). The MIP perfectly overlaps (green arrows). Their average shows an extra density compared to ours, on the inner junction of the microtubules (black arrows). However, we think this might be a noise-related artefact, as this density poorly shows up in the grayscale average (Figure 6.6D) and doesn't stand out from noise.

We currently do not know what the molecular identity of the MIP is; this is needed for knockdown/-out studies as well as methods like U-ExM. We hypothesize, due to its similarity in location and shape, that this MIP is composed of FAP67 (Figure 2.6, purple) (68).

Class average 3: an undefined mixture of structures?

Finally, the third main class average seems to show similar densities as those found in class 1, albeit a lot fainter (Figure 6.4, indicated by arrows colored equal to Figure 6.2). Based on their shape and mapped-back localization pattern in tomograms (Figure 6.5), we therefore suggest that this is an "in-between"/"mixed" class, with particles that STOPGAP couldn't reliably decide belonged to either class 1 or 2.

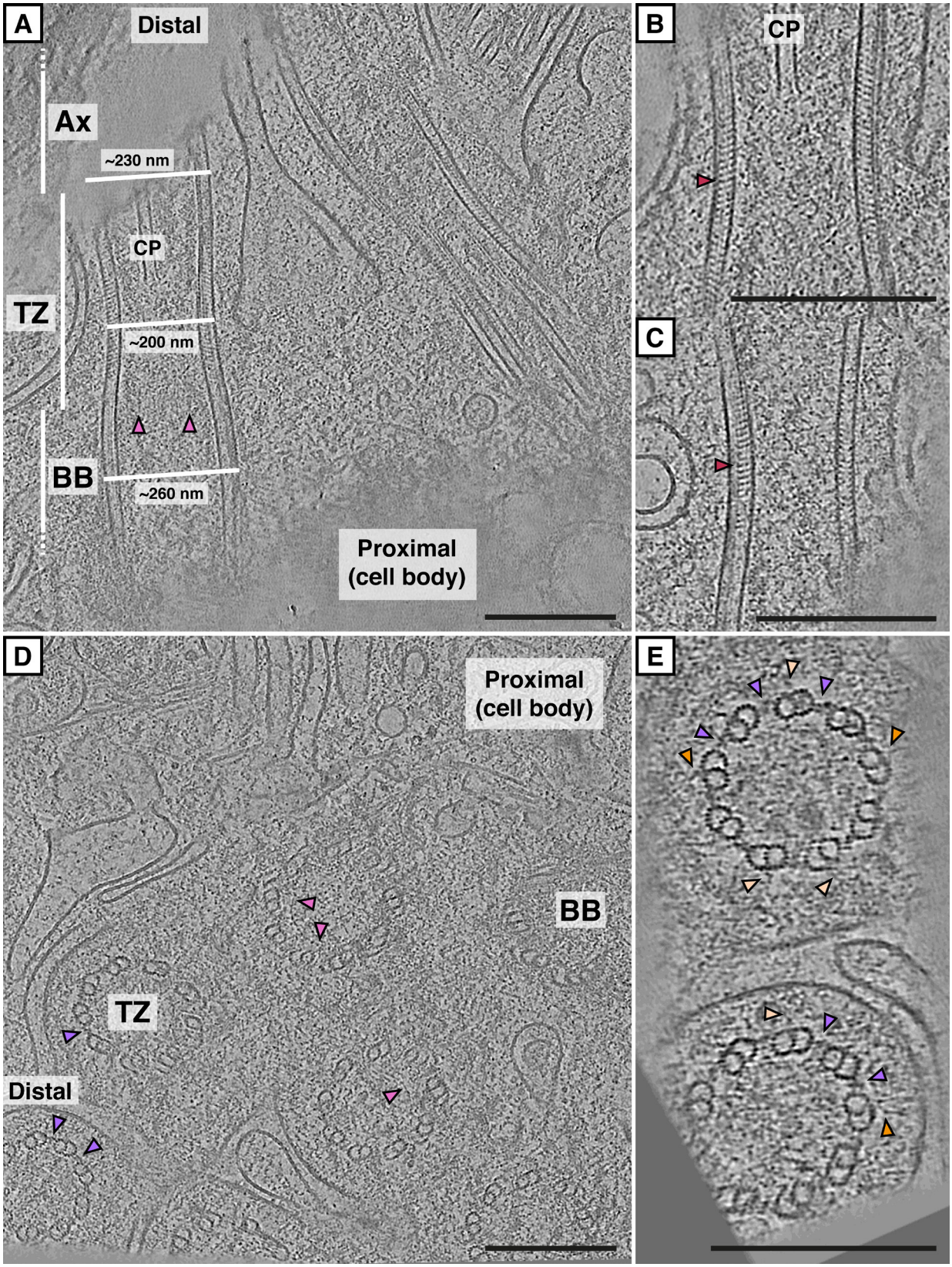

Figure 6.1. *In situ* examples of the ciliary transition zone in MTECs.

Arrowheads indicate densities of interest; red: MIP helix; purple: inter-MTD connectors; orange: putative Y-links, slightly visible; light orange: Y link locations, Y-links not visible; pink: apical centriolar ring (ACR). **(A)** Example MTEC tomogram, showing longitudinal cross-sections of two adjacent transition zones, and their characteristic hourglass shape, constricting in the middle of the TZ; **(B-C)** magnified views of MIP helices; **(D)** example MTEC tomogram, showing cross-sections of multiple basal body-TZ assemblies; **(E)** magnified cross-sectional view of two transition zones. All scalebars: 250 nm.

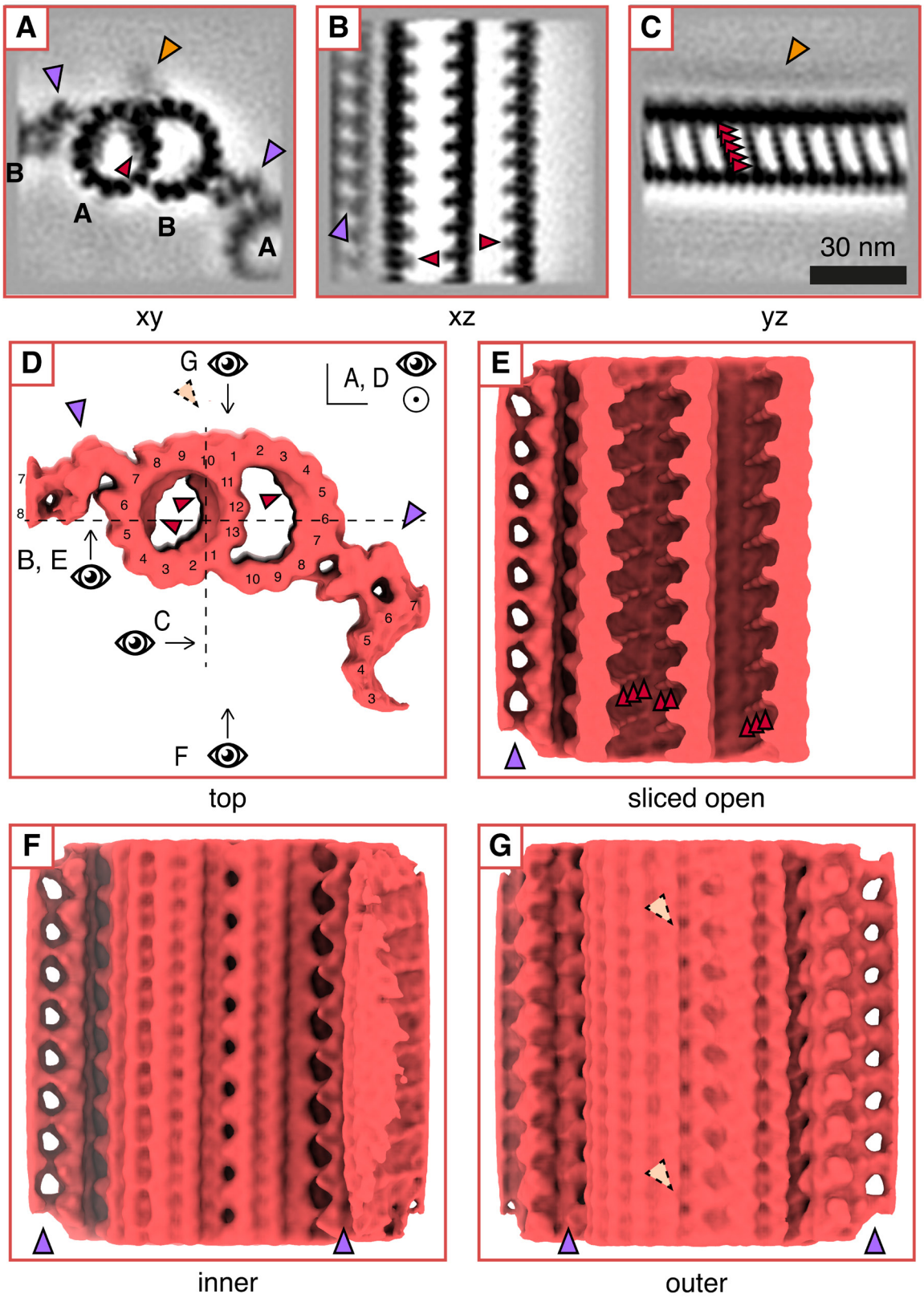

Figure 6.2. MTD class average 1: pronounced inner helix and inter-MTD connectors.
Arrows indicate densities of interest; purple: inter-MTD connectors; red: MIP helices; orange: putative Y-links (faint density, absent in isosurface representation (marked light orange)). **(A-C)** Grayscale slices through the xy, yz and xz planes; A- and B-tubules marked in (A); **(D-G)** isosurface representations; **(D)** top view, protofilaments numbered and perspectives indicated; **(E)** cross-section along the xy plane, showing the pronounced inner helical density; **(F)** view from inside the axoneme; **(G)** view from outside the axoneme.

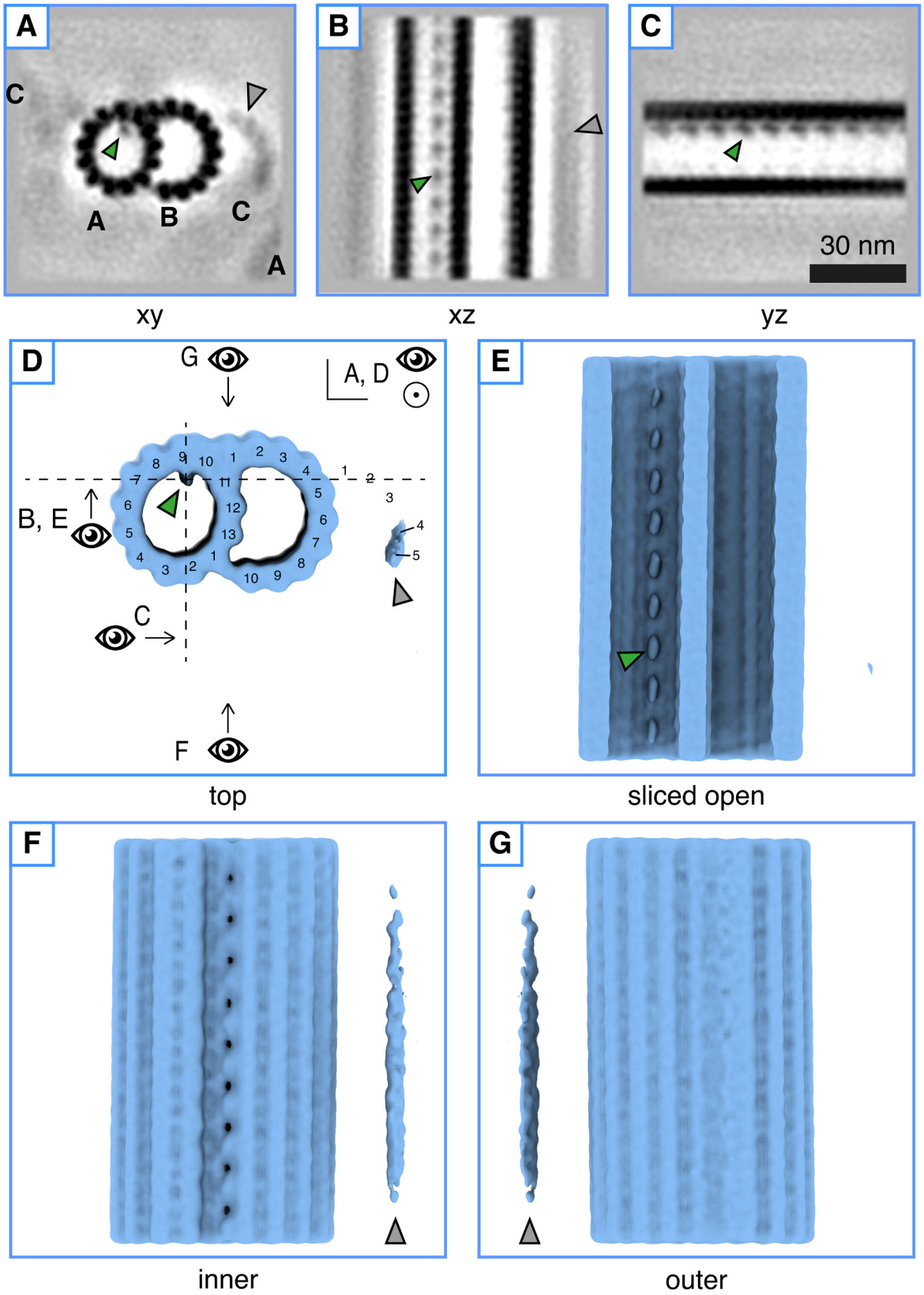

Figure 6.3. MTD class average 2: smooth microtubule wall and a MIP.

Arrows indicate densities of interest; dark green: microtubule inner protein (MIP) near protofilament A9; gray: C-tubule (faint density which is mostly absent in isosurface representation). **(A-C)** Grayscale slices through the xy, yz and xz planes; A-, B- and C- tubules marked in (A); **(D-G)** isosurface representations; top view, protofilaments are numbered and viewing points indicated; **(E)** cross-section along the xy plane, showing the MIP in the A-tubule; **(F)** view from inside the axoneme; **(G)** view from outside the axoneme.

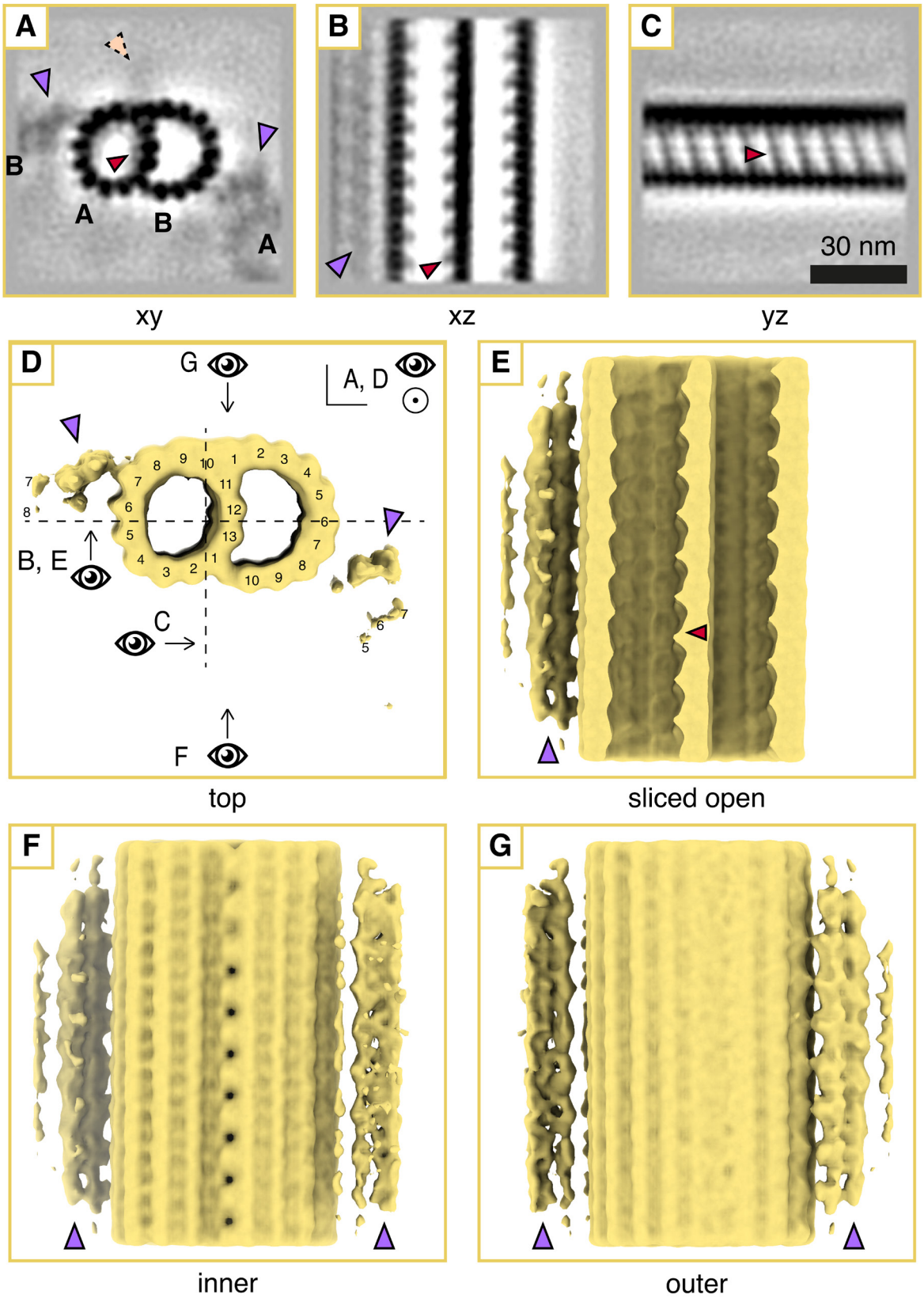

Figure 6.4. MTD class average 3: A mixture of structures?

Arrows indicate densities of interest, same as Figure 6.2; purple: inter-MTD connectors; red: inner helices; light orange: Y-links (faint density, absent in isosurface representation). **(A-C)** Grayscale slices through the xy, yz and xz planes; **(D-G)** isosurface representations; A- and B-tubules marked in (A); **(D)** top view, protofilaments are numbered and viewing points indicated; **(E)** cross-section along the xy plane, showing a faint helical density like in class 1; **(F)** view from inside the axoneme; **(G)** view from outside the axoneme.

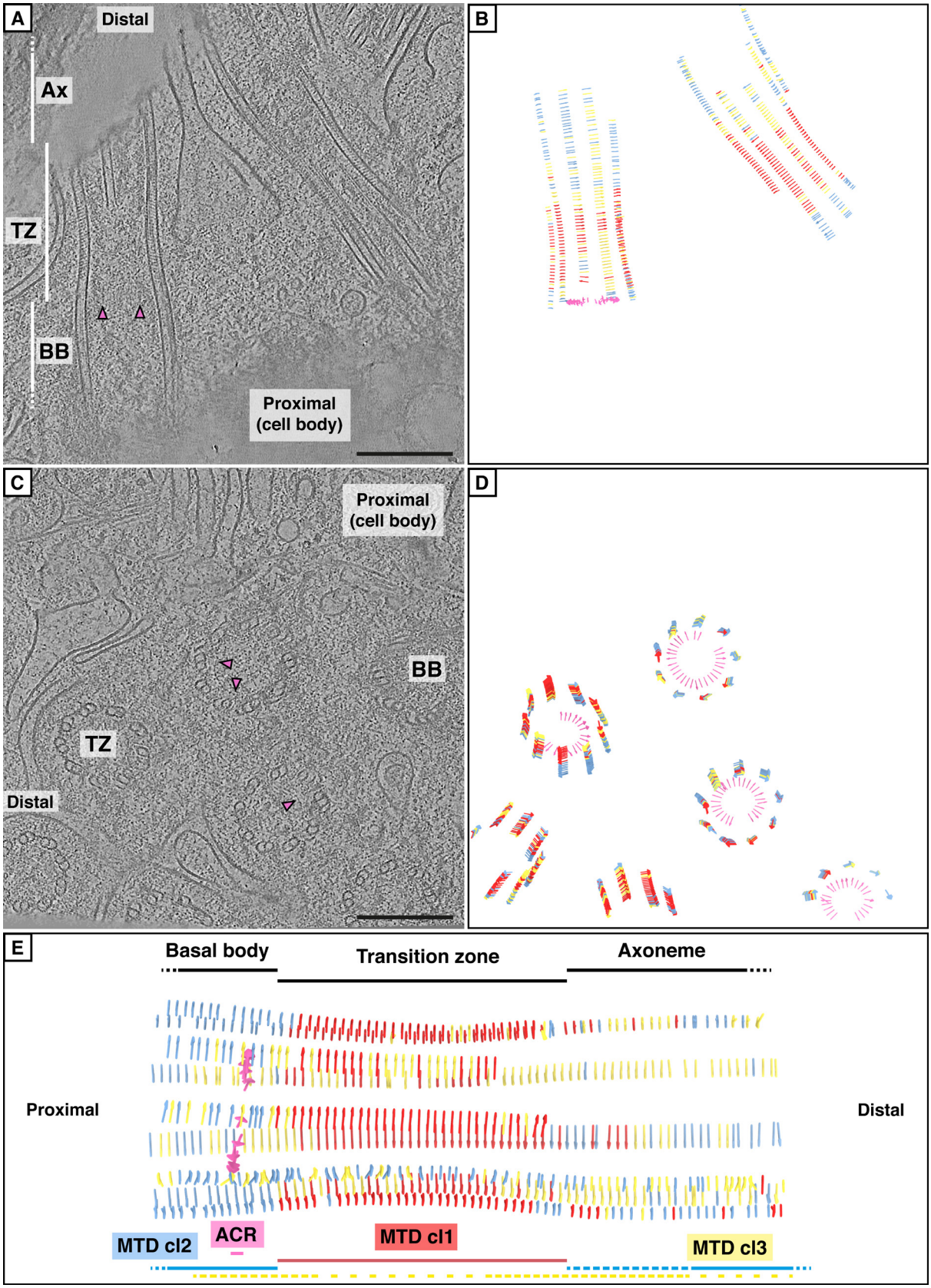

Figure 6.5. Positions of the MTD class averages mapped back into example tomograms.

(A,C) Example tomograms (same as in Figure 6.1), pink arrowheads indicate the ACR. Scalebars: 250 nm. **(B,D,E)** Particle positions and -orientations represented as arrows, mapped back into an empty 3D volume; (B) corresponding to (A) and (D) to (C); (E) from a different tomogram, moreover showing a schematic representation of the distribution of each particle class. Red: MTD class 1 (Figure 6.2); blue: MTD class 2 (Figure 6.3); yellow: MTD class 3 (Figure 6.4); pink: ACR (see Section 6.3).

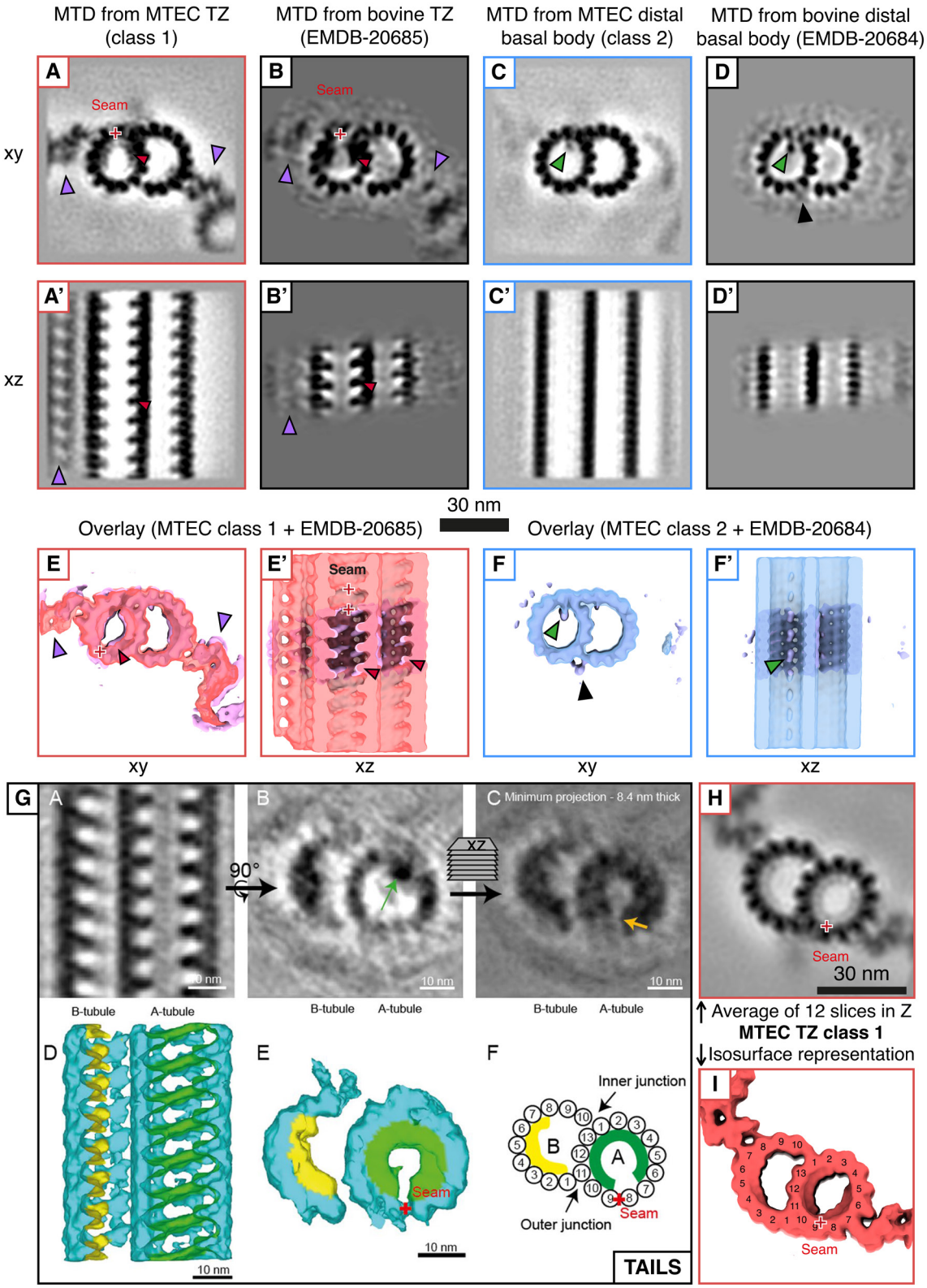

Figure 6.6. Comparison of MTEC MTD classes 1 and 2 with published structures.

Structures of interest are indicated with arrows; purple: inter-MTD connectors; pink: inner MTD helix; green: MIP on protofilament A9; black: extra density seen on the inner MTD junction in EMDB-20684. Red "+" indicates location of the A-tubule seam, in both the MT lattice and the MIP helix density. **(A-D)** Side-by-side comparisons of **(A,C)** grayscale averages of our MTD classes 1 and 2 and **(B,D)** published structures from BTEC TZs (EMDB-20685) and distal BBs (EMDB-20684) from (154); **(E-F)** 3D overlays of our main classes (transparent red/blue) with the maps from (154)(solid pink/lavender); **(G)** Inner helix in sperm tails (TAILS), adapted from (153); **(H-I)** Side-by-side comparison with our MTEC MTD class 1.

6.3 The distal ends of basal bodies in MTECs show a distinct apical ring

The distal ends of basal bodies in MTECs show a very distinct ring of densities, resembling chains on a bead (Figure 6.7). These densities are only visible in well-aligning tomograms, where they are strikingly obvious (Figure 6.7A). This ring appears to vary in size (~90-125 nm in diameter, see Figure 6.7B, C) and looks flexible, sometimes warping into elliptical shapes (Figure 6.7B, C, E). Adjacent to the apical ring sits a structure which is filamentous in appearance, and intersects the space between each MTT (light green arrowheads in Figure 6.7A, B), which I'll refer to as "inter-MTT projections". These projections appear flexible and heterogenic, and don't show up between every pair of MTTs. Moreover, another fainter, secondary inner ring is sometimes visible (Figure 6.7C, dark blue arrowheads) with a diameter of ~55 nm.

In each tomogram containing this part of the basal body, an attempt was made to manually pick each main ring density, in a methodical clockwise fashion (when looking proximal-to-distal, or bottom-up). After manually picking each particle of each ring, particle averaging and alignment using STOPGAP quickly converged to a rough de novo average of the apical ring (Figure 6.8). This rough average was then subjected to classification, trying to fit three classes; however, no distinct classes were found. Despite the number densities corresponding with the MTDs in roughly a 3:1 ratio, with 27 ±1.3 repeats per ring (9x3), no distinction could be found between each "bead on the chain", so a different periodicity or "triplet" demarcation could not be distinguished thus far.

The functions of the ACR, inner ring, and the inter-MTT projections, remain unknown. Although we have some leads, the molecular composition of these structures is not entirely clear yet. In an unpublished study probing localization of certain basal body proteins using ultrastructure-expansion microscopy (U-ExM) by Prof. Paul Guichard's lab, it was found that this exact region of the basal body contains a ring-shaped localization pattern of two proteins: the larger 260-kDa C2CD3 and smaller 13-kDa DIP13/NA14 protein (which are known to bind to each other). The ring they form in U-ExM has a diameter roughly corresponding to that of the ACR *in situ*. C2CD3, also known as OFD14, is a positive regulator of centriole length (156) importantly involved in the ciliopathy orofaciodigital (OFD) syndrome. Without it, basal bodies' propensity to properly assemble distal appendages and dock to the ciliary vesicle is disturbed in mammals (157), which through disturbed ciliogenesis and signaling defects (158) ultimately leads to OFD syndrome. AlphaFold (159) predicts that C2CD3 is likely globular in shape and has a structured core, but unstructured periphery. Propensity to form rings is not obvious from its structure. Recently, another pre-print paper came out that shows how C2CD3 might form a ring that is asymmetrically located in the apical end of the centriole (160); however, the authors hypothesize that this protein, together with another protein called LRRCC1, forms the "acorn", a filamentous asymmetrical structure that is different from the ACR. We hope to do a follow-up cryo-ET study on C2CD3 mutants, to see if the ring persists after disrupting the expression of this protein.

Two other proteins that U-ExM showed are present in the apical end of the centriole, but strongly localize to the central hub (so concentric with the ACR, but inside its ring) are Centrin, a very generic contractile calcium-binding centriole marker, and SFI1 (161), which is involved in spindle pole body formation (162). Perhaps these proteins are involved in forming the secondary inner ring; According to AlphaFold (159), the predicted structure of SFI1 is a single, extremely long, extended alpha-helical coiled-coil, which has no clear tertiary structure, so no clear folded domains, and should be too thin and flexible to properly observe by cryo-ET. We're therefore not sure if this is what's visible, but perhaps SFI1 is assembling into a multimeric higher-order structure, maybe via intermolecular alpha-helical coiled-coil interactions. Again, we could pursue doing a knockdown/-out study with SFI1 and see if this structure changes or disappears.

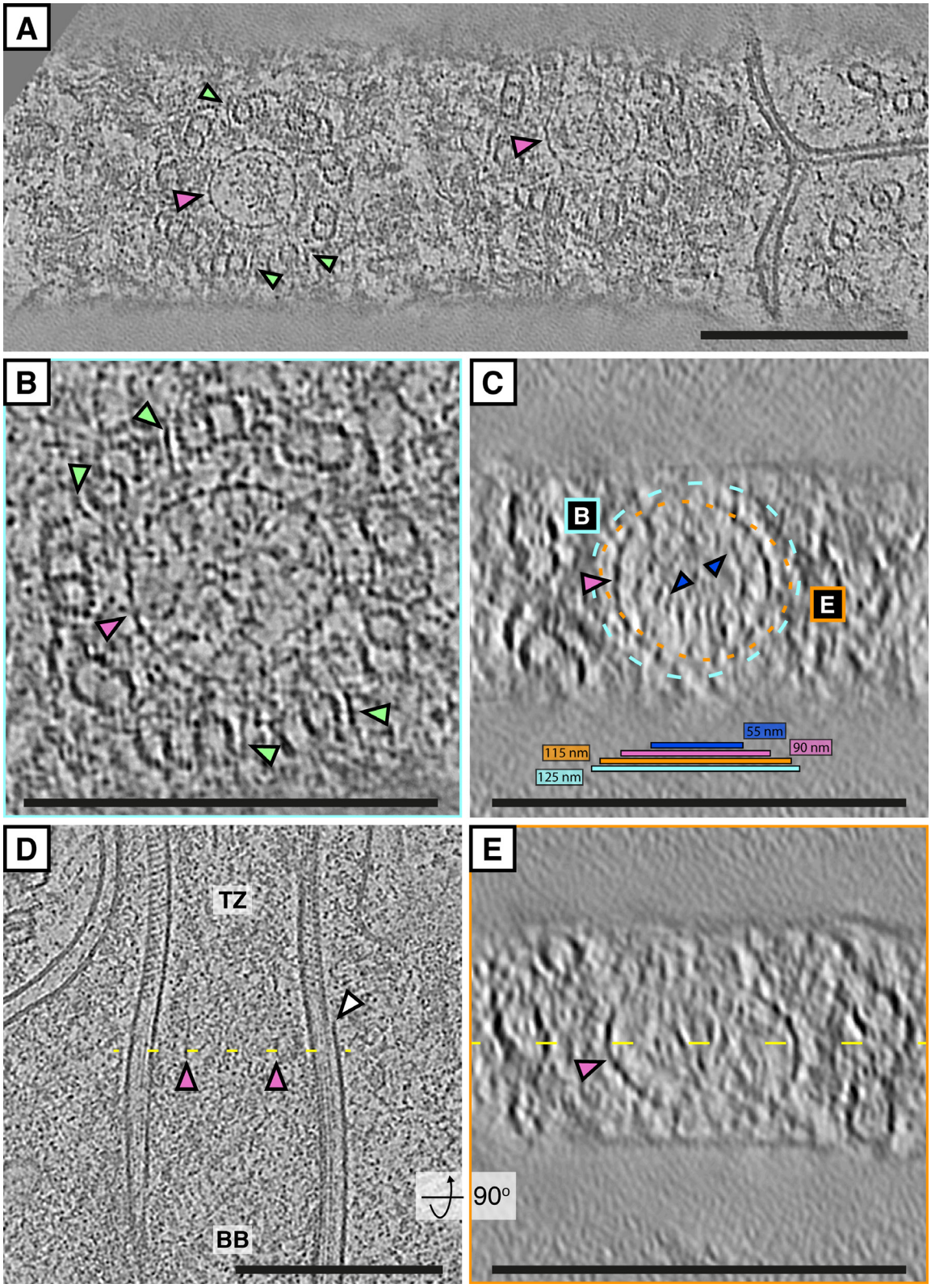

Figure 6.7. *In situ* examples of the apical centriolar ring (ACR) in MTECs.

Arrowheads indicate densities of interest; pink: ACR; light green: inter-MTT projections. **(A)** Two adjacent basal bodies showing the ACR; **(B)** ACR with a particularly large diameter, showing inter-MTT projections; **(C)** nearly perfectly circular ACR, showing a secondary inner ring (blue arrowheads); ACRs from (B)(light blue dashed circle) and (E)(orange dashed circle) are overlaid and measured to illustrate the variety in size and shape of the ACR; **(D)** TZ showing a side view of the ACR; white arrowhead: end of the basal body's C-tubule; **(E)** ACR from (D) viewed in-plane, clearly showing its warped shape. All scalebars: 250 nm.

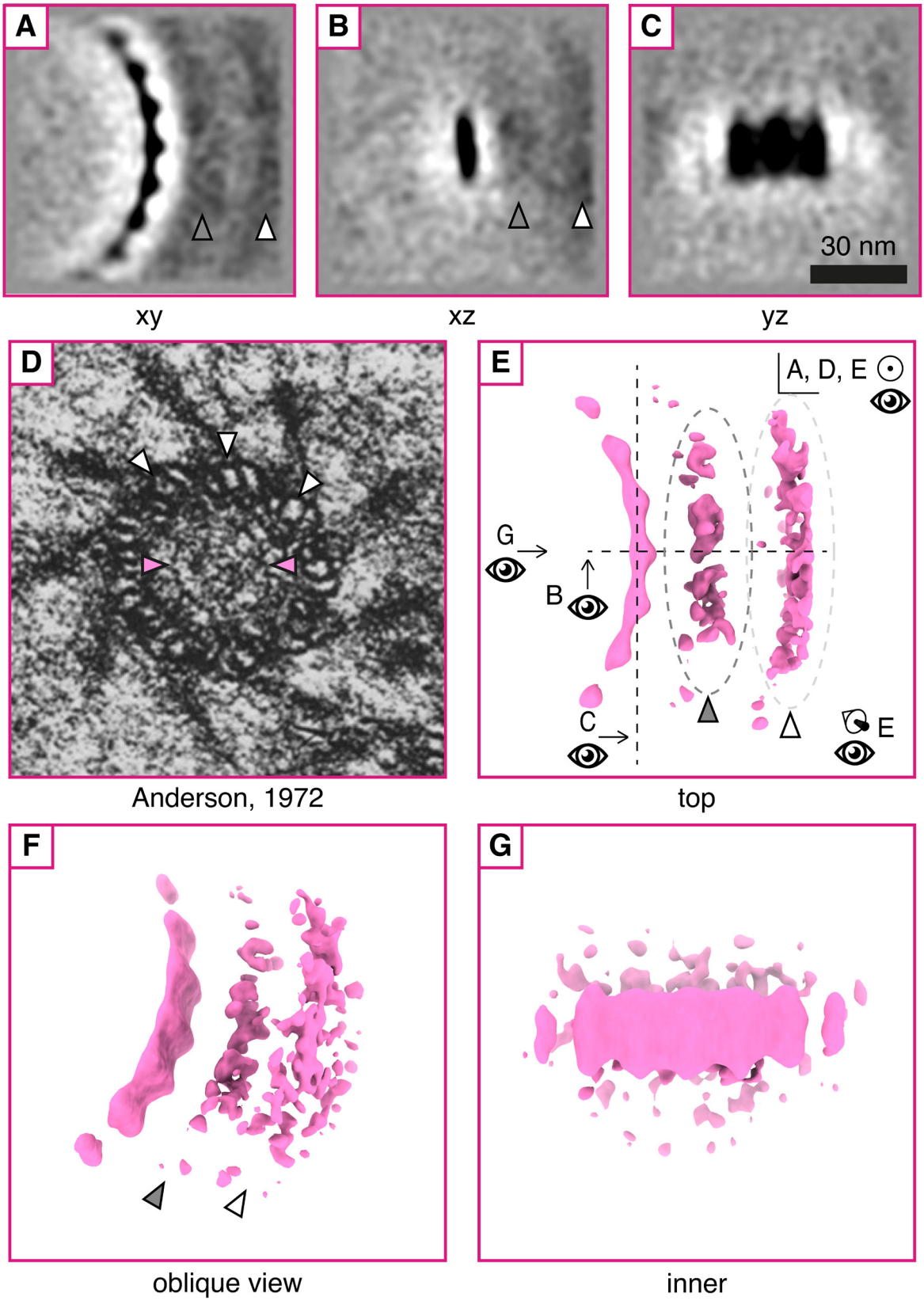

Figure 6.8. The apical centriolar ring: structural average.

Arrowheads indicate secondary densities; gray: unknown delocalized density; white: smeared out MTTs; pink: apical ring. **(A-C)** Grayscale slices through the xy, yz and xz planes; **(D)** Original micrograph of resin-embedded rhesus monkey oviduct cilia (152), showing the apical ring marked with pink arrows; **(E-G)** Isosurface representations; **(E)** Top view, viewing points are indicated; **(F)** Oblique view; **(G)** View from inside the centriolar barrel.

6.4 Future prospects: further analysis on MTECs

This project is still very much work in progress. This means there's a multitude of plans and ideas under development to explore before publication. I will list the ideas on the future of this project.

First of all, the current structural analyses can be pushed further. We only spent about a month or two on particle alignment optimization, and we think we can make significant gains there. For instance, besides further refining workflow details such as alignment masks and classification, the quality of the subtomograms for alignment can be greatly optimized. We will try tilt refinement (using WARP (55)) and 3D-CTF correction (with NovaCTF (45) or the new 3D-CTF implementation in Imod (42)). Even with preliminary analysis, we have resolved this region better than ever before, revealing many insights into the native MTEC transition zone. Yet there's surely much to improve, and we aim to maximize the resolution we can get out of this unique dataset.

Aside from technical improvements on subtomogram averaging, we also plan to further extend our analysis to create a comprehensive map of the ciliary base in MTECs. We will quantify the shape of the ACR, as it seems to flex and warp inside the cell, sometimes drastically. Correlation analysis with the shape of the surrounding centriole will reveal if these ACR distortions are caused by forces transmitted from the MTDs. We will also pick particles along the basal bodies and add their class averages to the transition zone analysis pipeline. Then we will create a robust, data-driven classification-based map of the entire basal body – transition zone – proximal axoneme superstructure, which hopefully gets us to the end goal: a comprehensive map of the native ciliary base, with all its major components as seen with cryo-ET. This would be similar to our work on *Chlamydomonas* shown in Figure 5.1, but in MTECs and extended to higher resolution thanks to the much larger MTEC dataset.

We also aim to assign molecular identities to the densities we're seeing, wherever possible. We will certainly include fluorescence localization of candidate components (such as C2CD3/OFD14 in case of the ACR) in collaboration with the "Centriole Lab" of Prof. Paul Guichard & Dr. Virginie Hamel (University of Geneva), similar to the strategy we took in (2,3). Ideally, we'd do knockdown/-out studies with proteins that we think are (part of) a structure, such as C2CD3/OFD14 in case of the ACR. Ideally, we'd also do functional knockdown/-out studies with proteins that localize to the structures. It will be time consuming to create mouse mutants, characterize the physiological phenotypes, and resolve the centriole/TZ structures by cryo-ET. However, we will make efforts on this front, in collaboration with the lab of Prof. Tim Stearns (Stanford University). This mutant work could indeed form the basis of a detailed follow-up study.

In addition, there is a wealth of information in these tomograms and surely observations that we haven't yet made. One observation we noted so far was possible connecting densities in the extracellular space between membranes of neighboring cilia. If true, this would be novel and could provide hints about the coordination of ciliary beating. However, additional examples must be added before expanding on this.

Finally, to link back to our *C. reinhardtii* study, we'd hope to see at least some intraflagellar transport (IFT). We assume there is little IFT due to the comparatively steady-state nature of multiciliated cells, which have their function primarily in motility as compared to the additionally robust signaling function of *Chlamydomonas* cilia. However, we do think that there has to be at least *some* IFT present to perform maintenance of ciliary components. Therefore, we plan to apply a directed template matching approach, in which we will use existing IFT averages from *C. reinhardtii* to search the tomograms for IFT complexes. We'd expect hits around the ciliary base (where anterograde IFT trains assemble in *Chlamydomonas*), and secondarily along the axoneme (trains that are already running inside the cilium). Since we'd be using pre-existing templates from other organisms, this has to be carefully curated, as to avoid model bias.

7 Chapter 3: observational differences between cryo-ET and classical EM

7.1 Introduction

In this short chapter I'll discuss what we expected to see in the *Chlamydomonas* ciliary transition zone, based on literature describing ultrastructure of the basal body apparatus and ciliary base using conventional EM techniques. In particular, seminal *Chlamydomonas* transition zone work performed by S. Geimer & Melkonian using room-temperature plastic-embedded EM (RT-TEM) in the early 2000s (140,163). We found that there was a disconnect between what we thought we should see, and what we actually observed using cryo-ET. Certain structures that are highly visible using classical EM methods proved to be nearly invisible using native contrast in cryo-ET, and vice versa. Here, I'll show a side-by-side comparison and attempt to explain the differences in observations between the different methods.

7.2 Classical EM methods

In order to make the comparison between methods, let's first briefly introduce the principles behind the method used in the literature we're comparing to, specifically resin-embedded RT-TEM. The basic principles behind RT-TEM, such as electron scattering and image acquisition, are largely the same as in cryo-TEM. The major difference is that RT-TEM relies more on amplitude contrast from high-atomic weight stains compared to cryo-ET's heavier reliance on phase contrast from low-atomic weight native samples (see Section 1.2.3). The sample preparation is however quite different.

Sample preparation

RT-TEM samples go through an elaborate sample preparation process, consisting of fixation, dehydration, resin embedding, sectioning and staining. Freeze-substitution is also possible, but won't be discussed here.

First, samples are fixed, using cross-linking agents such as formaldehyde or glutaraldehyde. The fixatives link most biomolecules together, so proteins to proteins, proteins to lipids, etcetera. Osmium tetroxide can also be used as extra pre-fixation step. It cross-links other types of molecules than aldehydes do, such as lipids; moreover, due to its high atomic weight, it can double as a contrast agent ("post-fixation staining").

Second, samples are dehydrated, usually with an organic solvent like ethanol or acetone. Water is slowly substituted by the solvent, by soaking in graded series of solvent solutions. This can also be done using frozen samples ("freeze substitution").

After replacement of water, samples are then resin-embedded, again using a graded series, usually with an epoxy- or acrylic resin. After curing (by heat or UV-radiation), the sample is now physically stabilized, and can be cut into thin sections with an ultramicrotome. A microtome contains a very small and precise knife, usually with a diamond edge, which cuts extremely thin slices (<80 nm, usually ~50 nm) off the resin-embedded sample. These slices are then collected on an EM grid, and stained ("post-stained") by treating the grid with contrast agent: usually first a uranyl acetate solution, second a lead acetate solution.

7.3 Observational differences

Let's now look at a side-by-side comparison of the *Chlamydomonas reinhardtii* ciliary transition zone, as observed in RT-TEM compared to cryo-ET (Figure 7.1). Panels A-J in the left half of Figure 7.1 show RT-TEM as published in (140), and depict ultra-thin cross-sections of the ciliary ultrastructure, showing distinct components of the proximal axoneme (panels A-B), transition zone (panels C-G) and basal body apparatus (panels H-J).

What's missing in cryo-ET

When looking at both halves of Figure 7.1, the ultrastructure of the ciliary base shows many of the same components in both techniques, such as the microtubule doublets and the stellate (H-shaped in longitudinal cross-section). However, interestingly, many components that appear very prominent due to strong staining in RT-TEM show up very poorly, or not at all, in cryo-ET. Specifically, this includes the Y-links (teal arrowheads, panels C-F and D'-E', K') that connect the MTDs to the ciliary membrane, double wedge-shaped "doublet outer projections" (164)(yellow arrowheads) that connect the stellate plate (which runs in the middle of the H-shaped stellate and forms the horizontal "bar" in the H, indicated with red asterisks) to the membrane (panels E, K, E' and K'), and finally, the transitional fibers (pink arrowheads) that anchor the basal body to the periciliary membrane (panels G-I, K, H', K').

Looking at the exact corresponding locations of these structures in cryo-ET (Figure 7.1, right half), very little structure or contrast is apparent there. The Y-links only show up as small MTD-associated stubs (teal arrows; see Figure 5.1 and Figure 5.3 for more *in situ* examples), with no density visible closer to the membrane. The transitional fibers do sometimes show up, especially when the fibers (which have a sheet-like appearance) are visualized perpendicular to the plane of the sheet they form (Figure 7.1H', pink arrowheads). Their visibility is however much less pronounced than in RT-TEM. Finally, the double wedge-shaped doublet outer projections, which should be central to the TZ at the height of the stellate plate, seem completely absent in cryo-ET (yellow broken arrowheads in Figure 7.1E', K').

Conversely: what's missing or overlooked in RT-TEM

It also works the other way around: some densities can look more pronounced in cryo-ET compared to RT-TEM. In this case, the MTD Sleeve (see Section 5.2, and Figure 5.1 and Figure 5.3 for more *in-situ* examples), which decorates the MTDs in the most distal portion of the TZ, could only be noticed using cryo-ET. Looking back at RT-TEM work, specifically Figure 7.1C, stained density is visible, but perhaps easily overlooked due to it closely hugging the MTD. We think this is the reason it hasn't been described before. Moreover, in RT-TEM side views (Figure 7.1K, at the height of the cross-section marked "C"), it's almost invisible. In cryo-ET, however, it shows up as a very pronounced density, which has strong contrast to its immediate surroundings (Figure 7.1C').

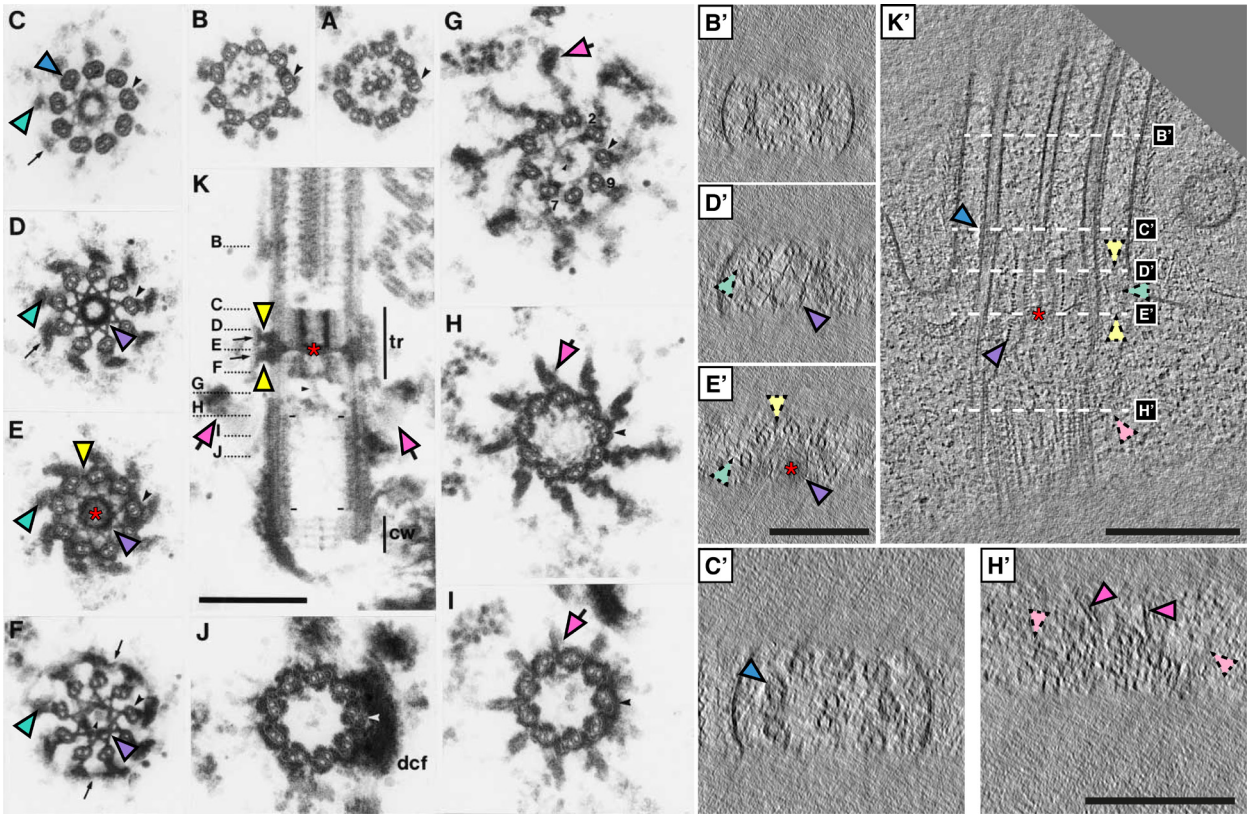

Figure 7.1. Side-by-side comparison of the *Chlamydomonas reinhardtii* transition zone: "traditional" EM (left) versus cryo-ET (right).

Arrowheads indicate structures of interest; "broken" lighter arrowheads denote the location of structures that are not easily visible, or seem absent entirely. Blue: MTD sleeve; teal: Y-links; purple: stellate; yellow: double wedge-shaped "doublet outer projections"; pink: transition fibers; red asterisk: stellate plate; **(A-J)** Ultra-thin sections of the *Chlamydomonas* basal body apparatus and transition zone using RT-TEM; **(B'-K')** cryo-ET of the same regions shown in (A-J/B-K), corresponding to the same letter there; **(B,B')** proximal axoneme, showing few differences between techniques; **(C,C')** distal end of stellate fiber showing the region of the MTD Sleeve (see Figure 5.1D,G; Section 5.2), which shows up strongly in (C')(blue arrowhead), but has possibly been overlooked in (C); **(D,D')** distal portion of the stellate fiber, showing pronounced densities around the positions of Y-links in (D)(teal arrowhead), but not in (D'); **(E,E')** stellate fiber at the stellate plate, showing how dense the plate appears in both techniques; again, Y-links and surroundings are stained strongly (teal arrowheads); **(K,K')** overviews of the full BB + TZ complex, cross-sectional planes which are visualized and compared in other panels are marked; **(H,H')** distal portion of the basal body, with transitional fibers (pink arrowheads) radiating out- and upwards towards the periciliary membrane. Panel (K'): 5 slices in Z averaged; panels (B'-H'): 10 slices in Z averaged; All scalebars: 250 nm

7.4 Hypothesis

All of these structures have important molecular functions that contribute to the TZ's gating/barrier function: the Y-links anchor the MTD's to the membrane while providing a platform for barrier-forming proteins (NPHP, MKS protein families), the transitional fibers anchor the basal body to the membrane and are involved in the barrier function as well, while the "doublet outer projections" (first observed in 1974 (164)) have no function assigned to them yet, despite the fact that they should be present in the available proteome of the *Chlamydomonas* transition zone (165). Since these double-wedge-shaped structures are so prominently present in such a crucial location, central to the TZ, we think they'll most likely have similarly important functions.

We do not suspect any of these structures are actually missing in cryo-ET tomograms, as they are all crucial parts of a functioning TZ. However, we do think that the mode of contrast formation plays a key role in these observational differences. In particular, we hypothesize that the affinity of these intrinsically unstructured, fibrous proteins for contrast agents in RT-TEM makes these proteins show up much more prominently, as compared to their native electron density in cryo-ET. These contrast agents are usually uranyl acetate and lead citrate, used in most RT-TEM staining protocols, including the example in Figure 7.1. Osmium tetroxide can also be used post-fixation; it has an added benefit as crosslinking agent (used for Figure 7.2A-B).

We think many of the BB/TZ-associated proteins form a gel-like meshwork, which apparently acts as a sponge, soaking up heavy metal stains and retaining them. This stronger affinity for stains might be exaggerated by artefacts inherent to RT-TEM such as protein aggregation caused by chemical fixation. The gel-like meshwork appearance of proteins, basically looking like empty cytosol in cryo-ET, is common around the basal body; many centriole/basal body proteins here seem to liquid-liquid phase-separate, which is hypothesized to be important for the basal body's many different functions across the cell cycle (95,97). We think the same is happening near and inside the TZ; one important observation that points towards this conclusion, is the complete absence of major macro-molecular complexes such as ribosomes and proteasomes in the entire TZ-BB-periciliary area, whereas in normal cytosol these are abundantly visible. An example of this (*Chlamydomonas* chloroplast) is shown in Figure 7.2; neither RT-TEM (panels A and B) nor cryo-ET (panel C) shows any of these differentially staining densities.

We think these phase separated compartments show up poorly in cryo-ET due to lower native contrast, which might actually better reflect the physiological situation. Multiple contrast-decreasing factors may be at play here: the very small diameter of individual filamentous protein strands (often single-stranded, too small for visibility in cryo-ET), the absence of any structured regions within these proteins, and most importantly, molecular crowding of surrounding cytoplasm, which raises the threshold at which structures start to provide relative contrast against the background. Denser fibrous structures with (partially) structured regions in them, such as the stellate fiber and the transitional fibers do show up (Figure 7.1H'), albeit less pronounced than in RT-TEM. When molecular crowding is taken away or ice vitrification quality is poor, the proteins in this region sometimes become visible, showing contrast with their surroundings. This happened in one particular case, seen in Figure 7.3. The tomogram depicted here shows a smashed cilium which seems to have leaked some of its contents into the surrounding buffer. Exactly at the location of the doublet outer projections, we now find a clearly visible double-wedge-shaped density (marked with yellow arrowheads). This image has been contrast-enhanced for visual aid, but it's clear in non-contrast-enhanced views as well.

Previous *in-situ* studies of phase-separated structures such as the nuclear pore (32,166) or the area surrounding the Golgi (33) show a very similar "empty" *in situ* appearance, even though these areas aren't empty either, especially in the case of the nuclear pore. In fact, some of the intrinsically disordered proteins inside the nuclear pore, called Nucleoporins, sometimes show up in the ciliary pore (63). Although other similarities between the nuclear pore and the ciliary pore such as a RanGTP/-GDP gradient and importin-β2 transport system exist (113,167), the physiological relevance and function of Nucleoporins in cilia is debated, as Nucleoporins don't show up in the proteome of isolated *Chlamydomonas* TZs (165).

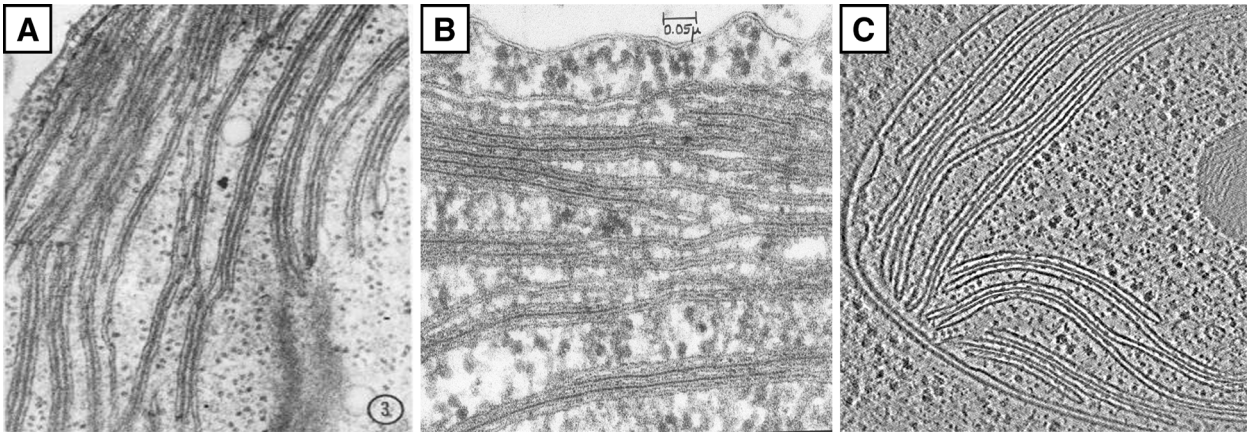

Figure 7.2. Side-by-side comparison of the *Chlamydomonas reinhardtii* chloroplast: "traditional" EM (left, middle) versus cryo-ET (right).

(A-B) RT-TEM micrographs of thylakoids in the chloroplast, stained post-fixation with osmium tetroxide and post-stained with uranyl acetate and lead citrate; images from (168)(A) and (169)(B); **(C)** Cryo-ET of thylakoids inside the chloroplast (170).

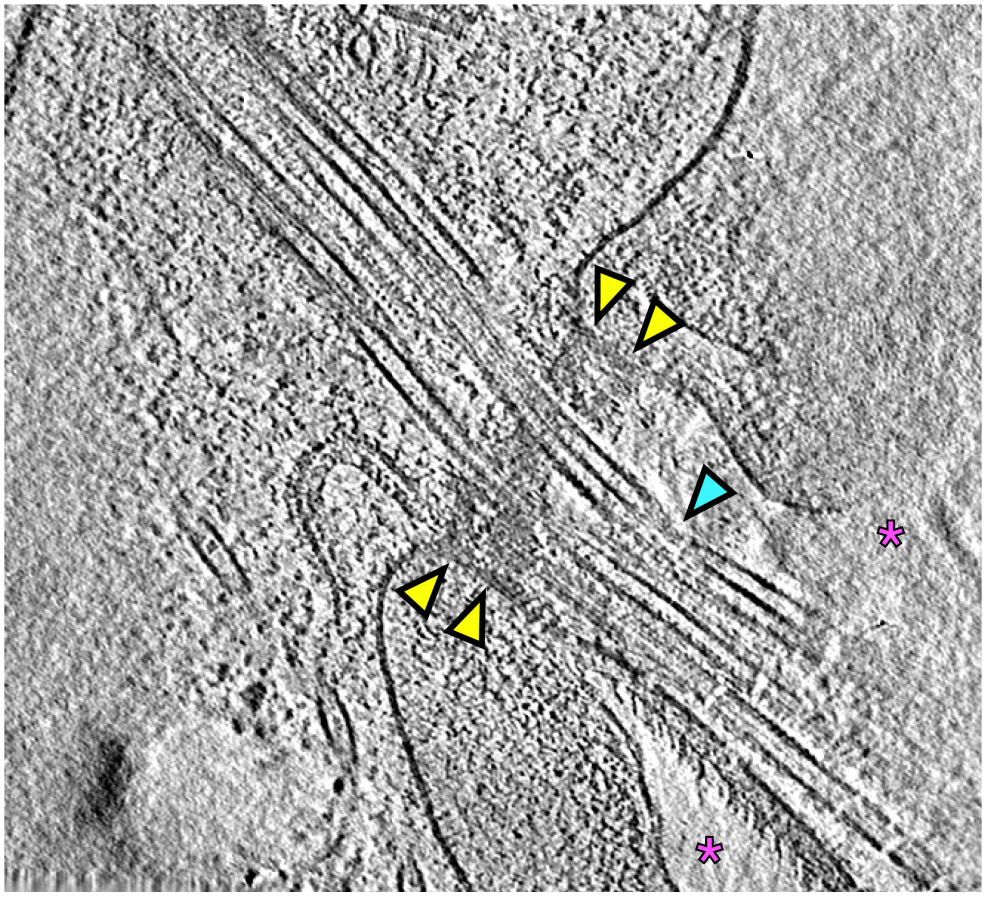

Figure 7.3. Cryo-ET of a broken *Chlamydomonas* cilium reveals previously unseen density in the area where the double wedge-shaped doublet outer projections should be.

This is a contrast-enhanced slice through a tomogram in our *Chlamydomonas* dataset, in which the cilium appears smashed, with broken MTDs (blue arrowhead) and ruptured ciliary membranes (pink asterisks). Its contents seem to have leaked to the surrounding buffer, exposing a dense region in the middle of the TZ (yellow arrowheads), which has the right localization (middle of the TZ) and appearance (double-wedge-shaped) to be identified as the “doublet outer projections” seen in Figure 7.1E, K and (140,164).

Overarching conclusions

In this thesis, I've discussed the outcome of two projects on the ciliary pore, one in *C. reinhardtii* and one in mouse tracheal epithelial cells (MTECs).

Despite the limited size of our dataset, we found that in *C. reinhardtii*, intraflagellar transport (IFT) particles are built into trains in a hierarchical, spatially resolved manner, with IFT-B forming a backbone, onto which IFT-A, then dynein-1b, then kinesin are built, before entry into the cilium. Moreover, we presented the first fully native *in situ* structure of the ciliary pore and transition zone (TZ), with components such as the stellate assembly, the MTD-bound portion of the Y-links, and a novel structure that we named the "MTD sleeve", and which seems to be involved in flagellar autotomy. We also found that visibility of TZ components was sometimes vastly different from classical EM observations, and were therefore very hard to see in some instances.

In MTECs, we obtained a large dataset containing many transition zones. These represent the first tomograms of the mammalian ciliary pore under fully native conditions. Data analysis is on-going, but we could already obtain particle averages of several structures associated with the microtubule doublet (MTD) in the transition zone. We also found multiple examples of a ring in the apical end of the basal body, the apical centriolar ring (ACR), of which we also obtained a subtomogram average. In MTECs, IFT was much less abundant than in *C. reinhardtii*. Fibrous structures in the TZ were equally hard to see as in the *C. reinhardtii* tomograms, as opposed to what we expected to see from literature.

Future perspectives

Having an *in situ* look at the ciliary transition zone and IFT assembly has provided a great perspective on what this enigmatic region looks like. However, many new ideas popped up, and many open questions still remain.

Still to come

We're still analyzing the MTEC tomograms, and we have a multitude of ideas for the further handling of this dataset (see Section 6.4). We plan to further optimize subtomogram alignment, using different masks and parameters. Moreover, we plan to improve tomogram quality by using tilt refinement using WARP (55) and by applying 3D-CTF correction. We also want to extend our analysis to the basal bodies, and create an overarching map of the ciliary base in MTECs, similar to the work we've done on *C. reindhardtii*. Finally, we like to do a thorough search for IFT, which thus far has still remained elusive in MTECs. We plan to use localized template matching, using a priori information from our work on *C. reinhardtii*.

Overcoming the major limitation: finding molecular identities

As powerful as it might be, cryo-ET still has a major limitation: the lack of tools to tag *in situ* structures for recognition. For the assignment of molecular identities of observed densities, we therefore need to do knockout/-down studies of likely protein candidates, and see if said density disappears. This is true for the extra IFT-B associated density and the MTD sleeve in *Chlamydomonas*, as well as for most of the densities we observed in MTECs (ACR, MIP helix, TZ inter-MTD connectors). This should be done in collaboration with competent labs like the Centriole Lab (Paul Guichard & Virginie Hamel, University of Geneva) and the lab of Tim Stearns (University of Stanford).

Further outlook

Other open questions remain, which are currently being addressed by the field. First of all, an atomic-resolution model of IFT would greatly help improve our knowledge on how IFT functions, by showing how selective cargo binding works. Once it's known where certain ciliary components bind on the IFT train, the dynamics of cargo loading can be followed under different conditions. Moreover, this would allow better insight into IFT train dynamics, and a better understanding of which model of IFT regulation applies: the balance-point model, the differential cargo loading model, the diffusion-ruler model, or a combination of these.

It would also be useful to use cryo-ET to probe the ciliary base in other organisms, as these can differ significantly between species, and these differences could provide important insights into ciliary function.

One final idea is to further investigate how liquid-liquid phase-separated compartments function around the basal body/TZ complex. We know they're there, due to the absence of many macromolecular complexes such as ribosomes without the presence of a membrane. But how exactly these unique environments aid in ciliary function, TZ barrier maintenance, and recruiting IFT proteins and their cargoes, remains to be further investigated.

Table of figures

Abbreviations

(Cryo-)EM	(Cryo-) Electron Microscopy
(Cryo-)ET	(Cryo-) Electron Tomography
AAA+ ATPase	ATPase belonging to ATPases Associated with diverse cellular Activities
AB/AM	Antibiotic/Antimycotic
ACR	Apical Centriolar Ring
AD-PKD	Autosomal Dominant Polycystic Kidney Disease
ALI	Air-to-Liquid Interface
ALMS	Alström Syndrome
APS	Ammonium Persulfate
Arl13b	ADP Ribosylation factor-Like GTPase protein 13B
AR-PKD	Autosomal Recessive Polycystic Kidney Disease
ART	Algebraic Reconstruction Technique
ATP	Adenosyl Triphosphate
BB	Basal Body
BBS	Bardet-Biedl Syndrome
BBSome	Bardet-Biedl Syndrome-related protein complex
BM	Basic Medium
BPE	Bovine Pituitary Extract
BSA	Bovine Serum Albumin
BTEC(s)	Bovine Tracheal Epithelial Cell(s)
C2CD3	C2 Domain-Containing 3 Centriole Elongation Regulator protein
Cby1	Chibby1 protein
CC (score)	Cross-Correlation
CC-[…] (strain)	Chlamy Center- (Chlamydomonas Resource Center strain designator)
CCD	Charge-Coupled Device
CCDC[…]	Coiled-Coil Domain Containing protein […]
CEMOVIS	Cryo-Electron Microscopy Of Vitreous Sections
CEP[…]	Centrosomal Protein of […] kDa
CLEM	Correlative Light Electron Microscopy
CM (+/- RA)	Complete Medium (+/- Retinoic Acid)
CMOS	Complementary Metal-Oxide-Semiconductor
CNN	Convolutional Neural Network
COPI/II	Coat Protein 1 / 2
CP	Central Pair (of singlet microtubules)
CT	Cholera Toxin
CTF	Contrast Transfer Function
D1bLIC	Abbreviation of: Dynein 1b Light Intermediate Chain Preferred naming: Cytoplasmic dynein 2 light intermediate chain 1
DAPs	Distal Appendages, also known as Transitional Fibers or Alar Sheets
ddH_2O/diH_2O	Double distilled/deionized water
DED	Direct Electron Detector
DIP13	13-kDa Deflagellation-Inducible Protein
DMEM:F12	Dulbecco's Modified Eagle Medium / Ham’s Nutrient Mixture F-12
DQE	Detective/Detector Quantum Efficiency
EDTA	Ethylenediaminetetraacetic acid

EGF	Epidermal Growth Factor
EHD1	Eps15-Homology Domain containing protein 1
EM	Electron Microscopy
EMA	Electron Microprobe Analysis
EtOH	Ethanol
EvC	Ellis van Crefeld Syndrome
FAP67	Flagellar Associated Protein 67
FBF1	Fas Binding Factor 1
FBS	Fetal Bovine Serum
FIB(-SEM)	Focused Ion Beam (- Scanning Electron Microscope combination)
FRAP	Fluorescence Recovery After Photobleaching
FSC	Fourier Shell Correlation
Gamma-TuRC	γ-Tubulin Ring protein Complex
GFP	Green Fluorescent Protein
GIS	Gas Injection System
GTP/GDP	Guanosine Triphosphate / Diphosphate
HBSS	Hank's Balanced Salt Solution
HCl	Hydrogen Chloride; muriatic acid
HPF	High-Pressure Freezing
HYLS	Hydrolethalus Syndrome
IDA(s)	Inner Dynein Arm(s)
IFT	Intraflagellar Transport
IFT-[…]	Intraflagellar Transport protein […]
IgG	Immunoglobulin G
JATD	Jeune Asphyxiating Thoracic Dystrophy; Jeune Syndrome
JBTS	Joubert Syndrome
KAP	Kinesin-Associated Protein
KIF17	Kinesin-like protein KIF17
LCA	Leber's Congenital Amaurosis
LECA	Last Eukaryotic Common Ancestor
LM (1)	Light Microscopy
LM (2)	Low Magnification
LRRCC1	Leucine-Rich Repeat and Coiled-coil Centrosomal protein 1
MAP(s)	Microtubule-Associated Protein(s)
MCC(s)	Multiciliated Cell(s)
MCP	Microchannel Plate
MDCK-II	Madin-Darby Canine Kidney II cells
MIP(s)	Microtubule Inner Protein(s)
MKKS	McKusick-Kaufman Syndrome
MKS	Meckel-Gruber Syndrome
MKS[…]	Meckel-Gruber Syndrome protein […]
MTD	Microtubule Doublet
MTEC	Murine/Mouse Tracheal Epithelial Cell
MTOC	Microtubule-Organizing Center
MTT	Microtubule Triplet
MWS	Marden-Walker Syndrome
NA	Numerical Aperture

NA14	Nuclear Autoantigen 14
NaCl	Sodium Chloride
$NaHCO_3$	Sodium Bicarbonate
N-DRC	Nexin-Dynein Regulatory Complex
NMR	Nuclear Magnetic Resonance
NPHP	Nephronophthisis
NPHP-[…]	Nephrocystin-[…], Nephronophthisis-related protein […]
Nu (+/- RA)	(+/- Retinoic Acid)
NUP(s)	Nucleoporin protein(s)
ODA(s)	Outer Dynein Arm(s)
OFD	Orofaciodigital Syndrome
OFD[…]	Orofaciodigital syndrome-related protein […]
OMA	Oculomotor Apraxia
PALM	Photoactivation Localization Microscopy
PBS	Phosphate Buffered Saline (solution)
PBST	Phosphate Buffered Saline solution with 0.1% Tween-20 detergent
PCD	Primary Ciliary Dyskinesia; Kartagener Syndrome (not always)
PCM	Peri-Centriolar Matrix / Material
PLK-[…]	Polo-Like Kinase […]
PolyE	Poly-glutamate; poly-glutamylated
PTFE	Polytetrafluoroethylene; Teflon
RA	Retinoic Acid
RanGTP/GDP	Ras-related Nuclear protein bound to GTP/GDP
ROCK	p160-Rho-associated Coiled Kinase
RP	Retinitis Pigmentosa
RPGRIP1L	((RP GTPase Regulator)-Interacting Protein 1)-Like protein; NPHP8
RS	Radial Spokes
RT-TEM	Room-Temperature Transmission Electron Microscopy
SAS-6	Spindle Assembly Abnormal Protein 6
scFV	Single-Chain Fragment Variable
SCLT1	Sodium Channel and Clathrin Linker protein 1
SDS	Sodium Dodecyl Sulfate
SEM	Scanning Electron Microscope/Microscopy
SF (+/- RA)	Serum-Free Medium (+/- Retinoic Acid)
SFI1	Suppressor of Fermentation-Induced loss of stress resistance protein 1
SIRT	Simultaneous Iterative Reconstruction Technique
SLS	Senior-Løken Syndrome
SNT	Single Neurite Tracker
SOFA	Site Of Flagellar Autotomy
SPA	Single Particle Analysis
STED	Stimulated Emission Depletion
STEM	Scanning Transmission Electron Microscopy
STORM	Stochastic Optical Reconstruction Microscopy
TAILS	Tail Axoneme Intra-Lumenal Spiral
TAP	Tris-Acetate-Phosphate buffered medium
TCTN[…]	Tectin protein […]
TEM	Transmission Electron Microscope/Microscopy

TEMED	Tetramethylethylenediamine
TF(s)	Transitional Fiber(s), also known as Distal Appendages or Alar Sheets
Tris	Tris-(hydroxymethyl)aminomethane
TTBK2	Tau Tubulin Kinase 2
Tulp3	Tubby-Like Protein 3
TV	Television
TZ	(Ciliary) Transition Zone
U-ExM	Ultrastructure Expansion Microscopy
VPP	Volta Phase Plate
WBP	Weighted Back-Projection
WT	Wildtype
YFP	Yellow Fluorescent Protein
ZnS	Zinc Sulfide

Bibliography

1. Hoek H van den, Klena N, Jordan MA, Viar GA, Schaffer M, Erdmann PS, et al. In situ architecture of the ciliary base reveals the stepwise assembly of IFT trains [Internet]. 2021 Nov [cited 2021 Nov 23] p. 2021.10.17.464685. Available from: https://www.biorxiv.org/content/10.1101/2021.10.17.464685v2

2. Klena N, Le Guennec M, Tassin A-M, van den Hoek H, Erdmann PS, Schaffer M, et al. Architecture of the centriole cartwheel-containing region revealed by cryo-electron tomography. EMBO J. 2020 Nov 16;39(22):e106246.

3. Le Guennec M, Klena N, Gambarotto D, Laporte MH, Tassin A-M, van den Hoek H, et al. A helical inner scaffold provides a structural basis for centriole cohesion. Sci Adv. 2020 Feb;6(7):eaaz4137.

4. Leeuwenhoek A van. Observationes microscopicae Antonii Lewenhoeck, circa particulas liquorum globosa et animalia. Acta Erud. 1682;

5. Granite. The Rayleigh Criterion for Microscope Resolution [Internet]. Edinburgh Instruments. [cited 2021 Nov 3]. Available from: https://www.edinst.com/blog/the-rayleigh-criterion-for-microscope-resolution/

6. Williams DB, Carter CB. Transmission electron microscopy: a textbook for materials science. 2nd ed. New York: Springer; 2008. 4 p.

7. Bäuerlein F. In Situ Architecture and Cellular Interactions of PolyQ Inclusions. 2018.

8. Arfan. How To Make An Electron Beam [Internet]. New Images Beam. 2018 [cited 2021 Nov 19]. Available from: http://www.enhancestyleteam.com/how-to-make-an-electron-beam/

9. Kochovski Z. Image analysis of molecular complexes present in cryo-tomograms of neuronal synapses [PhD thesis]. [Martinsried, Bayern, Deutschland]; 2014.

10. sfmb4e_0237.jpg (1027×967) [Internet]. [cited 2021 Nov 23]. Available from: https://digital.wwnorton.com/ebooks/epub/microbio4/OEBPS/images/sfmb4e_0237.jpg

11. Fukuda Y, Laugks U, Lučić V, Baumeister W, Danev R. Electron cryotomography of vitrified cells with a Volta phase plate. J Struct Biol. 2015 May;190(2):143–54.

12. Khoshouei M, Pfeffer S, Baumeister W, Förster F, Danev R. Subtomogram analysis using the Volta phase plate. J Struct Biol. 2017 Feb;197(2):94–101.

13. Danev R, Belousoff M, Liang Y-L, Zhang X, Eisenstein F, Wootten D, et al. Routine sub-2.5 Å cryo-EM structure determination of GPCRs. Nat Commun. 2021 Jul 15;12(1):4333.

14. Reimer L, Kohl H. Transmission electron microscopy: physics of image formation. 5th ed. New York, NY: Springer; 2008. (Springer series in optical sciences).

15. Ruskin RS, Yu Z, Grigorieff N. Quantitative characterization of electron detectors for transmission electron microscopy. J Struct Biol [Internet]. 2013 Dec [cited 2021 Nov 20];184(3). Available from: https://www.ncbi.nlm.nih.gov/sites/ppmc/articles/PMC3876735/

16. McMullan G, Faruqi AR, Henderson R, Guerrini N, Turchetta R, Jacobs A, et al. Experimental observation of the improvement in MTF from backthinning a CMOS direct electron detector. Ultramicroscopy. 2009 Aug;109(9):1144–7.

17. DE-Series – Direct Electron [Internet]. [cited 2021 Nov 23]. Available from: https://www.directelectron.com/de-series/

18. Grünewald K, Medalia O, Gross A, Steven AC, Baumeister W. Prospects of electron cryotomography to visualize macromolecular complexes inside cellular compartments: implications of crowding. Biophys Chem. 2002 Dec 1;100(1):577–91.

19. Grant T, Grigorieff N. Measuring the optimal exposure for single particle cryo-EM using a 2.6 Å reconstruction of rotavirus VP6. Sundquist WI, editor. eLife. 2015 May 29;4:e06980.

20. Fromm SA, Bharat TAM, Jakobi AJ, Hagen WJH, Sachse C. Seeing tobacco mosaic virus through direct electron detectors. J Struct Biol. 2015 Feb 1;189(2):87–97.

21. Liu Y-T, Zhang H, Wang H, Tao C-L, Bi G-Q, Zhou ZH. Isotropic Reconstruction of Electron Tomograms with Deep Learning [Internet]. 2021 Jul [cited 2021 Nov 19] p. 2021.07.17.452128. Available from: https://www.biorxiv.org/content/10.1101/2021.07.17.452128v1

22. Ding G, Liu Y, Zhang R, Xin HL. A joint deep learning model to recover information and reduce artifacts in missing-wedge sinograms for electron tomography and beyond. Sci Rep. 2019 Sep 5;9(1):12803.

23. Hagen WJH, Wan W, Briggs JAG. Implementation of a cryo-electron tomography tilt-scheme optimized for high resolution subtomogram averaging. J Struct Biol. 2017 Feb;197(2):191–8.

24. Wan W, Briggs JAG. Chapter Thirteen - Cryo-Electron Tomography and Subtomogram Averaging. In: Crowther RA, editor. Methods in Enzymology [Internet]. Academic Press; 2016 [cited 2021 Nov 21]. p. 329–67. (The Resolution Revolution: Recent Advances In cryoEM; vol. 579). Available from: https://www.sciencedirect.com/science/article/pii/S0076687916300325

25. Al-Amoudi A, Chang J-J, Leforestier A, McDowall A, Salamin LM, Norlén LPO, et al. Cryo-electron microscopy of vitreous sections. EMBO J. 2004 Sep 15;23(18):3583–8.

26. Al-Amoudi A, Díez DC, Betts MJ, Frangakis AS. The molecular architecture of cadherins in native epidermal desmosomes. Nature. 2007 Dec;450(7171):832–7.

27. Marko M, Hsieh C, Moberlychan W, Mannella CA, Frank J. Focused ion beam milling of vitreous water: prospects for an alternative to cryo-ultramicrotomy of frozen-hydrated biological samples. J Microsc. 2006 Apr;222(Pt 1):42–7.

28. Schaffer M, Engel BD, Laugks T, Mahamid J, Plitzko JM, Baumeister W. Cryo-focused Ion Beam Sample Preparation for Imaging Vitreous Cells by Cryo-electron Tomography. Bio-Protoc. 2015 Sep 5;5(17):e1575.

29. Schaffer M, Mahamid J, Engel BD, Laugks T, Baumeister W, Plitzko JM. Optimized cryo-focused ion beam sample preparation aimed at in situ structural studies of membrane proteins. J Struct Biol. 2017 Feb 1;197(2):73–82.

30. Engel BD, Schaffer M, Albert S, Asano S, Plitzko JM, Baumeister W. In situ structural analysis of Golgi intracisternal protein arrays. Proc Natl Acad Sci U S A. 2015 Sep 8;112(36):11264–9.

31. Engel BD, Schaffer M, Kuhn Cuellar L, Villa E, Plitzko JM, Baumeister W. Native architecture of the Chlamydomonas chloroplast revealed by in situ cryo-electron tomography. eLife. 4:e04889.

32. Albert S, Schaffer M, Beck F, Mosalaganti S, Asano S, Thomas HF, et al. Proteasomes tether to two distinct sites at the nuclear pore complex. Proc Natl Acad Sci U S A. 2017 Dec 26;114(52):13726–31.

33. Bykov YS, Schaffer M, Dodonova SO, Albert S, Plitzko JM, Baumeister W, et al. The structure of the COPI coat determined within the cell. eLife. 6:e32493.

34. Asano S, Engel BD, Baumeister W. In Situ Cryo-Electron Tomography: A Post-Reductionist Approach to Structural Biology. J Mol Biol. 2016;428(2):332–43.

35. Kuba J, Mitchels J, Hovorka M, Erdmann P, Berka L, Kirmse R, et al. Advanced cryo-tomography workflow developments – correlative microscopy, milling automation and cryo-lift-out. J Microsc. 2021;281(2):112–24.

36. Wolff G, Limpens RWAL, Zheng S, Snijder EJ, Agard DA, Koster AJ, et al. Mind the gap: Micro-expansion joints drastically decrease the bending of FIB-milled cryo-lamellae. J Struct Biol. 2019 Dec 1;208(3):107389.

37. Villa E, Schaffer M, Plitzko JM, Baumeister W. Opening windows into the cell: focused-ion-beam milling for cryo-electron tomography. Curr Opin Struct Biol. 2013 Oct 1;23(5):771–7.

38. Rigort A, Bäuerlein FJB, Villa E, Eibauer M, Laugks T, Baumeister W, et al. Focused ion beam micromachining of eukaryotic cells for cryoelectron tomography. Proc Natl Acad Sci U S A. 2012 Mar 20;109(12):4449–54.

39. Schaffer M, Pfeffer S, Mahamid J, Kleindiek S, Laugks T, Albert S, et al. A cryo-FIB lift-out technique enables molecular-resolution cryo-ET within native Caenorhabditis elegans tissue. Nat Methods. 2019 Aug;16(8):757–62.

40. Zheng SQ, Palovcak E, Armache J-P, Verba KA, Cheng Y, Agard DA. MotionCor2: anisotropic correction of beam-induced motion for improved cryo-electron microscopy. Nat Methods. 2017 Apr;14(4):331–2.

41. Wan W. williamnwan/STOPGAP [Internet]. 2021 [cited 2021 Nov 28]. Available from: https://github.com/williamnwan/STOPGAP

42. Kremer JR, Mastronarde DN, McIntosh JR. Computer visualization of three-dimensional image data using IMOD. J Struct Biol. 1996 Feb;116(1):71–6.

43. Castaño-Díez D, Kudryashev M, Arheit M, Stahlberg H. Dynamo: a flexible, user-friendly development tool for subtomogram averaging of cryo-EM data in high-performance computing environments. J Struct Biol. 2012 May;178(2):139–51.

44. Costa TRD, Ignatiou A, Orlova EV. Structural Analysis of Protein Complexes by Cryo Electron Microscopy. Methods Mol Biol Clifton NJ. 2017;1615:377–413.

45. Turoňová B, Schur FKM, Wan W, Briggs JAG. Efficient 3D-CTF correction for cryo-electron tomography using NovaCTF improves subtomogram averaging resolution to 3.4 Å. J Struct Biol. 2017;199(3):187–95.

46. Lehtinen J, Munkberg J, Hasselgren J, Laine S, Karras T, Aittala M, et al. Noise2Noise: Learning Image Restoration without Clean Data. ArXiv180304189 Cs Stat [Internet]. 2018 Oct 29 [cited 2021 Dec 3]; Available from: http://arxiv.org/abs/1803.04189

47. Buchholz T-O, Jordan M, Pigino G, Jug F. Cryo-CARE: Content-Aware Image Restoration for Cryo-Transmission Electron Microscopy Data. ArXiv181005420 Cs [Internet]. 2018 Oct 15 [cited 2021 Oct 7]; Available from: http://arxiv.org/abs/1810.05420

48. Pettersen EF, Goddard TD, Huang CC, Couch GS, Greenblatt DM, Meng EC, et al. UCSF Chimera--a visualization system for exploratory research and analysis. J Comput Chem. 2004 Oct;25(13):1605–12.

49. Moebel E, Martinez-Sanchez A, Lamm L, Righetto RD, Wietrzynski W, Albert S, et al. Deep learning improves macromolecule identification in 3D cellular cryo-electron tomograms. Nat Methods. 2021 Nov;18(11):1386–94.

50. Freeman Rosenzweig ES, Xu B, Kuhn Cuellar L, Martinez-Sanchez A, Schaffer M, Strauss M, et al. The Eukaryotic CO2-Concentrating Organelle Is Liquid-like and Exhibits Dynamic Reorganization. Cell. 2017 Sep 21;171(1):148-162.e19.

51. Albert S, Wietrzynski W, Lee C-W, Schaffer M, Beck F, Schuller JM, et al. Direct visualization of degradation microcompartments at the ER membrane. Proc Natl Acad Sci U S A. 2020 Jan 14;117(2):1069–80.

52. Collado J, Kalemanov M, Campelo F, Bourgoint C, Thomas F, Loewith R, et al. Tricalbin-Mediated Contact Sites Control ER Curvature to Maintain Plasma Membrane Integrity. Dev Cell. 2019 Nov 18;51(4):476-487.e7.

53. Tegunov D, Xue L, Dienemann C, Cramer P, Mahamid J. Multi-particle cryo-EM refinement with M visualizes ribosome-antibiotic complex at 3.5 Å in cells. Nat Methods. 2021 Feb;18(2):186–93.

54. Himes BA, Zhang P. emClarity: software for high-resolution cryo-electron tomography and subtomogram averaging. Nat Methods. 2018 Nov;15(11):955–61.

55. Tegunov D, Cramer P. Real-time cryo-electron microscopy data preprocessing with Warp. Nat Methods. 2019 Nov;16(11):1146–52.

56. Nachury MV, Mick DU. Establishing and regulating the composition of cilia for signal transduction. Nat Rev Mol Cell Biol. 2019 Jul;20(7):389–405.

57. Mitchell DR. Evolution of Cilia. Cold Spring Harb Perspect Biol. 2017 Jan 3;9(1):a028290.

58. Mitchison HM, Valente EM. Motile and non-motile cilia in human pathology: from function to phenotypes. J Pathol. 2017 Jan 1;241(2):294–309.

59. Hildebrandt F, Benzing T, Katsanis N. Ciliopathies. N Engl J Med. 2011 Apr 21;364(16):1533–43.

60. Badano JL, Mitsuma N, Beales PL, Katsanis N. The ciliopathies: an emerging class of human genetic disorders. Annu Rev Genomics Hum Genet. 2006;7:125–48.

61. Wheway G, Genomics England Research Consortium, Mitchison HM, Ambrose JC, Baple EL, Bleda M, et al. Opportunities and Challenges for Molecular Understanding of Ciliopathies–The 100,000 Genomes Project. Front Genet. 2019;10:127.

62. Hu Q, Milenkovic L, Jin H, Scott MP, Nachury MV, Spiliotis ET, et al. A septin diffusion barrier at the base of the primary cilium maintains ciliary membrane protein distribution. Science. 2010 Jul 23;329(5990):436–9.

63. Kee HL, Dishinger JF, Lynne Blasius T, Liu C-J, Margolis B, Verhey KJ. A size-exclusion permeability barrier and nucleoporins characterize a ciliary pore complex that regulates transport into cilia. Nat Cell Biol. 2012;14(4):431–7.

64. Breslow DK, Koslover EF, Seydel F, Spakowitz AJ, Nachury MV. An in vitro assay for entry into cilia reveals unique properties of the soluble diffusion barrier. J Cell Biol. 2013;203(1):129–47.

65. Omran H. NPHP proteins: gatekeepers of the ciliary compartment. J Cell Biol. 2010 Sep 6;190(5):715–7.

66. Barker AR, Thomas R, Dawe HR. Meckel-Gruber syndrome and the role of primary cilia in kidney, skeleton, and central nervous system development. Organogenesis. 2014 Jan 1;10(1):96–107.

67. Praveen K, Davis EE, Katsanis N. Unique among ciliopathies: primary ciliary dyskinesia, a motile cilia disorder. F1000prime Rep. 2015;7:36.

68. Ma M, Stoyanova M, Rademacher G, Dutcher SK, Brown A, Zhang R. Structure of the decorated ciliary doublet microtubule. Cell. 2019 Oct 31;179(4):909-922.e12.

69. Ichikawa M, Khalifa AAZ, Kubo S, Dai D, Basu K, Maghrebi MAF, et al. Tubulin lattice in cilia is in a stressed form regulated by microtubule inner proteins. Proc Natl Acad Sci U S A. 2019 Oct 1;116(40):19930–8.

70. Craddock TJA, Hameroff SR, Ayoub AT, Klobukowski M, Tuszynski JA. Anesthetics act in quantum channels in brain microtubules to prevent consciousness. Curr Top Med Chem. 2015;15(6):523–33.

71. Nonaka S, Shiratori H, Saijoh Y, Hamada H. Determination of left-right patterning of the mouse embryo by artificial nodal flow. Nature. 2002 Jul 4;418(6893):96–9.

72. Nonaka S, Tanaka Y, Okada Y, Takeda S, Harada A, Kanai Y, et al. Randomization of left-right asymmetry due to loss of nodal cilia generating leftward flow of extraembryonic fluid in mice lacking KIF3B motor protein. Cell. 1998 Dec 11;95(6):829–37.

73. Heuser T, Raytchev M, Krell J, Porter ME, Nicastro D. The dynein regulatory complex is the nexin link and a major regulatory node in cilia and flagella. J Cell Biol. 2009;187(6):921–33.

74. Ishikawa T. Cryo-electron tomography of motile cilia and flagella. Cilia. 2015;4(1):3.

75. Bui KH, Ishikawa T. 3D structural analysis of flagella/cilia by cryo-electron tomography. In: Methods in Enzymology. Academic Press Inc.; 2013. p. 305–23.

76. Bui KH, Sakakibara H, Movassagh T, Oiwa K, Ishikawa T. Asymmetry of inner dynein arms and inter-doublet links in Chlamydomonas flagella. J Cell Biol. 2009 Aug 10;186(3):437–46.

77. Bui KH, Yagi T, Yamamoto R, Kamiya R, Ishikawa T. Polarity and asymmetry in the arrangement of dynein and related structures in the Chlamydomonas axoneme. J Cell Biol. 2012 Sep 3;198(5):913–25.

78. Dutcher SK. Asymmetries in the cilia of Chlamydomonas. Philos Trans R Soc B Biol Sci. 2020 Feb 17;375(1792):20190153.

79. Kiesel P, Alvarez Viar G, Tsoy N, Maraspini R, Gorilak P, Varga V, et al. The molecular structure of mammalian primary cilia revealed by cryo-electron tomography. Nat Struct Mol Biol. 2020 Dec;27(12):1115–24.

80. Garcia G, Reiter J. A primer on the mouse basal body. Cilia. 2016;

81. Wilsman NJ, Farnum CE, Reed-Aksamit DK. Incidence and morphology of equine and murine chondrocytic cilia. Anat Rec. 1980;197(3):355–61.

82. Webber WA, Lee J. Fine structure of mammalian renal cilia. Anat Rec. 1975 Jul;182(3):339–43.

83. Ito D, Bettencourt-Dias M. Centrosome Remodelling in Evolution. Cells. 2018;7(7):71.

84. Godinho SA, Pellman D. Causes and consequences of centrosome abnormalities in cancer. Philos Trans R Soc Lond B Biol Sci. 2014 Sep 5;369(1650):20130467.

85. Nievergelt AP, Banterle N, Andany SH, Gönczy P, Fantner GE. High-speed photothermal off-resonance atomic force microscopy reveals assembly routes of centriolar scaffold protein SAS-6. Nat Nanotechnol. 2018;13(8):696–701.

86. Guichard P, Hamel V, Gönczy P. The Rise of the Cartwheel: Seeding the Centriole Organelle. BioEssays. 2018;40(4):1700241.

87. Al Jord A, Lemaître A-I, Delgehyr N, Faucourt M, Spassky N, Meunier A. Centriole amplification by mother and daughter centrioles differs in multiciliated cells. Nature. 2014;516(7529).

88. Mercey O, Levine MS, LoMastro GM, Rostaing P, Brotslaw E, Gomez V, et al. Massive centriole production can occur in the absence of deuterosomes in multiciliated cells. Nat Cell Biol. 2019 Dec;21(12):1544–52.

89. CentrosomNumbFig2.png (605×500) [Internet]. [cited 2021 Dec 1]. Available from: http://atlasgeneticsoncology.org/Deep/Images/CentrosomNumbFig2.png

90. Czarnecki PG, Shah JV. The ciliary transition zone: from morphology and molecules to medicine. Trends Cell Biol. 2012 Apr 1;22(4):201–10.

91. Tony Yang T, Su J, Wang W-J, Craige B, Witman GB, Bryan Tsou M-F, et al. Superresolution Pattern Recognition Reveals the Architectural Map of the Ciliary Transition Zone. Sci Rep. 2015 Sep 14;5(1):14096.

92. Garcia-Gonzalo FR, Reiter JF. Open Sesame: How Transition Fibers and the Transition Zone Control Ciliary Composition. Cold Spring Harb Perspect Biol. 2017 Jan 2;9(2):a028134.

93. Dutcher SK, O'Toole ET. The basal bodies of Chlamydomonas reinhardtii. Cilia. 2016 Jun 1;5(1):18.

94. Satir P, Christensen ST. Overview of structure and function of mammalian cilia. Annu Rev Physiol. 2007;69:377–400.

95. Woodruff JB, Ferreira Gomes B, Widlund PO, Mahamid J, Honigmann A, Hyman AA. The Centrosome Is a Selective Condensate that Nucleates Microtubules by Concentrating Tubulin. Cell. 2017 Jun 1;169(6):1066-1077.e10.

96. The material state of centrosomes: lattice, liquid, or gel? - ScienceDirect [Internet]. [cited 2021 Nov 17]. Available from: https://www.sciencedirect.com/science/article/pii/S0959440X20301640?via%3Dihub

97. Mittasch M, Tran VM, Rios MU, Fritsch AW, Enos SJ, Ferreira Gomes B, et al. Regulated changes in material properties underlie centrosome disassembly during mitotic exit. J Cell Biol. 2020 Feb 12;219(4):e201912036.

98. Stepanek L, Pigino G, Rosenbaum JL, Witman GB, Kozminski KG, Johnson KA, et al. Microtubule doublets are double-track railways for intraflagellar transport trains. Science. 2016;352(6286):721–4.

99. van Dam TJP, Townsend MJ, Turk M, Schlessinger A, Sali A, Field MC, et al. Evolution of modular intraflagellar transport from a coatomer-like progenitor. Proc Natl Acad Sci. 2013;110(17):6943–8.

100. Taschner M, Lorentzen E. The intraflagellar transport machinery. Cold Spring Harb Perspect Biol. 2016 Oct 1;8(10).

101. Jordan MA, Diener DR, Stepanek L, Pigino G. The cryo-EM structure of intraflagellar transport trains reveals how dynein is inactivated to ensure unidirectional anterograde movement in cilia. Nat Cell Biol. 2018 Nov;20(11):1250–5.

102. Wingfield JL, Mengoni I, Bomberger H, Jiang Y-Y, Walsh JD, Brown JM, et al. IFT trains in different stages of assembly queue at the ciliary base for consecutive release into the cilium. eLife. 2017 May 31;6:e26609.

103. Engel BD, Ludington WB, Marshall WF. Intraflagellar transport particle size scales inversely with flagellar length: revisiting the balance-point length control model. J Cell Biol. 2009 Oct 5;187(1):81–9.

104. Iomini C, Babaev-Khaimov V, Sassaroli M, Piperno G. Protein particles in Chlamydomonas flagella undergo a transport cycle consisting of four phases. J Cell Biol. 2001 Apr 2;153(1):13–24.

105. Ludington WB, Wemmer KA, Lechtreck KF, Witman GB, Marshall WF. Avalanche-like behavior in ciliary import. Proc Natl Acad Sci U S A. 2013 Mar 5;110(10):3925–30.

106. Ishikawa H, Marshall WF. Testing the time-of-flight model for flagellar length sensing. Mol Biol Cell. 2017 Nov 7;28(23):3447–56.

107. Hendel NL, Thomson M, Marshall WF. Diffusion as a Ruler: Modeling Kinesin Diffusion as a Length Sensor for Intraflagellar Transport. Biophys J. 2018 Feb 6;114(3):663–74.

108. Chien A, Shih SM, Bower R, Tritschler D, Porter ME, Yildiz A. Dynamics of the IFT machinery at the ciliary tip. eLife. 2017 Sep 20;6.

109. Chou H-T, Apelt L, Farrell DP, White SR, Woodsmith J, Svetlov V, et al. The Molecular Architecture of Native BBSome Obtained by an Integrated Structural Approach. Structure. 2019 Sep 3;27(9):1384-1394.e4.

110. Singh SK, Gui M, Koh F, Yip MC, Brown A. Structure and activation mechanism of the BBSome membrane protein trafficking complex. eLife. 2020 Jan 15;9:e53322.

111. Klink BU, Gatsogiannis C, Hofnagel O, Wittinghofer A, Raunser S. Structure of the human BBSome core complex. eLife. 2020 Jan 17;9:e53910.

112. Yang S, Bahl K, Chou H-T, Woodsmith J, Stelzl U, Walz T, et al. Near-atomic structures of the BBSome reveal the basis for BBSome activation and binding to GPCR cargoes. Carter AP, Akhmanova A, Lorentzen E, editors. eLife. 2020 Jun 8;9:e55954.

113. Dishinger JF, Kee HL, Jenkins PM, Fan S, Hurd TW, Hammond JW, et al. Ciliary entry of the kinesin-2 motor KIF17 is regulated by importin-β2 and RanGTP. Nat Cell Biol. 2010 Jul;12(7):703–10.

114. Ström A, Weis K. Importin-beta-like nuclear transport receptors. Genome Biol. 2001;

115. Garcia-Gonzalo FR, Reiter JF. Scoring a backstage pass: Mechanisms of ciliogenesis and ciliary access. J Cell Biol. 2012;197(6):697–709.

116. Sung C-H, Li A. Ciliary resorption modulates G1 length and cell cycle progression. Cell Cycle. 2011 Sep 1;10(17):2825–6.

117. Hartzell LB, Hartzell HC, Quarmby LM. Mechanisms of Flagellar Excision: I. The Role of Intracellular Acidification. Exp Cell Res. 1993 Sep 1;208(1):148–53.

118. Sanders MA, Salisbury JL. Centrin plays an essential role in microtubule severing during flagellar excision in Chlamydomonas reinhardtii. J Cell Biol. 1994;124(5):795–805.

119. Sanders MA, Salisbury JL. Centrin-mediated microtubule severing during flagellar excision in Chlamydomonas reinhardtii. J Cell Biol. 1989;108(5):1751–60.

120. Lohret TA, McNally FJ, Quarmby LM. A Role for Katanin-mediated Axonemal Severing during Chlamydomonas Deflagellation. Mol Biol Cell. 1998;9(5):1195–207.

121. Horani A, Nath A, Wasserman MG, Huang T, Brody SL. Rho-associated protein kinase inhibition enhances airway epithelial Basal-cell proliferation and lentivirus transduction. Am J Respir Cell Mol Biol. 2013 Sep;49(3):341–7.

122. Harris EH. 12 - Procedures and Resources. In: Harris EH, editor. The Chlamydomonas Sourcebook [Internet]. San Diego: Academic Press; 1989 [cited 2021 Nov 30]. p. 575–641. Available from: https://www.sciencedirect.com/science/article/pii/B9780123268808500171

123. Umen JG, Goodenough UW. Control of cell division by a retinoblastoma protein homolog in Chlamydomonas. Genes Dev. 2001 Jul 1;15(13):1652–61.

124. Li X, Zhang R, Patena W, Gang SS, Blum SR, Ivanova N, et al. An Indexed, Mapped Mutant Library Enables Reverse Genetics Studies of Biological Processes in Chlamydomonas reinhardtii. Plant Cell. 2016 Feb;28(2):367–87.

125. Lv B, Wan L, Taschner M, Cheng X, Lorentzen E, Huang K. Intraflagellar transport protein IFT52 recruits IFT46 to the basal body and flagella. J Cell Sci. 2017 May 1;130(9):1662–74.

126. Mueller J, Perrone CA, Bower R, Cole DG, Porter ME. The FLA3 KAP subunit is required for localization of kinesin-2 to the site of flagellar assembly and processive anterograde intraflagellar transport. Mol Biol Cell. 2005 Mar;16(3):1341–54.

127. Engel BD, Lechtreck K-F, Sakai T, Ikebe M, Witman GB, Marshall WF. Total internal reflection fluorescence (TIRF) microscopy of Chlamydomonas flagella. Methods Cell Biol. 2009;93:157–77.

128. Reck J, Schauer AM, VanderWaal Mills K, Bower R, Tritschler D, Perrone CA, et al. The role of the dynein light intermediate chain in retrograde IFT and flagellar function in Chlamydomonas. Mol Biol Cell. 2016 Aug 1;27(15):2404–22.

129. Higginbotham H, Bielas S, Tanaka T, Gleeson JG. Transgenic mouse line with green-fluorescent protein-labeled Centrin 2 allows visualization of the centrosome in living cells. Transgenic Res. 2004 Apr;13(2):155–64.

130. Mastronarde DN. Automated electron microscope tomography using robust prediction of specimen movements. J Struct Biol. 2005 Oct;152(1):36–51.

131. Zhang K. Gctf: Real-time CTF determination and correction. J Struct Biol. 2016 Jan;193(1):1–12.

132. Rohou A, Grigorieff N. CTFFIND4: Fast and accurate defocus estimation from electron micrographs. J Struct Biol. 2015 Nov;192(2):216–21.

133. Chen S, McMullan G, Faruqi AR, Murshudov GN, Short JM, Scheres SHW, et al. High-resolution noise substitution to measure overfitting and validate resolution in 3D structure determination by single particle electron cryomicroscopy. Ultramicroscopy. 2013 Dec;135:24–35.

134. Nickell S, Förster F, Linaroudis A, Net WD, Beck F, Hegerl R, et al. TOM software toolbox: acquisition and analysis for electron tomography. J Struct Biol. 2005 Mar;149(3):227–34.

135. Goddard TD, Huang CC, Meng EC, Pettersen EF, Couch GS, Morris JH, et al. UCSF ChimeraX: Meeting modern challenges in visualization and analysis. Protein Sci Publ Protein Soc. 2018 Jan;27(1):14–25.

136. Gambarotto D, Zwettler FU, Le Guennec M, Schmidt-Cernohorska M, Fortun D, Borgers S, et al. Imaging cellular ultrastructures using expansion microscopy (U-ExM). Nat Methods. 2019 Jan;16(1):71–4.

137. Nizak C, Martin-Lluesma S, Moutel S, Roux A, Kreis TE, Goud B, et al. Recombinant antibodies against subcellular fractions used to track endogenous Golgi protein dynamics in vivo. Traffic Cph Den. 2003 Nov;4(11):739–53.

138. Schindelin J, Arganda-Carreras I, Frise E, Kaynig V, Longair M, Pietzsch T, et al. Fiji: an open-source platform for biological-image analysis. Nat Methods. 2012 Jun 28;9(7):676–82.

139. Arshadi C, Günther U, Eddison M, Harrington KIS, Ferreira TA. SNT: a unifying toolbox for quantification of neuronal anatomy. Nat Methods. 2021 Apr;18(4):374–7.

140. Geimer S, Melkonian M. The ultrastructure of the Chlamydomonas reinhardtii basal apparatus: identification of an early marker of radial asymmetry inherent in the basal body. J Cell Sci. 2004 Jun 1;117(13):2663–74.

141. Quarmby LM. Chapter 3 - Deflagellation. In: Harris EH, Stern DB, Witman GB, editors. The Chlamydomonas Sourcebook (Second Edition) [Internet]. London: Academic Press; 2009 [cited 2021 Oct 14]. p. 43–69. Available from: https://www.sciencedirect.com/science/article/pii/B978012370873100040X

142. Bui KH, Yagi T, Yamamoto R, Kamiya R, Ishikawa T. Polarity and asymmetry in the arrangement of dynein and related structures in the Chlamydomonas axoneme. J Cell Biol. 2012 Sep 3;198(5):913–25.

143. Cole DG, Diener DR, Himelblau AL, Beech PL, Fuster JC, Rosenbaum JL. Chlamydomonas kinesin-II-dependent intraflagellar transport (IFT): IFT particles contain proteins required for ciliary assembly in Caenorhabditis elegans sensory neurons. J Cell Biol. 1998 May 18;141(4):993–1008.

144. Hou Y, Qin H, Follit JA, Pazour GJ, Rosenbaum JL, Witman GB. Functional analysis of an individual IFT protein: IFT46 is required for transport of outer dynein arms into flagella. J Cell Biol. 2007 Feb 26;176(5):653–65.

145. Toropova K, Zalyte R, Mukhopadhyay AG, Mladenov M, Carter AP, Roberts AJ. Structure of the dynein-2 complex and its assembly with intraflagellar transport trains. Nat Struct Mol Biol. 2019 Sep 1;26(9):823–9.

146. Jordan MA, Pigino G. The structural basis of intraflagellar transport at a glance. J Cell Sci. 2021 Jun 15;134(12):jcs247163.

147. Hibbard JVK, Vazquez N, Satija R, Wallingford JB. Protein turnover dynamics suggest a diffusion-to-capture mechanism for peri-basal body recruitment and retention of intraflagellar transport proteins. Mol Biol Cell. 2021 Jun 1;32(12):1171–80.

148. Hazime KS, Zhou Z, Joachimiak E, Bulgakova NA, Wloga D, Malicki JJ. STORM imaging reveals the spatial arrangement of transition zone components and IFT particles at the ciliary base in Tetrahymena. Sci Rep. 2021 Apr 12;11(1):7899.

149. Johnson KA, Haas MA, Rosenbaum JL. Localization of a kinesin-related protein to the central pair apparatus of the Chlamydomonas reinhardtii flagellum. J Cell Sci. 1994 Jun;107 (Pt 6):1551–6.

150. Fu G, Zhao L, Dymek E, Hou Y, Song K, Phan N, et al. Structural organization of the C1a-e-c supercomplex within the ciliary central apparatus. J Cell Biol. 2019 Dec 2;218(12):4236–51.

151. Luo W, Ruba A, Takao D, Zweifel LP, Lim RYH, Verhey KJ, et al. Axonemal Lumen Dominates Cytosolic Protein Diffusion inside the Primary Cilium. Sci Rep. 2017 Nov 17;7(1):15793.

152. Anderson RG. The three-dimensional structure of the basal body from the rhesus monkey oviduct. J Cell Biol. 1972 Aug;54(2):246–65.

153. Zabeo D, Heumann JM, Schwartz CL, Suzuki-Shinjo A, Morgan G, Widlund PO, et al. A lumenal interrupted helix in human sperm tail microtubules. Sci Rep. 2018 Feb 9;8(1):2727.

154. Greenan GA, Vale RD, Agard DA. Electron cryotomography of intact motile cilia defines the basal body to axoneme transition. J Cell Biol. 2020 Jan 6;219(1):e201907060.

155. Doerner JF, Delling M, Clapham DE. Ion channels and calcium signaling in motile cilia. eLife. 2015 Dec 9;4:e11066.

156. Thauvin-Robinet C, Lee JS, Lopez E, Herranz-Pérez V, Shida T, Franco B, et al. The oral-facial-digital syndrome gene C2CD3 encodes a positive regulator of centriole elongation. Nat Genet. 2014 Aug;46(8):905–11.

157. Ye X, Zeng H, Ning G, Reiter JF, Liu A. C2cd3 is critical for centriolar distal appendage assembly and ciliary vesicle docking in mammals. Proc Natl Acad Sci U S A. 2014 Feb 11;111(6):2164–9.

158. Hoover AN, Wynkoop A, Zeng H, Jia J, Niswander LA, Liu A. C2cd3 is required for cilia formation and Hedgehog signaling in mouse. Dev Camb Engl. 2008 Dec;135(24):4049–58.

159. Jumper J, Evans R, Pritzel A, Green T, Figurnov M, Ronneberger O, et al. Highly accurate protein structure prediction with AlphaFold. Nature. 2021 Aug;596(7873):583–9.

160. Gaudin N, Gil PM, Boumendjel M, Ershov D, Pioche-Durieu C, Bouix M, et al. Evolutionary conservation of centriole rotational asymmetry in the human centrosome [Internet]. Cell Biology; 2021 Jul [cited 2021 Nov 17]. Available from: http://biorxiv.org/lookup/doi/10.1101/2021.07.21.453218

161. Bouhlel IB, Laporte MH, Bertiaux E, Giroud A, Borgers S, Azimzadeh J, et al. SFI1 and centrin form a distal end complex critical for proper centriole architecture and ciliogenesis [Internet]. 2021 Oct [cited 2021 Oct 23] p. 2021.10.05.463184. Available from: https://www.biorxiv.org/content/10.1101/2021.10.05.463184v1

162. Kilmartin JV. Sfi1p has conserved centrin-binding sites and an essential function in budding yeast spindle pole body duplication. J Cell Biol. 2003 Sep 29;162(7):1211–21.

163. Geimer S, Melkonian M. Centrin scaffold in Chlamydomonas reinhardtii revealed by immunoelectron microscopy. Eukaryot Cell. 2005 Jul;4(7):1253–63.

164. CAVALIER-SMITH T. Basal Body and Flagellar Development During the Vegetative Cell Cycle and the Sexual Cycle of Chlamydomonas Reinhardii. J Cell Sci. 1974 Dec 1;16(3):529–56.

165. Diener DR, Lupetti P, Rosenbaum JL. Proteomic Analysis of Isolated Ciliary Transition Zones Reveals the Presence of ESCRT Proteins. Curr Biol. 2015 Feb;25(3):379–84.

166. Mosalaganti S, Kosinski J, Albert S, Schaffer M, Strenkert D, Salomé PA, et al. In situ architecture of the algal nuclear pore complex. Nat Commun. 2018 Jun 18;9(1):2361.

167. Kee HL, Verhey KJ. Molecular connections between nuclear and ciliary import processes. Cilia. 2013;2(1):11.

168. Goodenough UW, Levine RP. Chloroplast Ultrastructure in Mutant Strains of Chlamydomonas reinhardi Lacking Components of the Photosynthetic Apparatus. Plant Physiol. 1969 Jul;44(7):990–1000.

169. Ohad I, Siekevitz P, Palade GE. Biogenesis of chloroplast membranes. I. Plastid dedifferentiation in a dark-grown algal mutant (Chlamydomonas reinhardi). J Cell Biol. 1967 Dec;35(3):521–52.

170. Wietrzynski W, Schaffer M, Tegunov D, Albert S, Kanazawa A, Plitzko JM, et al. Charting the native architecture of Chlamydomonas thylakoid membranes with single-molecule precision. eLife. 2020 Apr 16;9:e53740.

Acknowledgments

First of all, I would like to thank my family (to whom I dedicate this thesis), my parents **Jos van den Hoek** and **Annelies Dassen**, and my sister **Hilde**, for providing an amazing, loving and warm home in which I always felt supported and accepted. Child-like curiosity and sparkly-eyed wonder about the world around us are qualities needed for research/academia. These are delicate traits, grown from a very early age, which need careful and constant fostering to develop. And here we are, so I guess you did something right there! I'm sure this thesis could have been written in Mandarin and you'd probably understand just as much from it, but that doesn't matter; you fully supported me all along and always showed genuine interest in what I do. Last year's been rough on us all, and I made the promise to defend my PhD before my mom's terminal illness got the best of her… and here we are! Hi mom, I'm on TV- ehm, I mean, my paper is out in pre-print form and is currently under revision at a major journal! *waves at imaginary camera*

But what really nudged me towards science: having two chemists as grandfathers, **Anton van den Hoek** and **Laurens Dassen**. Unfortunately, I was too young to learn from Anton before his passing, but Laurens has absolutely filled in for him ever since. I fondly remember sitting down as an 8-year old kid, going through the basics of carbon chain chemistry and petroleum refinery. I barely understood it at the time, but seeing someone so passionate about scientific topics really inspired me. Also it gave me a head start in my school career, eventually leading to pursue science more seriously, so I can't thank you enough for that. I'm glad you're still around to see the result.

However, although chemistry was my first love (actually it was volcanology, but let's leave that aside for now), biology was my second. For that, I have to thank my high school biology teachers: **Mr. Willems** and **Mr. Jacobs**. You two made sure I got all the basics right, and instilled a sense of wonder in me, which persists to this day.

Although I chose to study chemistry, it ended up being a great base to explore biology instead. My fellow students thought it was stupid to pursue biochemistry instead of physical chemistry, but that's where I really wanted to go. The hands-on visual world of structural biology was just way better for me than the theoretical world of physical chemistry. I'm sorry, guys! You'll have to blame Prof. Dr. **Piet Gros**, Dr. **Bert Janssen**, Dr. **Martin Lutz**, Dr. **Gert Folkers**, Prof. Dr. **Antoinette Killian** (and others), who made a lasting impression and shaped me into the structural biologist I am today. Talking to Prof. Dr. Piet Gros and Dr. Bert Janssen gave me the idea to dive into the world of cryo-EM and cryo-ET in the first place, and I can't thank you enough for that. I also need to give a quick shout-out to my previous project supervisors, Dr. **Jonas Dörr**, Dr. **Remco Rodenburg** and Dr. **Matti Pronker**, who all showed me that being cool and being a structural biologist could easily go hand in hand. You guys are my role models, and shaped me just as much as my professors did.

However, the role model I most importantly need to thank is the next big influence in my scientific career: my current supervisor and mentor, and the original architect of the projects presented in this thesis, Dr. **Ben Engel**. I had no idea what I was getting into, when I first was introduced to the concept of biological electron microscopy, let alone moving abroad for the first time simultaneously, getting thrown into the deep end of the pool. We clicked from day 1, at castle Ringberg… I still remember it as if it were yesterday. Entering such a prestigious department, I thought it was going to be all serious and suits from here on. But you showed me the real, fun, exciting, wondrous, and most importantly, *human* side of science, and what it means to be an academic (and that suits don't mix with scientists, I know right…!). I had originally planned to move on after my first half-year internship here, but you asked me to stay for a PhD. I thought "oh why the hell not, he's great to work with", and I'm so, so glad that I did. You did SO MUCH to support me and lift me up. Send me off to conferences. Challenge me. Get the best out of me. You're one of the best, most humane and genuinely awesome bosses anyone can wish for. And learn from! Cheers dude, I can't thank you enough!!!

Now, nothing of this would be possible without good funding and a properly established working environment. For that, I have to thank my real “Doktorvater”, Prof. Dr. **Wolfgang Baumeister**. Without Prof. Baumeister, this department and the current state of biological cryo-EM would be but a fever dream. The quality of research that came (and still comes) from this department is phenomenal, and I have to thank you for that. However, the department would be incomplete without Prof. Dr. **Jürgen Plitzko**, who takes care that the social environment goes above and beyond, and makes sure our bellies are filled with a beer or two on free Friday evenings. Thank you, and cheers! Also many thanks to the admin team at Helmholtz Pioneer Campus, who accommodated, funded and genuinely supported us the last couple of years or so. Dr. **Thomas Schwarz-Romond** and **Stephanie Montag**, you guys rock!!!

Huge thanks go out to my collaborators, on whom I relied to get our projects working and who had the complementary expertise to make them a success. Science is teamwork, and you’re an amazing team to work with! **Nikolai Klena** and **Gonzalo Alvarez Viar**, you’re awesome dudes and I loved hanging out with you on Titan and at conferences. Always a blast to be around you two, I hope we get to hang out on many more occasions! **Mareike Jordan** and **Maeva Le Guennec**, you taught me so much in those few weeks we spent on data analysis. I really look up to you and the work you did, which paved the way for my own. **Garrison Buss**, we got some real hands-on time during my stay in Stanford University, and I had so much fun with you. The birthday burger after a long but successful day of plunging cells was delicious (that particular batch of cells actually led to the best tomograms!). Hope to see you all again soon, and continue working on future projects!! Or just hang out at a conference, with a beer in hand ☺

Also huge thanks to the group leaders who made these collaborations possible. Prof. Dr. **Paul Guichard** and Dr. **Virginie Hamel**, I love that we could share insider jokes about Slipknot and the nine-pointed star on the *Chlamy* paper. Dr. **Gaia Pigino**, you’re such an enthousiastic and energetic group leader, I always enjoy your company! And Prof. Dr. **Tim Stearns**, with an encyclopedic knowledge about everything and all things “cilia”, and being just a really chilled out person to be around. I absolutely loved working together with all of you, and still do. Let’s keep this (IFT?) train rolling!

Thanks go out to my amazing friends (shoutout to my old study mates: the PG whatsapp group), concert buddies, and housemates, keeping me sane throughout the PhD. Especially my best friend **Rike**, who I met at the very beginning of my time at this lab. You opened up a whole world full of adventure and wonder for me. You know me through and through, we’ve been there for each other always, both during the good times and the bad. Our crazy travels are simply the best… I’m so glad we’re still going strong!!! Let’s keep that up! Cheers to many more years of exploring the wonders of this world together ☺

And last but not least: infinite thanks to my absolutely amazing labmates, both in the Baumeister department and the Engel lab! **Sahradha** and **Will**, and now **Ricardo**, you got me started in data analysis, which was a very steep learning curve for me… but you guys pulled it off! **Christos** and **Matthias**, thank for being such great friends in general, but also for helping my stressed self out with paperwork and generally providing super helpful tips for writing this thesis and preparing the defense (also to **Annika!**). **Lenka** and **Ricardo**, thanks for proofreading parts of this work which I wasn’t yet super familiar with. And of course: **EVERYONE ELSE at the Baumeister/Engel labs**, whom I regularly (used to) hang out with, playing volleyball, a game of kicker, or gathering for Friday evening beer sessions. I really miss going crazy at get-together parties with you, shouting along with our favourite 2000s angsty teen metal tunes… I wish we could’ve enjoyed a couple more of those. As I’ve spent quite some time in this department, there are too many names to call out, but you know exactly who you are. You guys really are the beating, social heart of this amazing department. I’m sad that our time together is almost over, but let’s absolutely stay in touch. I’ll miss you deeply.

And finally, thank you, **dear reader**! I hope you enjoyed my work ☺ Cheers!

Best wishes,

Hugo